Realtime Monitoring and Stability Diagnosis of Cutting Process by Applying Disturbance Observer

February 2016

A thesis submitted in partial fulfilment of the requirements for the degree of Doctor of Philosophy in Engineering

Keio University

Graduate School of Science and Technology
School of Integrated Design Engineering

Ryo Koike

Table of Contents

Parameters

Roman symbols

a	actual number
$\boldsymbol{A}(t)$	2×2 directional dynamic force coefficient matrix
$\boldsymbol{A}_0$	average value matrix for $\boldsymbol{A}$
$\boldsymbol{A}_0{}^*$	2×2 matrix defined as $[\boldsymbol{A}_0{}^*] = 1/2\pi\,[\boldsymbol{A}_0]$
a_{cut}	axial depth of cut
a_k	Fourier cosine series coefficient at frequency k
a_{lim}	critical depth of cut
$\boldsymbol{A}_m$	frequency component of m in $\boldsymbol{A}$
b	actual number
b_k	Fourier sine series coefficient at frequency k
$b(\phi_i)$	function to determine whether tooth immerses workpiece
C	constant value
c	actual number
c_0, c_1	coefficients of eigenvalue equation
c_x	damping coefficient in X direction
c_y	damping coefficient in Y direction
C_z	Coulomb friction force on driven stage
$C_{\theta z}$	Coulomb friction torque on screw in Z-axis ballscrew-driven stage
d	actual number
D_z	damping coefficient in driven stage
$D_{\theta z}$	damping coefficient of screw in Z-axis ballscrew-driven stage
$E[h']$	expectation value of $h'[n]$
F	radius of circular orbit
f	analyzed frequency
$\boldsymbol{F}_c(t)$	2×1 cutting force matrix
F_{cut}	cutting force in axial direction
F_{reac}	reaction force applied to driven stage by screw
F_{ri}	cutting force in radial direction
F_s	sampling frequency
F_{ti}	cutting force in tangential direction

F_x, F_y	x and y components of total dynamic cutting forces
F_{xi}, F_{yi}	x and y components of cutting force
$\boldsymbol{G}$	2×2 transfer function matrix
g	gravity acceleration
g_{dis}	cutoff rotational frequency of a low-pass filter in disturbance observer for cutting torque estimation
g_{disz}	cutoff rotational frequency of a low-pass filter in disturbance observer for cutting force estimation
g_{LPF}	cutoff rotational frequency of low-pass filter in pseudo differential to estimate rotational speed of motor shaft
g_{LPFz}	cutoff frequency of low-pass filter in pseudo differential to estimate rotational speed of screw in ballscrew-driven stage
$G_{xx}, G_{xy}, G_{yx}, G_{yy}$	components of transfer function matrix $\boldsymbol{G}$
$H(f)$	Fourier transform of $h(t)$ at frequency f
$H'[k]$	discrete Fourier transform value of $h'[n]$ at frequency k
$\boldsymbol{H'[k]}$	$k \times 1$ matrix having from $H'[0]$ to $H'[k-1]$ as its components
$h(t)$	time-domain signal
$h'[n]$	discretized signal about $h(t)$
$\boldsymbol{h'[n]}$	$n \times 1$ matrix having from $h'[0]$ to $h'[n]$ as its components
$h'_1[k], h'_2[k]$	temporary values during calculating fast Fourier transform
$\boldsymbol{h'_1[k], h'_2[k]}$	$k \times 1$ matrixes having from $h'_1[0]$ to $h'_1[k]$ or from $h'_2[0]$ to $h'_2[k]$ as their components respectively
h_c	uncut chip thickness
$H'_k[n]$	discrete Fourier transform value from $h'[n]$ to $h'[n+N-1]$ at frequency k
$\boldsymbol{I}$	identity matrix
i	integer number
I_a	motor current
$I_{h',k}[n]$	imaginary part of $M_{h',k}[n]$
J	inertia about motor shaft
j	imaginary unit defined as $j = \sqrt{-1}$
$J_{\theta z}$	inertia moment of screw
K	coupling stiffness in ballscrew-driven stage
k	frequency in discrete Fourier transform
K_c	cutting force coefficient in tangential direction
K_i	integer gain in P-PI controller
K_c	proportional gain for position in P-PI controller

K_r	cutting force coefficient in radius direction
K_t	motor torque coefficient
$K_{t\theta z}$	torque coefficient of servo motor for a screw in Z-axis ballscrew-driven stage
K_v	proportional gain for velocity in P-PI controller
k_x	stiffness in X direction
k_y	stiffness in Y direction
l	lead of screw
M	natural number
m	integer number
$M_{h',k}[n]$	moving Fourier transform value about from $h'[n]$ to $h'[n+N-1]$ at frequency k
M_x	mass of driven stage in X direction
M_z	mass of driven stage in Z direction
N	number of sampling points in analyzing window
n	integer number
N_r	spindle rotation in a minute
N_t	number of tooth
$O(*)$	landau symbol
p	constant value
$PS(k)$	power spectrum of discrete Fourier transform at frequency k
R	translation coefficient between screw and stage in ballscrew-driven stage
$\boldsymbol{r}(t)$	2×1 tool displacement matrix
$\boldsymbol{r}_0$	2×1 matrix of tool displacement at previous tooth period
$R_{h',k}[n]$	real part of $M_{h',k}[n]$
$\mathbf{R_m}(\omega_0, t)$	2×2 rotational matrix at $\omega_0 t$
s	complex variable in Laplace transform
s_t	feed per tooth
$\mathbf{S_{xy}}(t)$	2×1 matrix of time-domain signals
$\mathbf{S_{xy}}'[n]$	discretized $\mathbf{S_{xy}}(t)$
$\mathbf{S_{xy\_\omega_0}}$	2×1 matrix of frequency-domain signals about rotational frequency ω_0
$\mathbf{S_{xy_{out}}}(t)$	output of rotational filter
$\mathbf{S_{xy_{out}}}'[n]$	output of rotational digital filter
T	sampling time
t	time
T_a	time interval for integral process
T_{dis}	disturbance torque
T_{ext}	external torque

T_{fric}	friction torque
T_{int}	inertia torque
T_L	length of tool life
T_l	load torque
T_m	motor torque
T_p	tooth period
$V[h']$	variance of signal $h'[n]$
v	cutting speed
v_i	displacement of tool in radial direction
v_{i0}	dynamic displacement of previous tooth period
v_z	velocity of stage in ballscrew-driven stage
W	twiddle factor defined as $W = \exp(-j2\pi/N)$
$w(t)$	window function
$w_n'[n]$	discretized $w_n(t)$
$\boldsymbol{W^{nk}}$	$k \times n$ matrix having twiddle factor of $\exp(-j2\pi nk/N)$ as its components
$x(t)$	x component of time-domain signal on an XY plane
$x'[n]$	discretized signal about $x(t)$
$X_f(\alpha, \beta)$	continuous wavelet transform of a signal $x(t)$ at a scale coefficient α and translational value β at frequency f
x_t	displacement of tool in feed direction
X_{ω_0}	radius component at rotational frequency ω_0
$x_{\omega_0}(t)$	radius component in time domain on rotating coordinate at ω_0
$y(t)$	y component of time-domain signal on an XY plane
y_t	displacements of tool in feed and normal directions
Y_{ω_0}	tangential component at rotational frequency ω_0
$y_{\omega_0}(t)$	tangential component in time domain on rotating coordinate at ω_0
z	position of stage in ballscrew-driven stage

Greek symbols

α	scale coefficient for wavelet transform
$\alpha_{xx}, \alpha_{xy}, \alpha_{yx}, \alpha_{yy}$	directional dynamic milling force coefficients
$\alpha_{xx}{}^*, \alpha_{xx}{}^*, \alpha_{xx}{}^*, \alpha_{xx}{}^*$	components of $\boldsymbol{A_0}^*$
β	translational value for wavelet transform
δ	inverse-tangential value of κ
ΔJ	variation in inertia about motor shaft

ΔK_t	variation in motor torque coefficient
ε	phase shift between inner and outer modulations
θ	rotational angle of motor shaft
θ^{cmd}	angle command value of motor shaft
θ_{dif}	phase difference between X- and Y-components
θ_{init}	initial phase of a signal moving in a clockwise circular orbit on an XY plane
θ_z	rotational angle of screw in ballscrew-driven stage
κ	ratio between Λ_I and Λ_R
Λ	eigenvalue of characteristic equation
Λ_R, Λ_I	real part and imaginary part of eigenvalue Λ
μ	ratio between inner and outer modulations
σ	standard distribution of estimated disturbance jerk
τ	time operator for integration
τ_{reac}	reaction torque from driven stage to screw
ϕ_i	tool edge angle in milling model
ϕ_{st}, ϕ_{ex}	start and exit immersion angles
$\psi(t)$	mother wavelet
$\overline{\psi}$	conjugate complex of ψ
Ω	rotational speed of tool
ω	rotational speed of motor shaft
ω_0	rotational speed of a signal moving in a clockwise circular orbit on an XY plane
ω_c	rotational frequency of chatter
ω_{in}	rotational frequency of input signal
ω_t	tooth passing frequency
$\omega_{\theta z}$	rotational speed of screw in Z-axis stage

Superscripts

ref	reference value
$\widehat{}$	estimated value
$'$	discretized value

Subscripts

n nominal value

Abbreviations

CWT   Continuous Wavelet Transform

DFT   Discrete Fourier Transform

FFT   Fast Fourier Transform

MFT   Moving Fourier Transform algorithm

MV   Moving Variance algorithm

MV+MFT   integration of Moving Variance and Moving Fourier Transform

algorithms

NC   Numerical Control

PPR   Pulses Per Revolution

RDF   Rotational Digital Filter

SDFT   Sliding Discrete Fourier Transform

STFT   Short-Time Fourier Transform

1 Introduction

1.1 Key Technology for Intelligent Machine Tools

Development of numerical controlled (NC) machine tools has greatly contributed to progress in the production fields by providing a highly accurate and efficient machining process with precise motion control of the spindle and machine tool stage. Integrating a computer-based calculation technology, the NC machine tool was invented in 1952, and its functionality has progressed to become more adaptive to machining of various production shapes [1]. The repeatability of the NC machine tool is very high such that it can help manufacture large quantities of a product, all with the same quality, although for a long time, the machining accuracy depended on a worker's skill. Owing to these characteristics, the NC technique is now being widely applied to various machining processes such as cutting, grinding, polishing, laser machining, injection molding, and stamping. Additionally, combined and multi-axis machine tools have started being used in recent times to reduce the total machining time, making the NC technique more indispensable to performing several kinds of complex operations simultaneously [2].

In particular, the improvement of the machining resolution is one of the most important considerations because the accuracy of products abundantly depends on the machine tool's performance. Known as the "mother principle" [3], this principle indicates that higher machining resolution contributes directly and greatly to the progress of all research fields by providing new devices with an unprecedented accuracy, efficiency, and functionality. Moreover, increased production efficiency provides large economical and environmental benefits by reducing the energy consumption for machining. A ubiquitous technology is also being considered to realize a novel machining system that can be easily and safely deployed depending on the needs of the user. To satisfy these demands, many researches have been focusing on higher functionality of NC machine tools to enhance production efficiency, to achieve hyper-precise machining, to ensure safety, to guarantee high usability, and to develop a novel machining technique for difficult-to-cut materials.

Although the NC machine-tool technology has greatly progressed following the

research on manufacturing, unmanned machining causes unanticipated problems among industrial fields. Because several machining processes are automated by using the NC technique, accidents and aberrance during machining become difficult to detect manually. Although the NC machines possess the capability to execute the preprogrammed NC commands accurately, they continue to perform these commands even after unexpected situations, such as tool breakage and wrong tool-path planning, occur. In the worst case, a serious accident including injury or death occurs and the machine structures are damaged irreparably. Therefore, the development of a special function to recognize the machining state and enable the NC machine tools to maintain the stability and safety of processes is in strong demand. Also, highly accurate identification of mechanical characteristics is necessary for the optimum configuration of machining control. As a high-end technology to ensure hyper-usability and safety, the development of a self-diagnosis method needs to be acquired to identify the optimum machining condition easily without expert knowledge and skills, such that the NC machine tool has its own intelligence. These concepts are expected to lead to what is referred to as the "intelligent machine tool," and that is why many studies are geared toward process monitoring and system identification [4-8].

From a practical viewpoint, a process monitoring system needs to be adaptive to various problems in realtime without complex sensor systems and complicated operations. Moreover, a system identification method should be easy to perform and be applicable to most NC machine tools. Thus, this research provides a novel sensorless technique for aberrance detection during machining and efficient system identification by using servo information. In particular, the developed sensorless process monitoring system focuses on four types of problems with cutting: tool wear, tool collision, tool fracture, and chatter vibration. Furthermore, a self-diagnosis method for identifying a stable cutting condition is also proposed, which is feasible without any sensor devices and expert knowledge on the machining process.

This chapter discusses four types of problems related to cutting that this research focus on. In addition, recent studies on these problems are explained to clarify new challenges to this research.

1.2 Problems in Machining

Some accidents in machining are induced by human error and may be preventable by performing repeated reviews of how workers operate, to avoid wrong operations. However, some problems during cutting are unavoidable because they are caused by time-dependent deterioration. In either case, causes and mechanisms of each problem must be comprehended to develop an efficient detection or avoidance method. In this section, four types of problems with cutting—the focus of this research—are explained in detail.

1.2.1 Tool Wear

Tool wear, a problem that persists for a long time, is one of the unavoidable problems, until a material that never wears out can be invented. Tool wear occurs more particularly at the tool edges as shown in Fig. 1-1, which is an example of wear on a drill. According to Japanese Industrial Standards, every type of tool wear is defined for each tool as shown in Fig. 1-2 [9]. If an overworn tool continues to be used, it easily leads to a serious accident such as tool breakage. Therefore, the worn tool has to be changed at a proper time by monitoring the degree of wear progress in realtime.

Tool wear is commonly categorized according to its mechanism and worn point. Based on the mechanism, tool wear is categorized into abrasion, adhesion, diffusion, and chemical wear. These causes of tool wear are generally explained as follows [10].

Abrasion Wear

Abrasion occurs when a harder material (i.e., the tool) shears away small particles from the softer work material. However, the softer work material also removes small particles from the tool material, although at a smaller rate. The harder particles are caught between the hard tool and soft work material, causing
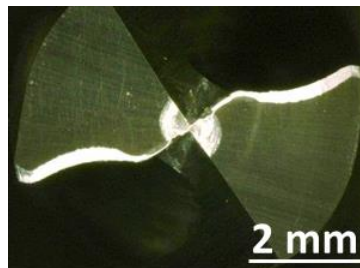

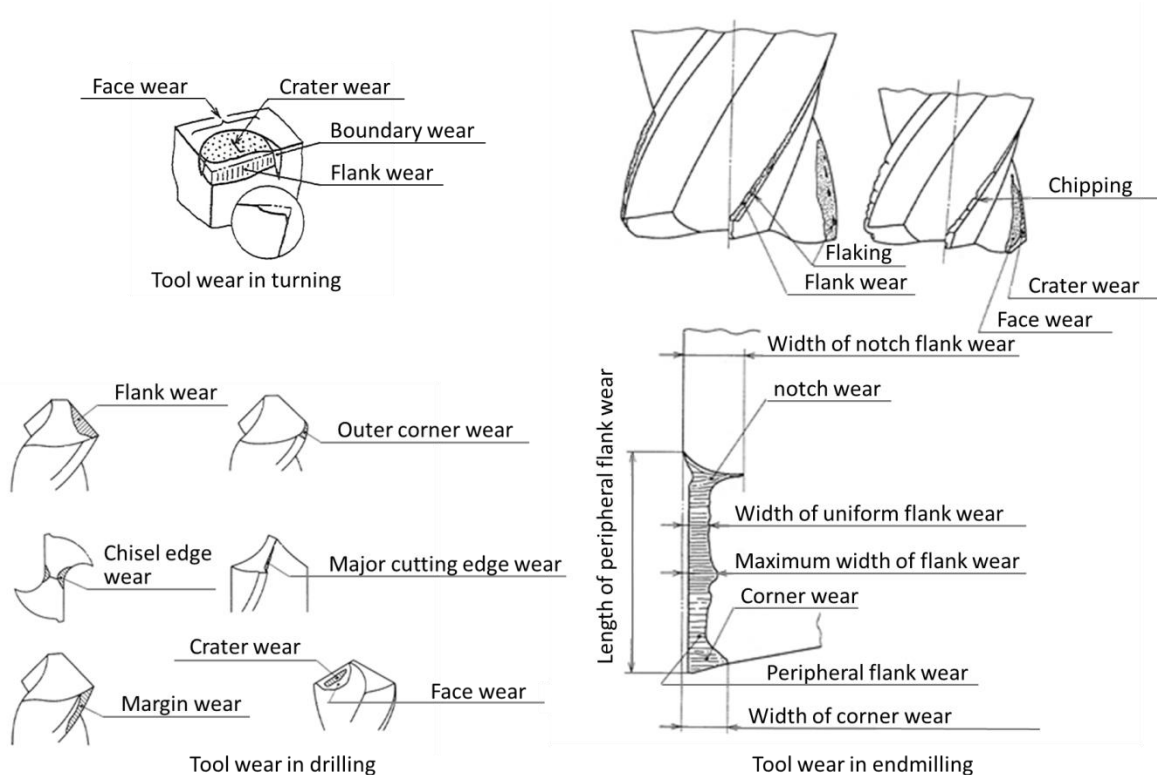Fig. 1-1 Chisel edge wear and flank wear.

Fig. 1-2　Definition of tool wear by JIS (Japanese Industrial Standards) [9].

additional abrasion wear. Tool and work materials contain carbides, oxides, and nitrides with hard microstructures; these cause abrasion wear during machining.

Adhesion Wear

Adhesion wear occurs when there is a relative motion between the two bodies that are under normal load and fragments of the softer work material adhere to the harder tool. The adhered material is unstable, separates from the cutting tool, and tears small fragments of the tool material. (omitted).

Diffusion Wear

Diffusion wear occurs when the temperature of the tool and of the work materials increases at contact zones. Because of this, the atoms in the two materials become restive and migrate to the opposite material where the concentration of the same atom is lower. (omitted).

Oxidation Wear

Oxidation wear occurs when the atoms in the cutting tool and/or work material form new molecules at the contact boundary where the area is exposed to the air (i.e., oxygen). Tungsten and cobalt in the cutting tool are oxidized close to the work surface-cutting tool flank, which leads to notch wear on the cutting tool. (omitted). [10]
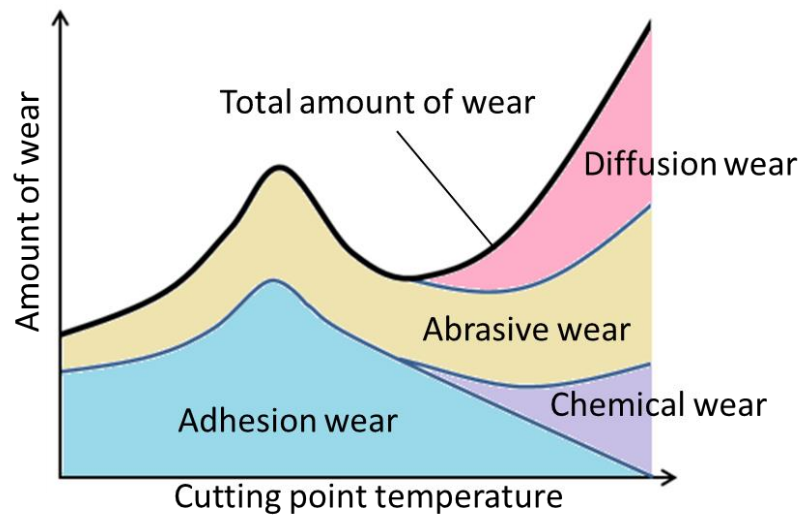
4

Fig. 1-3 Contribution rate in tool wear progress [11].

Regarding the contribution rate to tool wear progress, it is described as a function of the cutting point temperature as shown in Fig. 1-3 [11]. The total amount of wear increases at higher temperatures of the cutting point. Although it is clear from this relation that tool life can be expanded by using a lower cutting speed to suppress the heat generation because the total amount of wear increases at higher temperatures of the cutting point, it is not a fundamental solution because tool wear itself is unavoidable completely and cutting efficiency gets definitely lower.
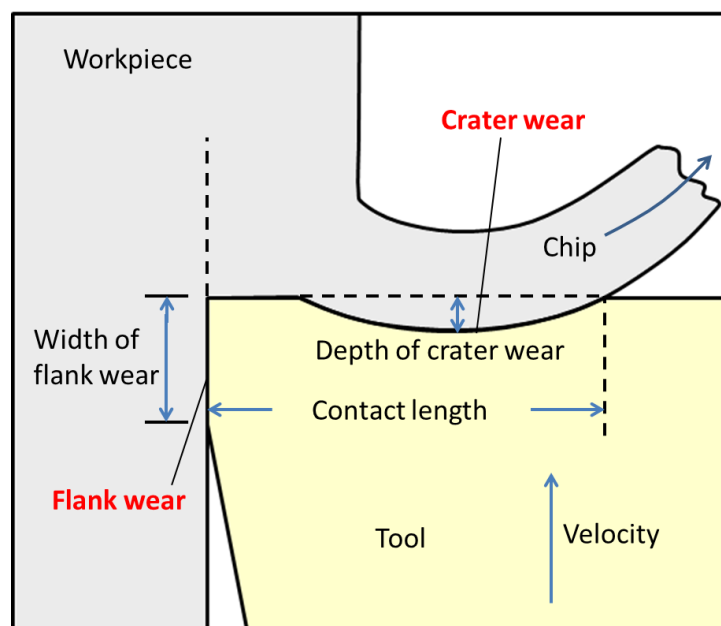

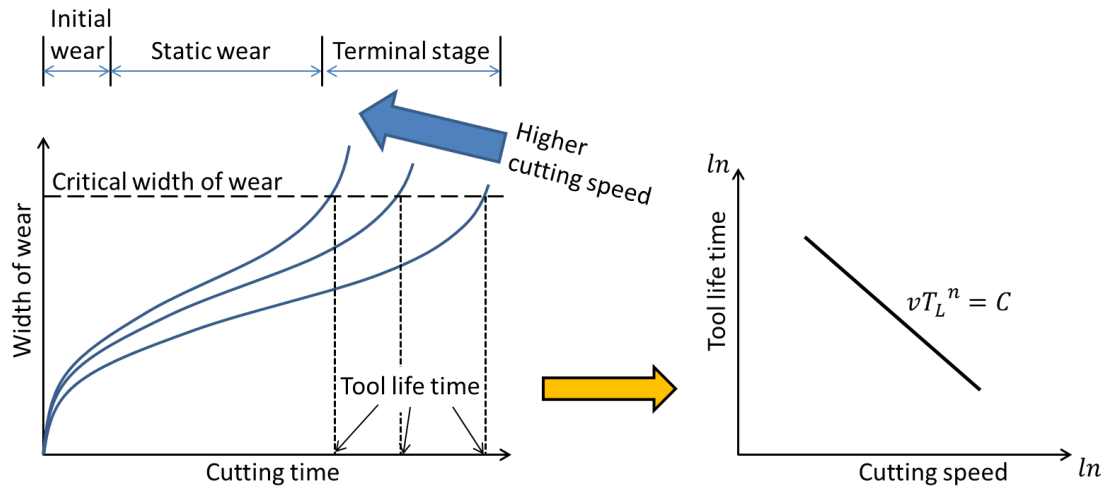**Fig. 1-4 Orthogonal cutting model [10].**

5

Fig. 1-5　Progress of flank wear [11].

In an orthogonal cutting model, tool wear can be categorized into crater wear and flank wear depending on which face is worn [10]. A wear promoted on a rake face is called crater wear, and that on a flank face is called flank wear as shown in Fig. 1-4, which depicts the orthogonal cutting model. Because of the flow direction of the chip and the cutting direction, the depth of crater wear and the width of flank wear gradually increase with machining time. In particular, the width of flank wear is comparably easier to measure and be used as a criterion to evaluate tool wear progress quantitatively [12-14]. Figure 1-5 shows primary flank wear progress according to machining time [11].

To predict the tool life limitation, Taylor experimentally derived a comprehensive tool life equation as follows [15]:

$$vT_L^p = C \tag{1-1}$$

where v [m/s] is the cutting speed, T_L [s] is the length of tool life, and p and C are constant values. By determining the values for the parameters p and C, it is possible to estimate tool life approximately. However, the repeatability of machining is not so high that p and C cannot be identified accurately even under the same cutting conditions because of the small individual difference in the tool and the work material. Therefore, process monitoring is important to determining a proper time to change the tool.

1.2.2　Tool Collision

NC machine tools have the characteristic of faithfully executing a premade NC

program, even if wrong commands are included in the program in error, e.g., a sign mistake, a wrong coordinate option, and an improper cutting condition. These mistakes can easily lead to a serious accident such as a collision between the mechanical structures.

Tool collision monitoring is of great importance for preventing damage to mechanical structures such as spindles. Although tool collision would be an avoidable problem if the program and the process are carefully checked, 60 % of severe spindle failures are in fact traced back to operator-induced collision between moving parts of a machine tool (Fig. 1-6) [16, 17]. Considering that the usage of multi-axis combined machine tools is gaining wide acceptance now, this rate is likely to increase in the near future because of complicated tool-path planning. The spindle components undergoing maximum damage from a collision
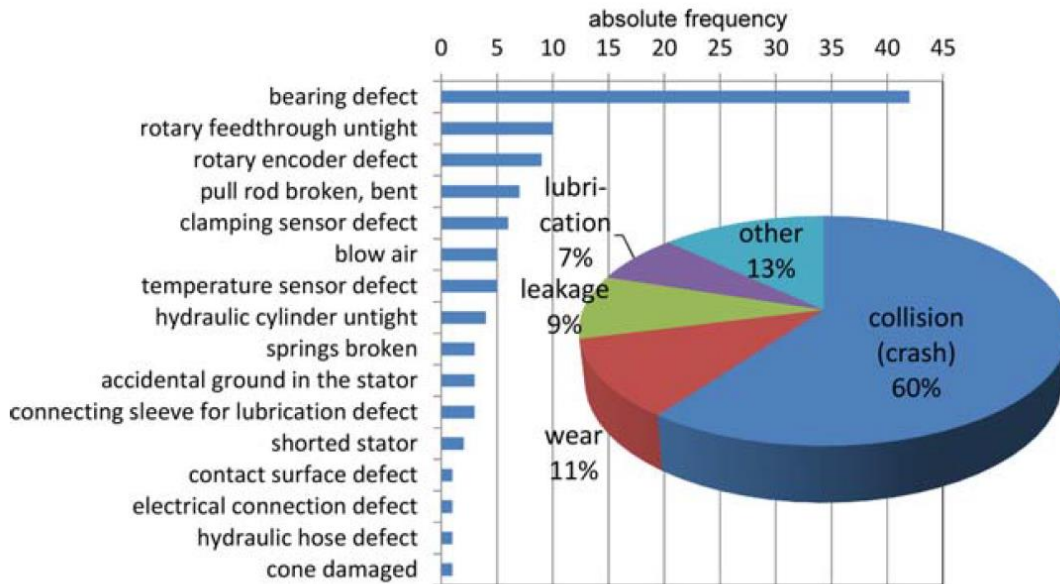
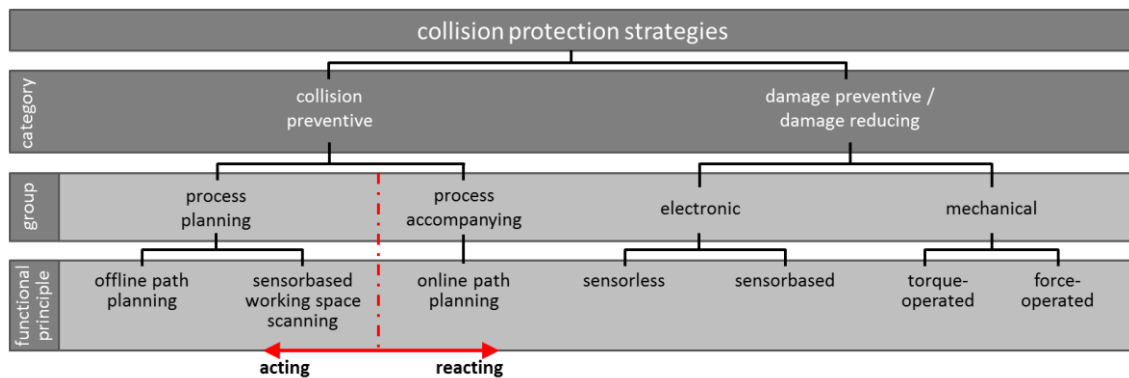Fig. 1-6   Failure causes of and damage to motor spindles [16].

Fig. 1-7   Overview of protective measures [18].

are rolling-element bearings. Because the contact areas between the rolling elements and the inner and outer races are small, the reaction forces during a collision per unit contact area may exceed the allowable interface pressure, which leads to initiation and propagation of cracks [18].

Abele presented an overview of collision protection strategies as shown in Fig. 1-7 [18]. The countermeasures against tool collision are categorized into two groups: prevention methods and damage-reduction methods. The prevention methods aim to avoid collision by using preliminary investigation of the process plan such as the tool path, cutting condition, and coordinates of the tool and workpiece. Some studies proposed a realtime collision prevention system by simulating the tool path by using a 3D model created from CAD/CAM [19, 20]. As a sensor-based method, Zhang proposed a stereo vision system with charge-coupled device cameras to create a 3D model [21]. Byrne proposed a collision avoidance method by measuring the relative distance between the tool and the workpiece by using an ultrasonic sensor [22]. Furthermore, some studies were carried out to simplify the complicated calculation for the 3D modeling [23]. Although these methods can certainly reduce collision in machine tools, they require much analysis time for accurate prediction and cannot avoid some collisions caused by unpredictable conditions such as tool breakage and inadequate settings of the workpiece and tool. Some collisions are avoidable by the scanning method using special measurement devices, but complex operations and measurement time are required to create the 3D model. If a wrong operation is performed during the measurement, the collision cannot be avoided completely. From this viewpoint, not only the prediction methods but also the damage reduction methods should be implemented simultaneously.

Presently, the available technical solutions for collision monitoring are as follows: bearing sensor rings embedded into the spindle motor [22], spindles that are lifted or tilted mechanically in the case of collisions [18], and ultrasonic and capacitive sensors [24]. Except when mounting the special mechanical structures, to reduce damage and avoid a secondary accident, the machine tool has to be stopped after a tool collision as soon as possible, i.e., high responsivity and reliability are necessary for collision detection. However, additional sensors, which lead to frequent maintenance and an increase in the failure rate, are undesired from the practical viewpoint. Furthermore, the detection method should be applicable even to unpredictable collisions in realtime.

To satisfy these demands, simplification can be an important challenge for

collision detection methods.

1.2.3   Tool Fracture

Tool fracture (Fig. 1-8) generally occurs when overload is applied to the tool edge. In other words, it is a beneficial criterion to evaluate the adequacy of the cutting condition, although tool fracture sometimes occurs even under a proper cutting condition because of non-uniformity of work materials, individual differences of the tool, and runout of the spindle shaft. In either case, the fractured tool should be changed as soon as possible because it can easily lead to tool breakage and a worse cutting accuracy, e.g., a larger burr and machining error, and lower machined surface quality. Particularly when drilling with a fractured tool, thread-shaped chips occur, entwine, and injure the workpiece surface and the tool holder as shown in Fig. 1-9.

However, the fracture on a tool edge is difficult to detect in realtime. In the case of a large fracture, the variation due to unstable machining such as larger vibration and unusual machining sound are certainly available signals for the detection. However, no remarkable change occurs during machining by using a tool having a small fracture and the process can continue. In order to detect small fractures, a direct observation using a microscope would be one of the most reliable approaches, but it is an impractical method because it requires frequent machining stoppage.

To detect tool fracture in the process, some researchers have proposed sensor-based detection methods. In an interrupted process like milling, the
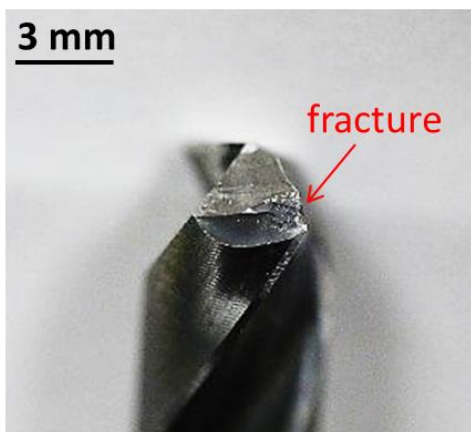

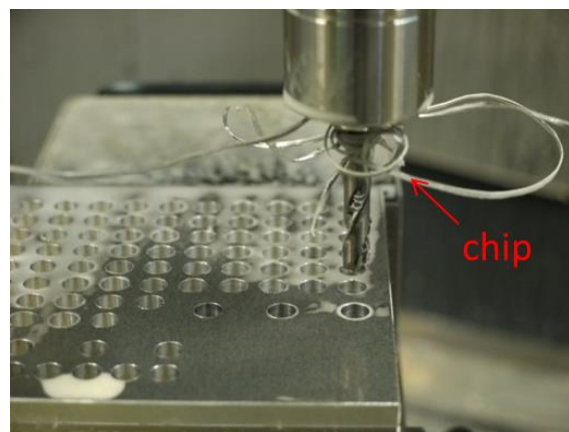Fig. 1-8   Fracture on a tool edge.   Fig. 1-9   Snuggling chips.

fractured edge induces a smaller cutting force than do the other non-fractured edges because the fractured edge cannot ensure enough depth of cut. Therefore, a tool edge fracture is detectable by measuring the cutting force or acoustic emission and applying a frequency analysis like Fourier transform [25-28]. In contrast, drill fracture detection is comparably difficult because the process is continuous and the fracture-induced change is infinitesimal. Furthermore, the sensor mounting space is strictly regulated in the general drilling process using cutting oil. Therefore, not only high accuracy but also the potential of application to the machining condition is a necessary consideration for the tool fracture detection method. Although several researchers showed that a drastic change in cutting force is detectable by using a dynamometer or an acceleration sensor when a tool breakage occurs [29-31], the author could not find a proposal that focuses on small tool fractures in drilling and clearly defines a relation between the scale of fracture and the fracture-induced variation in sensor signals.

1.2.4 Chatter Vibration

Chatter vibration exponentially grows because of interaction between the mechanical transfer function and the cutting process, and causes large dynamic displacements between the tool and workpiece. As a result, tool life reduces and machined surface quality deteriorates as shown in Fig. 1-10. Many studies have been conducted to clarify the chatter mechanism and analyze the stable cutting condition.

The main causes of chatter vibration are the "regenerative effect" and "modal coupling." The regenerative effect is a process involving uncut-chip thickness
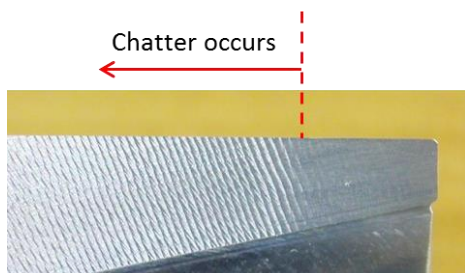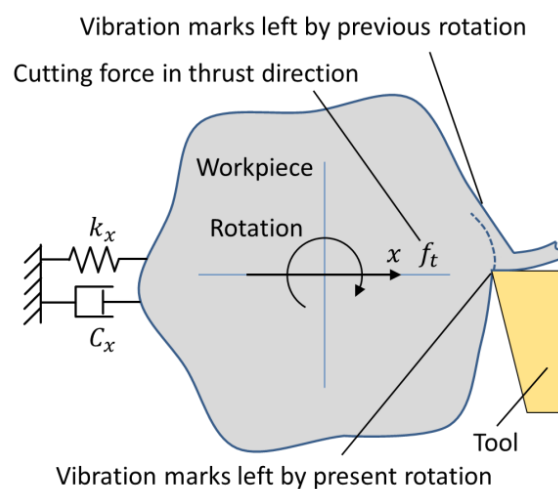
Fig. 1-10   Chatter mark on a machined surface.

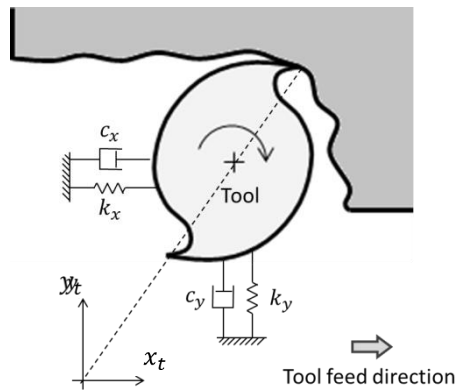Fig. 1-11   Regenerative effect in turning.

10

Fig. 1-12 Example of a rotational tool.

variation due to the surface waviness modulated by the previous cutting cycle as shown in   Fig. 1-11 [32]. Modal coupling is defined as an integration of some frequency modes and mainly occurs during machining with a rotational tool. In particular, the regenerative effect occurs in most cutting processes and generates self-excited chatter vibration. Many researches have focused on the regenerative chatter mechanism during the past few decades, e.g., Merritt theoretically explained the mechanism of self-excited chatter generation for an orthogonal cutting model [33]. Furthermore, several studies enhanced the prediction accuracy by introducing a dynamic cutting force effect to the cutting model [34, 35]. Compared with the continuous process, the interrupted process is difficult to analyze in the frequency domain. For the milling process, Altintas and Budak finally established a prediction method for chatter stability in 1995 [36], which is cited by many other researchers.

In contrast, modal-coupling-type chatter occurs because of the coupling of two vibration modes that have almost the same resonance frequency. It tends to occur when a long-type tool is used because the vibration modes normal to each other sometimes have similar modal parameters [37-39]. When cutting with a rotational tool like a milling tool as in Fig. 1-12, vibration in one mode easily affects another mode because of the tool rotation. However, modal-coupling-type chatter is rare compared with regenerative chatter, because its excitation condition is more strictly limited than the regenerative effect.

In both cases, information on the modal parameters of the tool or the workpiece is necessary to predict chatter stability. However, stability prediction sometimes does not agree with a real process because of identification errors for modal parameters. Therefore, accurate chatter detection and the identification of stable cutting conditions are necessary to ensure machining accuracy.

11

1.3 Process Monitoring Technology

1.3.1 State-of-the-Art Studies

The importance of process monitoring is widely acknowledged and many studies have been conducted to develop an efficient monitoring technology [4-8]. Teti et al. [4] surveyed recent studies for process monitoring and reported that monitoring techniques can be categorized into direct approaches and indirect approaches. Examples of the direct method are measurements by using cameras, radioactive isotopes, laser beams, and electrical resistance to evaluate such as the width of tool wear quantitatively. Although the direct methods certainly guarantee high accuracy of the evaluation of the machining state and the tool condition, these methods are difficult to perform in realtime because of access problems during machining, illumination, and the use of cutting fluid. In contrast, there are some measurable signals that help evaluate the cutting state as shown in Fig. 1-13 [4]. The indirect information is less accurate than direct measurement to monitor the machining state, but comparably easy to obtain by using additional sensors. By comparing signal features, Tlusty and Andrews reported that force information is one of the suitable means for process monitoring [40]. Although the signals close to the process are usually captured by mounting additional sensors on the machining space, this approach requires the
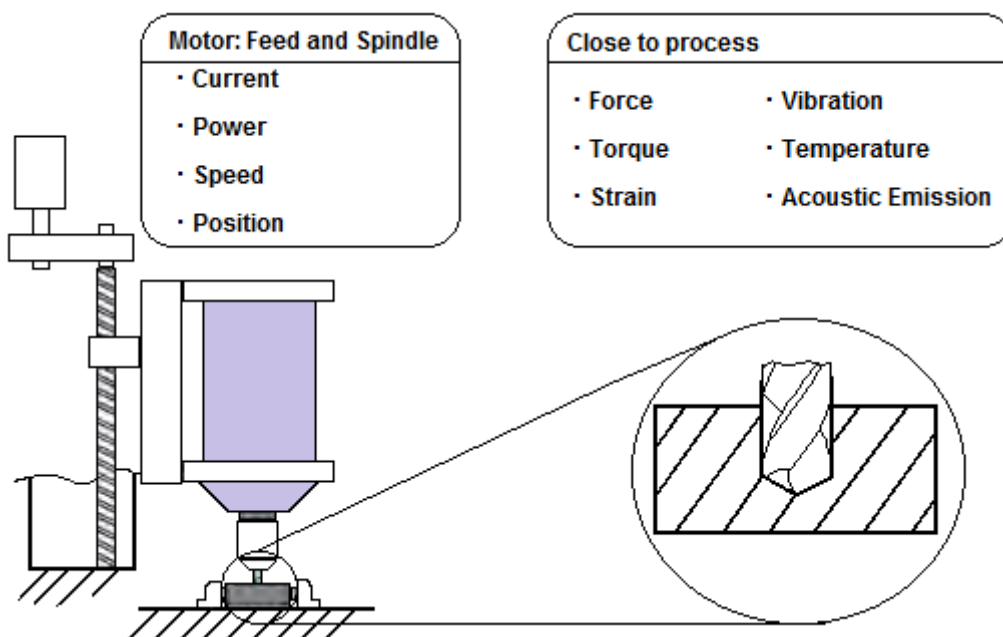

Fig. 1-13   Measurable phenomenon for online sensor monitoring [4].

regulation of the tool-path design, frequent maintenance, and higher cost. In particular, a force sensor mounted between the machine table and the workpiece holder leads to low machine-tool stiffness and machining accuracy because it measures the applied force based on the displacement. In contrast, armature current is used to estimate the cutting force without any negative effects on the machining space [41-43]. However, estimation accuracy is difficult to ensure because armature current information includes considerable noise when a clamp-type current sensor is used and some cutting force information is lost owing to filtering. Therefore, enhancing the monitoring accuracy of the indirect methods is one of the most important issues related to practical applications in industries.

As a new trend in the manufacturing technology, the advent of information technology has enabled a more efficient and sophisticated manufacturing system. For example, "Inderstrie 4.0" in Germany and "Industrial Internet" in the US are national projects to apply IoT (Internet of Things) technology in the industrial fields. In these projects, a super-high efficient manufacturing system by sharing precise demand predictions, an adaptive manufacturing system for varying-lot production of wider-ranging products, and ubiquitous supporting systems are being experimented via IoT. In this trend, the intelligent machine tool is one of the most important key technologies that are capable of gathering machining information as shown in Fig. 1-13, and controlling machining operation adaptively by sharing information with an enormous number of other similar machine tools.

Against this background, recent studies on process monitoring focus on indirect methods that can be easily fitted to machine tools to collect machining information efficiently.

1.3.2 New Challenges

Despite the almost overwhelming scope of monitoring solutions for diverse purposes as presented by scientific literature, industries remain reluctant to implement advanced process monitoring systems because of frequent maintenance, the limitation of the tool path design, and use of cutting fluid [4, 44]. Simplification is required with regard to monitoring algorithms and sensor technology [4, 45]. The "sensorless" approach focuses on using the information

provided by machine tool control and feed drives to carry out process monitoring instead of installing expensive and complicated external sensor systems [46, 47].

Additionally, the monitoring method needs to be an add-on technique, whereby it can be easily installed on commercial machine tools to collect machining information for a new industrial IoT-based system.

From this viewpoint, certain challenges need to be solved for advanced process monitoring:

- The number of additional devices must be as few as possible.
- No devices must be mounted on the machining space.
- Industries' concerns regarding cost and maintenance must be addressed.
- Accuracy that is high enough to detect problems must be guaranteed.

1.4 Identification of a Stable Machining Condition

1.4.1 State-of-the-Art Studies

Not only detection but also analysis is necessary for chatter stability because the mechanism is complicated and the stable cutting condition is difficult to identify. As explained in Section 1.2.4, several studies showed analysis methods of the stable cutting condition with respect to chatter vibration by constructing a cutting model. Compared with an orthogonal cutting model, the milling process is difficult to analyze in the frequency domain because of non-linearity of interrupted cutting. Research on the milling process led to the development of the chatter prediction method in 1995 [36]. In the same manner, several studies applied a frequency-domain model and proposed a stability prediction method for ball endmills [48] and micro tools [49]; a method introducing a process damping coefficient to enhance prediction accuracy in the low rotational region [50]; and a method applicable to continuous spindle speed variation [51]. Furthermore, a time-domain simulation approach is also adopted for a special tool like an unequal pitch cutter, which is difficult to analyze in the frequency domain [52].

However, stability prediction often does not agree with the realtime machining process, in spite of extensive research and improvements as explained before. This gap occurs because of the identification error of modal parameters, which must be accurately identified for the prediction methods that are based on a milling model. Generally speaking, hammering tests are conducted to analyze

modal parameters for a mechanical system. However, the coherence of the hammering test results is difficult to enhance because coherence changes because of a small difference in impact force. Expert knowledge to correctly treat measurement devices is also necessary to obtain an adequate analysis result. Furthermore, by developing a non-contact measurement method with magnetic force, Matsubara et al. [53] experimentally showed that the static stiffness of the tool changes according to the spindle rotation because of heat generation in bearings, centrifugal forces on rotation elements, lubrication oil films at contact points, and so on. This result indicates that stability prediction cannot enhance reliability based on modal parameters during machine stoppage, and that modal parameters should be identified only during machine movement.

In order to obtain high reliability, chatter stability should be identified by using results of real cutting tests, e.g., Quintana described stability lobes diagram by repeating real milling tests on a triangle-shaped workpiece with various spindle rotations [54]. Suzuki proposed an identification method for a transfer function of a mechanical system by applying the inverse analysis method to some milling tests [55]. Although these experimental identification methods are highly accurate and reliable, they warrant measurement devices and special-shaped workpieces and multiple rounds of milling tests.

1.4.2 New Challenges

Experimental approaches should be adopted to ensure identification accuracy involving chatter stability. Furthermore, practicability and usability are also necessary for identification of stable cutting conditions. Thus, the identification method should be simple to use and easy to apply to all machine tools. As a result, certain conditions should be satisfied to develop an efficient identification method.

- Does not require special analysis devices.
- Guarantees high usability.
- Ensures high accuracy.
- Is simple enough to perform.

1.5 Research Purpose

This section summarizes Chapter 1 and explains the purpose of this research.

Manufacturing technologies are still in a progressive state toward enhancing production efficiency and accuracy. These objectives can be met by developing and applying an automation technology for manufacturing systems. In contrast, worker expertise is still indispensable for selecting a proper tool, designing a tool path, modifying cutting conditions, and finishing the product. Although the industries consider automation of these processes vital, they are reluctant because the automation solution requires usage of additional sensors, which are expensive, require frequent maintenance, increase the failure rate, and reduce machine-tool stiffness.

Against this background, this study seeks to develop a sensorless process monitoring system for tool wear, tool collision, tool fracture, and chatter vibration based on the disturbance observer theory, which does not require additional measurement devices. Furthermore, development of a sensorless identification method for a stable cutting condition against chatter vibration is also carried out. In concrete terms, by applying the disturbance observer technique to the spindle and the ballscrew driven-stage control systems in a machine tool, the monitoring systems for cutting force variation due to tool wear, collision force in feed direction, fracture-induced vibration, and chatter-induced fluctuation in cutting force are developed. Additionally, novel signal processing methods named "Rotational Digital Filter" and "Moving Variance and Moving Fourier Transform" are developed to enhance detection accuracy. The practicability of both developed systems is experimentally evaluated with vertical 3-axis machining centers.

The proposed methods only utilize servo information, which is available from the machine-tool controller. It is easy to install on commercial machine tools as one of the programs, and does not require additional measurement devices. As a result, this research has great significance to making process monitoring practical, if detection and identification accuracy for abnormal states in machining is sufficiently high.

1.6 Organization of Dissertation

In Chapter 1, key technologies for intelligent machine tools and problems in machining are introduced. By explaining state-of-the-art technologies for process monitoring and stability diagnosis, the applicability and feasibility of sensorless approaches are clarified from the practical viewpoint, and the purpose of this research is declared.

Chapter 2 provides fundamentals to perform the proposed process monitoring and stability diagnosis methods. Furthermore, two kinds of novel signal-processing methods are proposed for improvement of the aberrance detection accuracy; one is "rotational digital filter (RDF)" which has a special characteristic to extract only a signal moving on a circular orbit in clockwise direction, and the other is "integration of moving variance and moving Fourier transform algorithms (MV+MFT)" which can detect chatter with a small number of computation. Additionally, how to construct a time-domain milling simulator is explained, which is applied to theoretically evaluate the proposed stability diagnosis method.

Chapter 3 summarizes experimental apparatuses and a parallel calculation system for the time-domain milling simulation. Furthermore, the applicability of the proposed method according to the encoder resolution is discussed with a time-domain simulation.

From Chapters 4 to 7 present the proposed process monitoring method for each problem in machining. Chapter 4 shows the cutting force and torque estimation using servo information in each axis ballscrew-driven stage and spindle control systems, which successfully captures the wear-induced increases in cutting force and torque in drilling and tapping in realtime. Applying the cutting force estimation algorithm, Chapter 5 shows that the tool collision can be detected with high responsiveness by monitoring a differential value of the estimated cutting force. Chapter 6 presents that drill fracture is detectable by employing the RDF to the estimated cutting force in X and Y directions. Chapter 7 describes that chatter can be detected independently from forced vibration in realtime by adopting the MV+MFT to the estimated cutting torque information.
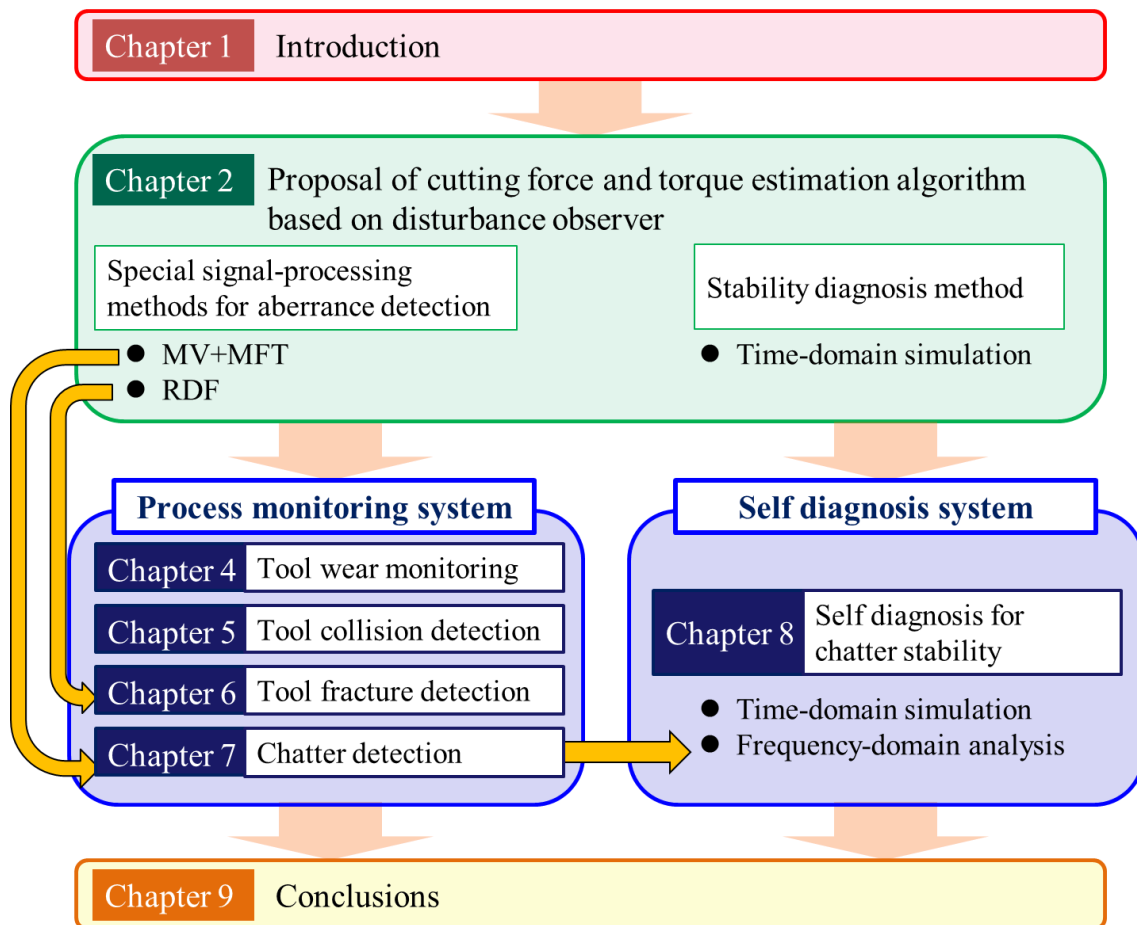
Fig. 1-14   Organization of dissertation.

Chapter 8 contains the experiment and discussion for the proposed stability diagnosis method to identify stable spindle rotations against chatter. The results of side milling tests and the time-domain milling simulation indicate that the stable spindle rotations can be identified by monitoring drastic chatter frequency shifts. Furthermore, the adequacy of the diagnosis result is discussed on the basis of the time-domain simulation and a frequency-domain analysis.

Finally, conclusions of the thesis are summarized in Chapter 9. The above organization of this thesis is summarized in Fig. 1-14.

2 Theories for Process Monitoring and System Identification

2.1 Introduction

A motion control method for mechanical structures in a machine tool must be carefully constructed to archive high machining accuracy, because tool displacements have direct effects on machining errors. Generally speaking, the P-PI control method, which introduces a proportional control (P control) for the angle and a proportional-integral control (PI control) for the angular velocity (Fig. 2-1), is applied to the driven-stage motors and spindles in most machine tools. Furthermore, to enhance the control performance and obtain the sophisticated functionality, modern control theory has drawn attention recently.

The performance of a control system is generally evaluated by two criteria; trajectory performance and robustness [56]. Additionally, positioning accuracy is an important factor for machining control. To enhance the trajectory performance and positioning accuracy, applying feed-forward compensation to a P-PI controller is an efficient method. On the other hand, a higher gain setting is an effective method to enhance the robustness of the control system. In a classical PID control system, the control gain must be increased to enhance the system robustness. However, the higher control gain leads to unexpected vibration and a dangerous movement of the controlled object because of extra-high trajectory performance. Additionally, feed-forward compensation is regarded as a pseudo-enhancement of gain, but the tradeoff relation between the trajectory performance and robustness cannot be fundamentally resolved because it also leads to unstable movement.

Alternatively, the disturbance observer is one of the modern control techniques to solve the tradeoff relation between the trajectory performance and robustness.
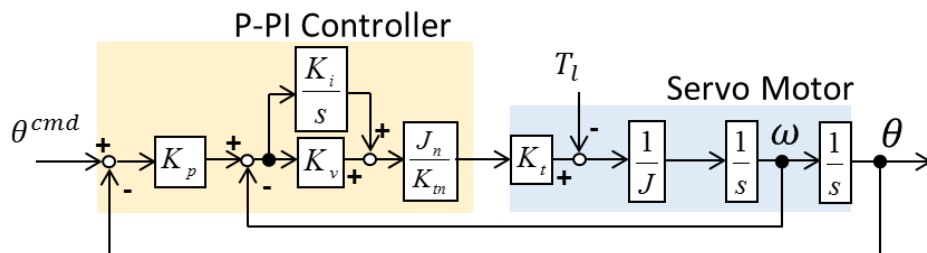

Fig. 2-1   Block diagram of a P-PI controlled system.

The disturbance observer is a technique to estimate a disturbance in a control system only from the servo information and some nominal parameters. The estimated disturbance information is fed forward to the current reference information in order to compensate the disturbance. Moreover, the disturbance observer enables the controller to design the trajectory performance and robustness separately. These merits are the reasons why the disturbance observer is widely introduced to the controllers of industrial robots and electric automobiles, and many studies have applied the disturbance observer to establish a new control theory.

In this study, the disturbance observer is utilized to estimate the cutting force and torque without any additional measurement devices. For a spindle and a ballscrew-driven stage controller, the cutting force and torque can be regarded as a disturbance that interferes with precise motion control. By analyzing the estimated cutting force and torque, process monitoring can be performed and stable cutting condition analysis would be possible. In this chapter, the disturbance observer theory and the analysis methods for the estimated disturbance are explained.

2.2 Disturbance Observer-Based Cutting Force and Torque Estimation

Although the original theory of the disturbance observer [57] is aimed at the robust control of a system, its aspect for disturbance estimation is a focus of this study. This section provides an explanation of disturbance observer theory and how to apply it to cutting force and torque estimations.

To explain the disturbance observer theory, a physical model of a simple drive motor is used. In Laplace domain, the dynamic equation is described as:

$$J\omega s + T_l = T_m \tag{2-1}$$

where J [kg·m²] is the inertia about the motor shaft, ω [rad/s] is the rotational
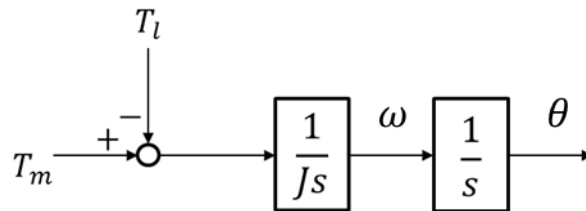

Fig. 2-2   Block diagram of motor.

speed of the motor shaft, T_l [Nm] is the load torque, and T_m [Nm] is the motor torque. The block diagram of this equation can be represented in the Laplace domain as shown in Fig. 2-2.

The load torque contains three kinds of components.

- Inertial torque T_{int}: The load works without contact, such as Coriolis torque and centrifugal torque.
- External torque T_{ext}: The load due to contact, such as reaction torque
- Friction torque T_{fric}: Mainly the sum of Coulomb and viscosity torques

Therefore, the following equation is satisfied.

$$T_l = T_{int} + T_{ext} + T_{fric} \tag{2-2}$$

Assuming that the motor current I_a [A] is regulated by a high-gain current controller and the output current completely coincides with its reference I_a^{ref} [A], the motor torque is described by introducing the motor torque coefficient K_t [Nm/A] as follows:

$$T_m = K_t I_a = K_t I_a^{ref} \tag{2-3}$$

Substituting Eqs. 2-2 and 2-3 to 2-1, the dynamic equation is represented as

$$J\omega s = K_t I_a^{ref} - \left(T_{int} + T_{ext} + T_{fric}\right) \tag{2-4}$$

The inertia moment of the spindle shaft J hardly changes but can vary because of axial runout. Thus, an inertia moment is represented as the sum of the nominal inertia J_n and its variation ΔJ:

$$J = J_n + \Delta J \tag{2-5}$$

The torque coefficient also varies because of magnetic flux distribution:

$$K_t = K_{tn} + \Delta K_t \tag{2-6}$$

By using these parameter variations, torque variations are represented in torque dimension variables as

- $\Delta J s$: changed inertia variation torque
- $\Delta K_t I_a^{ref}$: torque ripple due to the space harmonics

The sum of these torque variables and the load torque is defined as disturbance torque as

$$T_{dis} = T_l + \Delta J\omega s - \Delta K_t I_a^{ref} = T_{int} + T_{ext} + T_{fric} + (J - J_n)\omega s + (K_{tn} - K_t)I_a^{ref} \tag{2-7}$$

Equation 2-1 is transformed with the above torque variables as:

$$(J_n + \Delta J)\omega s + T_l = (K_{tn} + \Delta K_t)I_a^{ref} \tag{2-8}$$

Therefore, following dynamic equation can be derived:

$$J_n\omega s = K_{tn}I_a^{ref} - \left(T_l + \Delta J\omega s - \Delta K_t I_a^{ref}\right) \tag{2-9}$$

Furthermore, the dynamic equation is transformed with Eq. 2-7 as

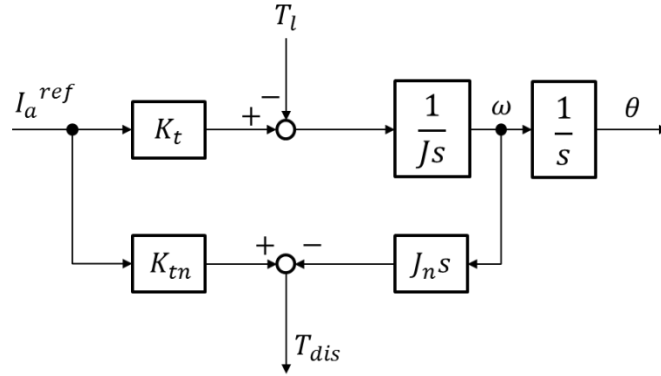$$T_{dis} = K_{tn}I_a^{ref} - J_n\omega s \tag{2-10}$$

Fig. 2-3　Disturbance torque estimation from the rotational speed.

　Figure 2-3 shows the block diagram of Eq. 2-10 in a Laplace-domain expression. This block diagram shows that the disturbance torque can be estimated when the current reference and rotational acceleration (the time differential value of the rotational speed) are detectable, because nominal values K_{tn} and J_n are constant.

　Current reference is easily obtained from a controller; on the other hand, a rotational acceleration sensor is hardly used because of less demand. Usually, the rotational speed is measured or estimated by using an encoder, a resolver, or a tachogenerator. To implement the system in Fig. 2-3, the rotational speed must be processed with a differential process. To suppress the high-frequency signal noise expanded by the differential process, a first-order low-pass filter is generally installed. Therefore, the disturbance torque is estimated as the following equation:

$$\hat{T}_{dis} = \frac{g_{dis}}{s + g_{dis}} T_{dis} \tag{2-11}$$

where g_{dis} [rad/s] is the cutoff rotational frequency of the low-pass filter. Then, the block diagram of Eq. 2-11 can be described as shown in Fig. 2-4.

　Figure 2-4 can be transformed to Fig. 2-5. This block diagram shows that the disturbance observer can be implemented with an integral process, without the differential process.

　The disturbance observer can estimate the disturbance information without any additional sensors. By analyzing the estimated disturbance information, the cutting states can be estimated without additional sensors.

　As mentioned in Chapter 1, many studies have implemented process monitoring by measuring cutting force and torque with dynamometers or armature current measurement. However, using additional sensors causes several problems, such as high cost and frequent maintenance. On the other hand,
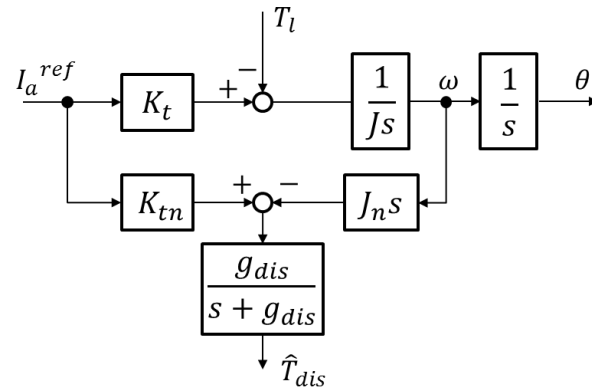
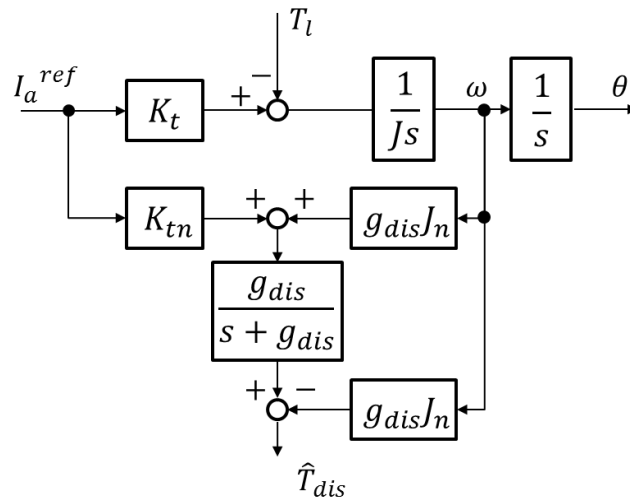Fig. 2-4 Disturbance torque estimation suppressing the noise.

Fig. 2-5 Disturbance torque estimation from the rotational speed
(constructed with integral process only).

disturbance observer-based monitoring would be useful to estimate the cutting torque, because the cutting torque is also a disturbance that interferes with the precise motion control of the spindle rotation. Furthermore, it uses only the servo information of the control system and never requires additional sensors.

The preceding explanation is the theory of the disturbance observer for a single inertia system such as a spindle control system. In the case of the spindle control system, the disturbance torque mainly includes cutting torque and friction torque, assuming that the parameter variations are negligibly small. To apply the disturbance observer to a ballscrew-driven stage control system, on the other hand, both the screw inertia moment and the driven-stage mass should be considered synthetically. Although the physical model becomes complex compared with the spindle, the disturbance observer also should be introduced to the
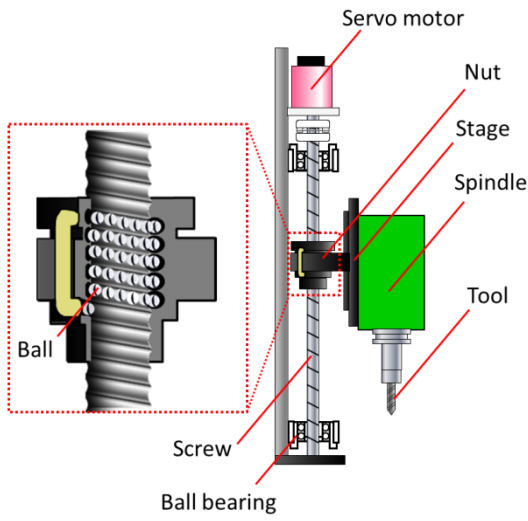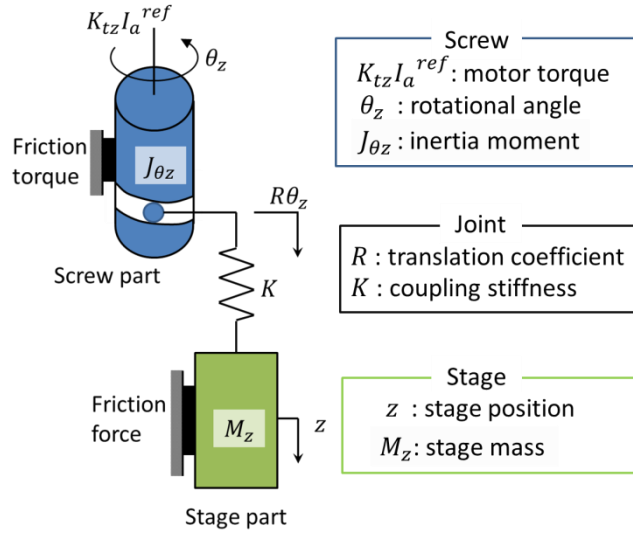
23

Fig. 2-6　Ballscrew-driven stage.

Fig. 2-7　Two-inertia system model.

ballscrew-driven stage system for cutting force monitoring in each axial direction.

　　The ballscrew-driven stage is a mechanical component constructed with a screw, a nut, and balls to convert the rotational movement to linear movement (Fig. 2-6). The ballscrew has sufficiently high stiffness to ensure stability even when a high load is applied to the controlled object. Therefore, it is widely used in machine tools for high-load metal cutting. On the other hand, time-dependent deterioration such as wear, low positioning accuracy due to large friction, and necessity of periodic maintenance for lubrication oil are demerits of the ballscrew structure. To analyze the ballscrew-driven stage physically, the rotational motion of the screw and the linear motion of the stage must be considered separately; thus, a multi-mass model is utilized. Though a two-mass model as shown in Fig. 2-7 is generally used, a four-mass model is used when precise analysis is necessary [58]. However, the four-mass model requires many parameters that must be identified accurately. Furthermore, coupling stiffness is difficult to identify in the case of a semi-closed loop control system in which the stage position is controlled indirectly with the rotational angle control of the screw. From this viewpoint, assuming that the coupling stiffness between the screw and the stage is sufficiently high, the two-mass model is similarly transformed into a single-mass model in this research.

　　First, to introduce the disturbance observer to the ballscrew-driven stage, dynamic equations for a screw and a driven stage must be established separately. In the case of a ballscrew-driven stage in a vertical direction, the dynamic equation of the screw during cutting is represented in the Laplace domain as

24

$$K_{t\theta z}I_a^{ref} = J_{\theta z}\omega_{\theta z}s + D_{\theta z}\omega_{\theta z} + C_{\theta z}\text{sgn}(\omega_{\theta z}) + \tau_{reac} \tag{2-12}$$

where $K_{t\theta z}$ [Nm/A] is the torque coefficient of the servo motor for the screw, $J_{\theta z}$ [kg·m²] is the inertia moment of the screw, $\omega_{\theta z}$ [rad/s] is the rotational speed of the screw, $D_{\theta z}$ [Nm/(rad/s)] is the damping coefficient, $C_{\theta z}$ [Nm] is the Coulomb friction torque, and τ_{reac} [Nm] is the reaction torque from the driven stage.

Considering a drilling process, the reaction force from the screw, the cutting force, the friction force, the gravity force, and the inertia force are applied to the driven stage. Therefore, the dynamic equation of the driven stage is described as follows:

$$F_{reac} = M_z v_z s + F_{cut} + M_z g + \left(D_z v_z + C_z \text{sgn}(v_z)\right) \tag{2-13}$$

where F_{reac} [N] is the reaction force applied to the driven stage, M_z [kg] is the mass of the driven stage, F_{cut} [N] is the cutting force, g [m/s²] is the gravity acceleration, D_z [N/(m/s)] is the damping coefficient, and C_z [N] is the Coulomb friction. As shown in Fig. 2-7, the translation between τ_{reac} and F_{reac} is expressed with translation coefficient R [m/rad] and coupling stiffness K [N/m] as follows:

$$F_{reac} = K(R\theta_z - z), \tau_{reac} = \frac{K(R\theta_z - z)}{R}, R = \frac{l}{2\pi} \tag{2-14}$$

where θ_z [rad] is the rotational angle of the screw, z [m] is the position of the driven stage, and l [m] is the lead of the screw. It is clear that $\omega_{\theta z} = \theta_z s$ and $v_z = zs$. Additionally, the reaction torque and the reaction force have a linear relation as

$$F_{reac} = \frac{l}{2\pi}\tau_{reac} \tag{2-15}$$

By substituting Eq. 2-14 to 2-13, following equation can be derived.

$$R\theta_z - z = \frac{M_z}{K}v_z s + \frac{1}{K}F_{cut} + \frac{M_z g}{K} + \frac{D_z v_z + C_z \text{sgn}(v_z)}{K} \tag{2-16}$$

Assuming that the coupling stiffness is sufficiently high ($K \to \infty$), Eq. 2-16 represents a linear relation between the rotational angle of the screw and the position of the driven stage as $z = R\theta_z$. Therefore, the rotational speed of the screw and the velocity of the driven stage also have a linear relation as

$$v_z = \frac{l}{2\pi}\omega_{\theta z} \tag{2-17}$$

Finally, the dynamic equation of the ballscrew-driven stage can be summarized as a single-mass model:

$$K_{t\theta z}I_a^{ref} = J_{\theta a}\omega_{\theta z}s + D_{\theta a}\omega_{\theta z} + C_{\theta a}\text{sgn}(\omega_{\theta z}) + \frac{l}{2\pi}(F_{cut} + M_z g)$$

(2-18)

where $\quad J_{\theta a} = J_{\theta z} + \left(\frac{l}{2\pi}\right)^2 M_z, \quad D_{\theta a} = D_{\theta z} + \left(\frac{l}{2\pi}\right)^2 D_z, \quad C_{\theta a} = C_{\theta z} + \left(\frac{l}{2\pi}\right)^2 C_z$

Therefore, the cutting force can be estimated on the basis of Eq. 2-18 by

$$F_{cut} = \frac{2\pi}{l}\left\{K_{t\theta z}I_a^{ref} - J_{\theta a}\omega_{\theta z}s - D_{\theta a}\omega_{\theta z} - C_{\theta a}\text{sgn}(\omega_{\theta z})\right\} - M_z g$$

(2-19)

The rotational speed of the screw is not directly measured with the encoder obtaining the angle information. Generally, it is acquired with a differential process on the encoder information. Assuming that the parameter variations are small enough, the cutting force can be estimated by nominalizing Eq. 2-19 and using a pseudo-differential process as follows:

$$\hat{F}_{cut} = \frac{2\pi}{l}\cdot\frac{g_{disz}}{s+g_{disz}}\left\{\frac{g_{LPFz}}{s+g_{LPFz}}K_{t\theta zn}I_a^{ref} - J_{\theta an}\hat{\omega}_{\theta z}s - D_{\theta an}\hat{\omega}_{\theta z} - C_{\theta an}\text{sgn}(\hat{\omega}_{\theta z})\right\} - M_z g$$

(2-20)

where $\qquad\qquad\qquad \hat{\omega}_{\theta z} = \frac{s\,g_{LPFz}}{s+g_{LPFz}}\theta_z$

where θ_z [rad] is the rotational angle of the screw available from the rotary encoder. In this case, a first-order low-pass filter is applied to the motor output information, i.e., $K_{t\theta zn}I_a^{ref}$, to compensate the phase delay caused by the filter. The block diagram of Eq. 2-20 is shown in Fig. 2-8. Considering that the gravity force term $M_z g$ is constant value, the following equation is satisfied because first-order low-pass filter passes static component without damping.

$$M_z g = \frac{g_{disz}}{s+g_{disz}}\cdot\frac{g_{LPFz}}{s+g_{LPFz}}\cdot M_z g$$

(2-21)

where $M_z g$ is a constant value. By substituting Eqs. 2-19 and 2-21 to Eq. 2-20, a following approximation equation can be obtained when the nominal values are almost same with the actual values.

$$\hat{F}_{cut} \approx \frac{g_{disz}}{s+g_{disz}}\cdot\frac{g_{LPFz}}{s+g_{LPFz}}\cdot F_{cut}$$

(2-22)

As a result, the cutting force can be estimated only from the motor current and the encoder information in the ballscrew-driven stage control system. The estimated cutting force is nearly equal to the cutting force filtered with second-order low-pass filter. Furthermore, this theory is applicable to X- and Y-stage control systems to estimate the X- and Y-direction cutting force by canceling the gravity force term.

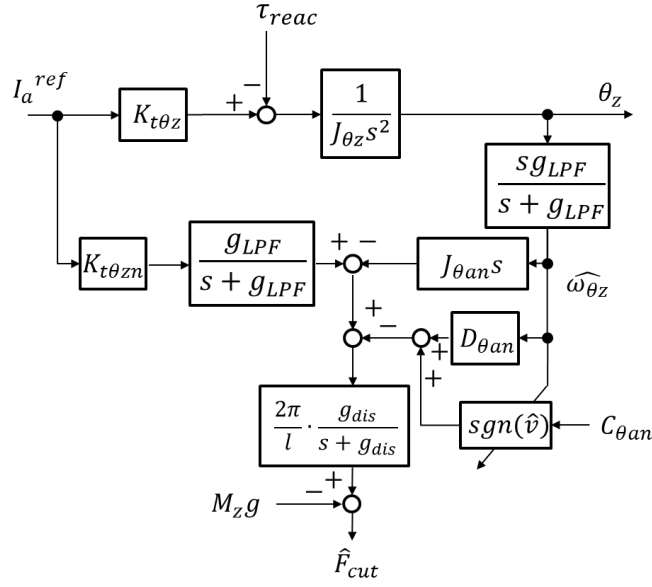The cutting toque can also be estimated from the spindle control system by

Fig. 2-8   Block diagram of the algorithm to estimate thrust force, based on disturbance observer theory.

$$\hat{T}_{cut} = \frac{g_{dis}}{s + g_{dis}}\left\{\frac{g_{LPF}}{s + g_{LPF}}K_t I_a^{ref} - J_n\hat{\omega}s - D_n\hat{\omega} - C_n\text{sgn}(\hat{\omega})\right\}$$

(2-23)

where
$$\hat{\omega} = \frac{s\, g_{LPF}}{s + g_{LPF}}\theta$$

Although the frequency response characteristics should be identified accurately to suppress the estimation error due to resonance, this research adopts the simple single inertia model because number of nominal parameters is comparatively small. As a result, the cutting torque and force in each direction can be estimated only from the servo information. By analyzing the estimated cutting force and torque, several kinds of problems in machining are detectable.

In case of tool wear monitoring, an increase in cutting force is a beneficial criterion [40]. Thus, the proposed algorithm would be directly utilizable to evaluate the progress of tool wear by estimating the cutting force and toque. Collision detection is also possible with the disturbance observer. As an efficient sensorless approach, Takakura proposed observer-based collision detection for an industrial robot arm, including the recovering motion [59]. Though the mechanical structures are different between the robot arm and the ballscrew, large external force would be applied when tool collision occurs in both systems.

Although several studies have proposed a tool fracture detection method for milling processes [25-28], a drill fracture detection method has rarely been

27

proposed. This is because the fracture-induced variation in cutting force is too small to detect and the use of cutting oil precludes mounting any sensors on a machine tool. As a sensorless approach, the armature current measurement does not require mounting a sensor on the machining space, but the estimation accuracy is not too high to detect an infinitesimal fluctuation due to drill fracture. From this viewpoint, the disturbance observer solves the sensor mounting problem and can detect a small cutting force variation due to tool fracture in drilling. This is just as valid for chatter detection. The frequency of chatter is generally too high to suppress actively and is out of the control frequency band. In this case, the armature current does not include chatter-induced fluctuation because the high-frequency information is lost because of filtering. On the other hand, the disturbance observer can estimate the force information with a wider frequency range by integrating the current information and the encoder signals and can detect the chatter. The fluctuation in the cutting force could be captured by applying a frequency analysis method to the disturbance information.

2.3 Signal Processing for Abnormal State Detection

Obviously, process monitoring should be performed in realtime to sufficiently ensure safety and reduce damage. Thus, the analysis method must be selected and modified carefully for the estimated disturbance force. In particular, the frequency resolution and the time response always have a tradeoff relation in a frequency analysis method. Furthermore, the computational load also should be considered because the calculation is performed in realtime with the NC device whose performance is not too high to process a complicated calculation. In this section, four kinds of frequency analysis methods are introduced, which are used in the proposed monitoring system: fast Fourier transform (FFT), continuous wavelet transform (CWT), integration of moving variance and moving Fourier transform, and rotational digital filter. The FFT and the CWT are conventional methods that are generally employed in typical realtime frequency analysis devices. On the other hand, the integration of moving variance and moving Fourier transform is a time-frequency domain analysis method developed for chatter analysis in this research, and has the same resolution as the discrete Fourier transform (DFT) but is specialized to reduce the computational load. The rotational digital filter is a novel signal processing method having a unique characteristic to extract a signal moving in the clockwise direction on an XY

plane, and was invented for drill fracture detection in this study. The two proposed methods are experimentally compared with the conventional methods to evaluate the performance and detection accuracy.

2.3.1 Fast Fourier Transform

The FFT is simply an algorithm that can compute the DFT much more rapidly than other available algorithms [60]. For this reason, the DFT algorithm is first explained in this section.

A Fourier transform identifies or distinguishes the different frequency sinusoids and their respective amplitudes that combine to form an arbitrary waveform. Mathematically, this relationship is stated as

$$H(f) = \int_{-\infty}^{\infty} h(t)\exp(-j2\pi ft)dt \tag{2-24}$$

where $h(t)$ is the waveform to be decomposed into a sum of sinusoids, $H(f)$ is the Fourier transform of $h(t)$, and $j = \sqrt{-1}$.

Frequency analysis is generally a procedure to require how much of each frequency component is included in the signal. Spectrum analysis is a well-known Fourier transform-based analysis method, which requires the absolute value of the Fourier transform called spectrum $|H(f)|$, and in some cases, power spectrum, which is the square of the absolute value $|H(f)|^2$. These values are useful criteria to identify the included frequency components and compare the amplitude of each component.

When the waveform $h(t)$ is sampled as a discrete waveform $h'[n]$ with a sampling time T, the Fourier transform of $H(f)$ can be approximated with $H'[k]$, which is the DFT of $h'[n]$, assuming that $h(t)$ is a periodic function of interval NT and does not include any frequency component higher than $1/(2T)$.

$$H'[k] = \sum_{n=0}^{N-1} h'[n] \ \exp\left(\frac{-j2\pi nk}{N}\right), k = 0, 1, \dots, \mathrm{N} - 1 \tag{2-25}$$

In the DFT, spectrum $|H'[k]|$ and power spectrum $|H[k]|^2$ are also applicable as in the Fourier transform.

If $N = 4$ and $W = \exp(-j2\pi/N)$, Eq. 2-25 can be written as

$$\begin{aligned}
H'[0] &= h'[0]W^0 + h'[1]W^0 + h'[2]W^0 + h'[3]W^0 \\
H'[1] &= h'[0]W^0 + h'[1]W^1 + h'[2]W^2 + h'[3]W^3 \\
H'[2] &= h'[0]W^0 + h'[1]W^2 + h'[2]W^4 + h'[3]W^6 \\
H'[3] &= h'[0]W^0 + h'[1]W^3 + h'[2]W^6 + h'[3]W^9
\end{aligned} \tag{2-26}$$

Furthermore, these equations can be summarized in matrix form as

$$\begin{bmatrix} H'[0] \\ H'[1] \\ H'[2] \\ H'[3] \end{bmatrix} = \begin{bmatrix} W^0 & W^0 & W^0 & W^0 \\ W^0 & W^1 & W^2 & W^3 \\ W^0 & W^2 & W^4 & W^6 \\ W^0 & W^3 & W^6 & W^9 \end{bmatrix} \begin{bmatrix} h'[0] \\ h'[1] \\ h'[2] \\ h'[3] \end{bmatrix} \tag{2-27}$$

or more compactly as

$$\boldsymbol{H'[k] = W^{nk} h'[n]} \tag{2-28}$$

where the boldface denotes a matrix.

Because $\boldsymbol{W^{nk}}$ and possibly $\boldsymbol{h'[n]}$ are complex, N^2 complex multiplications and $N \cdot (N-1)$ complex additions are necessary to perform the required matrix computation. The FFT algorithm reduces the number of multiplications and additions required in the computation of Eq. 2-27.

The following two equations are satisfied for the twiddle factor W.

$$W^m = W^{m \pm nN} \tag{2-29}$$

$$W^m = W^n \cdot W^{m-n} \tag{2-30}$$

By applying Eq. 2-29 to Eq. 2-27, the following equation is derived:

$$\begin{bmatrix} H'[0] \\ H'[1] \\ H'[2] \\ H'[3] \end{bmatrix} = \begin{bmatrix} 1 & 1 & 1 & 1 \\ 1 & W^1 & W^2 & W^3 \\ 1 & W^2 & W^0 & W^2 \\ 1 & W^3 & W^2 & W^1 \end{bmatrix} \begin{bmatrix} h'[0] \\ h'[1] \\ h'[2] \\ h'[3] \end{bmatrix} \tag{2-31}$$

The second step is to factor the square matrix in Eq. 2-31 as follows:

$$\overline{\boldsymbol{H'[k]}} = \begin{bmatrix} H'[0] \\ H'[2] \\ H'[1] \\ H'[3] \end{bmatrix} = \begin{bmatrix} 1 & W^0 & 0 & 0 \\ 1 & W^2 & 0 & 0 \\ 0 & 0 & 1 & W^1 \\ 0 & 0 & 1 & W^3 \end{bmatrix} \begin{bmatrix} 1 & 0 & W^0 & 0 \\ 0 & 1 & 0 & W^0 \\ 1 & 0 & W^2 & 0 \\ 0 & 1 & 0 & W^2 \end{bmatrix} \begin{bmatrix} h'[0] \\ h'[1] \\ h'[2] \\ h'[3] \end{bmatrix} \tag{2-32}$$

where W^0 is replaced to 1 as necessary. Note that an interchange has been taken between rows 1 and 2 in the multiplication of the two square matrices of Eq. 2-32, in which the row-interchanged vector is denoted by $\overline{\boldsymbol{H'[k]}}$. First, the number of computations is discussed.

$$\boldsymbol{h'_1[k]} = \begin{bmatrix} h'_1[0] \\ h'_1[1] \\ h'_1[2] \\ h'_1[3] \end{bmatrix} = \begin{bmatrix} 1 & 0 & W^0 & 0 \\ 0 & 1 & 0 & W^0 \\ 1 & 0 & W^2 & 0 \\ 0 & 1 & 0 & W^2 \end{bmatrix} \begin{bmatrix} h'[0] \\ h'[1] \\ h'[2] \\ h'[3] \end{bmatrix} \tag{2-33}$$

Focusing on the element $g_1[0]$, the computation includes one complex multiplication and one complex addition ($W^0 = 1$ is not reduced to unity in order to develop a generalized result).

$$h'_1[0] = h'[0] + W^0 h'[2] \tag{2-34}$$

Element $h'_1[1]$ is also determined by one complex multiplication and addition. Only one complex addition is required to compute $h'_1[2]$. This follows from the fact that $W^0 = -W^2$; hence

$$h'_1[2] = h'[0] + W^2 h'[2] = h'[0] - W^0 h'[2] \tag{2-35}$$

where the complex multiplication $W^0 h'[2]$ has already been computed in the determination of $h'_1[0]$ shown in Eq. 2-34. In addition, $h'_1[3]$ is computed by only one complex addition and no multiplications. The intermediate vector $\boldsymbol{h'_1[k]}$ is then determined by four complex additions and two complex multiplications.

In the next step, the following matrix multiplication is discussed.

$$\overline{\boldsymbol{H'[k]}} = \begin{bmatrix} H'[0] \\ H'[2] \\ H'[1] \\ H'[3] \end{bmatrix} = \begin{bmatrix} h'_2[0] \\ h'_2[1] \\ h'_2[2] \\ h'_2[3] \end{bmatrix} = \begin{bmatrix} 1 & W^0 & 0 & 0 \\ 1 & W^2 & 0 & 0 \\ 0 & 0 & 1 & W^1 \\ 0 & 0 & 1 & W^3 \end{bmatrix} \begin{bmatrix} h'_1[0] \\ h'_1[1] \\ h'_1[2] \\ h'_1[3] \end{bmatrix} \tag{2-36}$$

The term $h'_2[0]$ is determined by one complex multiplication and addition.

$$h'_2[0] = h'_1[0] + W^0 h'_1[1] \tag{2-37}$$

Element $h'_2[1]$ is computed by one addition because $W^0 = -W^2$. By similar reasoning, $h'_2[2]$ is determined by one complex multiplication and addition, and $h'_2[3]$ by only one addition.

Computation of $\overline{\boldsymbol{H'[k]}}$ by means of Eq. 2-32 requires a total of four complex multiplications and eight complex additions. Computation of $\boldsymbol{H'[k]}$ by Eq. 2-27 requires 16 complex multiplications and 12 complex additions. Note that the matrix factorization process introduces zeros into the factored matrices and reduces the required number of multiplications.

For $N = 2^M$ (i.e., $M = \log_2 N$), the FFT algorithm is a procedure for factoring an $N \times N$ matrix into M matrices (each $N \times N$ matrix) such that each of the
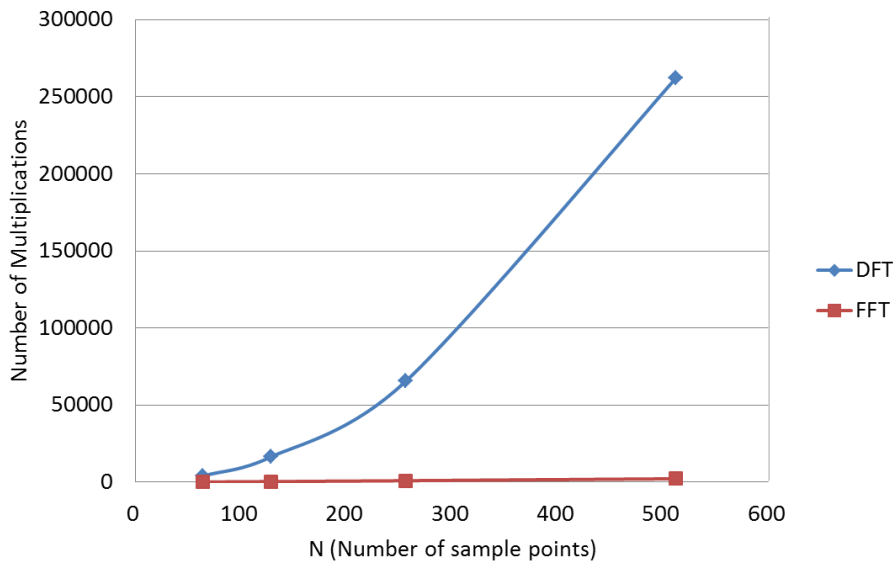

Fig. 2-9   Comparison of multiplications required by direct calculation and FFT algorithm.

factored matrices has the special property of minimizing the number of complex multiplications and additions. In this case, the FFT requires $NM/2$ complex multiplications and NM complex additions, whereas the direct method (shown in Eq. 2-27) requires N^2 complex multiplications and $N(N-1)$ complex additions. The number of multiplications for each N is given as shown in Fig. 2-9.

The matrix factoring procedure does introduce one discrepancy. Recall that the computation of Eq. 2-32 yields $\overline{H'[k]}$ instead of $H'[k]$; that is,

$$\overline{H'[k]} = \begin{bmatrix} H'[0] \\ H'[2] \\ H'[1] \\ H'[3] \end{bmatrix} \text{ instead of } H'[k] = \begin{bmatrix} H'[0] \\ H'[1] \\ H'[2] \\ H'[3] \end{bmatrix} \tag{2-38}$$

This rearrangement is inherent in the matrix factoring process and is a minor problem because it is straightforward to generalize a technique for unscrambling $\overline{H'[k]}$ to obtain $H'[k]$.

Rewrite $\overline{H'[k]}$ by replacing argument k with its binary equivalent

$$\overline{H'[k]} = \begin{bmatrix} H'[00] \\ H'[10] \\ H'[01] \\ H'[11] \end{bmatrix} \tag{2-39}$$

Observe that if the binary arguments of Eq. 2-39 are flipped or bit reversed (i.e., 01 becomes 10, 10 becomes 01, and so on), then

$$\overline{H'[k]} = \begin{bmatrix} H'[00] \\ H'[10] \\ H'[01] \\ H'[11] \end{bmatrix} \text{ flips to } \begin{bmatrix} H'[00] \\ H'[01] \\ H'[10] \\ H'[11] \end{bmatrix} = H'[k] \tag{2-40}$$

It is straightforward to develop a generalized result for unscrambling the FFT.

For $N > 4$, it is cumbersome to describe the matrix factorization process analogous to Eq. 2-32. For this reason, Eq. 2-32 can be translated in a graphical manner. For $N = 4$, the signal flow graph can be described as shown in Fig. 2-10.
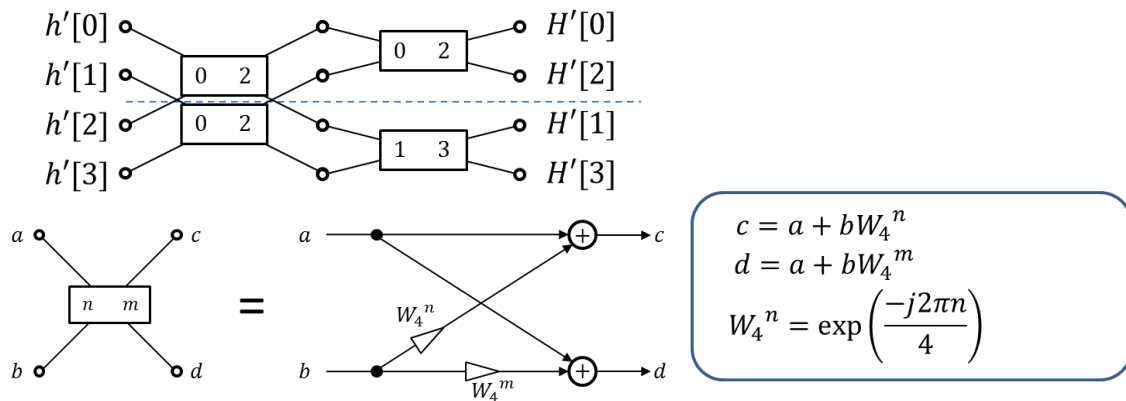

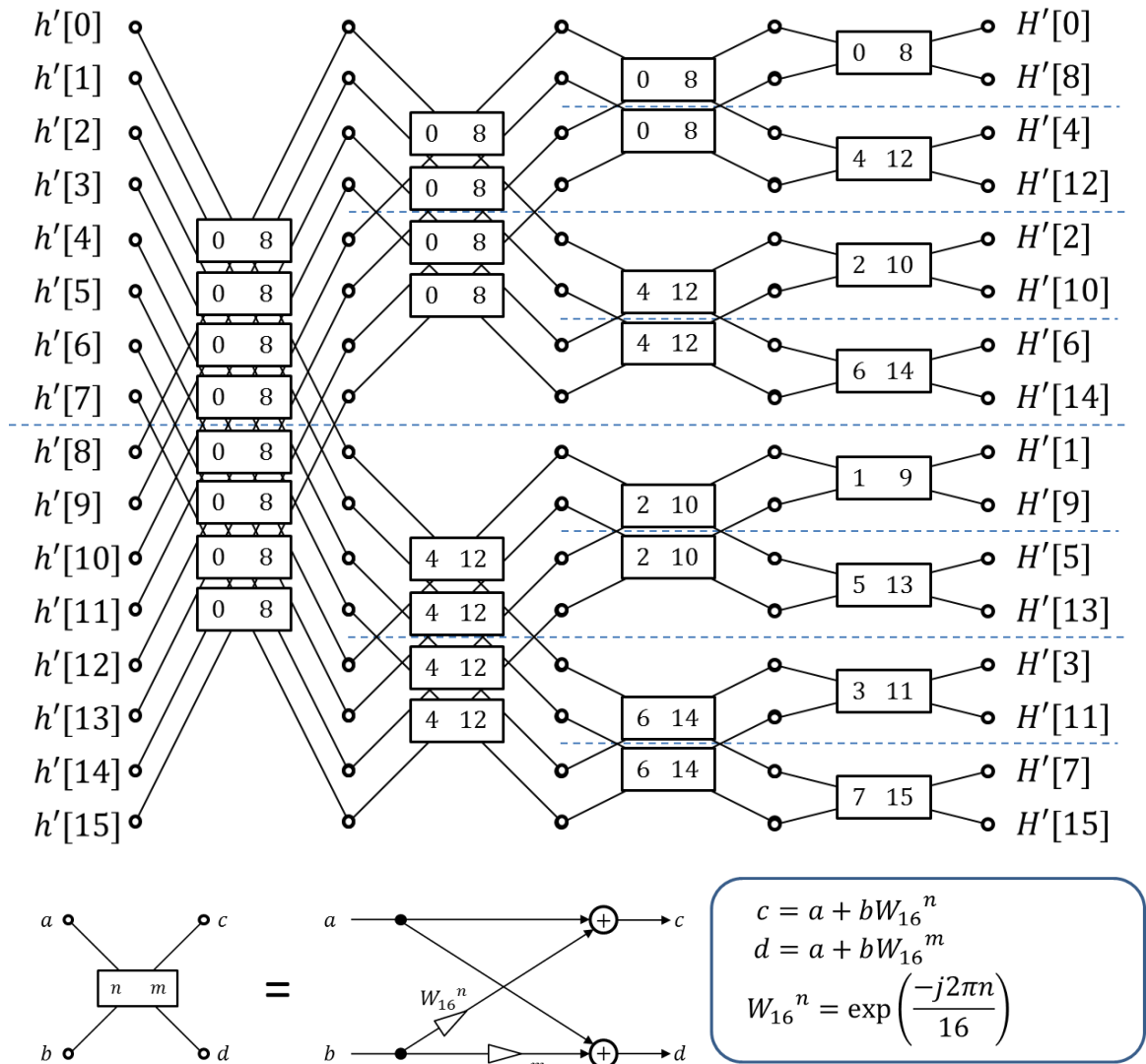Fig. 2-10 Signal flow graph of FFT when $N = 4$.

Fig. 2-11 Signal flow graph of FFT when $N = 16$.

This can be extended for other $N = 2^M$, e.g., for $N = 16$ as shown in Fig. 2-11.

In this section, the detail of matrix factoring procedure is omitted.

Recent progress of NC devices contributes to the development of a wide-frequency-range control. In other words, the computation load must be strictly regulated when an additional algorithm is installed on the NC controller. The FFT is an effective method to reduce the computation of DFT; however, it is difficult to perform within a short servo term. N must be a bit number so that the window width is not optioned freely. In order to overcome these challenges, a frequency analysis method integrating moving variance and moving Fourier transform algorithms is proposed in Section 2.3.3.

2.3.2 Continuous Wavelet Transform

FFT can distinguish frequency components in a signal for a wide frequency range; on the other hand, is not suited to detect a time-dependent variation in the signal. The widow width should be shortened to ensure the detection response, whereas it must be extended to enhance the frequency resolution. To capture the time-dependent variation and identify the frequency simultaneously, a short-time Fourier transform (STFT) is a well-known method that performs the DFT intermittently at some interval. However, when the same damping coefficient is given is mechanical systems, a high-frequency variation attenuates earlier than a low-frequency one because the motion energy is converted to the heat earlier because of the larger viscous friction. Although the same window width is utilized for all frequencies in the STFT algorithm, the window width should be changed according to the frequency. In order to overcome this challenge, the CWT algorithm was invented.

It is said that first practical usage of the CWT was for the seismology community. In 1984, Morlet introduced Gaussian-windowed sinusoids for the time-frequency analysis of an artificial earthquake wave to identify the prospect position (from the time variation) and the kinds of deposit (from the frequency) in oil-well drilling [61]. In order to adjust the window width properly according to the height of the frequency, the CWT employs scaling coefficients to make the window width inversely proportional to the analyzed frequency.

The CWT uses only one mother wavelet $\psi(t)$ to analyze the signal. A
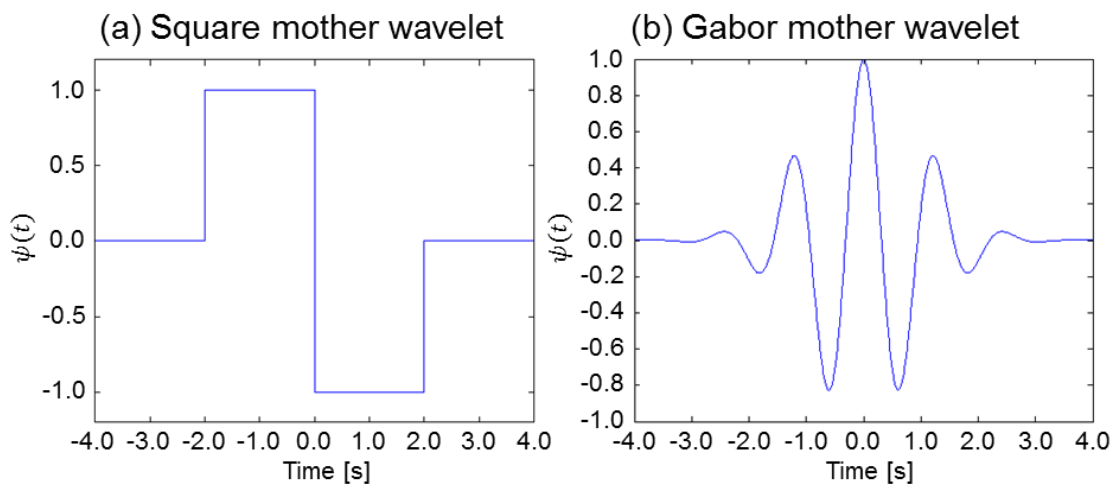

Fig. 2-12   Examples of the mother wavelet.

square-shaped wavelet is initially employed as shown in Fig. 2-12 (a). After that, a window function is applied and windowed wavelets such as the Gabor wavelet (Fig. 2-12(b)) are introduced to enhance the time resolution. In this case, an equation of the mother wavelet can be described as

$$\psi(t) = w(t)\exp(-j2\pi f\alpha t) \tag{2-41}$$

where $w(t)$ is a window function. By extending or shrinking the mother wavelet $\psi(t)$, the continuous wavelet transform of a signal $x(t)$ at a scale coefficient α and translational value β is expressed by the following integral:

$$X_f(\alpha, \beta) = \frac{1}{\sqrt{\alpha}} \int_{-\infty}^{\infty} x(t)\bar{\psi}\left(\frac{t-\beta}{\alpha}\right) dt \tag{2-42}$$

where $\bar{\psi}$ is the conjugate complex of ψ. The width and the amplitude of the mother wavelet can be modified by changing the scale coefficient α. Furthermore, the translational value β enables the wavelet to slide along with the time axis. The analyzed frequency f is generally included in the wavelet $\psi(t)$ as a twiddle factor, $\exp(-j2\pi f\alpha t)$. Combining Eq. 2-41 and 2-42, the following equation is derived.

$$X_f(\alpha, \beta) = \frac{1}{\sqrt{\alpha}} \int_{-\infty}^{\infty} x(t)w\left(\frac{t-\beta}{\alpha}\right) \exp(j2\pi f(t-\beta)) dt \tag{2-43}$$

Equation 2-43 indicates that the computation of CWT is similar to that of the DFT because the integral includes the multiplication of the analyzed signal and the twiddle factor as in Eq. 2-24. Although the time resolution can be enhanced with the CWT, the frequency-dependent scale variation due to the window function does not allow reducing the complex computation of CWT like the FFT algorithm. As a result, CWT should be used not for wide frequency-range analysis, but for a special frequency component. In the case of this research, the CWT would be a suitable method for drill fracture detection because the fracture-induced fluctuation in cutting force would depend on the spindle rotation, i.e., a special frequency.

The above two frequency (or time-frequency) analysis methods are conventionally applied not only for research purposes but also practical uses. On the other hand, two novel time-frequency analysis methods are dedicated to chatter and fracture detection in this research. By comparing their performance, the merits of the proposed methods will be theoretically and experimentally shown.

2.3.3　Moving Variance and Moving Fourier Transform

In this section, "integration of moving variance and moving Fourier transform algorithms (MV+MFT)" is proposed for chatter detection. Its performance is evaluated by comparing the number of computations.

The merit of the FFT is the reduction of the complex multiplications of DFT from N^2 to $N\log_2 N$ as explained above. In order to enhance the frequency resolution, the width of window N has to be extended and the number of computations grows. From this viewpoint, FFT has an efficient approach to realize the realtime characteristic and high-frequency resolution at the same time. On the other hand, the window width should be set to bit numbers, i.e., the frequency resolution and the time response cannot be fine-tuned arbitrarily. (The number of computations can be reduced most efficiently when the window width is a bit number, although the window width does not strictly have to be set to a bit number.)

These characteristics of FFT are well-known and are the reason why the FFT is widely applied as a frequency analysis method. In some cases, however, FFT is not applicable for realtime analysis because of a short update interval. Recent measurement devices have high performance to enhance the sampling period less than 100 μs even for a current measurement that takes a comparatively long time. When the window width is set to a large size, the complex matrix computation of FFT cannot be processed within a short time (such as 100 μs) even with a high-spec computer. Practically, the analysis should be performed at an interval of once in tens or hundreds samples, but it simply skips some analyzable information and deteriorates the analysis accuracy of the time-dependent variation. Parallel calculation with computer clusters or graphic processing units may enable processing of large computations in realtime; however, adapting these devices or systems causes the same troubles as mounting additional sensors.

To develop a sophisticated time-frequency analysis method for realtime chatter vibration, the following respects should be satisfied:

- Ability to evaluate the amplitude of the vibration
- Ability to distinguish whether the vibration frequency is the same as a harmonic of the spindle rotational frequency.

The chatter should be separately detected because the mechanism and the countermeasure are complicated as explained in Section 1.4.4. In milling, the

vibration is caused mainly by the regenerative effect or the resonance. The forced vibration due to an interrupted cutting process has a harmonic frequency of the spindle rotational frequency, and chatter due to the regenerative effect fluctuates at the other frequency. Therefore, in order to capture the chatter, it is necessary only to distinguish whether it is forced vibration or not, i.e., the exact chatter frequency need not be identified. To satisfy this purpose with a small computation and high-frequency resolution, MV+MFT is developed.

To evaluate the amplitude of a fluctuation in a signal, the moving average algorithm is explained first.

Assuming that only the amplitude is necessary for the evaluation and the frequency does not have to be identified, variance of the signal would be a suitable criterion. This is because the variance is theoretically equal to the average of power spectrum of all frequencies excepting its static component. The proof of this principle is given as follows.

The power spectrum of DFT $PS(k)$ for a signal $h'[n]$ is given as

$$PS(k) = |H'[k]|^2 = a_k{}^2 + b_k{}^2$$

where
$$H'[k] = \sum_{n=0}^{N-1} h'[n]\exp\left(\frac{-j2\pi nk}{N}\right) = a_k - jb_k$$

(2-44)

On the other hand, inverse DFT is described as

$$h'[i] = \frac{1}{N}\sum_{n=0}^{N-1} H'[n]\exp\left(\frac{j2\pi ni}{N}\right) = \frac{1}{N}\sum_{n=0}^{N-1}(a_i - jb_i)\exp\left(\frac{j2\pi ni}{N}\right)$$

(2-45)

Assuming that $h'[n]$ incudes only actual values, the Fourier series expansion of $h'[n]$ is given as

$$h'[i] = a_0 + \sum_{n=1}^{N-1}\left\{\frac{2a_i}{N}\cos\left(\frac{2\pi ni}{N}\right) + \frac{2b_i}{N}\sin\left(\frac{2\pi ni}{N}\right)\right\}$$

(2-46)

Each Fourier series can be required as the following equations:

$$a_i = \sum_{n=0}^{N-1} h'[n]\cos\left(\frac{2\pi nk}{N}\right), \qquad b_i = \sum_{n=0}^{N-1} h'[n]\sin\left(\frac{2\pi nk}{N}\right)$$

(2-47)

Here, the definition of variance $V[h']$ of signal $h'[n]$ is described as Eq. 2-48, where $E[h']$ is the expectation value of the signal $h'[n]$. (In case of Fourier series, the expectation value is the static component, i.e., $E[h'] = a_0$.)

$$V[h'] = \frac{1}{N}\sum_{k=0}^{N-1}(h'[k] - E[h'])^2$$

(2-48)

By substituting Eqs. 2-46 and 2-47, Eq. 2-48 can be transformed as follows:

$$V[h'] = \frac{2}{N}\sum_{k=0}^{N-1}\left[\sum_{i=1}^{N-1}\left\{\frac{a_i}{N}\cos\left(\frac{2\pi ki}{N}\right)\right\} + \sum_{i=1}^{N-1}\left\{\frac{b_i}{N}\sin\left(\frac{2\pi ki}{N}\right)\right\}\right]^2 \tag{2-49}$$

Because of the orthogonality of the trigonometric functions, the following equations are satisfied, where m and n are integer numbers, and N is a integer number larger than 1.

$$\sum_{k=0}^{N-1}\left\{\cos\left(\frac{2\pi mk}{N}\right)\cdot\cos\left(\frac{2\pi nk}{N}\right)\right\} = \begin{cases} \frac{N}{2} & (m = n) \\ 0 & (m \neq n) \end{cases}$$

$$\sum_{k=0}^{N-1}\left\{\cos\left(\frac{2\pi mk}{N}\right)\cdot\sin\left(\frac{2\pi nk}{N}\right)\right\} = 0 \tag{2-50}$$

$$\sum_{k=0}^{N-1}\left\{\sin\left(\frac{2\pi mk}{N}\right)\cdot\sin\left(\frac{2\pi nk}{N}\right)\right\} = \begin{cases} \frac{N}{2} & (m = n) \\ 0 & (m \neq n) \end{cases}$$

By applying these equations, Eq. 2-49 can be transformed as follows:

$$V[g] = \frac{2}{N}\sum_{k=0}^{N-1}\left[\sum_{i=1}^{N-1}\left\{\left(\frac{a_i}{N}\right)^2\cdot\frac{N}{2} + \left(\frac{b_i}{N}\right)^2\cdot\frac{N}{2}\right\}\right] = \frac{1}{N}\sum_{i=1}^{N-1}(a_i{}^2 + b_i{}^2) = \frac{1}{N}\sum_{i=1}^{N-1}PS(i) \tag{2-51}$$

As shown in Eq. 2-51, the variance is certainly equal to the average value of the DFT power spectrum excepting the static component. Furthermore, skipping the division with N in the variance calculation, the sum of the power spectrum excepting the static component is acquirable.

Although the variance is usable to evaluate the amplitude of the signal as above, the number of computations is not small, as summarized in Table 2-1.

Table 2-1 Number of computations to obtain variance.

	Multiplication	Addition
①　Average calculation	1	$N - 1$
②　Difference between each sampling and the average	N	–
③　Square values of ②	–	N
④　Average of ③	1	$N - 1$
Total number of computations	$N + 2$	$3N - 2$

The number of computations is certainly smaller than that of FFT. This would be an adequate result because the variance calculation cannot identify the frequency information as in FFT. The number of computations for variance proportionally increases according to N, whereas the computation increase in FFT is proportional to $N\log_2 N$. Computation load of an algorithm is generally evaluated by using the Landau symbol $O(N)$ for the variance calculation, and
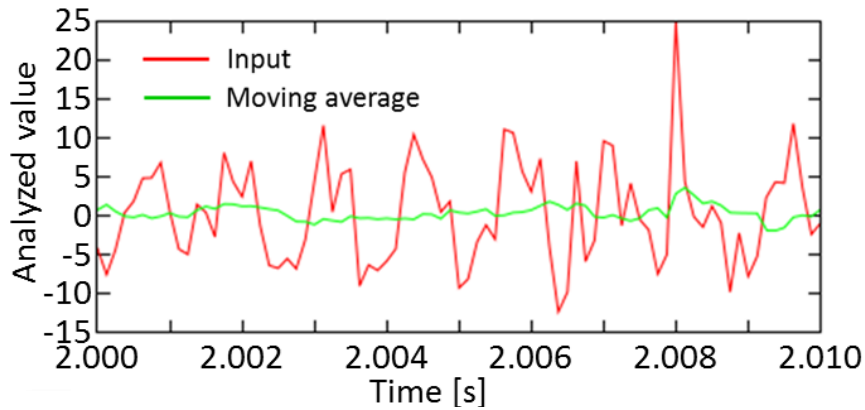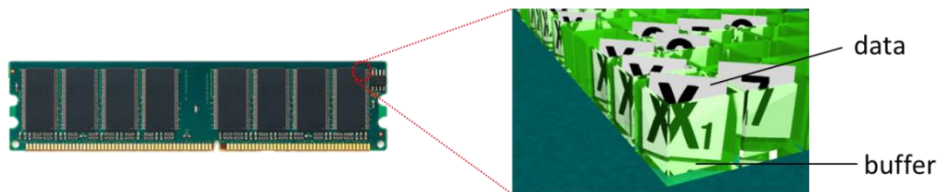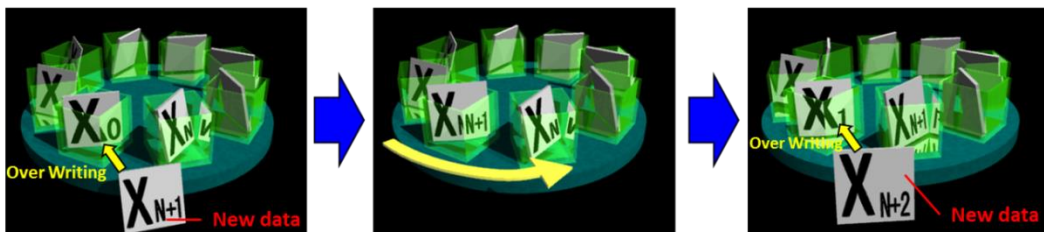
Fig. 2-13   Moving average algorithm.

Fig. 2-14   Concept of a ring buffer.

$O(N\log N)$ for FFT.

When the window width is set to N, the number of computations naturally becomes larger than N. However, the number of computations can be reduced to less than N under some special conditions. The moving average algorithm should be a good example that requires the number of computations to be less than N.

The moving average algorithm is a signal processing method to reduce signal noise by continuously calculating the average of samples in the window as shown in Fig. 2-13. If the calculation is performed faithfully following the definition of the average, $N-1$ additions and one division (multiplication) are required, then, the algorithm is regarded as $O(N)$. However, the number of computations can be reduced more by leaving the past samples with a memory structure.

A ring buffer is a data structure that uses a single fixed-size buffer as if it were connected end-to-end. A new data item always overwrites the oldest data in this data structure as shown in Fig. 2-14, and this repetition looks as if a ring-shaped structure is rotating and storing new data in order. It is generally used to compensate time lag caused by the difference of processing time between devices such as from a computer to a printer. In order to apply the ring buffer to the moving average algorithm, sampling data divided by N are stored to the ring buffer. Where the oldest data is $x'[n]/N$, the newest data is $x'[n+N-1]/N$ in the ring buffer, and the average from $x'[n]$ to $x'[n+N-1]$ is A_n, the average in the next step A_{n+1} (i.e., the average value of from $x'[n+1]$ to $x'[n+N]$) is available as follows:

$$A_{n+1} = A_n - (x'[n] - x'[n+N])/N \tag{2-52}$$

First, the oldest data in the ring buffer, $x'[n]/N$, is subtracted from A_n. Then, the new data $x'[n+N]$ is divided by N and the obtained value $x'[n+N]/N$ is added to A_n and stored into the ring buffer. Through this procedure, the average value in the next step A_{n+1} can be obtained. In this case, the special conditions can be said that the N past data are left and the average in the previous step is already known. As a result, the average value of each interval can be required only with one multiplication (division) and two additions. In other words, the number of computations does not change even if the larger N is selected, and the algorithm is evaluated as $O(1)$.

This research has a discussion whether an $O(1)$ algorithm can be constructed like the moving average to reduce the number of computations, and proposes a "moving variance algorithm."

The variance for the population including $x'[n], x'[n+1], \dots, x'[n+N-1]$ is defined as

$$V_n[x'] = \frac{1}{N} \sum_{i=n}^{n+N-1} (x_i - E_n[x'])^2 \tag{2-53}$$

where $E_n[x']$ is the average value of the population. Considering the variance at the next step $V_{n+1}[x']$, the average of the next step $E_{n+1}[x']$ differs from the former step $E_n[x']$, although only the oldest and the newest data can be treated in the ring buffer. Thus, the values of $(x'[i] - E_n[x'])$ cannot be stored in the buffer because they have to be rewritten when $E_n[x']$ changes.

To overcome this problem, Eq. 2-53 is expanded as

$$V_n[x'] = \frac{1}{N} \sum_{i=n}^{n+N-1} (x[i] - E_n[x'])^2$$

$$= \frac{1}{N} \sum_{i=n}^{n+N-1} x_i{}^2 - 2 \cdot E_n[x'] \cdot \frac{1}{N} \sum_{i=n}^{n+N-1} x_i + \frac{1}{N} \cdot N \cdot (E_n[x'])^2 \qquad (2\text{-}54)$$

$$= \frac{1}{N} \sum_{i=n}^{n+N-1} x_i{}^2 - (E_n[x'])^2 = E_n[(x')^2] - (E_n[x'])^2$$

This development of a formula indicates that the variance can be derived by calculating the difference between the average of square values $E_n[(x')^2]$ and the square values of the average $(E_n[x'])^2$ On the basis of the fact that the moving average requires one multiplication and two additions at each interval, the average of square values requires two multiplications and two additions. In this case, $x'[i]^2/N$ should be stored in the ring buffer. At the same time, another ring buffer is prepared to store $x'[i]/N$ to calculate $(E_n[x'])^2$, which requires two multiplications and two additions. Finally, the variance can be derived by calculating the difference between $E_n[(x')^2]$ and $(E_n[x'])^2$. To perform this algorithm, the values of $E_n[(x')^2]$ and $(E_n[x'])^2$ must already be known, and the values of $x'[i]/N$ and $x'[i]^2/N$ must be stored in each ring buffer. The number of computations for this algorithm is summarized in Table 2-2.

Table 2-2　Number of computations for moving variance.

Procedure	Multiplication	Addition
① Moving average for $x'[i]^2$	2	2
② Moving average for $x'[i]$	1	2
③ Square values of ②	1	–
④ Difference between ① and ③	–	1
Total number of computations	4	5

As a result, the moving variance algorithm can be performed with only five additions and four multiplications in each interval. The number of computations is independent of N, and the algorithm can be regarded as $O(1)$.

Although the amplitude of the fluctuation in the estimated disturbance torque could be evaluated with the moving variance algorithm, the extraction method for a special frequency component is also required to distinguish chatter from the captured vibration.

Unexpected large vibration in milling is mainly chatter vibration or forced vibration.

Forced vibration is caused by resonance; thus, its frequency can be predicted as a harmonic of the spindle rotation frequency, to which the chatter frequency does not fit. Therefore, by eliminating the power spectrum of a special frequency component from the total power spectrum derived by the moving variance, the power spectrum of chatter can be monitored in realtime.

As explained, the direct calculation of DFT requires N^2 complex multiplications and $N \cdot (N-1)$ complex additions for the frequency coefficient k from 0 to $N-1$; thus, the algorithm is $O(N^2)$. However, not all frequency components have to be analyzed; only some harmonics of the spindle rotation frequency should be monitored for chatter detection. For the direct calculation of the single frequency DFT, N complex multiplications and $(N-1)$ complex additions are required, i.e., the algorithm is $O(N)$. In order to reduce the amount of the computation for realtime usage, an $O(1)$ algorithm called "sliding discrete Fourier transform (SDFT)" is proposed in some studies [62].

The SDFT algorithm performs an N-sample DFT on time samples within a sliding window as shown in Fig. 2-15. The definitions of the DFT for the window shown in (a) and the shifted window shown in (b) are described as
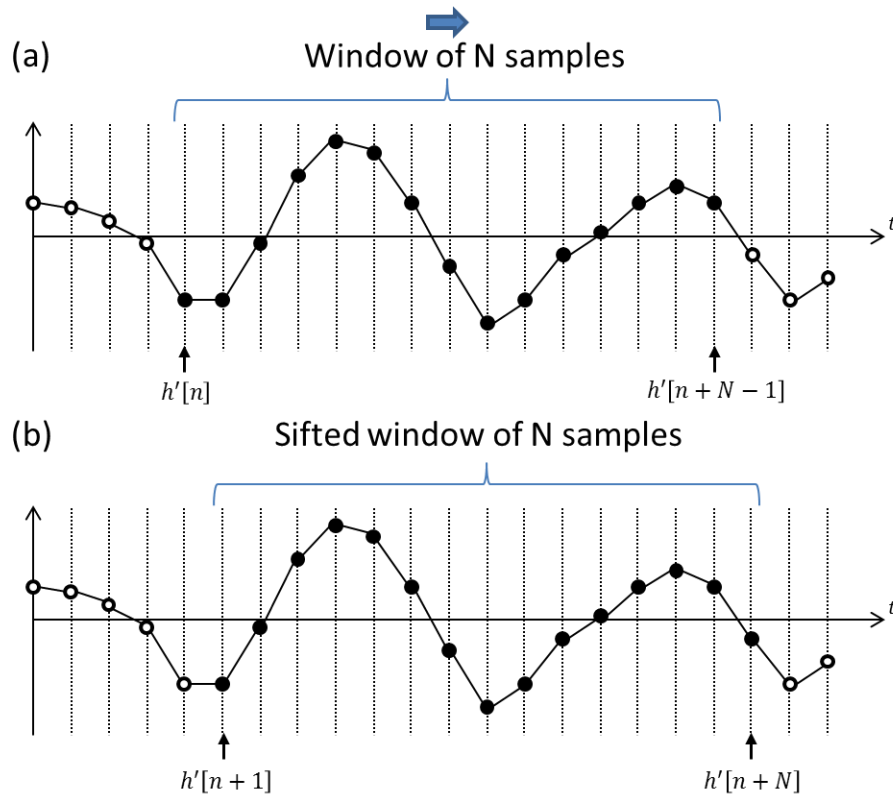

Fig. 2-15 SDFT of N samples: (a) Before sifting, (b) after sifting.

$$H'_k[n] = \sum_{m=0}^{N-1} h'[n+m] \exp\left(\frac{-j2\pi mk}{N}\right)$$

$$H'_k[n+1] = \sum_{m=0}^{N-1} h'[n+1+m] \exp\left(\frac{-j2\pi mk}{N}\right) \qquad (2\text{-}55)$$

where k is an analyzed frequency.

These equations can be combined as

$$H'_k[n+1] = H'_k[n] \exp\left(\frac{j2\pi k}{N}\right) + h'[n+N] - h'[n] \qquad (2\text{-}56)$$

As a result, the single-frequency DFT can be continuously performed under the conditions in which the previous DFT value $H'_k[n]$ and the past data from $h'[n]$ to $h'[m+N-1]$ are already known. In this case, only one complex multiplication and two complex additions are required, and the algorithm can be regarded as $O(1)$.

By the way, the number of computations for one complex multiplication can be translated to four actual multiplications and two actual additions. The number of computations for one complex addition can be translated to two actual additions in the same manner. Thus, the number of computations for SDFT is four actual multiplications and six actual additions. Additionally, two actual multiplications and one actual addition are required to derive the power spectrum $|H'_k|^2$. In total, six actual multiplications and seven actual additions are required for the power spectrum calculation. This is already small enough to use in realtime; however, the number of computations can be reduce more by assuming that the analyzed signal h' is an actual wave.

This research proposes the following algorithm, called "moving Fourier transform" (MFT), to determine the DFT power spectrum for the actual wave h' in the sliding window.

$$M_{h',k}[n] = \sum_{m=0}^{N-1} h'[n+m] \exp\left(\frac{-j2\pi k(n+m)}{N}\right) = R_{h',k}[n] + jI_{h',k}[n] \qquad (2\text{-}57)$$

Corresponding to the definition of DFT shown in Eq. 2-25, the MFT value $M_{h',k}$ has a phase lag to the DFT value H'_k as follows:

$$M_{h',k}[n] = \sum_{m=0}^{N-1} h'[n+m] \exp\left(\frac{-j2\pi km}{N}\right) \exp\left(\frac{-j2\pi kn}{N}\right) = H'_k[n] \exp\left(\frac{-j2\pi kn}{N}\right) \qquad (2\text{-}58)$$

The real part $R_{h',k}$ and the imaginary part $I_{h',k}$ can be calculated as the moving average of $h'[n]\cos(-2\pi kn/N)$ and $h'[n]\sin(-2\pi kn/N)$ as

$$R_{h',k}[n] = R_{h',k}[n-1] - h'[n]\cos\frac{2\pi kn}{N} + h'[n+N]\cos\frac{2\pi k(n+N)}{N}$$

(2-59)

$$I_{h',k}[n] = I_{h',k}[n-1] - h'[n]\sin\frac{2\pi kn}{N} - h'[n+N]\sin\frac{2\pi k(n+N)}{N}$$

Furthermore, the power spectrum of MFT is equal to that of DFT:

$$\left|M_{h',k}[n]\right|^2 = \left|H'_k[n]\exp\left(\frac{-j2\pi kn}{N}\right)\right|^2 = |H'_k[n]|^2$$

(2-60)

By employing the ring buffers to calculate the moving average of $h'[n]\cos(-2\pi kn/N)$ and $h'[n]\sin(-2\pi kn/N)$, the MFT value $M_{h',k}[n]$ can be obtained with two actual multiplications and four actual additions. Summing with the power spectrum calculation, four actual multiplications and five additions are required for the MFT algorithm. Unlike SDFT, the MFT ignores the phase characteristic of the analyzed signal; however, it can determine the power spectrum with fewer computations.

By integrating the moving variance (MV) and MFT algorithms, the chatter can be separately monitored as shown in the block diagram in Fig. 2-16. The total power spectrum is calculated with the MV. In order to distinguish the forced vibration components, the MFT is adapted to all harmonics of the spindle rotation frequency. Finally, the chatter power spectrum is determined from the difference of the total power spectrum and the forced power spectrum.

Table 2-3 shows the comparison of the number of computations between FFT and MV+MFT for $N = 512$, where 10 MFTs are simultaneously performed. Note that the number of computations for FFT becomes larger with larger N.
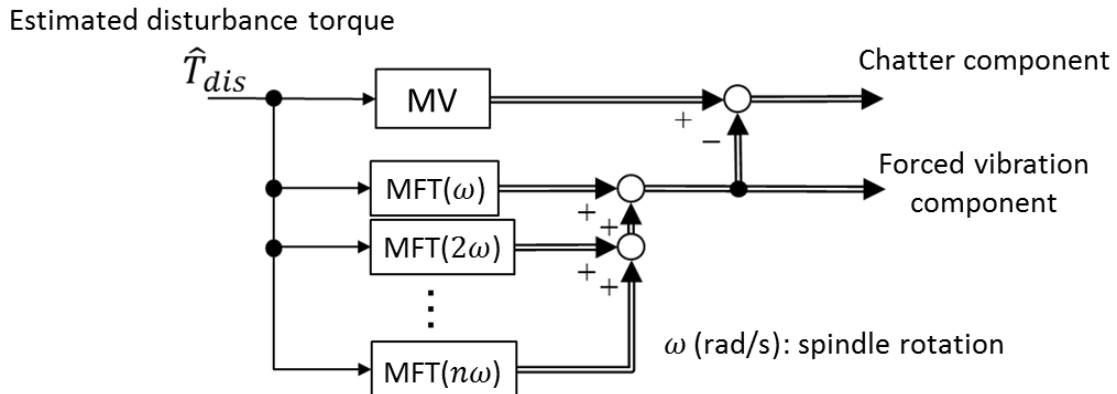

Fig. 2-16 Proposed chatter detection algorithm flow.

Table 2-3 Number of computations for FFT and MV+MFT ($N = 512$).

	FFT	MV+MFT
Calculation order	$O(N\log N)$	$O(1)$
Actual addition	10238	64
Actual multiplication	19456	55
Frequency resolution (F_s: sampling frequency)	F_s/N	F_s/N

Although some conditions must be satisfied to perform the MV+MFT, the number of computations for MV+MFT is significantly smaller than that for FFT. Furthermore, both methods have the same analysis resolution for frequency difference because their origins are DFT in the same manner. As other merits of MV+MFT, the widow width N can be set arbitrarily; it does not have to be set to a bit number and the number of computations. The tradeoff relation between the computation load and the frequency resolution is also solved.

It can be said that the MV+MFT is a hyper-low-computation load algorithm that can be realized by regulating the purpose to distinguishing the chatter from the other vibrations, i.e., the chatter frequency itself is not focused on. In this research, the performance of the MV+MFT is evaluated by measuring the computation time and comparing it with that of FFT, and the practicability is evaluated by applying it to the estimated disturbance torque of the spindle.

2.3.4 Rotational Digital Filter

To detect a drill fracture more accurately, a novel digital filter called a "rotational digital filter" (RDF) is proposed in this section. The rotational digital filter has a unique function passing only a signal moving in the clockwise direction at a certain rotational speed. A drill generally rotates in the clockwise direction on an XY plane from the spindle side. Thus, the fracture-induced fluctuation in cutting force would be captured more accurately.

When a signal moves in a clockwise circular orbit in the XY plane, the phase lag of the x-component against that of the y-component becomes $\pi/2$ radians as follows:

$$\begin{bmatrix} x(t) \\ y(t) \end{bmatrix} = \begin{bmatrix} F\sin(\omega_0 t + \theta_{init}) \\ F\sin\left(\omega_0 t + \theta_{init} + \dfrac{\pi}{2}\right) \end{bmatrix} \qquad (2\text{-}61)$$

where $x(t)$ and $y(t)$ are the x- and y-components of the signal, ω_0 [rad/s] is the rotational speed, F is the radius of the circular orbit, and θ_{init} [rad/s] is the initial phase. In this study, because the fracture-induced cutting force rotates along with spindle rotation, $x(t)$ and $y(t)$ respectively correspond to the x- and y-components of the cutting force, ω_0 [rad/s] is the rotational speed of the spindle, and F [N] is the magnitude of the cutting force projected on the XY plane. It is necessary to monitor F to detect a tool fracture because its magnitude depends on the fracture.

By adapting a rotating coordinate at ω_0 rad/s in the clockwise direction alternative to ordinary x-y coordinates, the radius of the circular orbit F in the XY plane can be monitored easily (Fig. 2-17). The x- and y-components of the signal are transformed to the rotating coordinates as follows:

$$\begin{bmatrix} x_{\omega_0}(t) \\ y_{\omega_0}(t) \end{bmatrix} = \begin{bmatrix} \cos \omega_0 t & -\sin \omega_0 t \\ \sin \omega_0 t & \cos \omega_0 t \end{bmatrix} \begin{bmatrix} x(t) \\ y(t) \end{bmatrix} \tag{2-62}$$

where $x_{\omega_0}(t)$ is the radius component and $y_{\omega_0}(t)$ is the tangential component. Upon substituting Eq. 2-61 into Eq. 2-62, $x_{\omega_0}(t)$ and $y_{\omega_0}(t)$ are given by

$$\begin{bmatrix} x_{\omega_0}(t) \\ y_{\omega_0}(t) \end{bmatrix} = \begin{bmatrix} \cos \omega_0 t & -\sin \omega_0 t \\ \sin \omega_0 t & \cos \omega_0 t \end{bmatrix} \begin{bmatrix} F \sin(\omega_0 t + \theta_{init}) \\ F \sin\left(\omega_0 t + \theta_{init} + \dfrac{\pi}{2}\right) \end{bmatrix} = \begin{bmatrix} F \sin \theta_{init} \\ F \cos \theta_{init} \end{bmatrix} \tag{2-63}$$

Thus, the radius of the circular orbit F can be obtained by calculating the geometric mean of the radius and tangential components as

$$F = \sqrt{x_{\omega_0}{}^2 + y_{\omega_0}{}^2} \tag{2-64}$$

However, this coordinate transformation does not serve to reduce noise in the input signal. A transform method such as a Fourier transform is required to extract the rotation signal like a filter. Therefore, this research proposes a theory
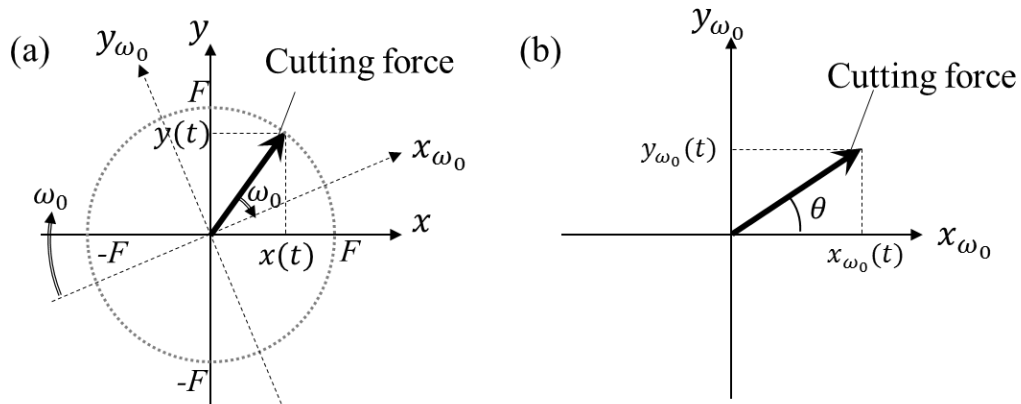

Fig. 2-17 (a) Cutting force rotating at ω_0 in the clockwise direction in XY plane; (b) cutting force on the rotation coordinate in the clockwise direction.

to transform a time-domain signal in the XY plane to a frequency domain signal in a rotating coordinate system. The radius and tangential components in the frequency domain are defined as

$$\mathbf{S}_{xy\_\omega_0} = \lim_{T_a \to \infty} \frac{1}{2T_a} \int_{-T_a}^{T_a} \mathbf{R_m}(\omega_0, t)\mathbf{S}_{xy}(t)\, dt$$

(2-65)

where $\mathbf{S}_{xy\_\omega_0} = \begin{bmatrix} X_{\omega_0} \\ Y_{\omega_0} \end{bmatrix}$, $\mathbf{R_m}(\omega_0, t) = \begin{bmatrix} \cos\omega_0 t & -\sin\omega_0 t \\ \sin\omega_0 t & \cos\omega_0 t \end{bmatrix}$, $\mathbf{S}_{xy}(t) = \begin{bmatrix} x(t) \\ y(t) \end{bmatrix}$

where X_{ω_0} and Y_{ω_0} are respectively the radius and tangential components in the frequency domain, and $\mathbf{R_m}(\omega_0, t)$ is the rotational matrix at $\omega_0 t$. If $x(t)$ and $y(t)$ do not include a frequency component of ω_0, $\mathbf{S}_{xy\_\omega_0}$ becomes a zero matrix because of the orthogonality of trigonometric functions. In other words, only the frequency component of ω_0 in the input signal should be considered. The x- and y-components of ω_{in} rad/s in the input signal can be represented as

$$\begin{bmatrix} x(t) \\ y(t) \end{bmatrix} = \begin{bmatrix} F\sin(\omega_{in}t + \theta_{init}) \\ F\sin(\omega_{in}t + \theta_{init} + \theta_{dif}) \end{bmatrix}$$

(2-66)

where θ_{dif} [rad] is the phase difference between the x- and y-components. Then, $\mathbf{S}_{xy\_\omega_0}$ must satisfy

$$\mathbf{S}_{xy\_\omega_0} = \begin{cases} \mathbf{0} & (\omega_0 \neq \omega_{in}) \\ \dfrac{F}{2}\begin{bmatrix} \sin\theta_{init} - \cos(\theta_{init} + \theta_{dif}) \\ \cos\theta_{init} + \sin(\theta_{init} + \theta_{dif}) \end{bmatrix} & (\omega_0 = \omega_{in}) \end{cases}$$

(2-67)

The geometric means of X_{ω_0} and Y_{ω_0} are represented as follows:

$$\left| \mathbf{S}_{xy\_\omega_0} \right| = \sqrt{X_{\omega_0}{}^2 + Y_{\omega_0}{}^2} = F\sqrt{\frac{1 + \sin\theta_{dif}}{2}}$$

(2-68)

If $\theta_{dif} = \pi/2$ rad, i.e., the input signal rotates in the clockwise direction, the geometric mean is equal to F. On the other hand, if $\theta_{dif} = -\pi/2$ rad, i.e., the input signal rotates in the counterclockwise direction, the geometric mean is zero even though the frequency of the input signal is ω_0. Thus, this characteristic may be used to extract a signal rotating in the clockwise direction.

Furthermore, based on this characteristic, a digital filter that passes only a signal rotating in the clockwise direction at a certain frequency, like a finite impulse response filter, could be created. The above theory transforms a time domain signal in the x-y coordinate system to a frequency domain signal in a rotating coordinate system. Therefore, inverse transformation from the frequency domain signal to the time domain signal is also possible. From this viewpoint, to obtain only a signal rotating in the clockwise direction at a certain frequency ω_0, the inverse transformation can be represented as

$$\mathbf{S}_{\mathrm{xy\_out}}(t) = \mathbf{R_m}^{-1}(\omega_0, t)\mathbf{S}_{\mathrm{xy}\_\omega_0} \tag{2-69}$$

where $\mathbf{S}_{\mathrm{xy\_out}}(t)$ is the signal rotating at frequency ω_0. However, to obtain $\mathbf{S}_{\mathrm{xy}\_\omega_0}$, both limits of integration need to be infinity, as shown in Eq. 2-65. Because the response time must be regulated to create a filter, a window function w_n is generally applied, by which a filter that passes only a signal rotating in the clockwise direction at frequency ω_0 can be represented as

$$\mathbf{S}_{\mathrm{xy\_out}}(t) = \mathbf{R_m}^{-1}(\omega_0, t)\frac{1}{2T_a}\int_{-T_a+t}^{T_a+t} w_n(\tau - t)\mathbf{R_m}(\omega_0, \tau)\mathbf{S}_{\mathrm{xy}}(\tau)\, d\tau$$

$$= \frac{1}{2T_a}\int_{-T_a+t}^{T_a+t} w_n(\tau - t)\mathbf{R_m}(\omega_0, \tau - t)\mathbf{S}_{\mathrm{xy}}(\tau)\, d\tau \tag{2-70}$$

where $w_n(t) = 0$ if $|t| \geq T_a$.

In the discrete domain, Eq. 2-70 is represented as

$$\mathbf{S}_{\mathrm{xy\_out}}'[0] = \frac{1}{N}\sum_{n=0}^{N-1} w_n'[n]\begin{bmatrix} \cos\dfrac{\omega_0 n}{F_s} & \sin\dfrac{\omega_0 n}{F_s} \\ -\sin\dfrac{\omega_0 n}{F_s} & \cos\dfrac{\omega_0 n}{F_s} \end{bmatrix}\mathbf{S}_{\mathrm{xy}}'[n] \tag{2-71}$$

where $w_n'[n] = 0$ if $n < 0$ or $n \geq N$,

and $\mathbf{S}_{\mathrm{xy\_out}}'[0]$ is the present output of the digital filter; $\mathbf{S}_{\mathrm{xy}}'[n]$, the past input of n sampling times before; N, the order of the digital filter; and F_s [Hz], the sampling frequency. In other words, this digital filter outputs the average values of the past samplings with proper compensations applied by rotational matrices. This digital filter passes only signals rotating in the clockwise direction at a special frequency. We call this signal processing theory an RDF, and we use it to monitor fracture-induced fluctuations in a disturbance force rotating in the clockwise direction on the XY plane. Before applying the RDF to real data, several time-domain simulation tests were carried out to confirm the characteristics of RDF.

2.4 Identification Method for Stable Machining Condition

Tool wear is an unavoidable problem, and a worn tool must be changed at the proper time. In addition, tool fracture should be detected because it can be regarded as a signal of overload. If tool wear is promoted excessively or tool facture happens on the tool edge, the cutting condition should be justified to low-load. On the other hand, chatter stability is not simple enough to be suppressed with a low-load cutting condition because it generates an interaction

of the dynamics of the tool and the waviness of workpiece surface. To identify a stable condition against chatter, its mechanism should be discussed.

2.4.1 Milling Model for Regenerative Chatter Mechanism

To predict chatter stability in milling, a cutting model like Fig. 2-18 is usually used to discuss the regenerative effect. Referring to the chatter stability prediction method proposed by Altintas [36], the regenerative effect theoretically can be explained as follows. The displacements of the feed and the normal directions are represented with x_t and y_t respectively. When the tool-edge angle is ϕ_i, the displacement of the tool in radial direction v_i is represented as

$$v_i = -x_t \sin\phi_i - y_t \cos\phi_i \tag{2-72}$$

In the milling process, the uncut chip thickness can be represented as a function for ϕ_i as follows:

$$h_c(\phi_i) = [s_t \sin\phi_i + (v_{i0} - v_i)]b(\phi_i) \tag{2-73}$$

where s_t is the feed rate per tooth and v_{i0} is the dynamic displacement of the previous tooth period. $b(\phi_i)$ is a function to determine whether the tooth immerses the work, expressed as

$$b(\phi_i) = \begin{cases} 1 & \text{where} \quad \phi_{st} \le \phi_i \le \phi_{ex} \\ 0 & \text{where} \ \phi_i \le \phi_{st} \text{ or } \phi_{ex} \le \phi_i \end{cases} \tag{2-74}$$

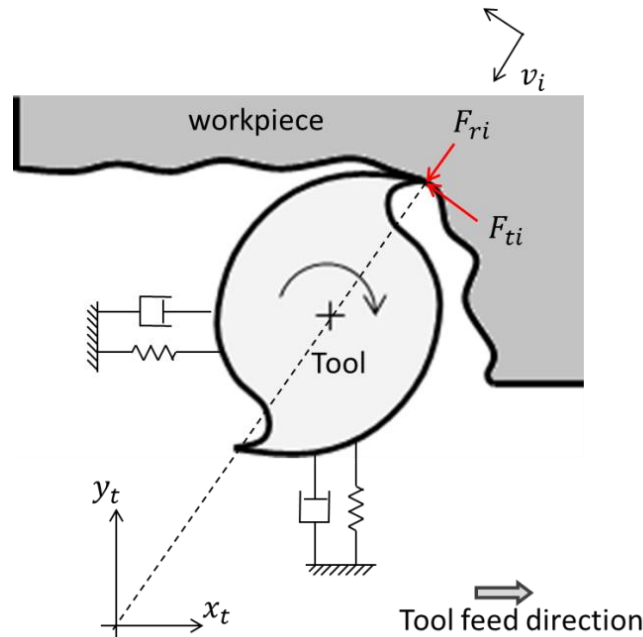where, ϕ_{st}, ϕ_{ex} are the start and exit immersion angles. Eq. 2-73 can be

Fig. 2-18   Dynamic milling model with two degrees of freedom.

transformed to the x-y coordinate expression as

$$h_c(\phi_i) = [x_t \sin\phi_i + y_t \cos\phi_i] b(\phi_i) \tag{2-75}$$

In Eq. 2-75, the static component of the chip thickness $s_t \sin\phi_j$ is eliminated because it does not contribute to the dynamic chip load regeneration mechanism.

The cutting force is defined as a product of the cutting coefficient and the cutting area; thus, the cutting force in the tangential and radial directions can be represented by introducing the axial depth of cut a_{cut}:

$$F_{ti} = K_c a_{cut} h_c(\phi_i), F_{ri} = K_r F_{ti} \tag{2-76}$$

where K_c, K_r are cutting coefficients. These cutting forces can be translated into x and y components as

$$F_{xi} = -F_{ti} \cos\phi_i - F_{ri} \sin\phi_i , F_{yi} = +F_{ti} \sin\phi_i - F_{ri} \cos\phi_i \tag{2-77}$$

Summing the cutting forces of each tooth, the total dynamic cutting forces on the tool can be determined as

$$F_x = \sum_{i=0}^{N_t-1} F_{xi} , F_y = \sum_{i=0}^{N_t-1} F_{yi} \tag{2-78}$$

where N_t is the number of teeth on the tool.

By substituting Eqs. 2-75 and 2-77 into Eq. 2-78, the following resultant matrix equation can be obtained:

$$\begin{Bmatrix} F_x \\ F_y \end{Bmatrix} = \frac{1}{2} a_{cut} K_c \begin{bmatrix} \alpha_{xx} & \alpha_{xy} \\ \alpha_{yx} & \alpha_{yy} \end{bmatrix} \begin{Bmatrix} x_t \\ y_t \end{Bmatrix} \tag{2-79}$$

where directional dynamic milling force coefficients are given by

$$\alpha_{xx} = \sum_{i=0}^{N_t-1} -b(\phi_i)[\sin 2\phi_i + K_r(1 - \cos 2\phi_i)]$$

$$\alpha_{xy} = \sum_{i=0}^{N_t-1} -b(\phi_i)[(1 + \cos 2\phi_i) + K_r \sin 2\phi_i]$$

$$\alpha_{yx} = \sum_{i=0}^{N_t-1} b(\phi_i)[(1 - \cos 2\phi_i) - K_r \sin 2\phi_i] \tag{2-80}$$

$$\alpha_{xy} = \sum_{i=0}^{N_t-1} b(\phi_i)[\sin 2\phi_i - K_r(1 + \cos 2\phi_i)]$$

The matrix expression of Eq. 2-79 is

$$\{F_c(t)\} = \frac{1}{2} a_{cut} K_c [A(t)]\{r(t)\} \tag{2-81}$$

In milling, $[A(t)]$ is periodic at tooth passing frequency $\omega_t = N_t \Omega$ or tooth period $T_p = 2\pi/\omega_t$, and thus can be expanded into Fourier series:

$$[A(t)] = \sum_{m=-\infty}^{\infty} [A_m] e^{jm\omega_t t} \quad \text{where} [A_m] = \frac{1}{T_p} \int_0^{T_p} [A(t)] e^{-jm\omega_t t} \, dt \tag{2-82}$$

In the most simplistic approximation, the average component of the Fourier series expansion is considered, i.e., $m = 0$:

$$[A_0] = \frac{1}{T_p} \int_0^{T_p} [A(t)] \, dt \tag{2-83}$$

where each integrated function is given as

$$\alpha_{xx} = \frac{N_t}{2} [\cos 2\phi - 2K_r \phi + K_r \sin 2\phi]_{\phi_{st}}^{\phi_{ex}}$$

$$\alpha_{xy} = \frac{N_t}{2} [-\sin 2\phi - 2\phi + K_r \cos 2\phi]_{\phi_{st}}^{\phi_{ex}}$$

$$\tag{2-84}$$

$$\alpha_{yx} = \frac{N_t}{2} [-\sin 2\phi + 2\phi + K_r \cos 2\phi]_{\phi_{st}}^{\phi_{ex}}$$

$$\alpha_{xy} = \frac{N_t}{2} [-\cos 2\phi - 2K_r \phi - K_r \sin 2\phi]_{\phi_{st}}^{\phi_{ex}}$$

The dynamic milling expression Eq. 2-81, as a result, can be reduced to

$$\{F_c(t)\} = \frac{1}{2} a_{cut} K_c [A_0] \{r(t)\} \tag{2-85}$$

Therefore, the dynamic cutting force matrix can be determined from the dynamic displacements of the tool in the X and Y directions.

The relation between the tool displacements and the dynamic cutting force also can be represented by employing the transfer function matrix at the cutter and workpiece contact zone. The transfer function matrix is

$$[G(j\omega)] = \begin{bmatrix} G_{xx}(j\omega) & G_{xy}(j\omega) \\ G_{yx}(j\omega) & G_{yy}(j\omega) \end{bmatrix} \tag{2-86}$$

where $G_{xx}(j\omega)$ and $G_{yy}(j\omega)$ are the direct transfer functions in the X and Y directions, and $G_{xy}(j\omega)$ and $G_{yx}(j\omega)$ are the cross-transfer functions. The vibrations at the present time t and previous tooth period $t - T_p$ are defined as

$$\{r(t)\} = \{x_t(t), y_t(t)\}^T, \{r_0\} = \{x_t(t - T_p), y_t(t - T_p)\}^T \tag{2-87}$$

The transfer function matrix shows the ratio between the displacements and the applied force. In the frequency domain, therefore, the vibrations at the chatter frequency ω_c are represented as

$$\{r(j\omega_c)\} = [G(j\omega_c)]\{F_c\}e^{j\omega_c t}, \{r_0(j\omega_c)\} = \{r(j\omega_c)\}e^{-j\omega_c T_p} \tag{2-88}$$

The difference of these vibrations is a significant factor to calculate the uncut chip thickness:

$$\{r_d(j\omega_c)\} = \{r(j\omega_c)\} - \{r_0(j\omega_c)\} = [1 - e^{-j\omega_c T_p}][G(j\omega_c)]\{F_c\}e^{j\omega_c t} \tag{2-89}$$

where $\omega_c T$ is the phase delay between the vibrations at successive tooth periods

T. Substituting $\{\boldsymbol{r}_d(j\omega_c)\}$ into the dynamic milling Eq. 2-85, the following equation can be derived.

$$\{\boldsymbol{F_c}\}e^{j\omega_c t} = \frac{1}{2}a_{cut}K_c[1 - e^{-j\omega_c T_p}][\boldsymbol{A_0}][\boldsymbol{G}(j\omega_c)]\{\boldsymbol{F_c}\}e^{j\omega_c t} \qquad (2\text{-}90)$$

To have a solution excepting $\{F\} = \boldsymbol{0}$, its determinant must be zero.

$$\det\left[[\boldsymbol{I}] - \frac{1}{2}a_{cut}K_c[1 - e^{-j\omega_c T_p}][\boldsymbol{A_0}][\boldsymbol{G}(j\omega_c)]\right] = 0 \qquad (2\text{-}91)$$

To linearize the non-linear part $[1 - e^{-j\omega_c T_p}]$, the eigenvalue of the characteristic equation is described as

$$\Lambda = -\frac{N_t}{4\pi}a_{cut}K_c[1 - e^{-j\omega_c T_p}] \qquad (2\text{-}92)$$

The resulting characteristic equation becomes

$$\det[[\boldsymbol{I}] - \Lambda[\boldsymbol{A_0}^*][G(j\omega_c)]] = 0$$

where $\qquad [\boldsymbol{A_0}^*] = \frac{1}{2\pi}[\boldsymbol{A_0}] = \begin{bmatrix} \alpha_{xx}^* & \alpha_{xy}^* \\ \alpha_{yx}^* & \alpha_{yy}^* \end{bmatrix}$ $\qquad (2\text{-}93)$

The eigenvalue of the above equation can easily be solved for a given chatter frequency ω_c by calculating a following quadratic function.

$$\Lambda^2 + c_0\Lambda + c_1 = 0$$

where
$$c_0 = G_{xx}(j\omega_c)G_{yy}(j\omega_c)(\alpha_{xx}^*\alpha_{yy}^* - \alpha_{xy}^*\alpha_{yx}^*),$$
$$c_1 = \alpha_{xx}^*G_{xx}(j\omega_c) + \alpha_{yy}^*G_{yy}(j\omega_c)$$
$\qquad (2\text{-}94)$

By separating the eigenvalue to a real and an imaginary part as $\Lambda = \Lambda_R + j\Lambda_I$ and substituting $e^{-j\omega_c T_p} = \cos\omega_c T_p - j\sin\omega_c T_p$ in Eq. 2-92, the critical axial depth of cut at chatter frequency ω_c can be derived as

$$a_{lim} = -\frac{2\pi}{N_t K_c}\left[\frac{\Lambda_R(1 - \cos\omega_c T_p) + \Lambda_I\sin\omega_c T_p}{(1 - \cos\omega_c T_p)} + j\frac{\Lambda_I(1 - \cos\omega_c T_p) - \Lambda_R\sin\omega_c T_p}{(1 - \cos\omega_c T_p)}\right] \qquad (2\text{-}95)$$

Because the imaginary part of Eq. 2-95 is zero, the ratio Λ_I/Λ_R can be determined as

$$\kappa = \frac{\Lambda_I}{\Lambda_R} = \frac{\sin\omega_c T_p}{1 - \cos\omega_c T_p} \qquad (2\text{-}96)$$

Substituting κ into Eq. 2-95, the chatter-free axial depth of cut is found as

$$a_{lim} = -\frac{2\pi\Lambda_R}{N_t K_c}(1 + \kappa^2) \qquad (2\text{-}97)$$

Therefore, when a chatter frequency is given, the corresponding chatter limit in terms of the axial depth of cut can be determined from Eq. 2-97. Furthermore, the chatter frequency ω_c at tooth period T is represented as

$$\omega_c T_p = \cos^{-1}\frac{\kappa^2 - 1}{\kappa^2 + 1} = -\cos^{-1}2\delta \tag{2-98}$$

where
$$\delta = \tan^{-1}\kappa$$

Thus, if k is an integer number,

$$\omega_c T = \pi - 2\delta + 2k\pi = \varepsilon + 2k\pi \tag{2-99}$$

where $\varepsilon = \pi - 2\delta$ is the phase shift between the inner and outer modulations (present and previous vibration marks). The spindle speed N_r [rev/min] is simply calculated by finding the tooth passing period T_p [s]:

$$T_p = \frac{1}{\omega_c}(\varepsilon + 2k\pi) \rightarrow N_r = \frac{60}{N_t T_p} \tag{2-100}$$

As a conclusion, the relation between the spindle speed and the critical axial depth of cut can be determined by analyzing the interaction between the transfer functions of the machine tool system and the dynamic cutting forces. Additionally, the cutting coefficient of the work material also must be identified. Then, the stability lobes can be drawn with following procedures:

① Select a chatter frequency from the transfer functions around a dominant mode.
② Solve the eigenvalue equation (Eq. 2-94).
③ Calculate the critical depth of cut from equation (Eq. 2-97).
④ Calculate the spindle speed from Eq. 2-100 for each stability lobe of $k = 0, 1, 2, ...$
⑤ Repeat steps ① to ④ by scanning the chatter frequencies around all dominant modes of the structure evident on the transfer functions.

2.4.2 Concept for Identification

The prediction method for chatter stability explained in the previous section can draw a stability-lobes diagram as shown in Fig. 2-19 (the parameters are given in Table 2-4 as an example). The critical depth of cut locally becomes larger at some spindle rotation regions, which are called stability pockets. Although the stability pocket should be identified accurately to enhance the cutting efficiency, an accurate analysis is difficult because the stability lobes are drawn on the basis of modal parameters that change according to the spindle rotation and heat generation. On the other hand, chatter frequency information is also analyzable with a frequency-domain milling model, but this is rarely focused on. Chatter frequency gradually becomes higher with faster spindle rotation and suddenly

Table 2-4 Modal parameters of a tool to draw Fig. 2-19.

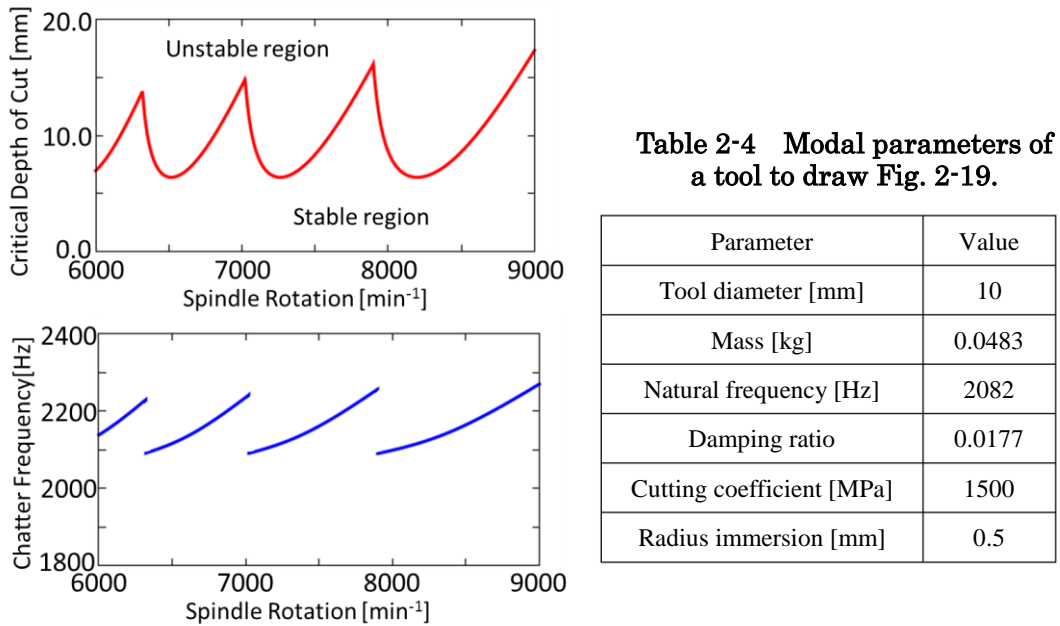| Parameter	Value
Tool diameter [mm]	10
Mass [kg]	0.0483
Natural frequency [Hz]	2082
Damping ratio	0.0177
Cutting coefficient [MPa]	1500
Radius immersion [mm]	0.5

Fig. 2-19　(a) Critical depth of cut and (b) chatter frequency along with the spindle rotation in milling.
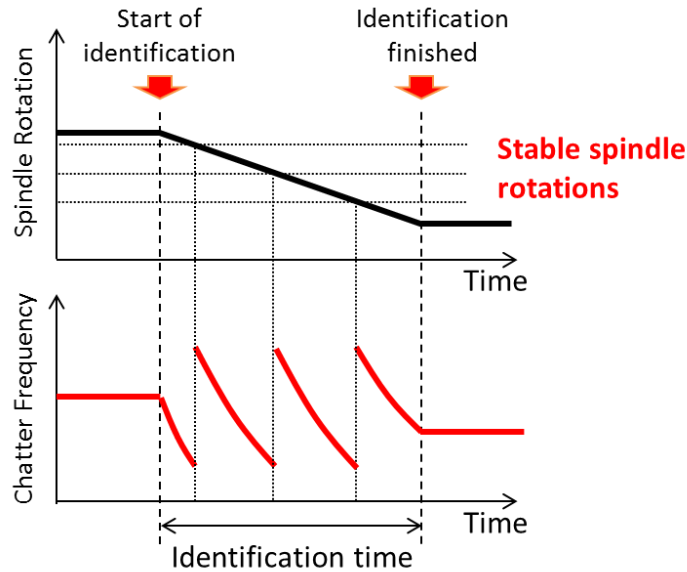
Fig. 2-20　Concept of the proposed identification method for stable spindle rotations.

shifts lower at the stability pocket. This characteristic would be useful to identify the stability pocket accurately.

In this study, the spindle rotation is continuously decreased during chatter as shown in Fig. 2-20. If the chatter frequency behaves as shown in the frequency-domain analysis, chatter frequency would gradually become lower and drastically shift higher at some spindle rotations. These spindle rotations can be

54

regarded as the stability pockets. As a result, the stability pocket in milling can be identified with only one milling test. However, the chatter frequency shift is explained in the frequency domain. Therefore, it is necessary to confirm whether the frequency shift actually occurs even if the spindle rotation time-dependently changes.

2.5 Time-Domain Milling Simulator

The drastic shift of the chatter frequency when decreasing the spindle rotation is a phenomenon that is explained by frequency-domain analysis. However, frequency domain analysis assumes that the response time is infinite, whereas the spindle rotation changes with time. As a result, the identified spindle rotations would vary from the actual stable spindle rotations. Although the identification error would be suppressed if the milling time can be ensured long enough, the time of diagnosis should be short to avoid damage to the tool and the machine tool. Therefore, the identification error should be discussed corresponding to the spindle variation rate.

To analyze the time-dependent variation of physical phenomena, a time-domain simulation is an effective approach. The time-domain simulation for dynamics sequentially progresses by calculating the force distribution and the movement alternately for each step. For example, movement of a single degree-of-freedom (1-DOF) spring-damper-mass system in the time domain can be simulated as shown in Figs. 2-21 to 2-23. Considering the force distribution in the 1-DOF system, the external force, the elastic force from the spring, and the friction force are applied to the mass as shown in Fig. 2-21. By calculating the resultant force and dividing it by the amount of mass, the acceleration can be obtained. Thus, the velocity and the displacement of the mass are also determined by integrating the acceleration with a step time. After that, the elastic force and the friction force can be updated on the basis of the obtained displacement and velocity information, and these procedures are repeated until the end time of the simulation. This simulation can be realized with code in the C language as shown in Fig. 2-22; the simulated behavior of the displacement is shown in Fig. 2-23. The simulation result actually corresponds to the given natural frequency. This basic repetition is the same even if the system has a complicated transfer function and multiple masses. By converting the transfer
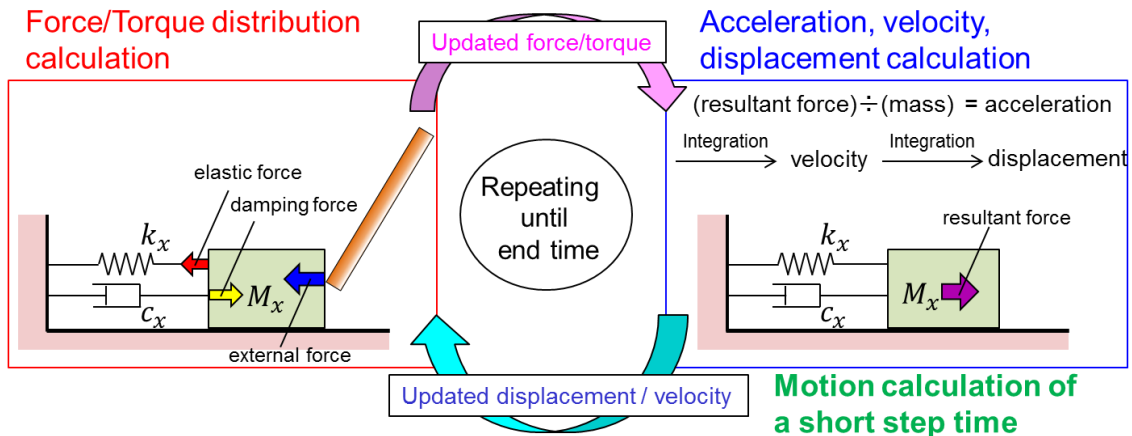
Fig. 2-21   Procedures for a motion simulation of a 1-DOF spring-damper-mass system.

```c
#include <stdio.h>
#include <math.h>

#define    REPEAT     10000
#define    DELTA_T    0.0001

#define    Mx    10.0 //mass
#define    cx    50.0 //damping coefficient
#define    kx    39478.6 //stifness

int main(void){

    double Fext = 0.0, Fresul = 0.0; //external and resultant force
    double x = 0.0, xd = 0.0, xdd = 0.0; //displacement, velocity, acceleration
    FILE *fp;
    fp = fopen("data.dat", "w");

    for(int i=0; i<REPEAT; i++){   //main loop
        if(i==1000)Fext = 10000.0; else Fext = 0.0;
        Fresul = Fiext – (cx * xd + kx * x);
        xdd = Fresul / Mx;
        xd += xdd * DELTA_T;
        x += xd * DELTA_T;

        fprintf(fp, "%lf¥t%lf¥n", DELTA_T*i , x); //saving data
    }

    return 0;
}
```

Natural frequency is 10 Hz

Resultant force calculation

Acceleration, velocity and displacement calculation
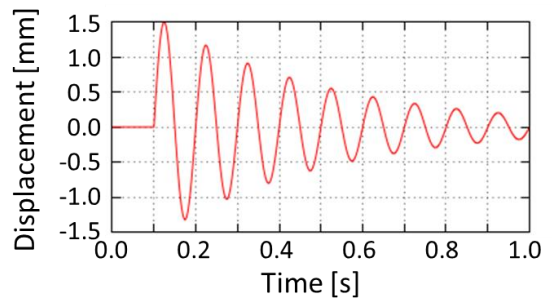
Fig. 2-23   Simulation result (displacement).

Fig. 2-22   An example of C-language code for motion simulation of a 1-DOF spring-damper-mass system.

function to a difference equation in the discrete domain, the displacement of the system is determined by calculating the resultant force applied to the system in every step.

In order to create a milling model in the time domain, the determination of the applied external force (cutting force) to the tool must be carefully discussed because the regenerative effect also must be considered, whereas the tool can be modeled as a 2-DOF spring-damper-mass system in the X and Y directions.

The regenerative effect is caused by the interaction between the present vibration of the tool and the surface waviness of workpiece left by the previous tooth passing. Generally, the cutting force is defined as the product of a cutting coefficient and the width of cut. From this viewpoint, the simulation should be created with a surface profile method. As shown in Fig. 2-24, the workpiece surface is expressed with profiles in the proposed simulation. The procedures are explained as follows.

① The width of cut is obtained by linear interpolation and the cutting force is determined and applied to the dynamics of the X and Y directions.

② The tool edge position is updated from the rotational angle and the
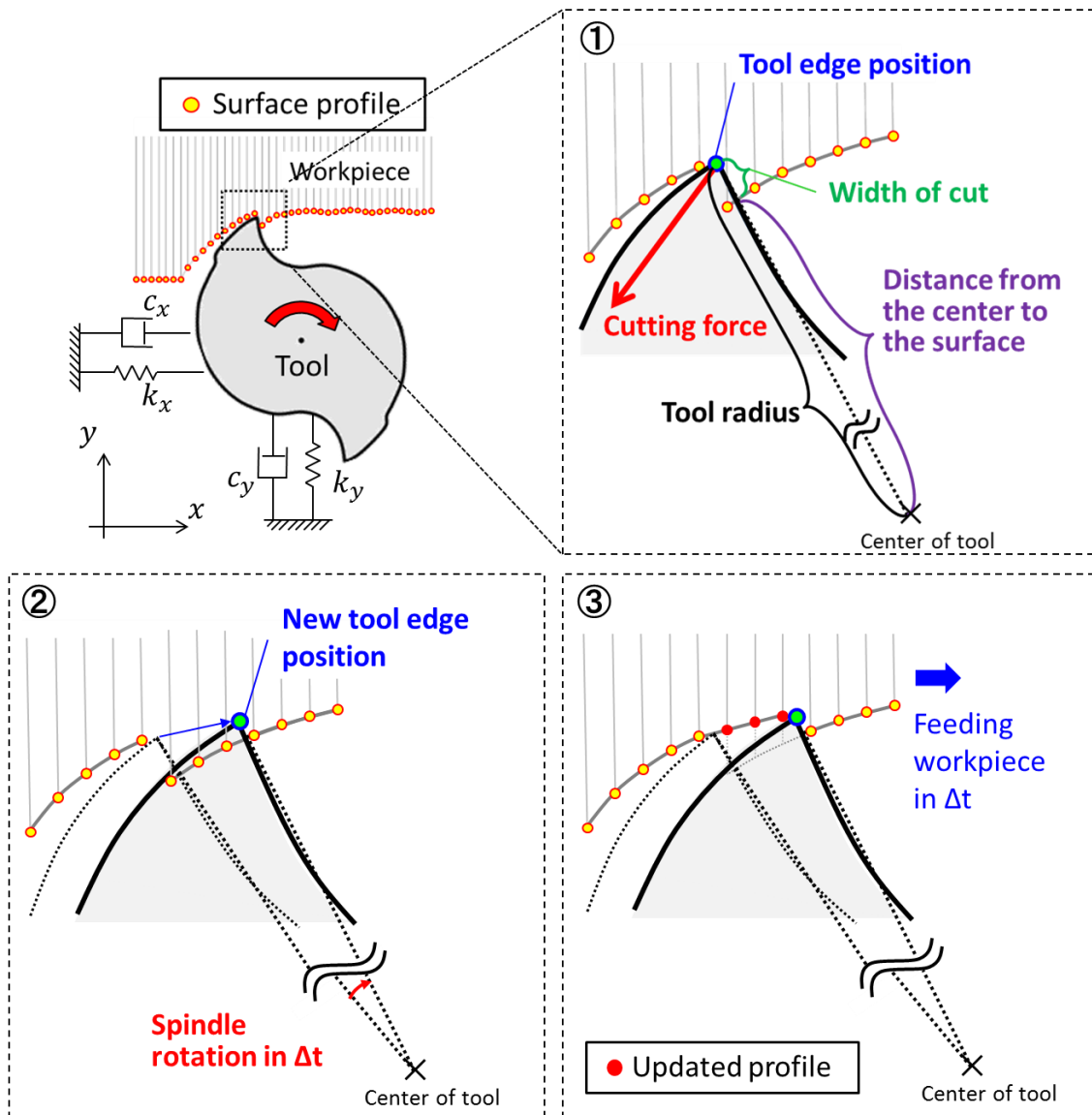
Fig. 2-24　Procedures for the time-domain milling simulation.

displacement of the tool, on the basis of the integrations for the rotational speed and the tool acceleration with a short step time.

③ The profiles between the present tool edge position and the previous one are updated with linear interpolation. Additionally, the profiles are slightly fed on the basis of the feed rate option.

④ The procedures from ① to ③ are repeated until the end time of the simulation.

Furthermore, the tool lead is expressed by laminating the simulation layers that have different rotation angles, as shown in Fig. 2-25.

The chatter vibration occurs because of the vibrational modes of the tool, and the stability lobes can be drawn for the each vibrational mode. When the transfer function of the system has more than two vibrational modes, multiple stability lobes are drawn in the stability diagram. In this case, the lowest lobes are dominant and regarded as the critical depth of cut, i.e., the dominant stability lobes are written by the vibrational mode that has a largest compliance. Furthermore, the stiffness of the coupling modes is generally high compared with that of the direct modes. Thus, the first-order direct mode tends to draw the dominant lobes; that is why we approximated the tool transfer function with a 2-DOF system on the XY plane for the time domain simulation.
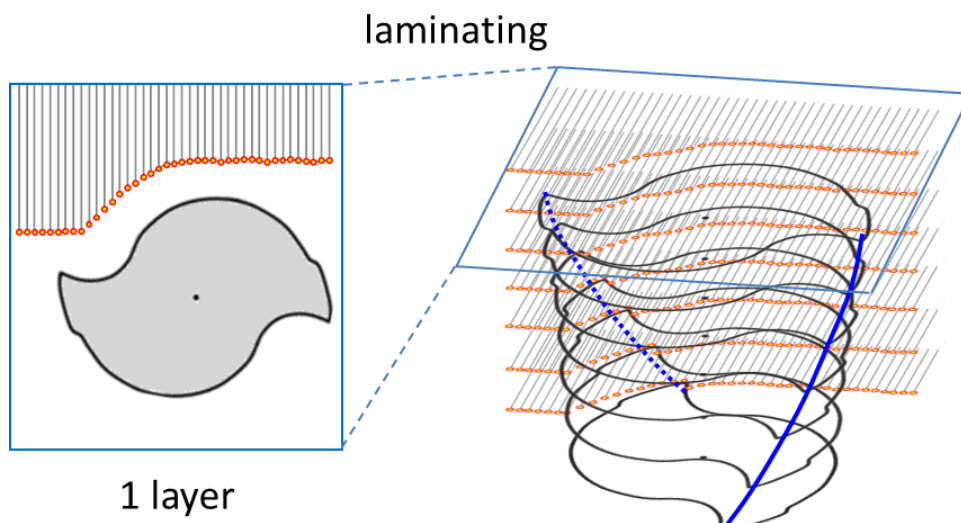
Fig. 2-25 Tool lead expression in the proposed simulation.

2.6 Summary

The significant theories for the proposed process monitoring methods and self-diagnosis system are introduced in this chapter. The contents are summarized as follows.

1. By explaining disturbance observer theory with a physical model, its applicability to the cutting force/torque estimation is theoretically indicated.

2. The FFT and CWT are explained as conventional signal processing methods.

3. The MV+MFT and RDF are proposed as new sophisticated signal processing methods for chatter detection and drill fracture detection. The performance of the proposed methods will be experimentally compared with that of conventional methods in later chapters.

4. A concept of a self-diagnosis method for stable spindle rotations against chatter is described on the basis of a frequency-domain analytical prediction method for chatter stability in milling.

5. Procedures to create a time-domain milling simulation are described to confirm the adequacy of the proposed diagnosis method.

3 Simulator and Experimental Setup

In Chapter 2, the fundamental theories for observer-based process monitoring and stable cutting condition identification are presented. In the cutting force/torque estimation algorithm, the nominal parameters must be set correctly to reduce the error of estimation; therefore, the nominal parameters should be preliminarily identified accurately.

This chapter introduces mechanical parameters and configurations of 3-axis vertical machine tools used in this research. Moreover, the nominal parameters for the cutting force and torque estimations are summarized.

3.1 Configurations of Machine Tool

Configuration of controller also has influences with estimation accuracy of the observer. For example, the differential process for discrete variables like encoder pulse information causes high-frequency noise in the estimated velocity information, which is called "quantization error noise" and able to be suppressed by applying a high-resolution encoder. Furthermore, the estimation frequency range of disturbance information is regulated with the servo frequency of controller. Generally speaking, the sampling frequency of the encoder signal is higher than the update frequency of the current reference; thus, the multi-rate sampling method is sometimes applied for the disturbance estimation, which assumes that the current information has a zero-order holding characteristic and conducts the calculation of the disturbance estimation at the sampling frequency of encoder. Because the quantization error noise generally can be reduced with higher sampling rate, the estimation accuracy can be ensured with the multi-rate sampling method. Moreover, this is an effective method to expand the estimation frequency range for the disturbance information.

In this study, two machine tools are utilized to confirm the adequacy of the proposed methods: TC-S2C, and S500X1 (both are produced by Brother Industry Ltd). The appearances of machine tools are shown in Figs, 3-1 and 3-2, and the configurations are summarized Tables 3-1 and 3-2 respectively. The both machines employ a same P-PI controller for the spindle and the each axis control

Fig. 3-1 Appearance of the machine tool 1 in this research (Brother Industries, Ltd. TC-S2C).

Fig. 3-2 Appearance of the machine tool 2 in this research (Brother Industries, Ltd. S500X1).

system. The remarkable differences between the both machines are the update frequency of current information and the rotary encoder resolution of the spindle. Although the update frequencies of current reference are different in both machine tools, the multi-rate sampling method is applied to TC-S2C in order to enhance the frequency of cutting force/torque estimation. The encoders of spindles originally have resolutions of only 1024 PPR (pulses per revolution) in both machine tools; thus, the resolutions are enhanced to 17 bit PPR in TC-S2C and 20 bit PPR in S500X1 with an electric multiplication method. On the other hand, the ballscrew-driven stages have same encoder resolution in both machine tools. In short, the controller and encoder introduced to the S500X1 have higher performances than that used in TC-S2C. These differences might have influences on the estimation accuracy of cutting torque particularly in high frequency domain.

Therefore, the S500X1 is only used for the chatter experiments in this study because the frequency information higher than 300 Hz is not necessary to detect the tool wear progress and tool fracture, which is much lower than the update frequency of current reference in TC-S2C as 2000 Hz. (The discussion of cutoff frequency modification for collision detection is held in Chapter 4 and concludes that 53.3 Hz is proper, which is sufficiently smaller than 2000 Hz.)

Table 3-1　Characteristics of the machine tool 1 (TC-S2C).

3 axis vertical machine tool	TC-S2C (Brother Industry Ltd.)
Rotary encoder resolution for the spindle	131072 PPR (17bit)
Rotary encoder resolution for XYZ axis	1048576 PPR (20bit)
Sampling frequency of the encoder information	8000 Hz
Update frequency of the current reference	2000 Hz

Table 3-2　Characteristics of the machine tool 2 (S500X1).

3 axis vertical machine tool	S500X1 (Brother Industry Ltd.)
Rotary encoder resolution for the spindle	1048576 PPR (20bit)
Rotary encoder resolution for XYZ axis	1048576 PPR (20bit)
Sampling frequency of the encoder information	8000 Hz
Update frequency of the current reference	8000 Hz

The cutoff frequency of low-pass filters in the disturbance observer and the pseudo differential process is an important factor to enhance the accuracy of the proposed process monitoring and stability identification. The signal noise should be suppressed to monitor the amplitude of the cutting force and torque; on the other hand, high-frequency information should not be eliminated when a frequency analysis is performed on the estimated cutting force and torque. Thus, the cutoff frequency also should be modified properly for each problem.

In this research, drilling and tapping are focused on as targets of the wear monitoring. In drilling and tapping, the static components in the cutting force and torque are the most reliable criteria to capture the wear progress. Thus, the cutoff frequency should be set low to suppress high-frequency noise. In case of the collision detection, the cutoff frequency should be set high from the viewpoint of the time response, while it should be set low for the signal-noise suppression. In other words, a balanced modification is demanded for the cutoff frequency.

In contrast, the cutoff frequency should not be set low for the tool fracture and chatter detection because a frequency analysis would be employed to capture a periodic variation in cutting force/torque due to tool fracture or chatter. From this viewpoint, the cutoff frequency for tool fracture detection should be set to higher than 267 Hz because the tool fracture is detected by monitoring a cutting force fluctuation at the spindle rotation frequency and the maximum spindle rotation is 16000 min^{-1} ($\fallingdotseq$ 267Hz) in S500X1.

For the chatter detection, the cutoff frequency should be higher than at least 800 Hz which is the observed chatter frequency in the milling test of this research. However, the chatter-induced fluctuation could be captured even if the cutoff frequency is lower than 800 Hz because the first-order low-pass filter does not drastically suppress high-frequency information. Furthermore, when the cutoff frequency is higher than 800 Hz, the quantization error noise gets too large to observe the wave shape of estimated cutting torque. As a conclusion of these discussions, the cutoff frequency is set to as shown in Table 3-3.

Table 3-3　Disturbance observer gain and
cutoff frequency of LPF in pseudo-differential process.

	g_{dis}[rad/s]	g_{LPF} [rad/s]
Tool wear monitoring	500	500
Tool collision detection	335	335
Tool fracture detection	3500	3500
Chatter detection	3500	3500

Considering the other causes for the estimation error, heat deformation is also significant, which leads to large contact pressure between mechanical parts. In this case, large energy is consumed even under the same movement operation; thus, an error occurs in the cutting force/torque estimation. When the process monitoring has to be performed for a long time, the static error due to heat generation also should be carefully monitored.

3.2 Characteristics of Machine Tool

When the disturbance observer is used to enhance the robustness of the control system, characteristics of the controlled object have to be well understood. In particular, the torque coefficient, the mass of movable parts and the inertia moment of rotational parts have to be accurately identified because these values are nominalized to apply to the disturbance estimation.

On the other hand, this research is focusing on observer-based process monitoring; thus, the error of nominal value does not effect on the robustness of the control system. However, the nominal-parameter error directly has influences on the estimation accuracy of cutting force and torque.

Although the nominal value simply can be set based on the designed value, the actual value often varies from the designed value because of the runout of rotational components, the torque ripple in motor, and so on. From the practical viewpoint, the nominal values should be identified based on idling experiments. By conducting several idling tests on the spindle and ballscrew-driven stage, the mechanical parameters are identified as shown in Tables from 3-4 to 3-7, which correspond to that in Eqs. 2-20 and 2-23.

$$\hat{F}_{cut} = \frac{2\pi}{l} \cdot \frac{g_{dis}}{s + g_{dis}} \left\{ \frac{g_{LPF}}{s + g_{LPF}} K_{t\theta zn} I_a^{ref} - J_{\theta an}\hat{\omega}_{\theta z}s - D_{\theta an}\hat{\omega}_{\theta z} - C_{\theta an}\text{sgn}(\hat{\omega}_{\theta z}) \right\} - M_z g$$

(2-20)

where
$$\hat{\omega}_{\theta z} = \frac{s g_{LPF}}{s + g_{LPF}} \theta_z$$

$$\hat{T}_{cut} = \frac{g_{dis}}{s + g_{dis}} \left\{ \frac{g_{LPF}}{s + g_{LPF}} K_t I_a^{ref} - J_n\hat{\omega}s - D_n\hat{\omega} - C_n\text{sgn}(\hat{\omega}) \right\}$$

(2-23)

where
$$\hat{\omega} = \frac{s g_{LPF}}{s + g_{LPF}} \theta$$

The details of the idling tests are explained in Chapter 4.

The nominal mass in each axis is enormously larger than the designed value shown in Table 3-8. This is because the inertia moment of the screw is included to construct a single mass model as explained in Chapter 2.

Table 3-4   Each parameter of X-axis nominal model.

Nominal viscous friction coefficient D_{an}	732 N/(m/s)
Nominal Coulomb friction C_{an}	94.0 N
Nominal total mass of X axis M_{an}	227.0 kg
Lead of screw l	16 mm

Table 3-5   Each parameter of Y-axis nominal model.

Nominal viscous friction coefficient D_{an}	1025 N/(m/s)
Nominal Coulomb friction C_{an}	151.0 N
Nominal total mass of Y axis M_{an}	325.0 kg
Lead of screw l	16 mm

Table 3-6　Each parameter of Z-axis nominal model.

Nominal mass of Z axis M_{zn}	175 kg
Nominal viscous friction coefficient D_{an}	1968 N/(m/s)
Nominal Coulomb friction C_{an}	240 N
Nominal total mass of Z axis M_{an}	380 kg
Lead of screw l	16 mm

Table 3-7　Each parameter of spindle nominal model.

Nominal inertia moment of spindle J_n	0.0048 kg・m^2
Nominal viscos friction coefficient	5.0×10^{-5} Nm・min
Nominal Coulomb friction	0.1062 Nm

Table 3-8　Each designed value of each stage mass and spindle inertia moment.

Designed mass of x stage	55.0 kg
Designed mass of y stage	140.5 kg
Designed mass of z stage	188.0 kg
Designed inertia moment of spindle	0.0048 kg・m^2

3.3 Discussion for Encoder Resolution

As shown in Tables 3-1 and 3-2, this research employs machine tools having 17 bit or 20 bit PPR rotary encoders in their spindle and ballscrew-driven stage servo motors. To estimate the cutting force and torque accurately, encoder resolution is a dominant factor because the quantum error induces large noise when the resolution is not sufficiently high. Therefore, this section evaluates the quantum error of each encoder resolution with a simple time-domain simulation.

The quantum error generally gets larger with higher motor rotational speed, thus, the spindle rotation is set to 16000 min^{-1} (maximum speed in S500X1). Figure 3-3 shows the simulation result of 10 bit PPR resolution. By applying FFT analysis to the simulated noise and requiring maximum amplitude spectrum, amplitude of noise is evaluated with each encoder resolution as shown in Fig. 3-4. The simulation result certainly shows that the quantum error-induced noise gets smaller with higher resolution and lower cutoff frequency. Although other causes such as torque ripple negatively influences on the estimation accuracy, the

obtained relation would be useful to know the required encoder resolution for cutting force and torque monitoring, e.g., the encoder resolution must be at least higher than 17 bit PPR to distinguish 1 Nm fluctuation in high frequency as 4000
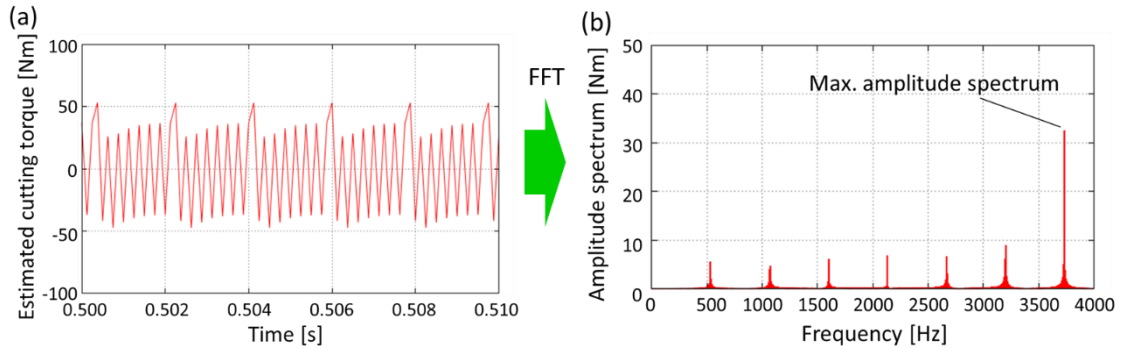
Fig. 3-3   Quantum error-induced noise in estimated cutting torque:
(a) in time-domain simulation result, (b) amplitude spectrum of FFT.
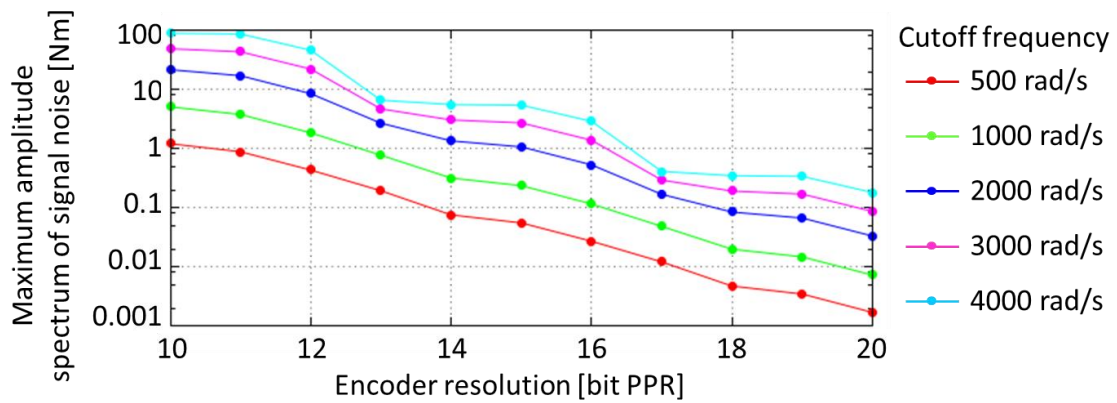
Fig. 3-4   Maximum amplitude spectrum of noise in estimated cutting torque
with each encoder resolution and cutoff frequency of low-pass filter.
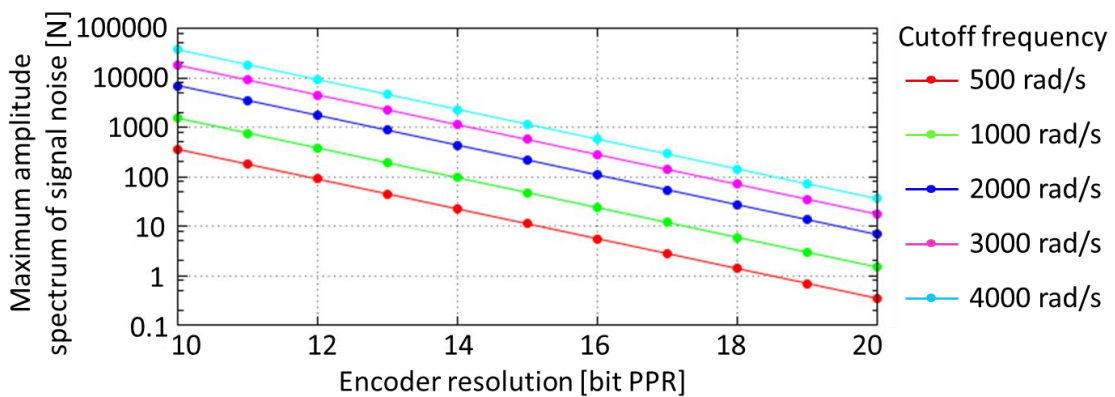
Fig. 3-5   Maximum amplitude spectrum of noise in estimated cutting force
with each encoder resolution and cutoff frequency of low-pass filter.

rad/s. This approach is also applicable to the ballscrew-driven stage. The screw rotates at 3125 min^{-1} when the feed rate is 50000 mm/min (maximum feed rate of TC-S2C). Figure 3-5 summarizes the relation between the amplitude of noise due to quantum error and the encoder resolution. The signal noise gets smaller with higher encoder resolution and lower cutting frequency in the same manner with the estimated cutting torque.

This research applies 3500 rad/s cutoff frequency to the cutting torque estimation algorithm to detect chatter, thus, 17 bit PPR would be enough high resolution for the spindle control system because chatter-induced fluctuation in cutting torque is clearly larger than 1 Nm. Furthermore, 20 bit PPR would be enough high resolution for the ballscrew-driven stage controller to detect aberrances because it can suppress the quantum error to 36 N even under the high screw rotation as 3125 min^{-1} and high cutoff frequency as 4000 rad/s. Considering that the original encoder resolution is 10 bit PPR, it is clear that the enhancement method like electric multiplication is indispensable to suppress the signal noise due to quantum error.

In both estimations of cutting torque and force shown in Fig. 3-4 and 3-5, the signal noise can be approximately reduced by half by increasing the encoder resolution of 1 bit. Based on this characteristic, the required encoder resolution can be clarified according to the amplitude and frequency of the expected fluctuation due to the aberrance.

3.4 Simulator Setup

In order to perform a time-domain milling simulation, a parallel calculation system with a graphical processing unit (GPU) is constructed based on CUDA (Compute Unified Device Architecture) modules in this research.

The CUDA is a parallel computing platform and application programing interface (API) model invented by NVIDIA Corporation. [63] It enables dramatic increases in computing performance by harnessing the power of GPU which has a lot of processors for various computations. Since its introduction in 2006, CUDA has been widely deployed to thousands of applications and focused in research papers of various fields; astronomy, biology, chemistry, physics, data mining, manufacturing, finance, and other computationally intense fields.
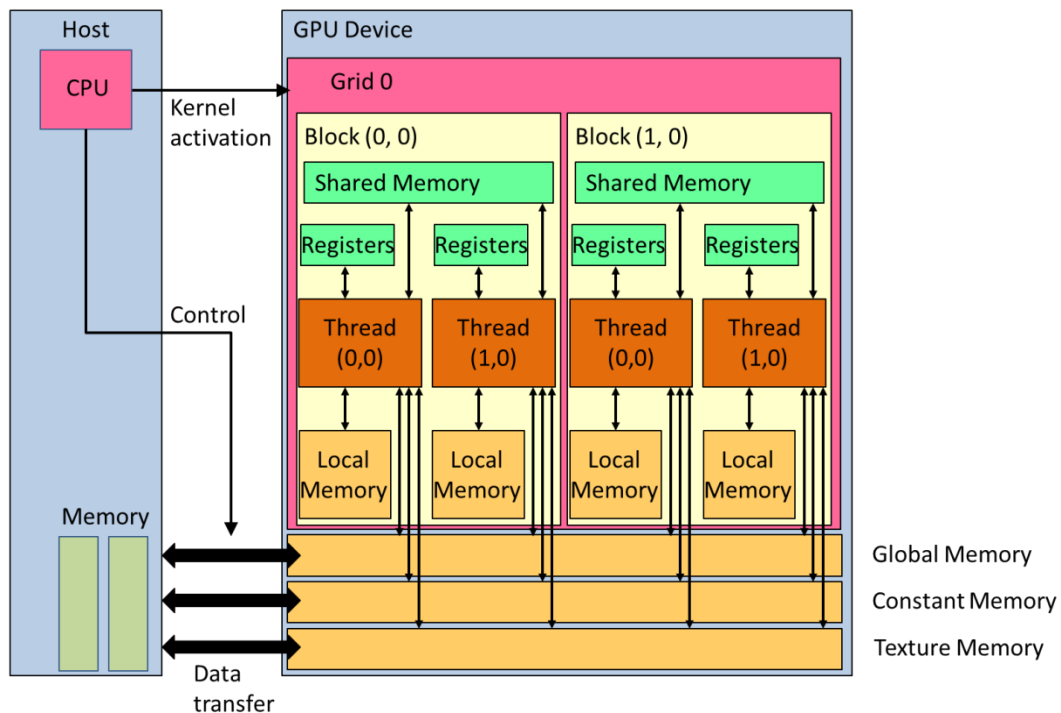
Fig. 3-6   Data transfer diagram among GPU and host device.

Following points are typically explained as basic concepts for CUDA [64].

● CUDA-enabled GPUs are separate devices that are installed in a host computer.

● GPUs run in a memory space separate from the host processor.

● CUDA programs utilize kernels, which are subroutines callable from the host that execute on the CUDA device.

● The basic unit of work on the GPU is a thread.

● The largest shared region of memory on the GPU is called global memory.

Figure 3-6 shows a pattern diagram of the structure of GPU and host device. Originally, GPU is an add-on device to enhance the graphic performance of computer, although it is preliminarily set to some recent personal computers. Compared with general CPUs (central processing units) in host devices, GPUs have a lot of processors to perform a parallel computation because graphical process usually includes iterative computations. The procedures of parallel computation can be described as follows.

① The host device ensures memory sections in both host device and GPU.

② Parameters in the host memory are sent to the GPU memory.

③ The host device calls a kernel function which is precompiled in the GPU device. (By providing thread programs to blocks and processing with each register, the parallel computation is started.)

④　The computation results are transferred from the GPU memory and the host memory.

⑤　The computation results are saved in the host device and the ensured memory sections are released.

Although the parallel calculation is not useful for sequential processes, it can efficiently reduce the computation time for repetition processes.

Considering the proposed time-domain milling simulation to parallelize, the workpiece surface is expressed with the surface profiles having xyz coordinate data, and a same calculation is applied to each profile such as the tool-workpiece contact determination. Furthermore, same cutting force computation is performed for each layer to obtain the total cutting force. These computations

Table 3-9　Conditions for a time-domain milling simulation.

Cutting coefficient MPa	1500
Natural frequency of the tool Hz	2082
Damping ratio of tool	0.177
Mass of the tool kg	0.0483
Time step μs	2
Number of layers	64
Number of surface profiles in one layer	32768

Table 3-10　Performance of the computer for parallel calculation.

CPU	Intel Core i7 4770K
Operating system	CentOS 6.5
GPU	NVIDIA Geforce TITAN BLACK
CUDA version	6.0

Spindle rotation： 9000 → 5400 min^{-1}　　　Feed rate： 1575 → 945 mm/min
Override changing rate： 50 %/s (7200 min^{-1} and 1260 mm/min are standard)
Cutting time : 2.0 sec

Time-domain simulation with CPU
CPU: Intel® core ™ i7-2640M 2.80GHz

Computation time: **13h 15min 9sec**

CUDA time-domain simulation
GPU: NVIDIA GeForce TITAN black

Computation time: **9min 36sec**
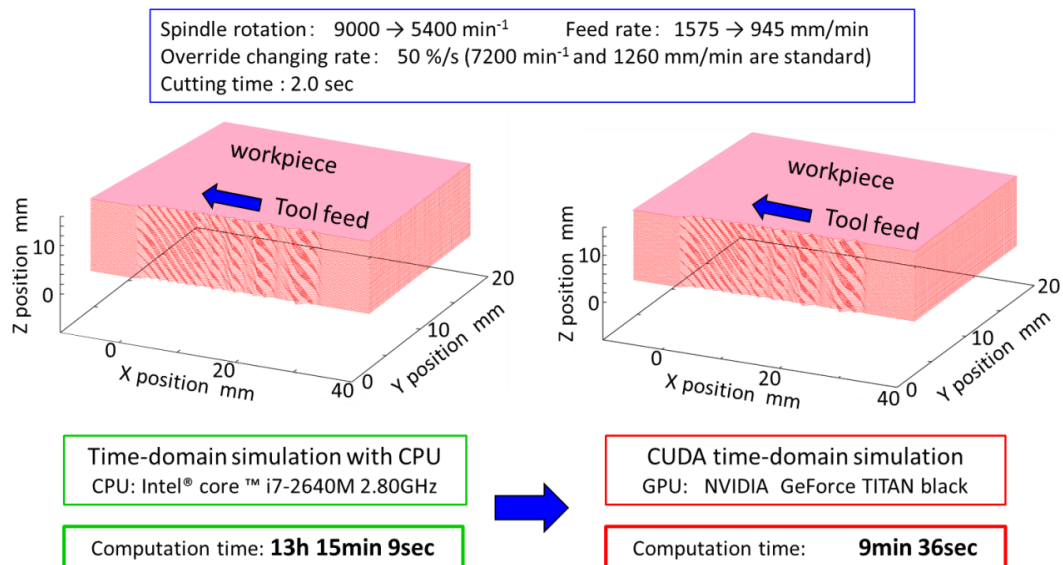
Fig. 3-7　Calculation time reduction in the time-domain milling simulation with CUDA.

could be parallelized based on CUDA.

One of the simulation results of the proposed milling simulator is shown in Fig. 3-7, where the simulation conditions are summarized in Table 3-9, and the details of parallel calculation system are shown in Table 3-10. In case of CPU calculation, it takes more than 13 hours to obtain the result; however, the calculation time can be reduced less than 10 min by parallelizing the simulation program with the CUDA technique. As a result, the CUDA system processes the simulation program 83 times as fast as the CPU calculation in this milling simulation.

From these results, a parallel calculation is decided to be employed for the time-domain milling simulation in this research.

4 Tool Wear Monitoring System

4.1 Introduction

As explained in Chapter 1, tool wear is researched on by many researchers as one of the unavoidable problems in process. Regarding the wear monitoring technique, sensorless approaches recently gather attention because of the practicability. In this chapter, the adequacy of the proposed observer-based tool wear monitoring is evaluated through drilling and tapping tests. The cutting force and torque estimations are carried out by installing the proposed estimation method and capturing the wear-induced increase.

4.2 Disturbance Observer-Based Monitoring System for Tool Wear

As explained in Section 2.2, current reference and angle information are
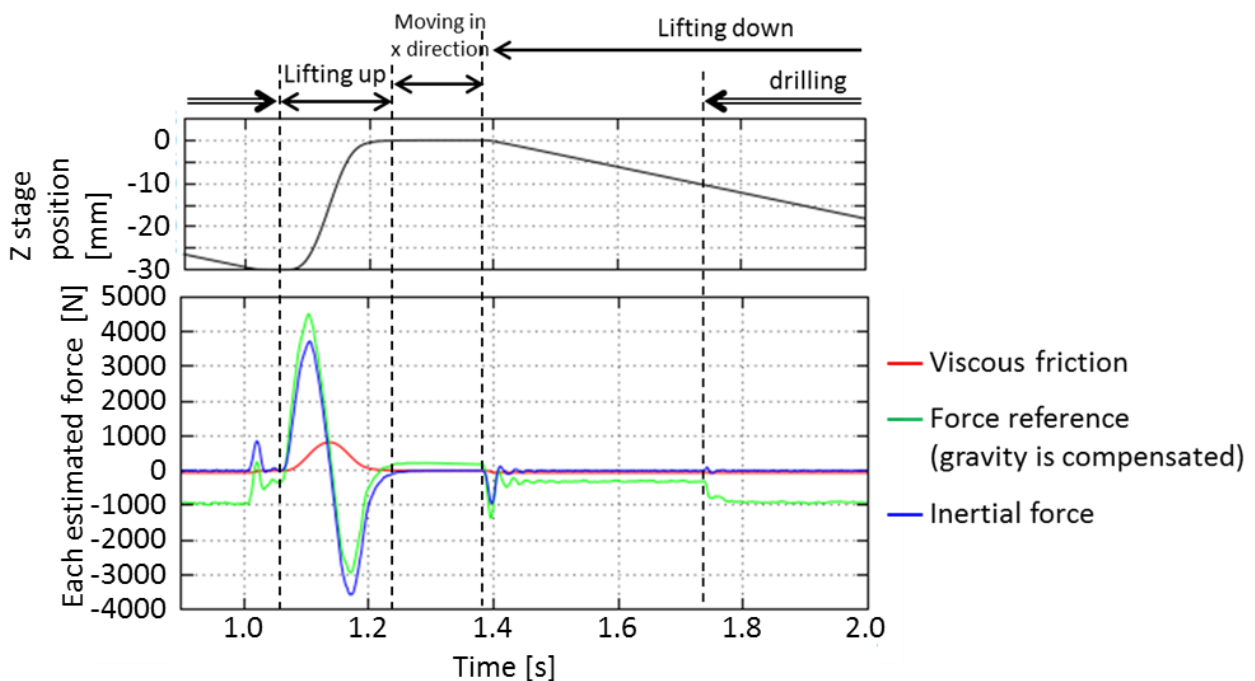
Fig. 4-1   Each estimated value gained from the servo information of the Z-axis ballscrew-driven stage servo motor.
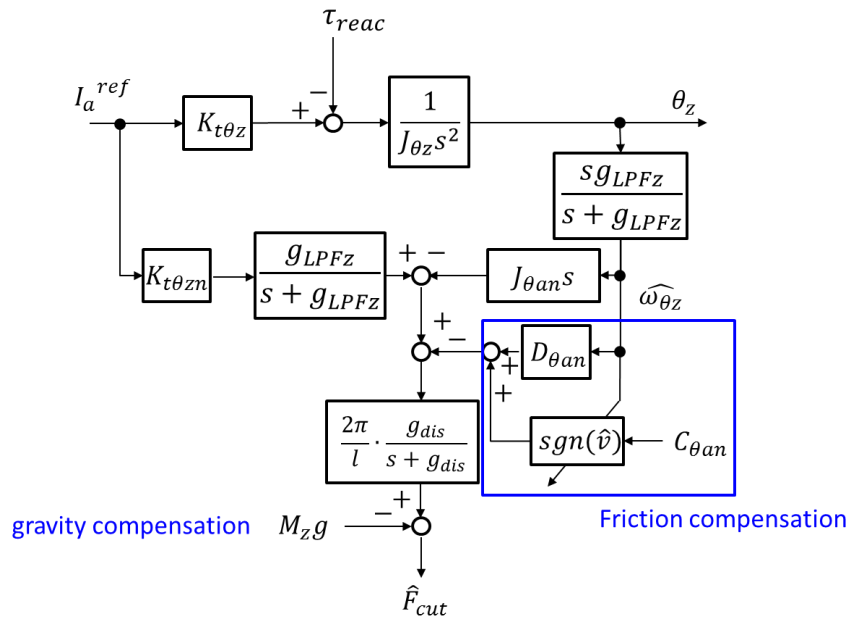
Fig. 4-2   Cutting force estimation algorithm.

available as servo information in spindle and stage control systems. Considering a ballscrew-driven stage control system, position of linear stage can be required from the screw angle with conversion coefficient. Moreover, the velocity and the acceleration of the linear stage can be estimated with a differential process. Based on these variables and the nominal parameters given in Tables from 3-4 to 3-7, various information can be estimated only form the servo information during drilling as Fig. 4-1. The nominal parameters are determined through an idling test, which can suppress the estimation error most efficiently. By integrating the estimated information, cutting force and torque can be derived.

When the observer-based monitoring is applied to a controller of a stage in vertical direction, the gravity force and friction compensation must be adopted. Furthermore, a first-order low-pass filter is installed to the current reference information in the proposed method as shown in Fig. 4-2 in order to compensate the phase difference caused by the low-pass filter in the pseudo-differential process.

4.3 Wear Monitoring Test in Drilling and Tapping

The tool wear monitoring is focusing on drilling and tapping in this research.
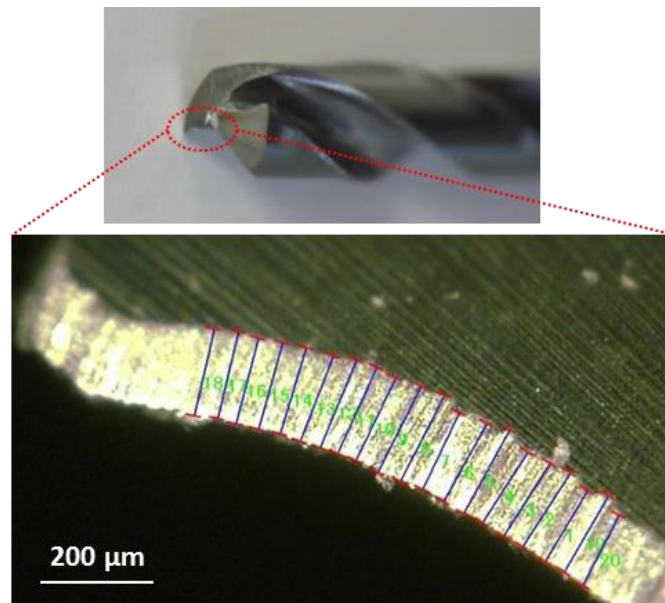
Fig. 4-3　20 measurement sections on flank wear.

Table 4-1　Cutting condition to progress the tool wear in drilling.

Tool	ϕ 6mm drill	ϕ 3mm drill
Rotational speed [min^{-1}]	796	4300
Feed rate [mm/ min]	19	130
Hole shape	20-mm-depth blind hole	15-mm-depth blind hole
Workpiece	Stainless (SUS304)	Carbon steel (S45C)
Type of cut	Wet cutting	

4.3.1　Flank Wear of Drill

　　To evaluate the tool wear progress, flank wear is a beneficial criterion because its width gradually increases with machining time. Although, the depth of creator wear also progresses gradually with the machining time, the width is easier to measure precisely with a microscope than the depth; thus, the flank wear measurement is performed on drills and taps in this study.

　　To confirm the tendency of tool wear progress on a drill, blind-hole drilling is performed under the cutting condition shown in Table 4-1, and the average width of flank wear is calculated with 20 evaluation sections on the tool edge as shown in Fig. 4-3. Carbide drills with 3- and 6-mm diameters as well as M3×0.5 and M6×1.0 spiral taps are prepared.

　　Fig. 4-4 and 4-5 show the relation between the average width of the flank wear and the number of drilled holes on the stainless alloy and on the carbon steel alloy,
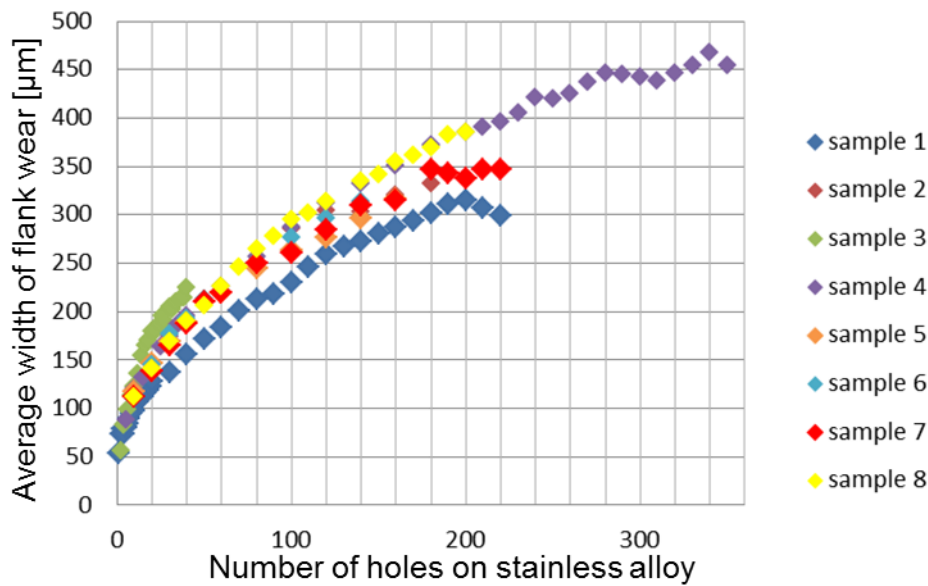
Fig.4-4   Relation between number of holes on stainless alloy
and width of flank wear (ϕ 6 mm).
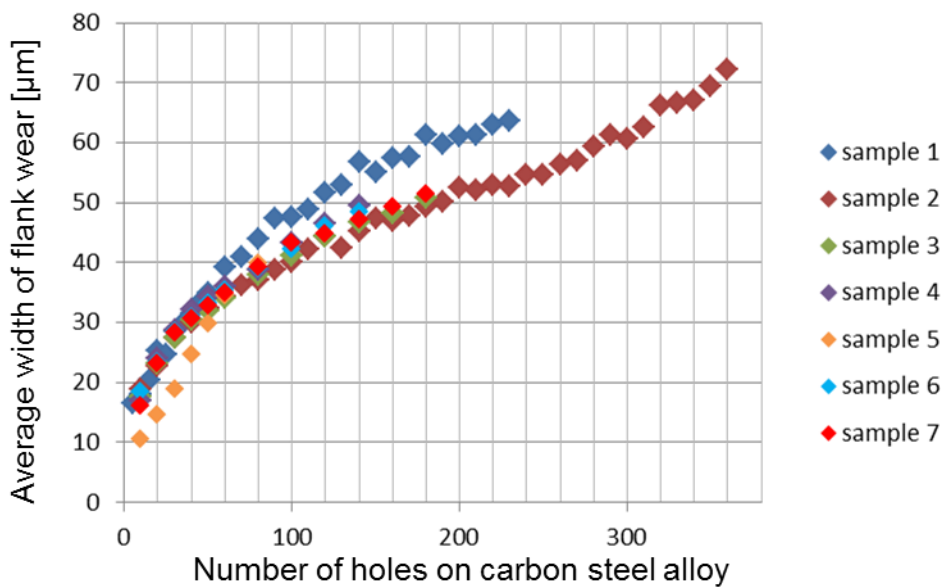
Fig. 4-5   Relation between number of holes on carbon steel alloy
and width of flank wear (ϕ 3 mm).

respectively, under the conditions presented in Table 4-1, i.e., the relation between the tool wear progress and the machining time. The flank wear measurement tests are carried out until the tool edge chips as shown in Fig. 4-6

The width of the flank wear increases gradually and clearly at the tool edges for both the 3 mm diameter and the 6 mm diameter drills. By comparing these results based on the cutting conditions in Table 4-1, the proposed observer-based wear monitoring in drilling is evaluated.

74

flank surface
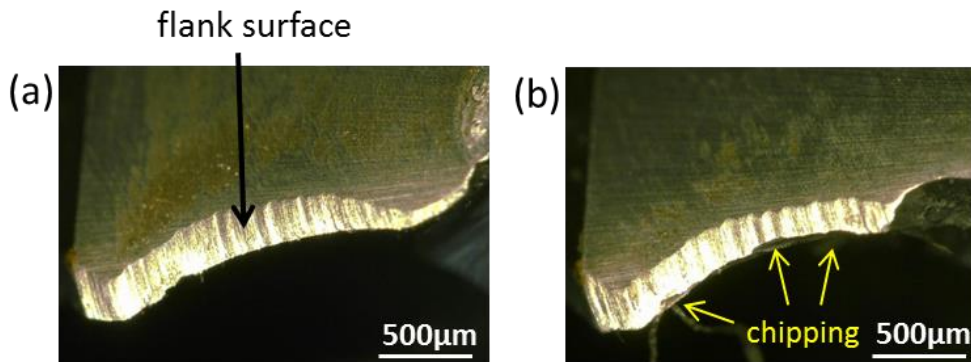
Fig. 4-6   The appearance of a tool edge: (a) before chipping (b) after chipping.

4.3.2 Wear-Induced Increase in Cutting Force and Torque in Drilling

Figures 4-7 and 4-8 show the time-dependent variations of the thrust force (cutting force in the tool-axial direction) and cutting torque estimated with the proposed method under intermittent drilling operation. Although some fluctuation is observed in the estimated thrust force during the nondrilling time, the error ranges from -100 N to 150 N even in the high-speed feeding of the stage. The fluctuation from 1.4 s occurred because of the coupling stiffness and the stage mass. Though a two-mass system should be adopted to suppress the fluctuation, doing so would increase the number of parameters and they would have to be identified accurately. Furthermore, the coupling stiffness is high enough to not disturb the thrust force estimation, as shown in Fig. 4-7. Thus, a single-mass model is utilized in this study.

Ten cutting force and torque monitoring tests on the aluminum alloy under the conditions in Table 4-2 and ten or twenty tool wear progress tests under the conditions in Table 4-1 are alternately conducted to confirm the wear-induced increase in the cutting force and torque. The tests are conducted until the breakage of the tool. Figures 4-9 and 4-10 respectively show the increases in the

Table 4-2   Drilling condition for cutting force and torque estimations.

Tool	ϕ 6mm drill	ϕ 3mm drill
Rotational speed [min⁻¹]	9000	9000
Feed rate [mm/ min]	1800	1350
Hole shape	20mm-depth blind hole	15mm-depth blind hole
Workpiece	Aluminum (A2017)	Aluminum (A2017)
Type of cut	Wet cutting	

estimated thrust force and cutting torque with tool wear progress in a test with one of the sample drills with 6-mm diameter; in these figures, the diamond plots represent the estimated values in the 10 cutting tests and the circular plots represent their average in each period. The estimated cutting force and torque are seen to increase owing to the wear progress. Furthermore, the variation of the cutting force and torque in each period is so small that a threshold could be used to determine the appropriate time for changing the tool. To confirm the repeatability of the proposed method, the wear-induced increases in the
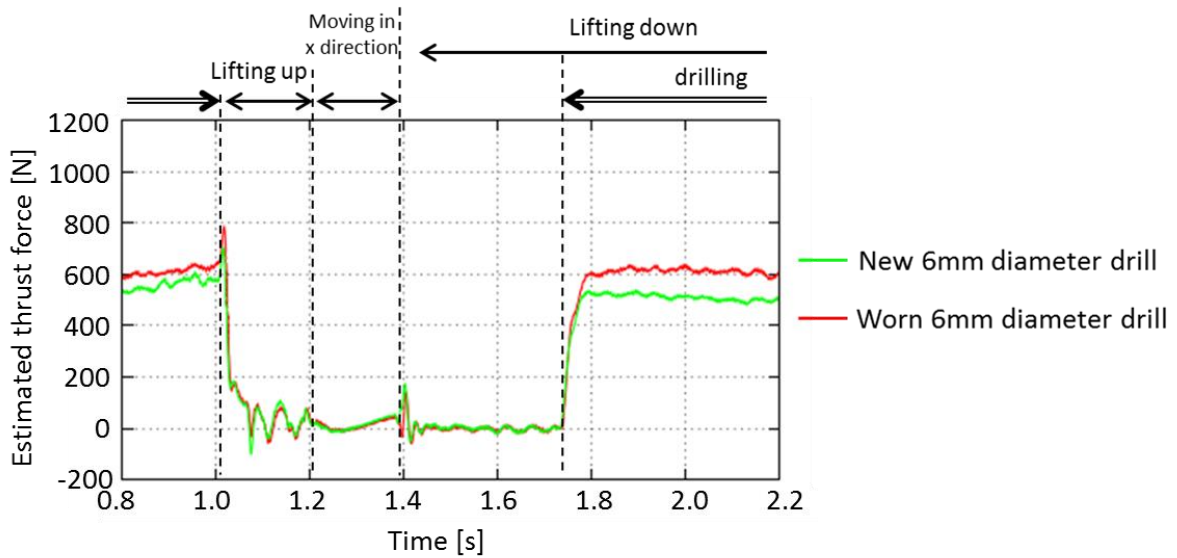
Fig. 4-7   Thrust force estimation by the proposed method.
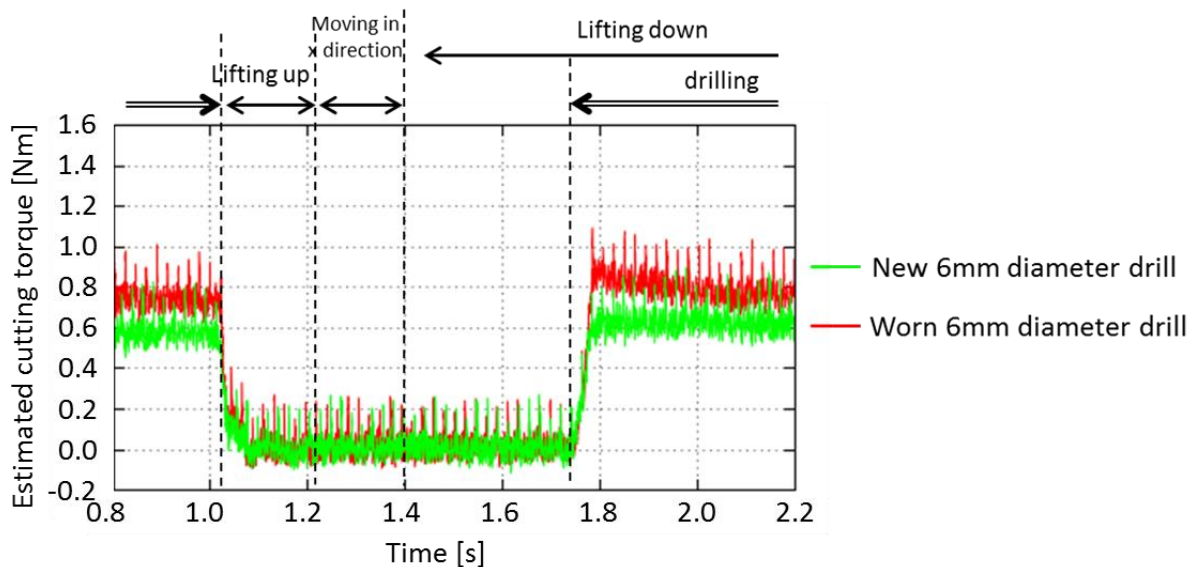
Fig. 4-8   Cutting torque estimation by the proposed method.

estimated thrust force and cutting torque are monitored, and the results are summarized in Figs. 4-11 and 4-12, respectively, where each plot shows the average value for the 10 monitoring tests. In all the tests with 7 sample drills, the estimated thrust force and cutting torque are found to increase with the tool wear progress. Some samples show a sudden increase in the cutting force after the occurrence of chipping at the tool edge. Thus, a sudden increase of more than 100 N can be used as a criterion of tool life limitation in drilling tests with 6-mm drills.
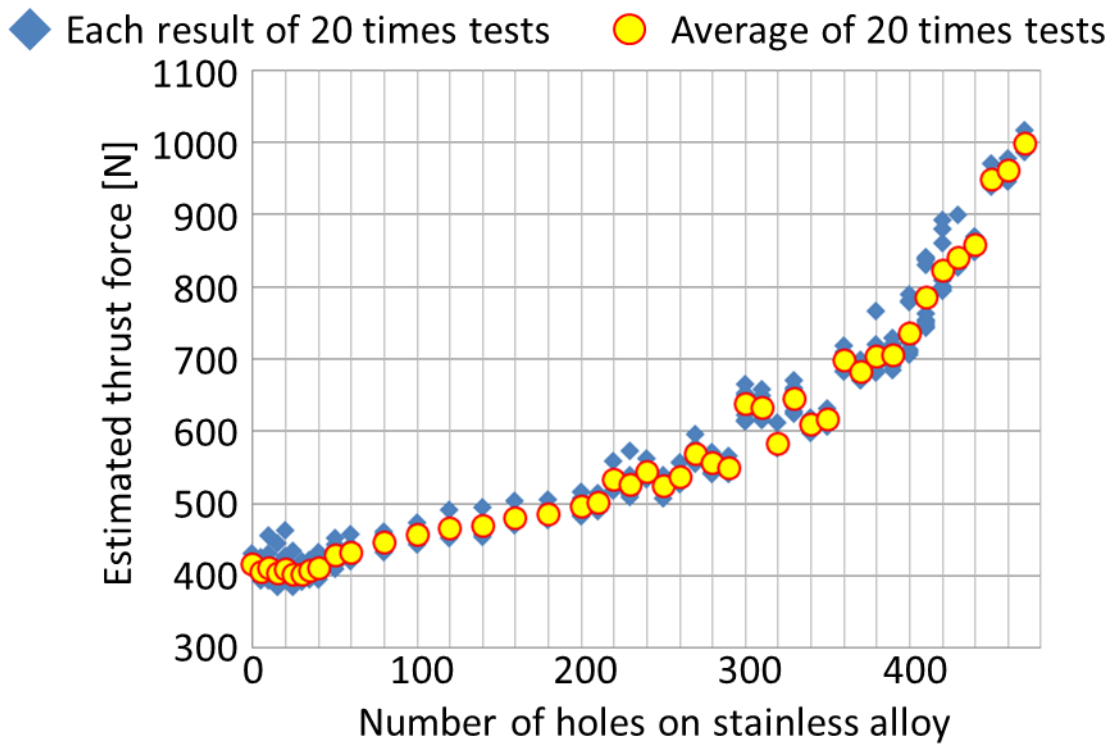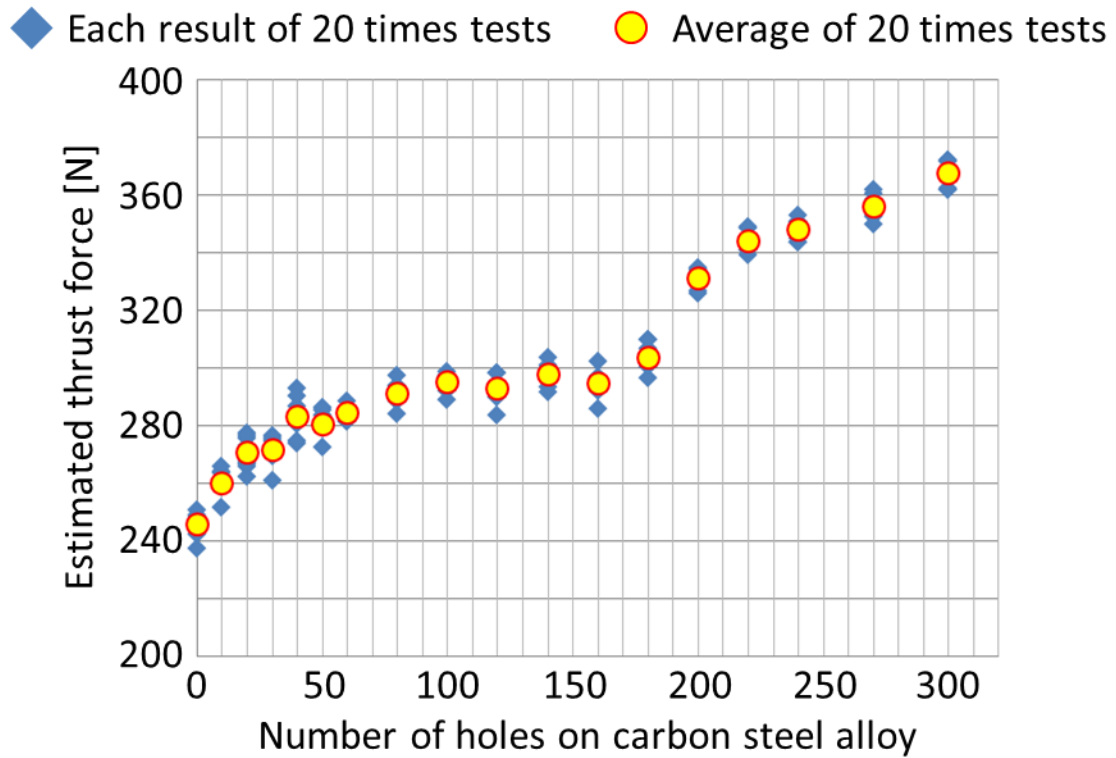
Fig 4-9   Relation between progress of tool wear and
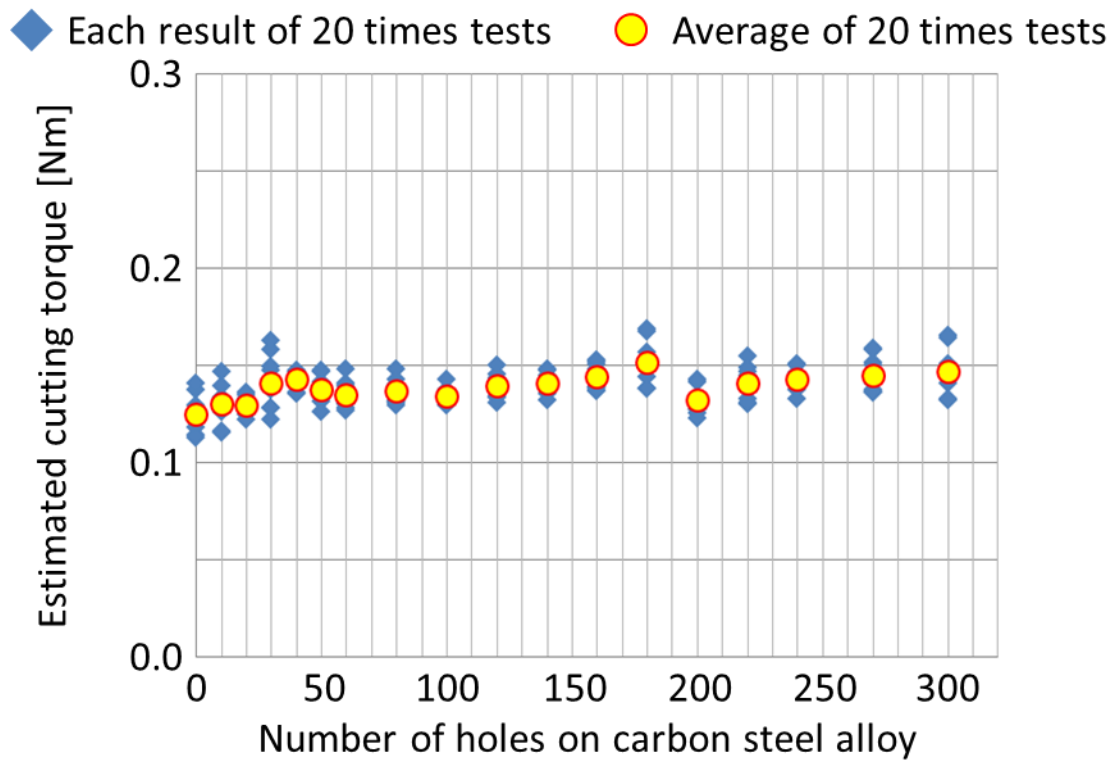the estimated thrust force of 6 mm drill.
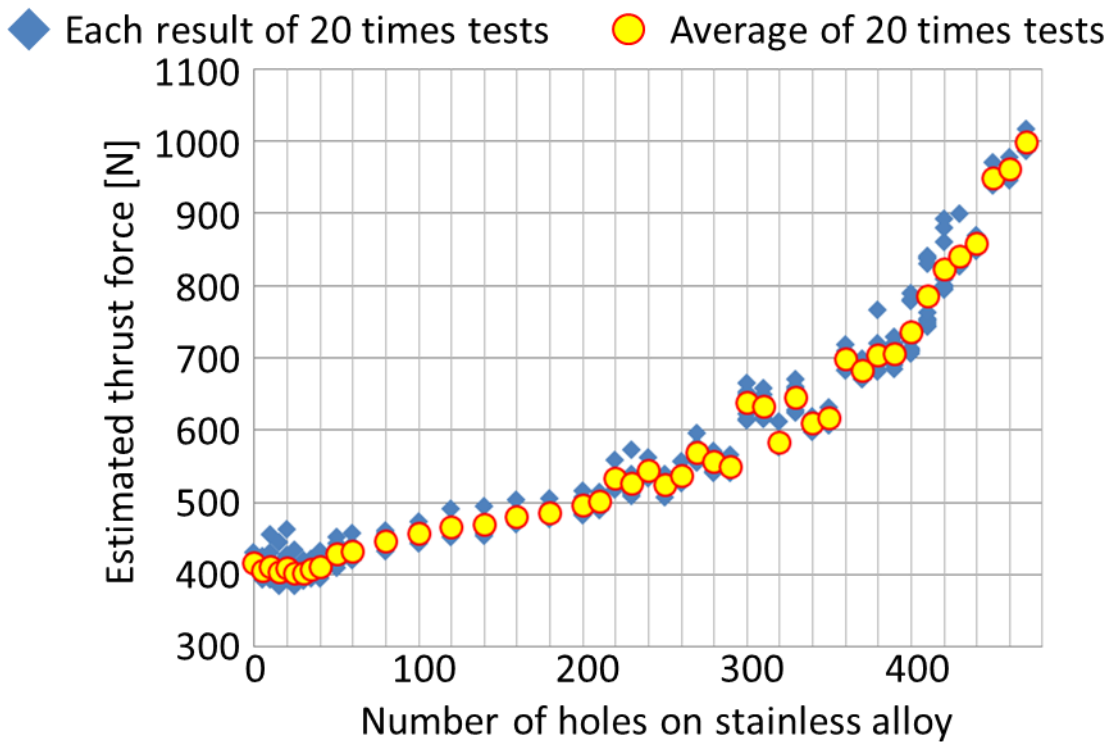
Fig. 4-10   Relation between progress of tool wear and
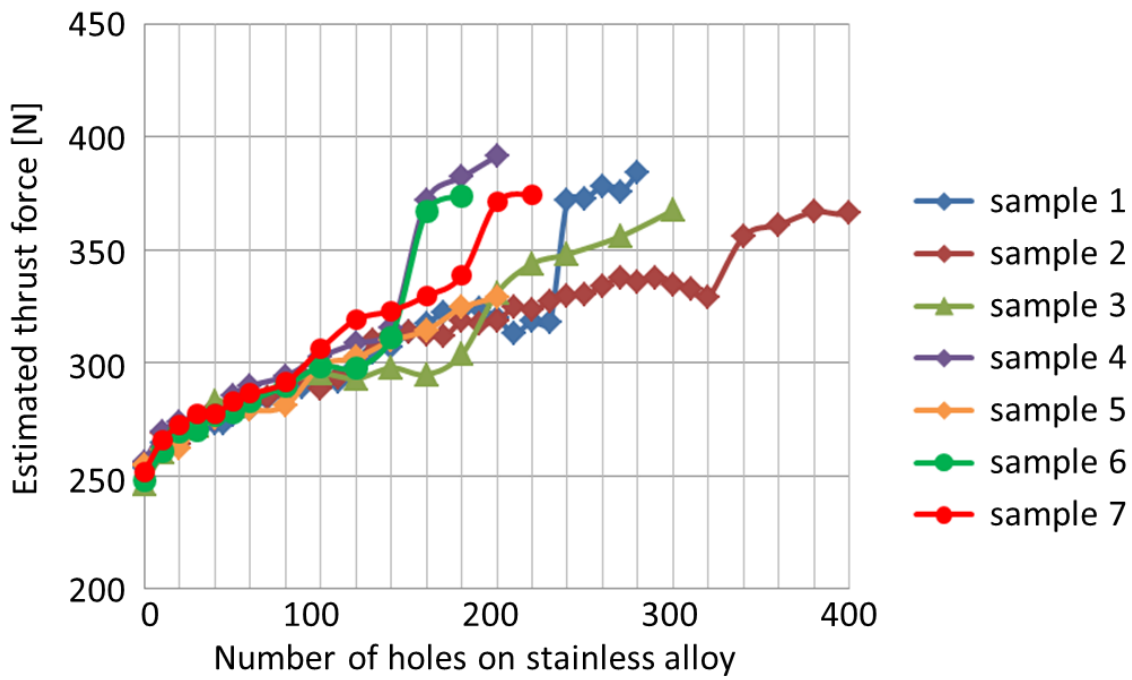the estimated cutting torque of 6 mm drill.
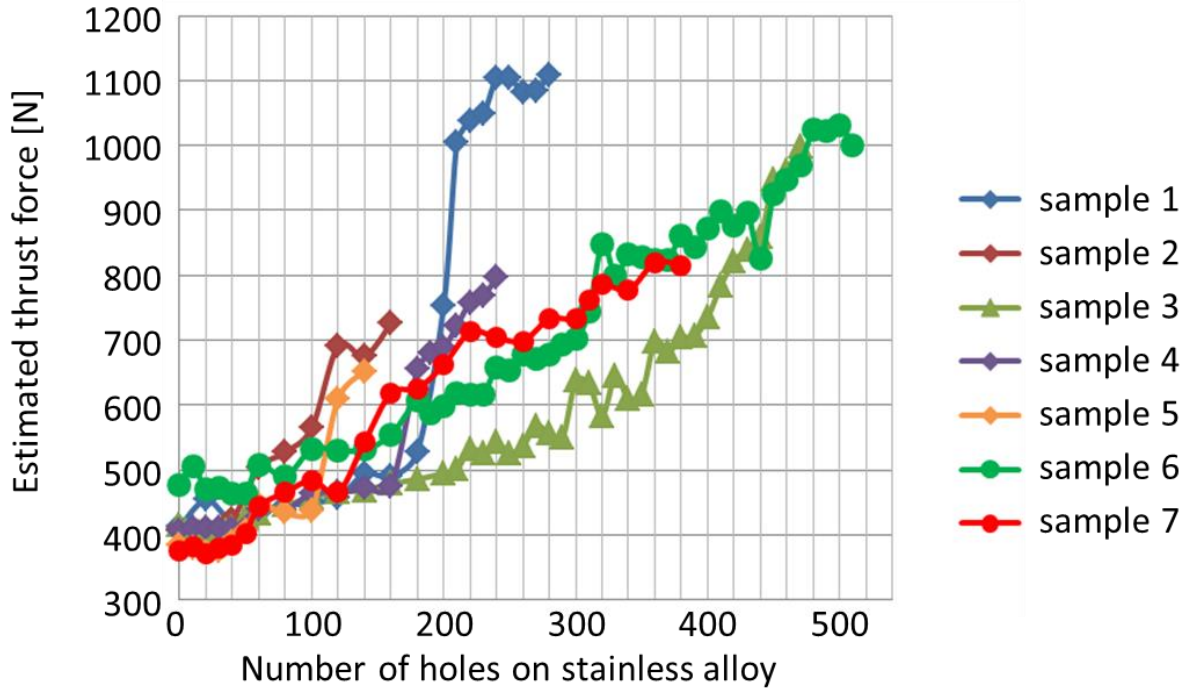
Fig. 4-11　Relation between progress of tool wear and
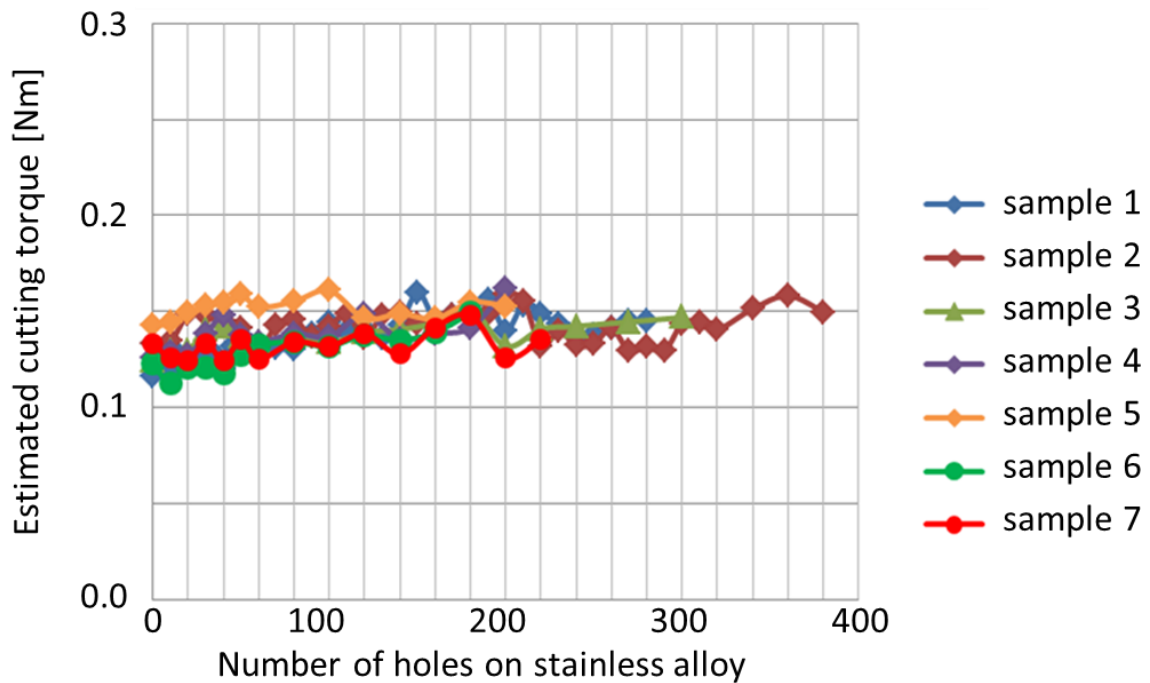the average of estimated thrust force of 6 mm drill.
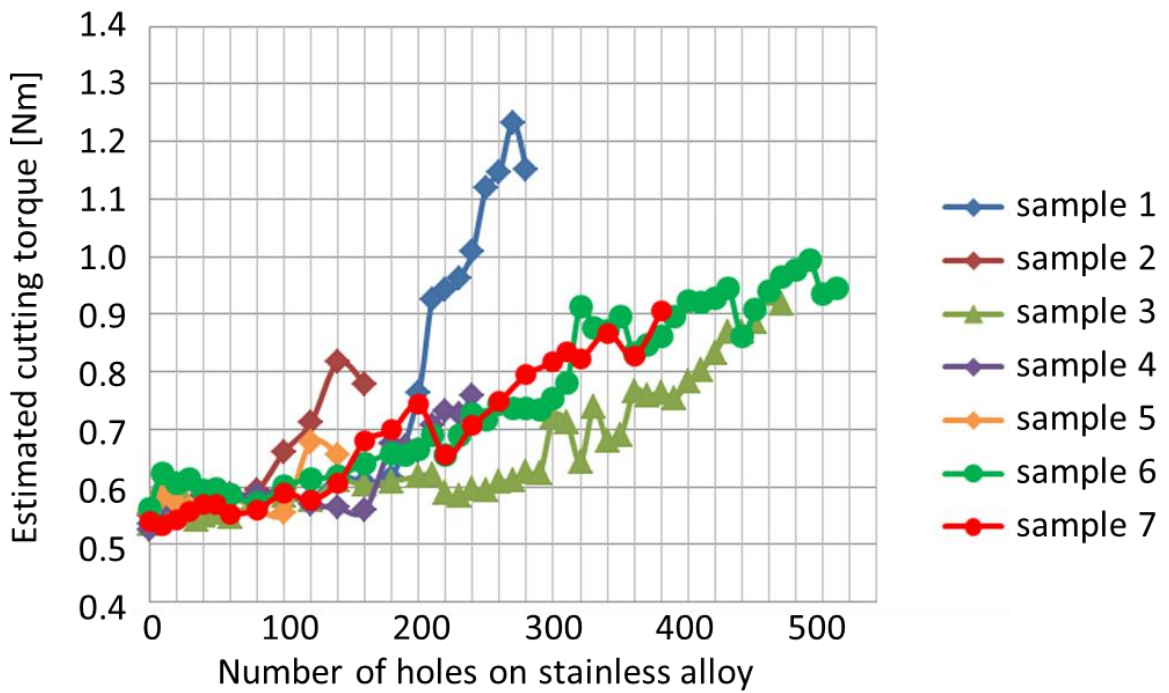
Fig. 4-12　Relation between progress of tool wear and
the average of estimated cutting torque of 6 mm drill.

The same experiments are conducted with 7 samples of 3-mm-diameter drills.

Figs. 4-13 and 4-14 show the wear-induced increases in the estimated cutting force and torque of one sample. Although the estimated thrust force increases gradually with the tool wear progress as shown in Fig. 4-13, no remarkable changes in the estimated cutting torque are observed, as shown in Fig. 4-14. In the case of drilling with a small-diameter tool, the cutting torque becomes so small that its variation is difficult to detect. Therefore, monitoring of the estimated thrust force is a suitable method for determining the time at which a small diameter drills needs to be changed. Figures 4-15 and 4-16 show the result of repeatability tests with 3-mm-diameter drills. A sudden increase in the thrust force is also observed in the tests performed using 3-mm-diameter drills. After a sudden change of more than 40 N occurs in the estimated thrust force, chipping is observed on the tool edge in this experiment. This result is also applicable as a criterion of tool life limitation. Furthermore, no remarkable change is observed in the cutting torque even after the wear progress.

Disregarding the sudden increases in the estimated thrust force and cutting torque, on the basis of the obtained results, the thresholds of thrust force for tool life limitation can be set to 800 N for 6-mm drills and 330 N for 3-mm drills. As a result, it can be concluded that the proposed method is feasible for determining the appropriate time for changing the tools by detecting the sudden increase in the cutting force and torque and setting the thresholds.

◆ Each result of 20 times tests   ○ Average of 20 times tests

Fig. 4-13   Relation between progress of tool wear and
the estimated thrust force of 3 mm drill.

◆ Each result of 20 times tests   ○ Average of 20 times tests

Fig. 4-14   Relation between progress of tool wear and the estimated
cutting torque of 3 mm drill.

Fig. 4-15   Relation between progress of tool wear and
the average of estimated thrust force of 3 mm drill.

Fig. 4-16   Relation between progress of tool wear and
the average of estimated cutting torque of 3 mm drill.

Table 4-3 Cutting condition to progress the tool wear in tapping.

Types of tap	M6×1.0	M3×0.5
Rotational speed [min^{-1}]	2120	4300
Feed rate [mm/ min]	2120	2150
Depth of screw holes [mm]	12	6
Depth of pilot holes [mm]	15	8
Workpiece material	Carbon steel (S45C)	Carbon steel (S45C)
Type of cut	Wet cutting	
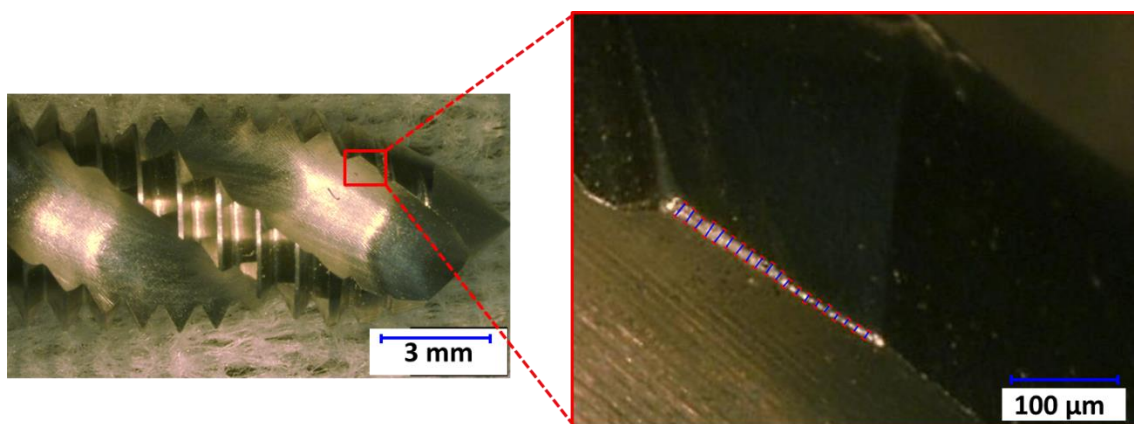
After tapping of 700 holes

Fig. 4-17 Flank wear surface and evaluation sections on tool edge of tap drill.

4.3.3 Flank Wear of Tap Drill

To investigate the wear progress on the tap drills under the cutting conditions in Table 4-3, the widths of the flank wear are measured with a microscope. The average width of the flank wear is obtained by setting 20 evaluation sections on the flank wear surface as shown in Fig. 4-17. Figure 4-18 shows the relation between the average width of the flank wear and the number of tapped holes. It is clear that tool wear is promoted in tapping under the cutting conditions in Table 4-3. The tapping tests are also conducted using M3×0.5 spiral taps. Although the flank wear is measured with the microscope, no remarkable change is observed at the tool edge, as shown in Fig. 4-19. However, the increase in cutting torque is clearly observed in the monitoring tests explained later. The tool life limitation of M3×0.5 spiral taps should be discussed including the cutting torque monitoring results.
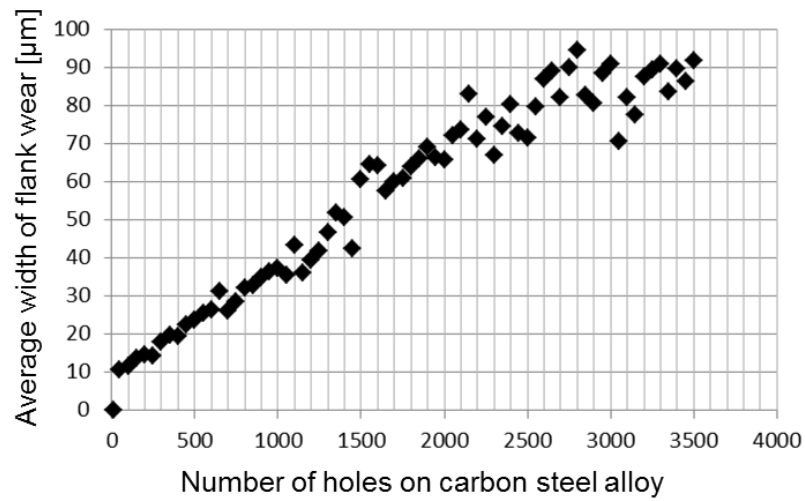
83

Fig. 4-18　Relation between average width of flank wear
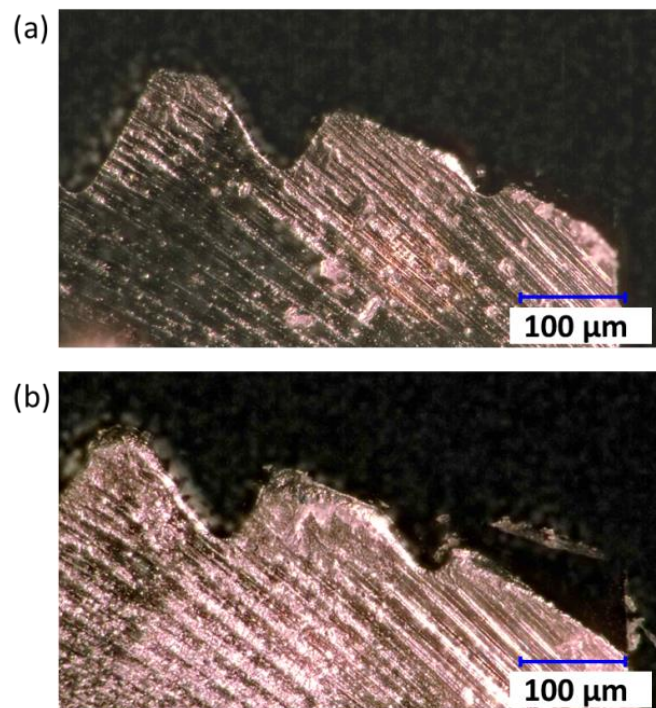and number of holes on carbon steel.

Fig. 4-19　Flank wear of M3×0.5 tap drill; (a) after tapping
of 20 holes, (b) after tapping of 1300 holes.

4.3.4　Wear-Induced Increase in Cutting Force and Torque in Tapping

In this test, an M6×1.0 spiral tap is used after drilling a pilot hole with a

diameter of 5 mm. The spiral tap fractures after drilling of 2500 holes, as shown in Fig. 4-20. However, the tapping test is continued because of the high cutting accuracy of the tool, which is verified using a grade-2 screw gauge. The spiral tap breaks after tapping of 3580 holes. The relation between the estimated thrust force and the tool wear progress is as shown in Fig. 4-21. In the tapping tests, the estimated thrust force does not increase remarkably, unlike that in the drilling tests. Furthermore, the thrust force decreases drastically after the occurrence of fracture. The estimated thrust force varies from -100 N to 150 N. However, the wear-induced increase in the estimated cutting torque is clearly observed, as shown in Fig. 4-22. After fracture occurs, the estimated cutting torque does not increase and it fluctuates from 2.0 Nm to 3.0 Nm. From these results, it can be
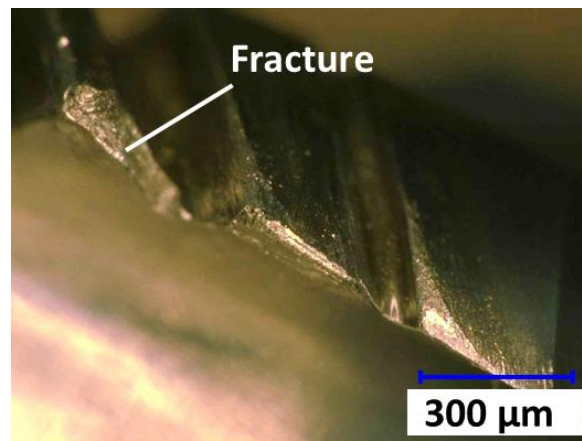
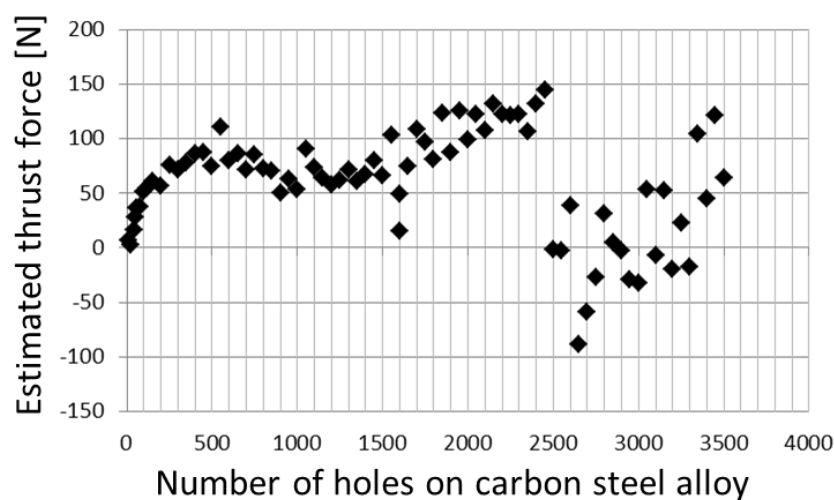Fig. 4-20   Fractured tap after tapping of 2500 holes.

Fig. 4-21   Relation between estimated thrust force and
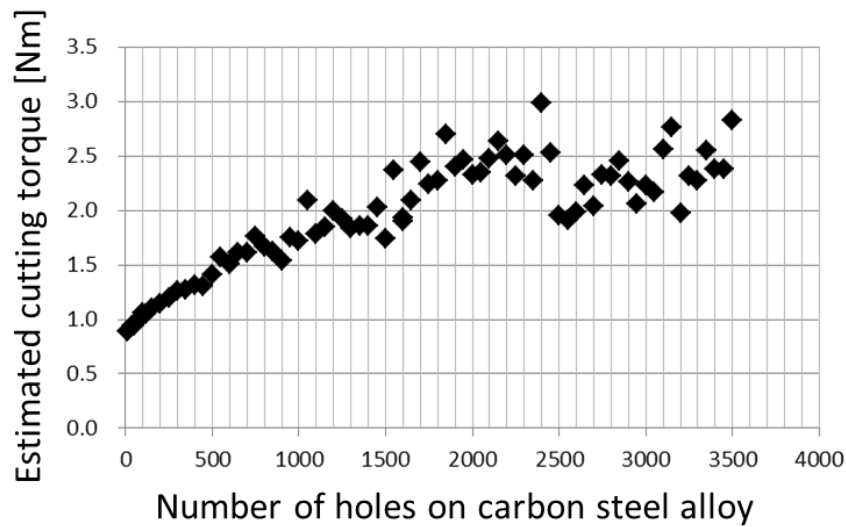progress of tool wear on tap drill.

Fig. 4-22   Relation between estimated cutting torque and
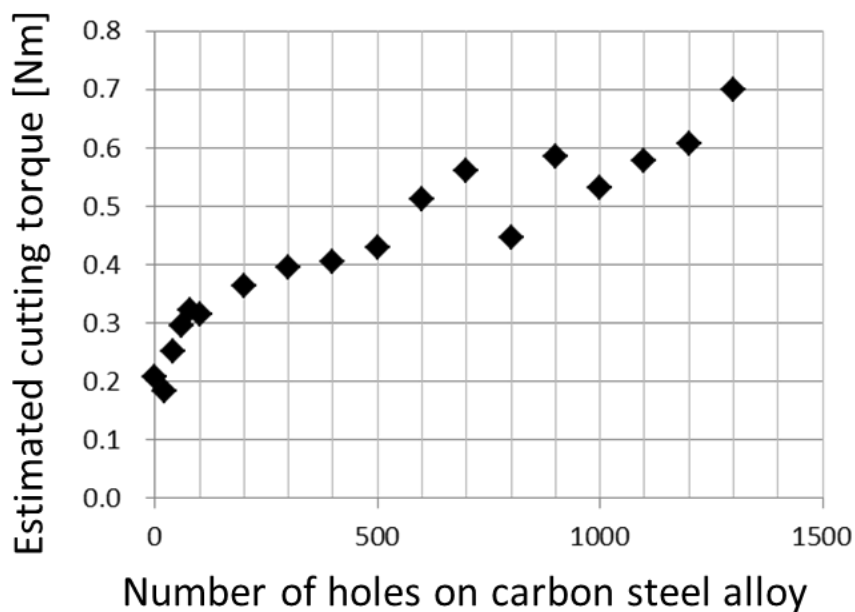progress of tool wear on tap drill.

Fig. 4-23   Increase in cutting torque due to tool wear
progress with M3×0.5 tap drill.

said that the estimated cutting torque is a suitable criterion for detecting the tool wear progress, because the thrust force hardly contributes to the tapping process, and a 2.5-Nm threshold would be suitable for determining the tool life limitation.

The tests are also conducted using M3×0.5 spiral taps. Although the flank wear is measured with the microscope, no remarkable change is observed at the tool edge, as explained in the previous section. However, the estimated cutting torque increases gradually with the tool wear progress, as shown in Fig. 4-23.

Together with the results for the M6 tap, the above results indicate that setting a threshold to three times higher value than initial torque will be appropriate for determining the tool life limitation of the tap. As a result, it can be confirmed that the proposed method is a practical approach for monitoring tool wear progress because it satisfactorily detects the wear-induced increase in the cutting torque in the tapping process without any additional sensors.

These results are obtained from the servo information in the ballscrew-driven stage control system; however, the friction force and torque vary according to the heat generation. Figure 4-24 shows the behavior of low-frequency error in the estimated cutting force in idling tests at the maximum feed rate of 50000 mm/min. Although, this is the result about X direction, the Z-direction ballscrew-driven stage also applies the same mechanical structures. The estimation error includes modeling errors of the machine structures. Because the friction varies due to heat generation, the low-frequency error changes gradually as shown in Fig. 4-24. After performing the idling movement enough, the low-frequency error differs from the initial value by 55 N at maximum which may be said as certifiable accuracy of the proposed method. However, the low-frequency error can be reduced by idling operation, i.e., generating heat in the mechanical structure in advance.

To enhance the accuracy of the proposed wear monitoring method, the change in friction according to the operating time should be investigated, or the idling operation should be performed repeatedly before machining.
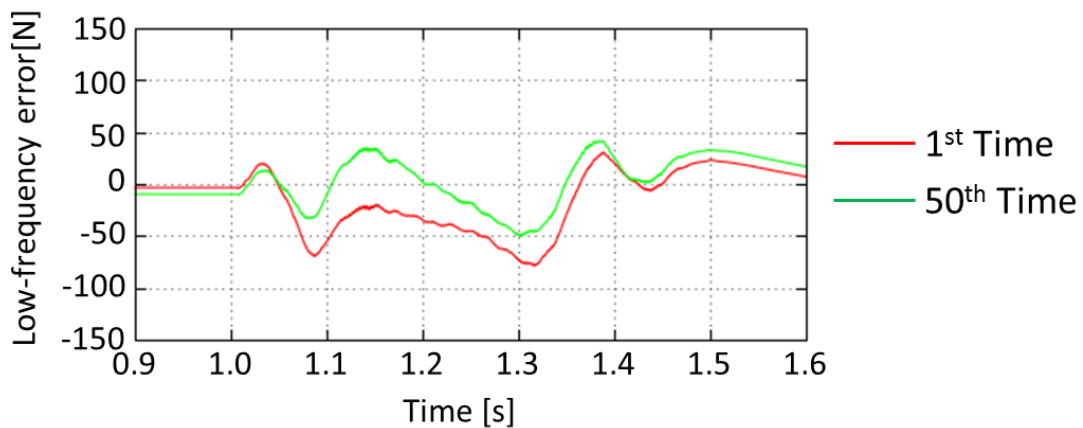

Fig. 4-24　Difference of low-frequency error in X direction between the 1st and 50th time experiments.

4.4 Summary

In this chapter, a sensorless tool wear monitoring method in drilling and tapping is proposed by using servo information in a spindle and a ballscrew-driven stage controller.

The cutting torque and thrust force are successfully estimated by constructing physical models of the spindle and the ballscrew-driven stage and applying the disturbance observer technique. Experimental results for the drilling process show that the wear-induced increase in the thrust force of 3-mm- and 6-mm-diameter drills can be captured using the proposed method. Although the estimated cutting torque also increases with tool wear progress in drilling with 6-mm diameter drills, no remarkable change in the cutting torque can be observed in drilling with 3-mm-diameter drills. Experimental results for the tapping process show that the increase in the cutting torque can be monitored in tapping tests with both the M6×1.0 and the M3×0.5 spiral taps. However, the thrust force cannot be used as a criterion of tool wear progress because no obvious change is observed even after the wear of the tool.

From these results and on the basis of the estimated thrust force for drills and the estimated cutting torque for tap drills, the tool wear progress can be accurately monitored using the proposed method without any additional sensors.

5 Tool Collision Detection System

5.1 Introduction

The main cause of tool collision in a machine tool is human-induced wrong operation. When a NC machine tool continuously performs a provided program without any special countermeasures, a second accident and a critical damage on the machine structure are unavoidable. Although several studies have proposed collision prediction methods by constructing a 3D model and simulating the movement of mechanical components according to the given tool path in order to confirm whether tool collision will occur or not [29, 30], they cannot deal with the case in which the tool and the workpiece are wrongly set. It is difficult to perfectly avoid a tool collision; thus, damage reduction also should be considered.

In this research, a disturbance observer-based tool collision detection method is proposed. In the concrete terms, the proposed method detects the collision-induced fluctuation in the estimated cutting force in each axis by using a pseudo-differential process. In order to confirm the adequacy of the proposed method, several tool collision experiments are performed in this chapter.

5.2 Proposal of Collision Force Estimation Method

Although the collision detection would be possible by using the proposed cutting force estimation algorithm because it does not compensate the collision force, this research introduces a pseudo differential to the estimated cutting force. The differential value of the estimated cutting force is defined as "disturbance jerk" and used to detect the collision-induced fluctuation in the estimated cutting force. Firstly, this section explains the reason why the estimated cutting force is not used for collision detection directly.

The behavior of the estimated cutting force in X direction is shown in Fig. 5-1 when the x stage is fed at 50000 mm/min (maximum feed rate of the used machine tool) without collision, where the nominal parameters are given as shown in Chapter 3. The red line shows the estimated disturbance force and the green line shows the moving average of 0.05 s window for the estimated
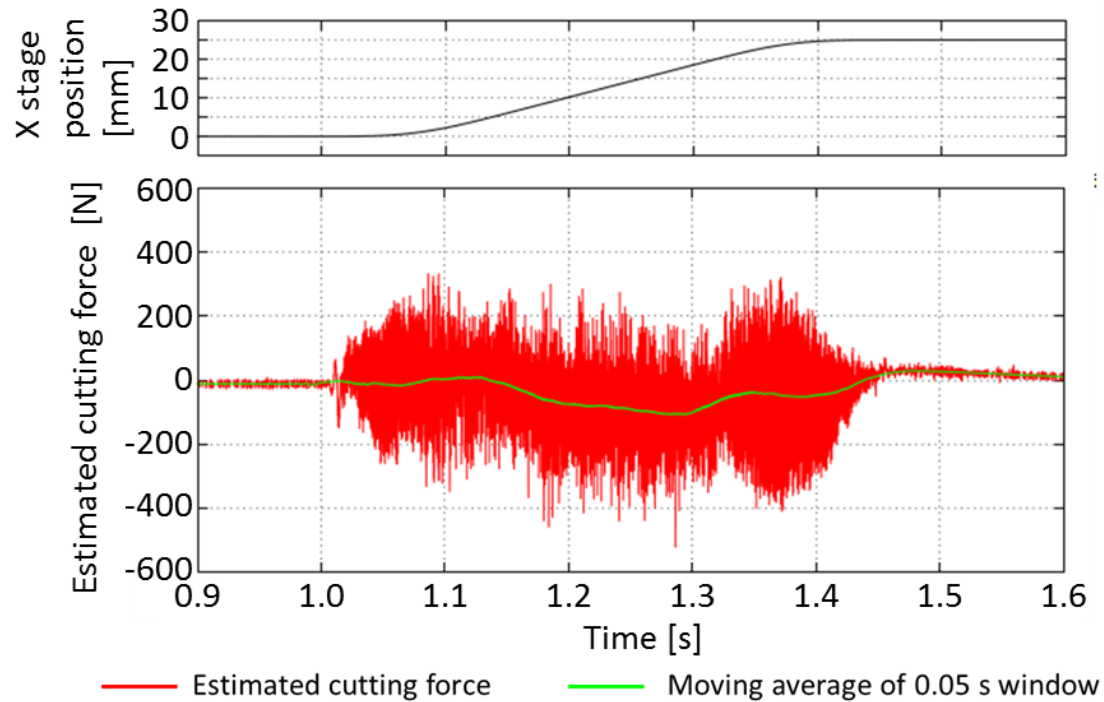
Fig. 5-1   Estimation result in X direction: red line represents the estimated cutting force; green line represents the moving average of 0.05 s.

disturbance force respectively, where the cutoff frequency is 2000 rad/s here.

Because the misjudgment must be avoid to ensure the reliability of the detection system, the threshold has to be higher than the signal noise during idling movement as shown in Fig. 5-1. On the other hand, excessively-high threshold may cause the detection delay and miss the collision-induced fluctuation. Therefore, a proper threshold setting method should be discussed from the viewpoint of the reliability and the time response.

In order to confirm the characteristic of the high-frequency noise, the probability distribution of the difference between the estimated disturbance force and the moving average is shown in Fig. 5-2. This distribution incudes 3200 samples from 1.05 s to 1.45 s shown in Fig. 5-1, and its average is -0.473 N and its standard deviation is 144.2 N. Additionally, a theoretical standard distribution which has the same average and standard deviation is also shown in Fig. 5-2 as a green line. The both distributions may fit each other well. In order to evaluate the degree of coincidence among two populations, χ^2 test is generally used. When the significance level is set to 5 % and the χ^2 test is performed on the 3200 samples, the test result shows that the high frequency noise has a standard distribution because the upper probability p is 0.3349.
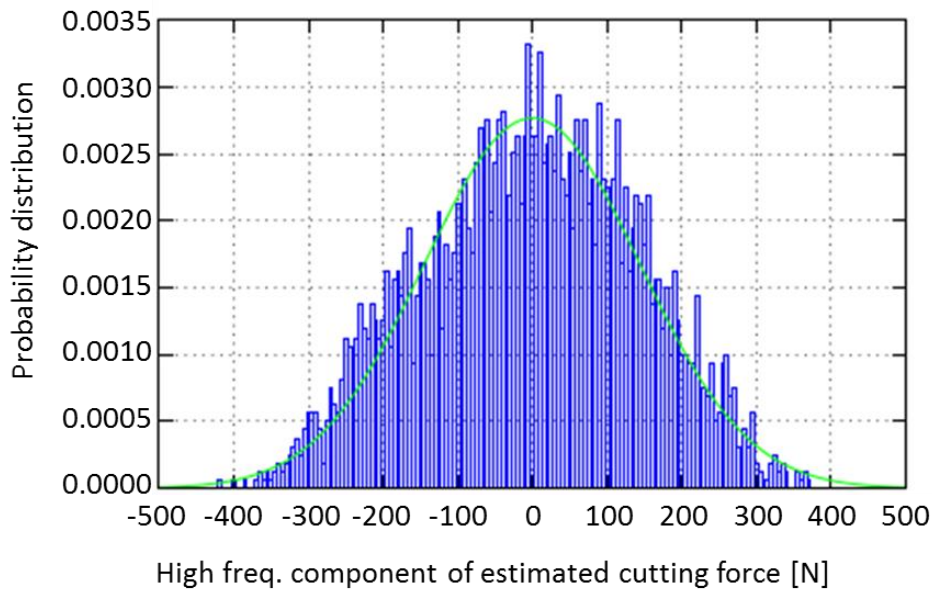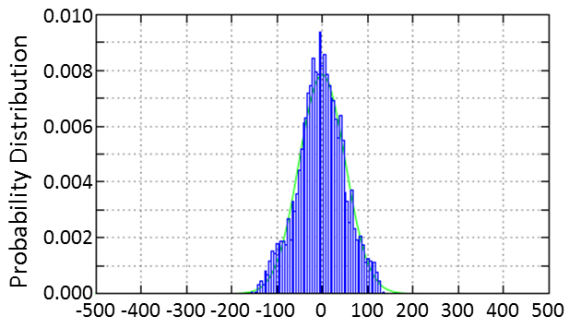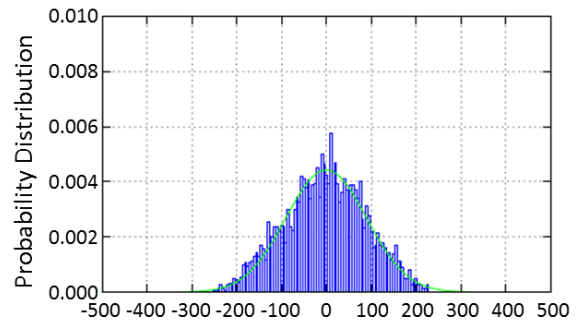
Fig. 5-2   Probability distribution of high frequency component of estimated
cutting force: green line represents normal distribution.
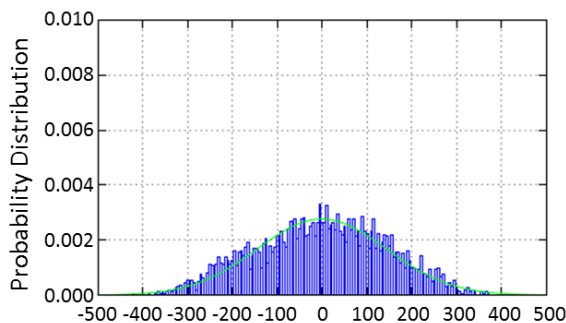
(a) Cutoff frequency 1000 rad/s

(b) Cutoff frequency 1500 rad/s

(c) Cutoff frequency 2000 rad/s

(d) Cutoff frequency 2500 rad/s
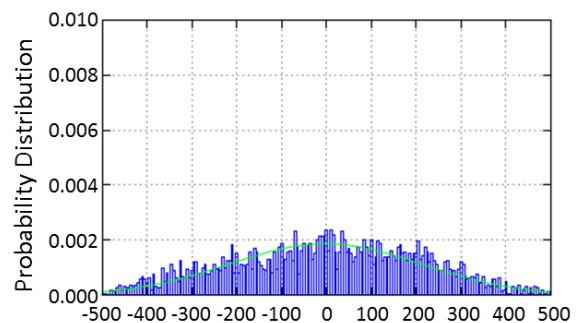
Fig. 5-3   Probability distribution of high frequency component of estimated disturbance force
(a) cutoff frequency of 1000 rad/s, standard deviation σ = 50.65 N, (b) that of 1500 rad/s, σ = 90.01 N
(c) that of 2000 rad/s, σ = 144.2 N, (d) that of 2500 rad/s, σ = 215.7 N.

Even in case that the cutoff frequency is 500, 1000, 1500 rad/s, the each high frequency noise has a standard distribution. Thus, the proper threshold is theoretically decided based on the upper probability of the standard distribution. Typical upper probability of the standard distribution is summarized in Table 5-1.

Table 5-1 Upper probability of standard deviation.

Threshold	Upper probability
μ (Average)	0.500
$\mu + \sigma$	0.159
$\mu + 3\sigma$	1.35×10^{-3}
$\mu + 4\sigma$	3.17×10^{-5}
$\mu + 5\sigma$	2.87×10^{-7}
$\mu + 6\sigma$	9.87×10^{-10}
$\mu + 7\sigma$	1.28×10^{-12}

According to the Table 5-1, even in case of ($\mu + 3\sigma$) threshold which is often used for the abnormal state detection statistically, this system is expected to cause more than 10 times misjudgments in 1 s because the sampling frequency is 8000 Hz ($8000 \times 1.35 \times 10^{-3} = 10.8$). Although the number of the misjudgments can be reduced once three years in case of ($\mu + 7\sigma$) threshold, the threshold is 1009 N when the cutoff frequency is set to 2000 rad/s. As explained above, the threshold should be as low as possible not to miss the collision.

To enhance the detection reliability even with a low threshold, the criterion should be changed from one-data-based determination to multi-data-based determination. For example, the probability that five samples exceeds the ($\mu +$ 3σ) threshold continuously is sufficiently small as $(1.35 \times 10^{-3})^5 = 4.48 \times 10^{-15}$, which is expected to happen once 884 years when the sampling frequency is 8000Hz. Furthermore, the threshold itself can be set to lower without reliability reduction.

However, not only high frequency noise but also the error of low frequency components (shown as moving average) should be discussed. In case of idling test, the moving average value of the estimated disturbance force always has to be zero theoretically, but about 100 N error is confirmed in the moving average as shown as the green line in Fig. 5-1. This low-frequency error would occur due to the parameter variation of the torque coefficient and the mass, the friction
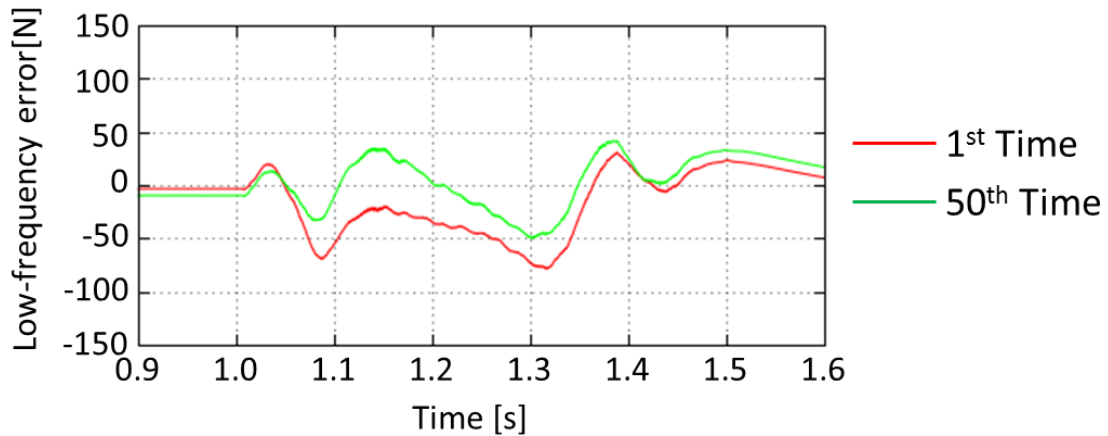
Fig. 5-4　Difference of low-frequency error in X direction
between the 1st and 50th time experiments.

identification error, and the heat generation in the mechanical components. It is known that the heat generation leads to the change in the contact pressure between the mechanical components like linear guides and bearings. As a result, the friction changes according to the normal force variation. Figure 5-4 is the behaviors of low-frequency components in the estimated disturbance force under the same condition with the experiment of Fig. 5-1. In this test, the difference of the estimated disturbance force along with the number of experiments is evaluated by repeating the same operation continuously. As a result, the first time result and 50th times result have 55 N difference at the maximum. This error is difficult to predict and would be a critical problem for the threshold determination for the collision detection.

As a conclusion of the above discussion, the multi-data-based determination is actually a useful method to set the threshold according to the probability theory, but it is not applicable if the low-frequency error cannot be compensated sufficiently. Therefore, we decide to apply a pseudo differential process to the estimated disturbance force, although low-frequency components are generally eliminated with a high-pass filter. The collision-induced fluctuation in the estimated disturbance force would be drastic and able to be emphasized with a differential process. Furthermore, phase lead characteristic of the differential process would enhance the detection response at the same time.

From the above reasons, the pseudo differential value of the estimated disturbance force, which is defined as "disturbance jerk" and its amplitude is expressed with the units of "N/s" or "kN/s", is utilized to detect a tool collision in

this study. Thus, the characteristic of the pseudo differential value should be analyzed to adjust the detection system properly.

As one of the example, the behavior of the pseudo differential value is shown in Fig. 5-5, where the x stage is fed at 50000 mm/min and cutoff frequency is set to 1000 rad/s (the analysis is performed on the same data of the experiment shown in Fig. 5-1). The signal noise gets larger during acceleration/deceleration than during uniform motion. Considering that the amplitude of the signal noise does not change remarkably in Fig. 5-1 and the differential process expands particularly the high frequency components, the frequency components would be different in each section. In order to analyze the frequency components included in the disturbance jerk, the FFT analysis is performed and the result is shown in Fig. 5-6. The quantum error generates not a white noise but a signal noise including 1000, 2000, 4000 Hz components mainly, which would relate to the
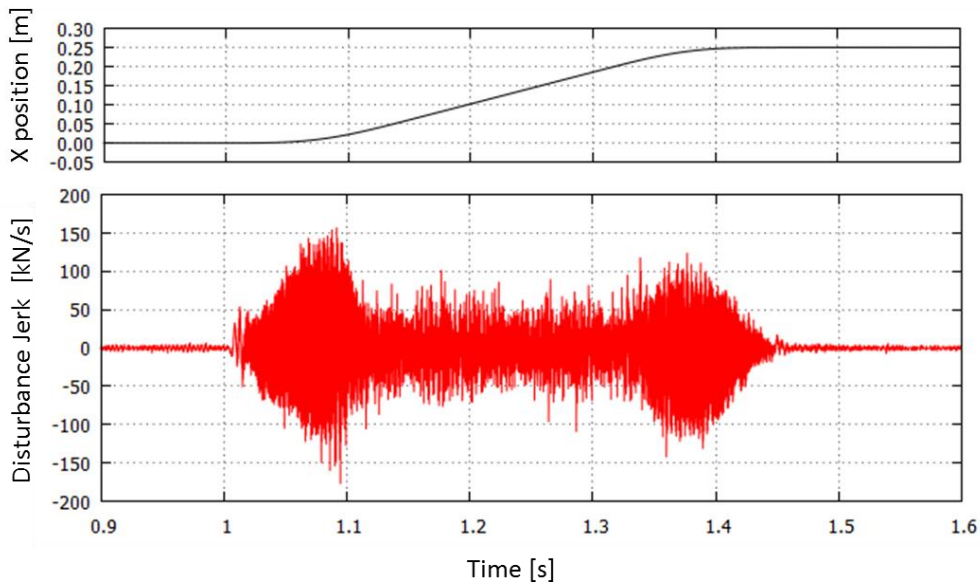

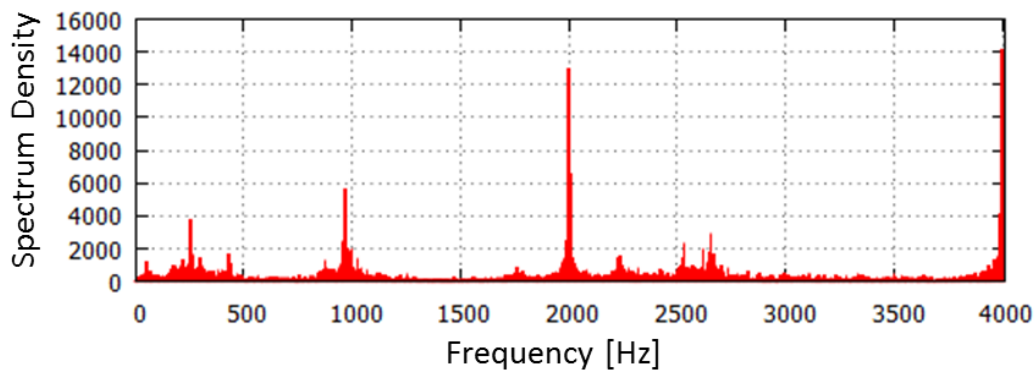Fig. 5-5   The disturbance jerk estimation in X direction.

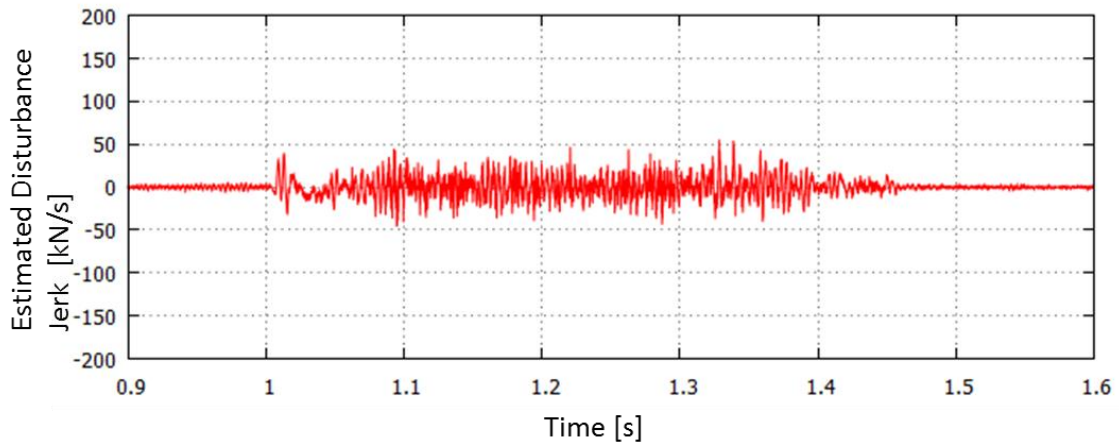Fig. 5-6   The FFT analysis of estimated disturbance jerk.

Fig. 5-7　The signal-processed disturbance jerk.

sampling frequency of 8000 Hz. The collision-induced variation in the disturbance jerk would be a pulse wave, then, various frequency components are included Therefore, the disturbance jerk would be usable for the collision detection even if the 1000, 2000, 4000 Hz components are eliminated.

In this test, the 1000 and 2000 Hz components are eliminated with second-order IIR notch filter and the 4000 Hz component is omitted by second-order moving average.

Introducing the above signal processing, the behavior of the obtained estimated disturbance jerk is shown in Fig. 5-7 (the cutoff frequency is set to 1000 rad/s). Compared with Fig. 5-5, the signal noise is suppressed. This result also indicates that the signal noise in the acceleration/deceleration section includes 1000, 2000, 4000 Hz components more than the other sections, however, it is difficult to find a fundamental reason. This would depend on the NC controller's configuration, but this research does not discuss it in detail because it is not a significant problem to establish the collision detection system.

In order to determine a proper threshold, the distribution of the estimated disturbance jerk is discussed here. The probability distribution of the estimated disturbance jerk of 3200 samples is as shown in Fig. 5-8; its average is 0.3 kN/s, and its standard deviation is 13.2 kN/s. The standard distribution is also drawn in Fig. 5-8, which has the same average and deviation. When the cutoff frequency is set to 1000 rad/s, the distribution of the disturbance jerk looks fit to the standard distribution, however, the χ^2 test result shows that the upper probability is almost zero and denies that the population is a standard

95
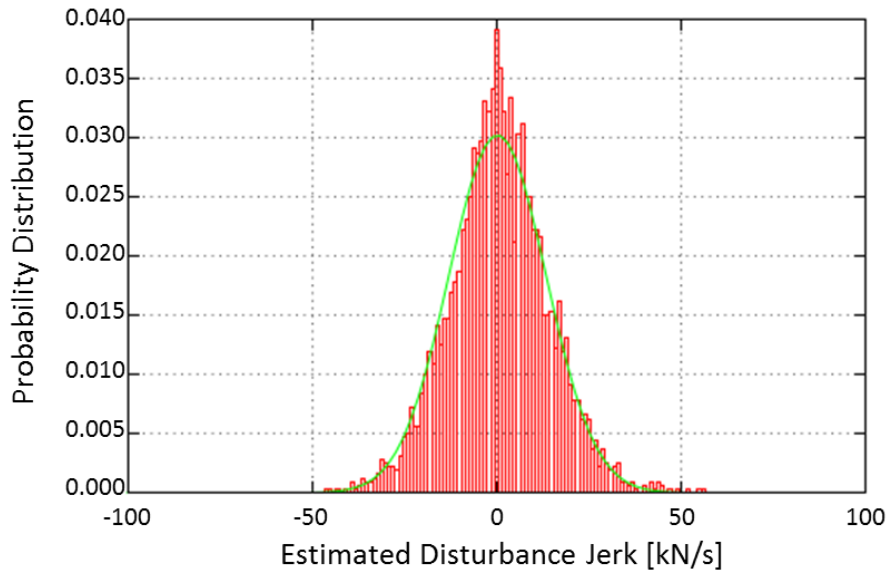
Fig. 5-8 Probability distribution of the estimated disturbance jerk:
green line represents normal distribution.

distribution. This is because two samples exceed the value of $(\mu + 4\sigma)$ in 3200 samples. The upper probability of $(\mu + 4\sigma)$ is so small as 3.17×10^{-5} which expectedly happens only once in 31546 samples. Thus, it is abnormal that the two samples exceed the value of $(\mu + 4\sigma)$ in only 3200 samples when the population is the standard distribution. In this case, the probability distribution function should be derived approximately by collecting enough data. This function varies according to the cutoff frequency, thus, the cutoff frequency modification should be discussed preferentially.

When the collision occurs with a 7 mm diameter drill and the cutoff frequency is set to 1000 rad/s, the estimated disturbance jerk fluctuates as shown in Fig. 5-9 corresponding to the idling test result shown in Fig. 5-7, where the feed rate is 50000 mm/min. The maximum value of the disturbance jerk is less than 70 kN/s in an idling test, on the other hand, the peak value of the disturbance jerk reaches 280 kN/s in a collision test. Therefore, this result already indicates that the collision detection sufficiently can be performed with the disturbance jerk monitoring. Here, to identify the proper cutoff frequency, two evaluation factors are introduced; time response to detect the collision as soon as possible, and robustness to distinguish the collision without mistakes. The time response of the proposed method can be easily evaluated by measuring the time at which the disturbance jerk signal exceeds a threshold. On the other hand, there would be
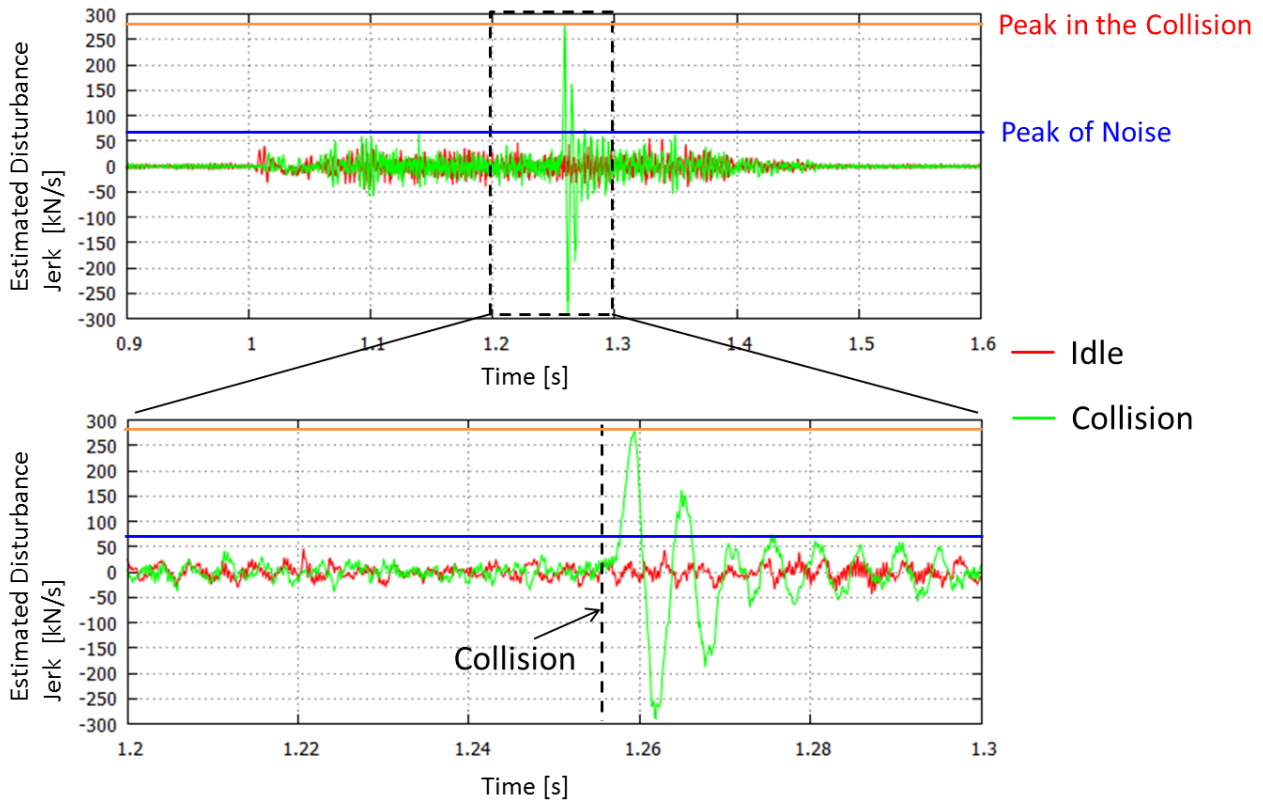
Fig. 5-9 The estimated disturbance jerk (cutoff frequency: 1000rad/s): red line represents the result of an idle test; green line represents the result of the collision test.

several ways to evaluate the robustness of the detection. In this research, the detection robustness is defined as the ratio between the collision-induced peak and the noise-induced peak values as shown in Fig. 5-9, which may be a clear criterion to distinguish the collision signal from the signal noise.

By calculating the ratio of the peak values for each cutoff frequency, the relation shown in Fig. 5-10 is derived, where it shows three results of collision experiments with 7 mm diameter tools. The derived relation indicates that the robustness can be enhanced when the cutoff frequency is set to from 300 to 400 rad/s. Although the peak ratio would be theoretically larger with a smaller cutoff frequency because of the noise reduction, low frequency fluctuation during accelerating/decelerating due to parameter variation would be a dominant factor in the disturbance jerk fluctuation when the cutoff frequency is set to too low. That would be why the peak ratio has a local maximum value. By calculating the average of obtained three cutoff frequencies at which local maximum peak ratio is observed, 335 rad/s is determined as the proper cutoff frequency to enhance the detection robustness.
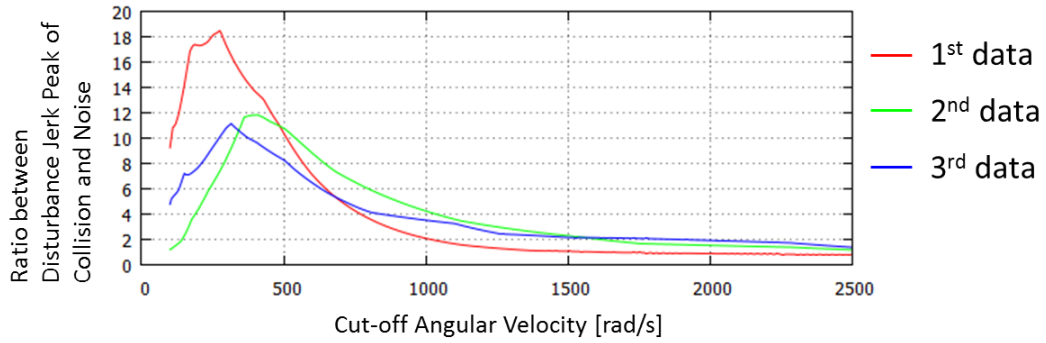
Fig. 5-10   The ratio between disturbance jerk peak of collision and noise.
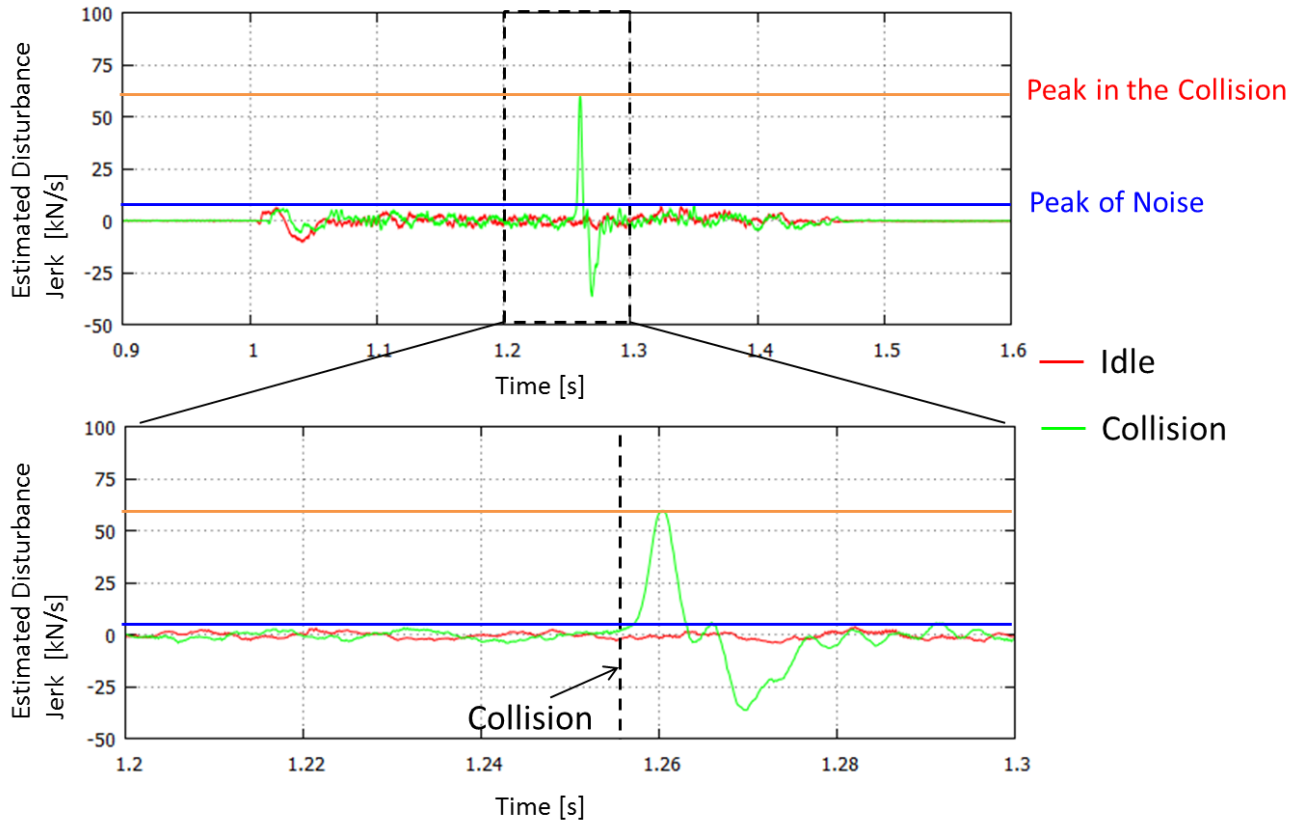
Fig. 5-11   The estimated disturbance jerk (cutoff frequency: 335rad/s): red line represents the result of an idle test; green line represents the result of the collision test.

When the cutoff frequency is set to 335 rad/s, a drastic fluctuation is clearly observed as shown in Fig. 5-11. The collision peak is 59.7 kN/s and the noise peak is 6.19 kN/s, and the peak ratio is 9.6 as a result.

As a next step, the time response of detection is also evaluated based on the

98

Fig. 5-12　Relation between cutoff angular velocity and +7 σ threshold exceed time.

experimental result. In this discussion, the collision time is required by measuring the distance between the tool and the workpiece in advance and corresponding to the position response.
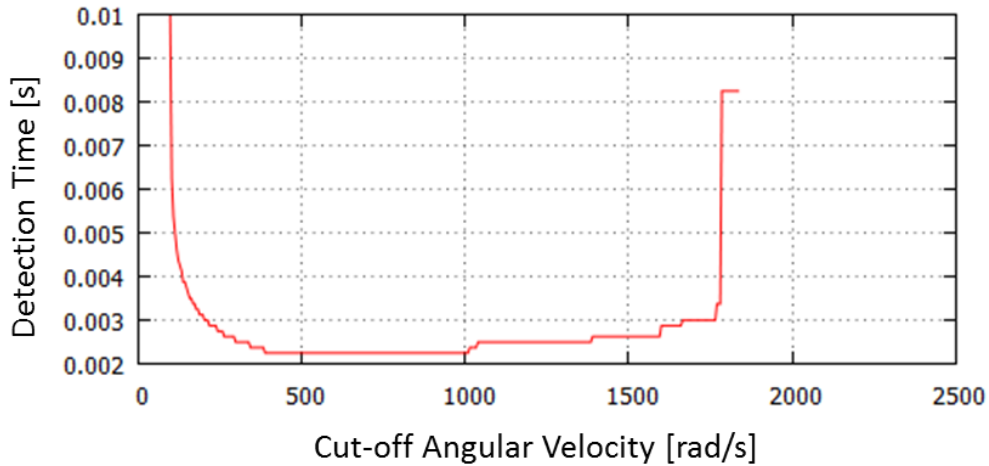
A low-pass filter usually causes larger phase delay with lower cutoff frequency in the signal. Alternatively, the noise reduction effect of the low-pass filter enables the threshold to get lower. Considering these points related to the detection response time, the time-response evaluation is performed by setting a threshold of (μ + 7σ) and measuring the time until the disturbance jerk exceeds the threshold. The detection time with each cutoff frequency is summarized in Fig. 5-12. In this result, the detection time is not shown in the region higher than 1840 rad/s because the disturbance jerk does not exceed the (μ + 7σ) threshold.

The relation between the detection time and the cutoff frequency indicates that the tool collision can be detected within only 3 ms when the cutoff frequency is set to from 220 to 1700 rad/s. Furthermore, the detection-time variation is only 0.5 ms with the cutoff frequency from 300 to 1600 rad/s. From this viewpoint, the cutoff frequency has an insignificant effect on the detection time, excepting the region lower than 300 rad/s and higher than 1600 rad/s.

As a conclusion, we determine the proper cutoff frequency as 335 rad/s to enhance the robustness and the time response performance of the collision detection based on the disturbance jerk estimation.

The remaining problem is a threshold determining procedure. When the distribution is not standard, it should be analyzed by repeating experiments
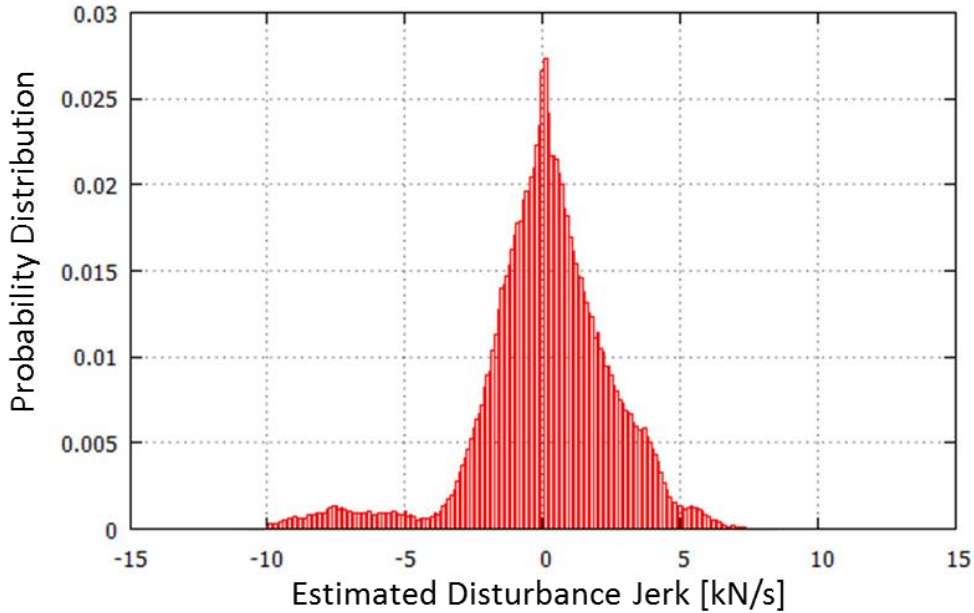
Fig. 5-13   Distribution of the estimated disturbance jerk.

many times. In this research, 180000 samples of the estimated disturbance jerk are collected with 50 times idling tests and their distribution is shown in Fig. 5-13, whose average is 0.062 kN/s, the standard deviation is 2.43 kN/s, the maximum value is 8.48 kN/s, and the minimum value is -10.42kN/s. In case that the threshold is set to (μ + 5σ =12.15kN/s), no sample exceeds it in all 180000 samples. Assuming that the upper probability of (μ + 5σ) is less than 1/180000, the probability to continuously exceed the threshold three times is less than 1.71×10^{-16} (once 2.31×10^4 years), although the disturbance jerk samples are not independent each other because high-frequency components are filtered.

Furthermore, the signal noise gets smaller with lower feed rate and this discussion is performed with the idling test data taken at maximum feed rate. From this viewpoint, the threshold is utilizable even for other feed rates. Although idling tests should be conducted at each feed rate, the test has to be repeated so many times and it is against the demand of simplification.

In order to ensure the robustness of the detection, (μ + 6σ) threshold (=14.58kN/s) is employed as an enough high value and the situation is regarded as tool collision when the disturbance jerk exceeds the threshold three times continuously. If the distribution were standard, the probability of this situation is equal to 1.71×10^{-28}.

100

Summarizing the above discussion, the characteristics of the disturbance jerk-based tool collision is explained as follows.

① The cutoff frequency of low-pass filters in disturbance observer and pseudo differential process is set to 335 rad/s.

② The threshold is set to 14.58 kN/s (= $\mu + 6\sigma$) based on the standard deviation σ of the noise.

③ The system regards the situation as tool collision when the disturbance jerk exceeds the threshold three times continuously.

On the basis of the proposed detection method, the adequacy of the proposed method is experimentally evaluated in the next section.

5.3 Tool Collision Test

The spindle bearing would be broken during the collision experiments if the tool is set to the tool holder. In order to avoid the damages on the spindle, a tool holder is directly set to the Z-axis stage by mounting a jig shown in Fig. 5-14.

5.3.1 Tool Collision in Horizontal Direction

The toll collision in horizontal direction of tool physically would have some delay because of the tool deflection, compared with axial direction. Furthermore,
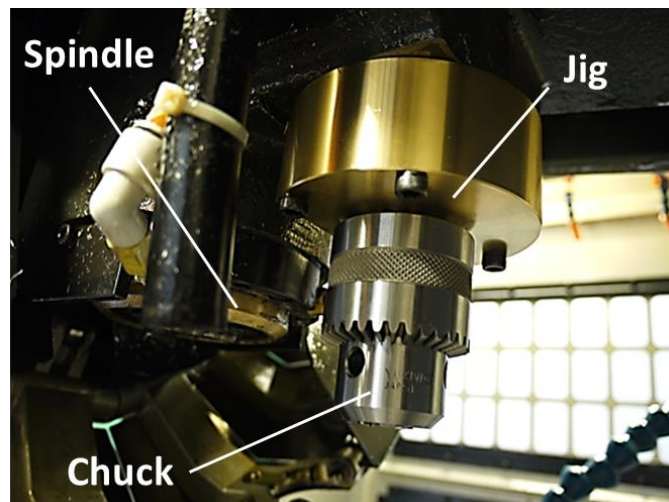

Fig. 5-14   The jig mounted on the Z stage.

Table 5-2　Experimental condition.

Direction	Horizontal direction (X-axis)
Tool Diameter	7 mm, 5 mm, 3 mm
Feed condition	50000 mm/min, 25000 mm/min, 5000 mm/min, Acceleration (10 m/s^2), Deceleration (-10 m/s^2)
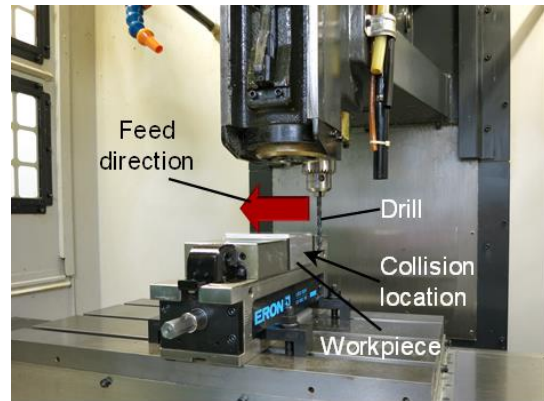
Fig. 5-15　Tool path in X direction.

the tool would be easily broken and the collision force would be small when the tool diameter is small. To confirm these points, the collision tests are performed in X direction firstly.

　The validity of the proposed method is confirmed with three kinds of stage feed rates (50000, 25000, 5000 mm/min) and three kinds of tools having different diameters (7, 5, 3 mm). Additionally, the tests are also conducted including the tool collision during accelerating or decelerating the stage. Totally, 15 kinds of collision experiments are conducted as shown in Table 5-2. Figure 5-15 shows the appearance of the experiment.

Fig. 5-16   Results of collision tests at max. feed rate (50000 mm/min)
in horizontal direction (X-axis).

Figure 5-16 shows the behaviors of the disturbance jerk at the moment different diameter drills collides at 50000 mm/min (maximum feed rate). In terms of the results of 7 and 5 mm diameter drills, the disturbance jerk clearly exceeds the threshold of 14.58 kN/s (= $\mu + 6\sigma$). In 3 mm diameter drill, 22 samples get larger than the threshold. As a result, the proposed method actually has an ability to detect the tool collision even in case of 3 mm diameter tool. However, the collision detection would be difficult when the tool diameter is less than 3 mm.
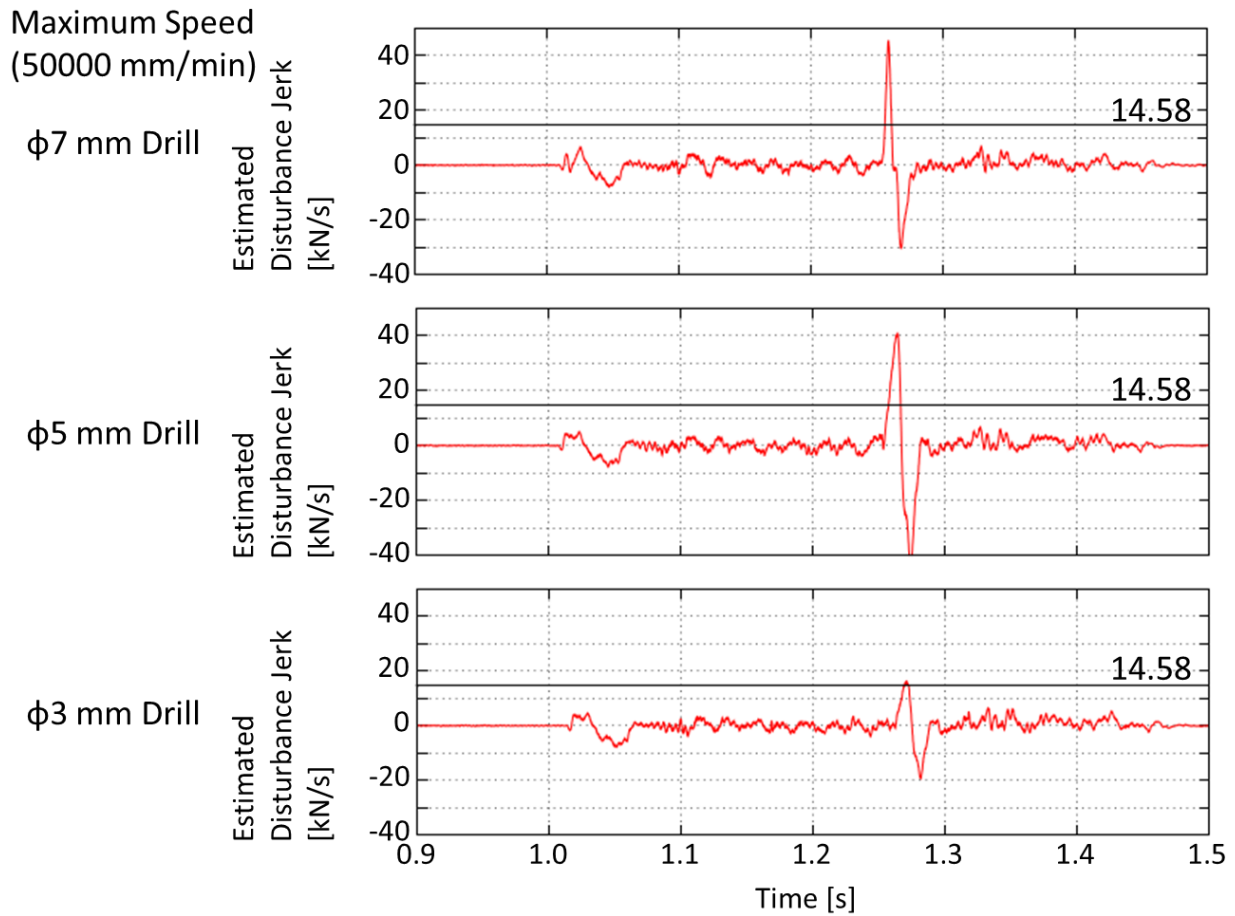
25000 mm/min

φ7 mm Drill

φ5 mm Drill

φ3 mm Drill

Fig. 5-17   Results of collision tests at 50 % of max. feed rate (25000 mm/min) in horizontal direction (X-axis).

Figure 5-17 shows the monitoring results at 25000 mm/min (50% of maximum) feed rate. The collisions with 7 and 5 mm diameter drills are detectable with the proposed method. However, the fluctuation due to the collision with a 3 mm diameter drill does not exceed the threshold, although the fluctuation itself can be observed in the estimated disturbance jerk.

Therefore, the collision with the 3 mm diameter drill has a possibility to be detected by changing the other threshold determination. For example, a dynamic threshold would be useful which changes according to the movement of the stage. Because the variation of the disturbance jerk in acceleration section (from 1.0 to 1.1 s) is larger, a lower threshold is available in other sections by analyzing the distribution in each section separately. However, the method should not be changed finely based on the signal features from the viewpoint of versatility.

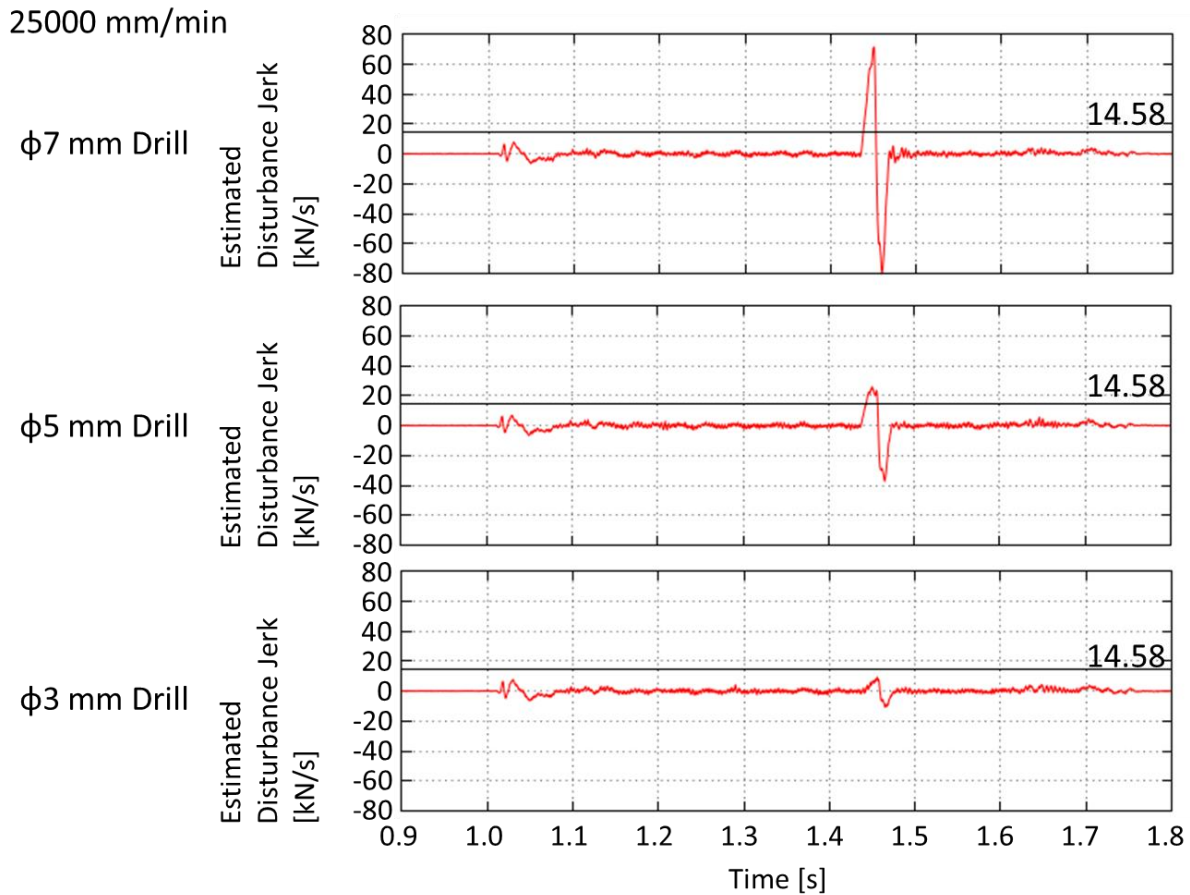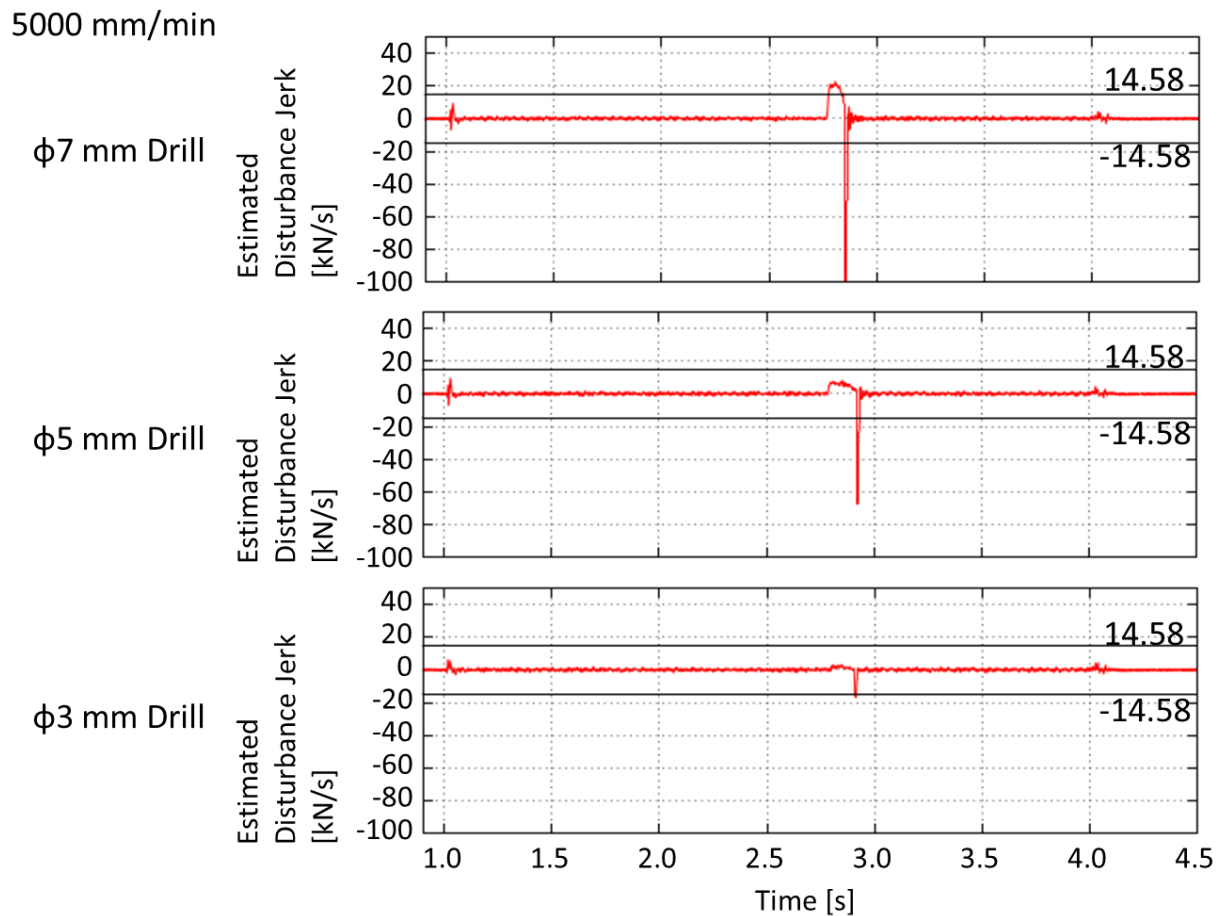**5000 mm/min**

φ7 mm Drill

φ5 mm Drill

φ3 mm Drill

Fig. 5-18   Results of collision tests at 10 % of max. feed rate (5000 mm/min) in horizontal direction (X-axis).

Figure 5-18 shows the experimental results at 5000 mm/min (10% of maximum) feed rate. In these experiments, the tool shows different behaviors with previous experiments at 50000 and 25000 mm/min feed rate. The tool collision causes from 2.75 s in all experiments, and after that, the elastic deformation of the tools is observed for about 1.5 s. This phenomenon is also confirmed from the disturbance jerk increase like a square wave, which indicates that the applied disturbance force proportionally and gradually increases from 2.75 s. Moreover, tool breakage occurs at about 2.90 s and it is observable as a pulse wave in the estimated disturbance jerk. It indicates that the disturbance force drastically removes by the tool breakage. In other words, the tool contact is detectable in case of 7 mm diameter drill before tool breakage because the disturbance jerk signal exceeds in the elastic deformation section.

As a result, the proposed method successfully detects the tool collision with all

Acceleration

φ7 mm Drill

φ5 mm Drill

φ3 mm Drill
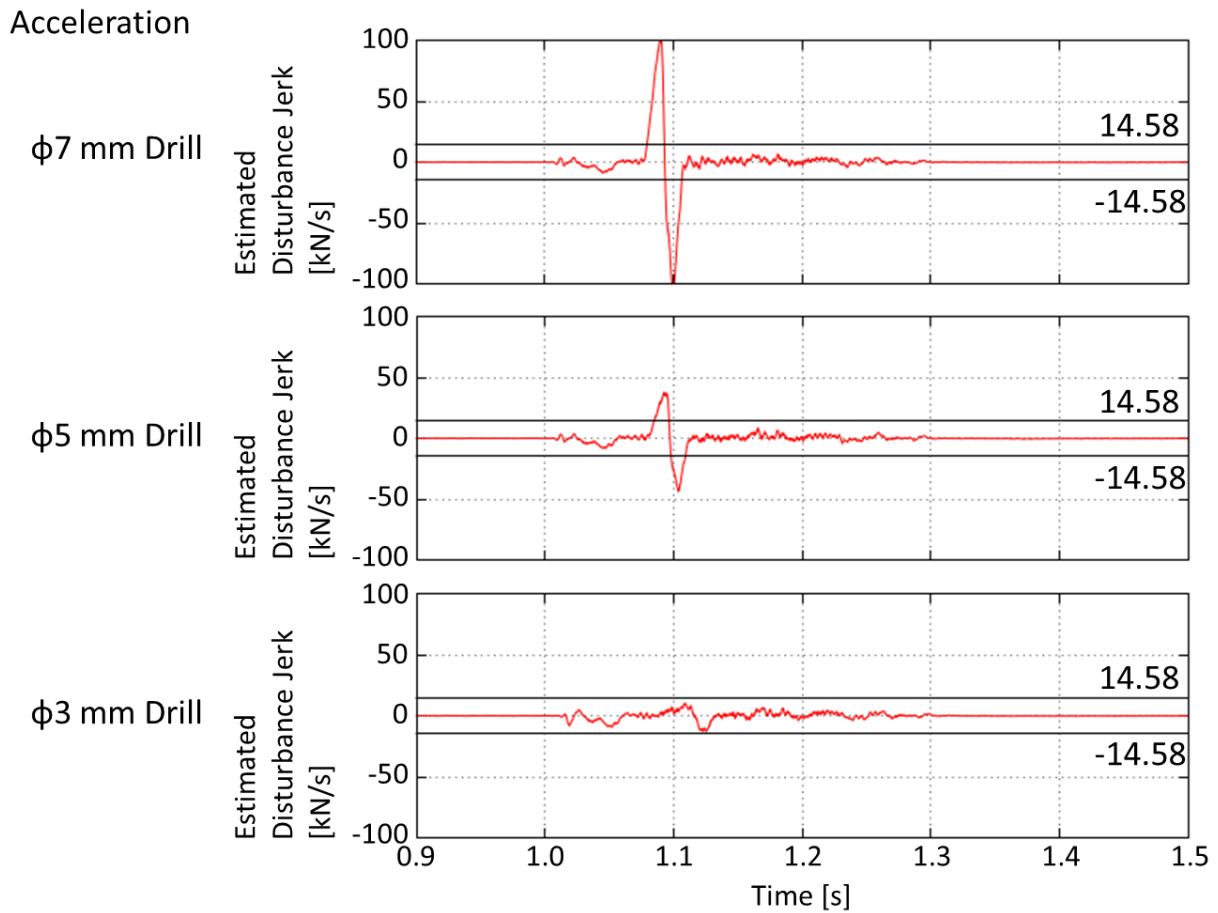
Fig. 5-19   Results of collision tests during accelerating
in horizontal direction (X-axis).

experimental results with 7mm, 5mm and 3mm diameter drills.

The collision during accelerating is also focused on this experiment.

Figure 5-19 shows the behavior of the estimated disturbance jerk when the tool collision occurs during the x-stage acceleration. In case of 7 and 5 mm diameter drills, the collision-induced fluctuations clearly exceed the threshold, then, the tool collisions are detectable. On the other hand, the estimated disturbance jerk does not exceed the threshold at the tool collision with the 3 mm diameter drill.

As previously noted, it may be detectable with a different threshold determination because the fluctuation due to the collision is slightly confirmed.
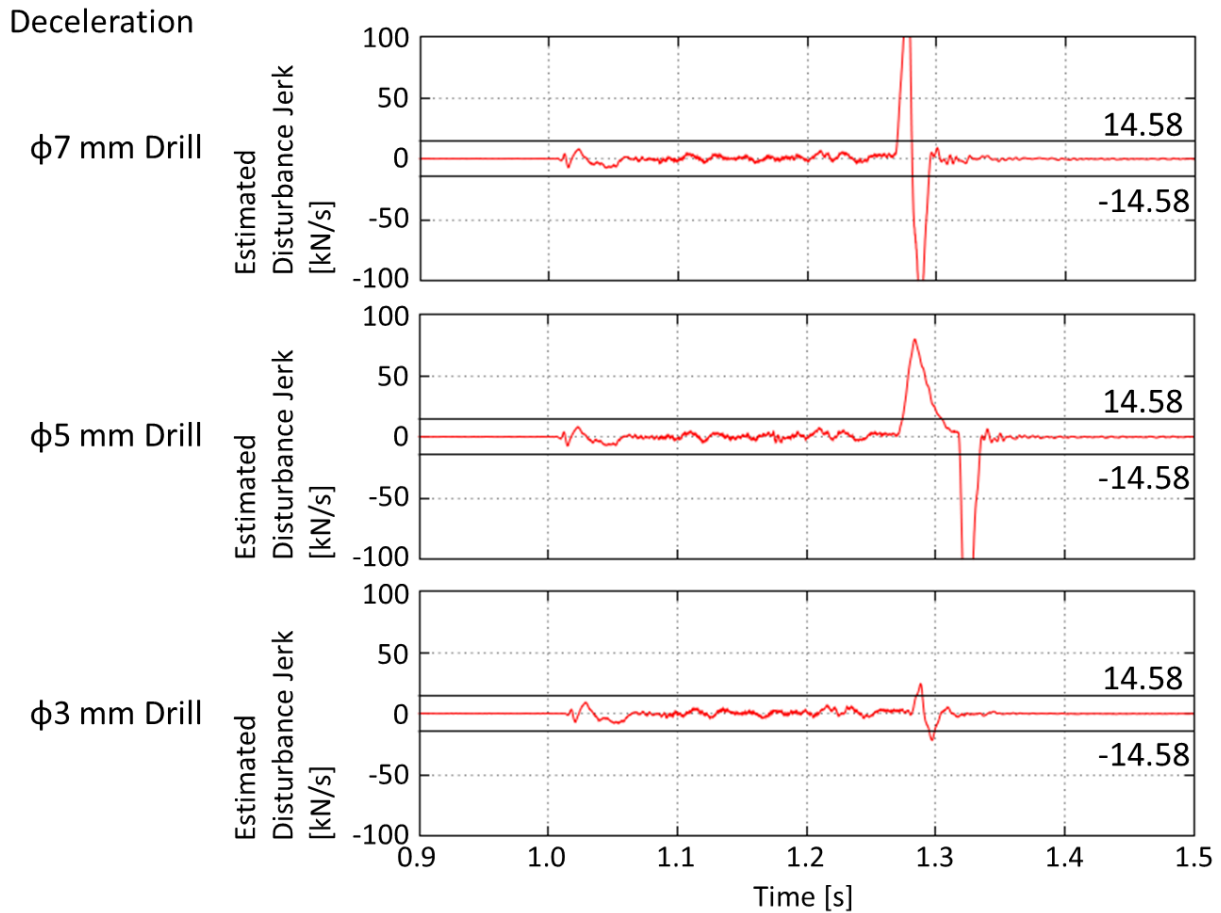
Fig. 5-20   Results of collision tests during decelerating
in horizontal direction (X-axis).

The similar experiments are also conducted for a tool collision in the deceleration section as shown in Fig. 5-20. As a result, the proposed method actually detects the fluctuation due to collision with 7, 5, and 3 mm diameter drills.

Summarizing the collision experiments in X direction, it is clear that the tool collision can be detected when the tool diameter is 5 mm and over regardless of feed rate. However, the collision with 3 mm diameter drill cannot be detected at some feed rates because the small diameter tool breaks so easily not to generate a large disturbance force fluctuation. The fluctuation itself in the disturbance jerk can be slightly confirmed; therefore, the collision has a possibility to be detected by adapting a dynamic threshold, which varies according to the stage motion, even in case of 3 mm diameter drills.

The above experimental results are summarized in Table 5-3.

Table 5-3　Summery of X-direction collision experiments.

	Max.	50% of Max.	10% of Max.	Acceleration	Deceleration
7mm	○	○	○	○	○
5mm	○	○	○	○	○
3mm	○	△	○	△	○

○…Success　△…Need to Improve

5.3.2　Tool Collision in Axial Direction

The collision in axial direction generates large collision force and easily leads to a critical damage on the spindle parts like bearings because the tool hardly deforms when compressed in the axial direction. Therefore, the collision detection system for axial direction is indispensable.

The ballscrew-driven stages for X axis and Z axis have a same rotary encoder resolution and the same P-PI control method is applied to them. Thus, the proper cutoff frequency for X-axis collision detection (335 rad/s) would be also available for Z-axis collision detection to enhance the robustness and the time

Table 5-4　Experimental Condition.

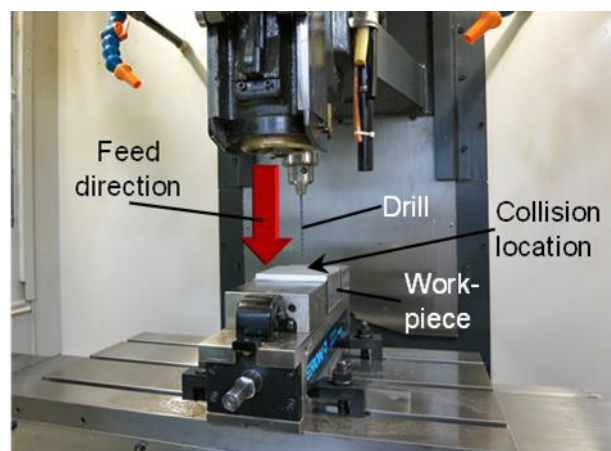| Direction	Vertical direction (Z axis)
Tool Diameter	3 mm
Feed condition	50000 mm/min, 25000 mm/min, 5000 mm/min, Acceleration (10 m/s^2), Deceleration (-10 m/s^2)

Fig. 5-21　Tool path in Z direction.

response.

When the Z-axis collision tests are performed, only 3 mm diameter drills are used because the collision force would be too large to avoid a serious damage on the Z-axis ball screw stage, although spindle damage is avoidable by using the jig. For the same reasoning, 150 mm length long-type drill is selected, which is easy to break. By using five kinds of feed rate, (50000, 25000, 5000 mm/min, and acceleration/deceleration) the Z-axis collision tests are conducted as summarized in Table 5-4. Figure 5-21 shows the appearance of the experiment.

The idling tests are conducted for Z-axis movement, and the distribution of the disturbance jerk is analyzed. As a result, the average is -0.54 kN/s and the standard deviation is 5.36 kN/s. From this result, the threshold is set to 32.16 kN/s(= μ + 6σ) in the Z-axis tool collision tests.

In case of that the feed rate is set to 50000 and 25000 mm/min, the tool collision can be detected as shown in Fig. 5-22. In Fig. 5-22 (a), the estimated disturbance jerk exceeds the threshold three times because the broken tool hits the workpiece repeatedly.
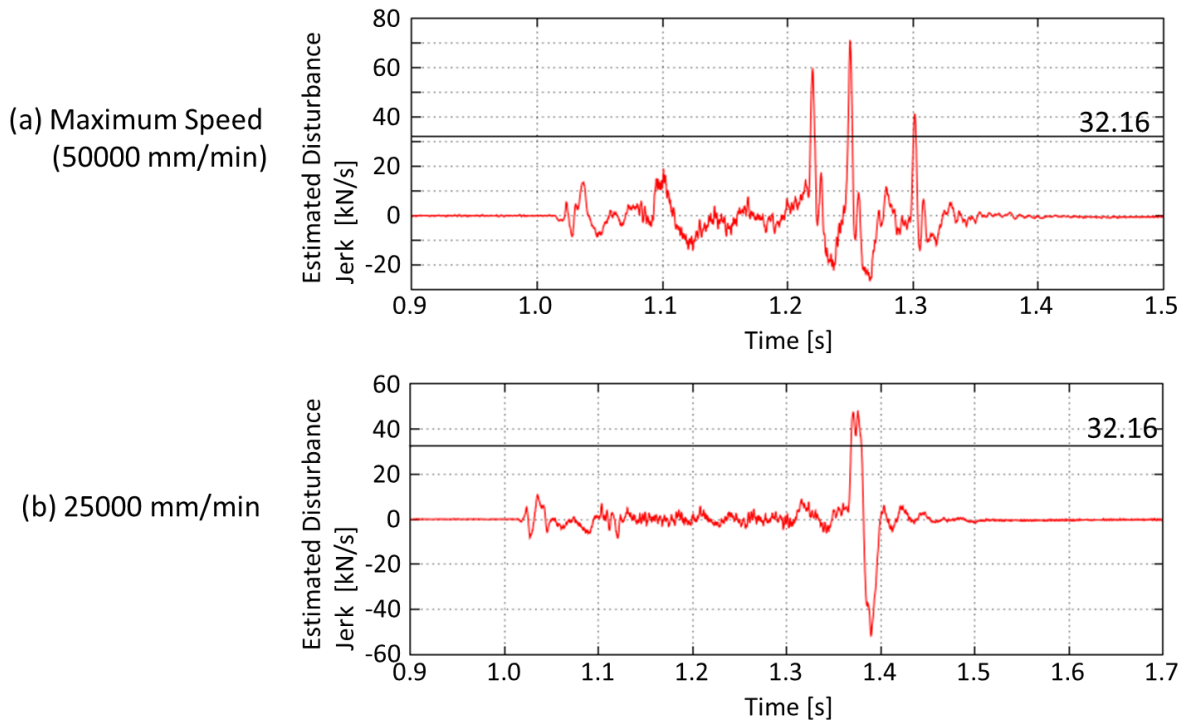
Fig. 5-22   The result of collision tests in Z direction: (a) maximum speed (50000 mm/min), (b) 50% of maximum speed (25000 mm/min).

(a) Acceleration
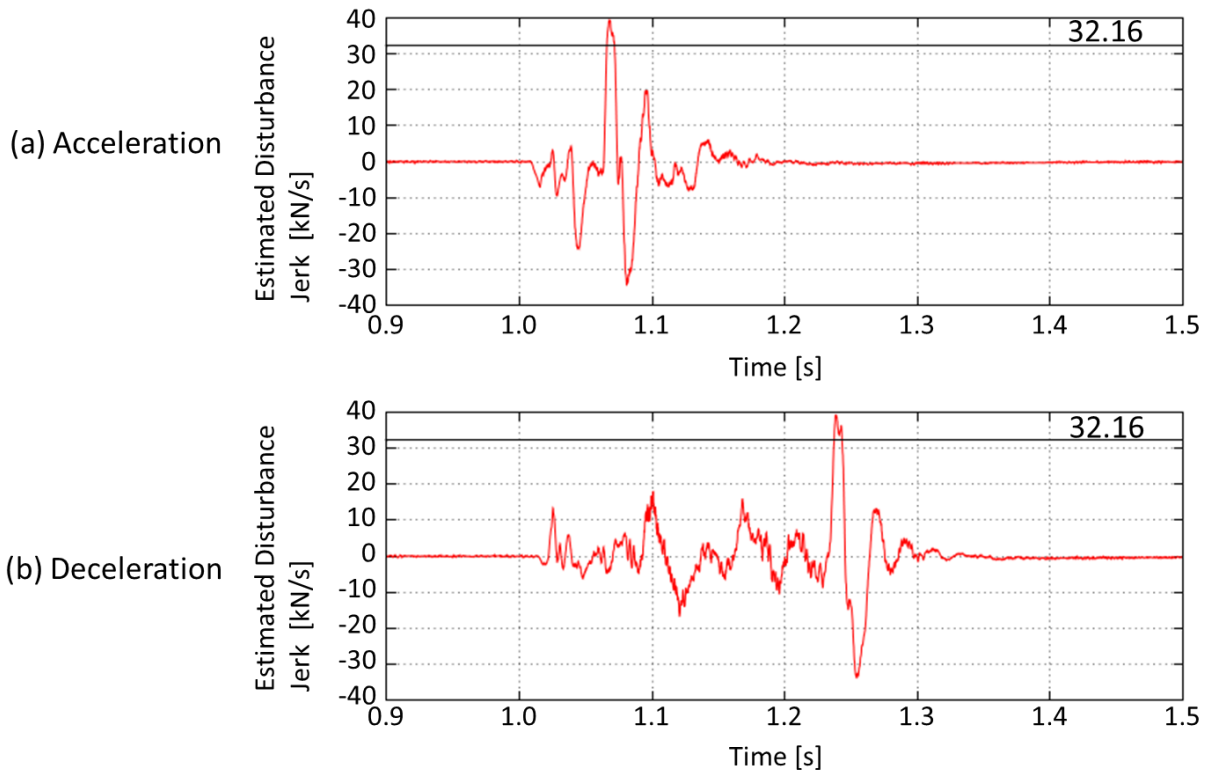
(b) Deceleration

Fig. 5-23　The result of collision tests in Z direction (a) acceleration, (b) deceleration.
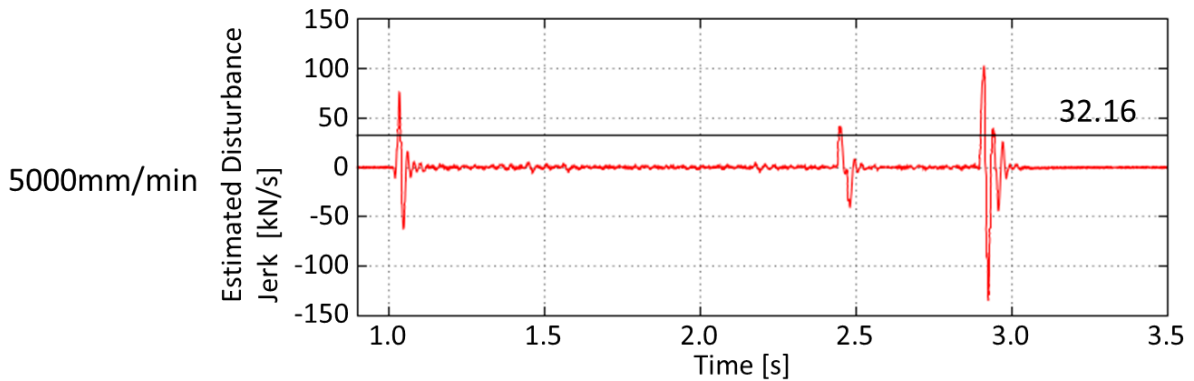
5000mm/min

Fig. 5-24　The result of collision test in 5000 mm/min in Z direction.

Then, the behavior of the disturbance jerk when the collision occurs during accelerating/decelerating the z stage is shown in Fig. 5-23, where the feed rate is set to 50000 mm/min. In both cases, the disturbance jerk clearly gets larger than the threshold of $(\mu + 6\sigma)$.

As a next, the collision experiment at the feed rate of 5000 mm/min is shown in Fig. 5-24. The estimated disturbance jerk exceeds when the collision occurs. However, a large fluctuation in the disturbance jerk is observed during accelerating/decelerating, which is not observed in the X-axis collision tests.

Furthermore, the misdetection occurs because this fluctuation exceeds the threshold, which is generated at the resonance frequency of the stage. Although it is an infinitesimal vibration for the position control, the error becomes large in the disturbance jerk dimension. In this case, a two mass system model should be adopted; however, the number of parameters which has to be identified increases. This is against the simplification for the versatility. From this viewpoint, the dynamic threshold may be a useful method to avoid a misdetection.

The above Z-axis collision experimental results are summarized in Table 5-5.

Table 5-5　Summary of the Z-axis collision experiments.

	Max.	50% of Max.	10% of Max.	Acceleration	Deceleration
3mm	○	○	△	○	○

○···Success　△···Need to be improved

5.4 Summary

In this chapter, the applicability of the observer-based cutting force estimation to tool collision detection is discussed through the abundant experiments. By requiring the differential value of the disturbance force named "disturbance jerk," the collision force is captured based on the servo information in the x and z ballscrew-driven stage control system. The archived results are summarized as follows.

1. To explain the reason why the disturbance jerk is employed to tool collision detection in the proposed method, the estimated disturbance information is analyzed based on the probability theory. Furthermore, the modification method is proposed for the cutoff frequency of low-pass filters in the disturbance observer and the pseudo differential process on the basis of the evaluation of time response and robustness.

2. In the horizontal direction, tool collisions with 7 and 5 mm diameter drills can be detected by setting a threshold on the estimated disturbance jerk information. On the other hand, collision with a 3 mm diameter tool cannot be detected with the static threshold because the collision-induced fluctuation is not so large to exceed the threshold.

3. During accelerating/decelerating the z stage, the fluctuation at the resonance frequency is observed in the estimated disturbance jerk when the feed rate is set to 5000 mm/min. The collisions at the other feed rate are successfully detected with the proposed method.

6 Tool Fracture Detection System

6.1 Introduction

A tool fracture is a useful criterion to evaluate the cutting condition and predict a tool breakage because it generally occurs when an extra load is applied on the tool edge. However, excepting a large fracture which should be regarded as a tool breakage, tool fracture detection in drilling is hardly proposed because the fracture-included variation is small and the sensor mounting space is difficult to ensure due to usage of cutting oil. Therefore, a new approach has to be created to detect a small vibration caused by the drill fracture.

As explained in Section 2.3.4, this research proposes drill fracture detection based on the disturbance observer in the x and y ballscrew-driven stages. Furthermore, a novel signal processing method named "rotational digital filter (RDF)" is proposed to enhance the fracture detection accuracy, which has a unique characteristic to pass only a signal which is rotating in clock-wise direction on an XY plane. In this chapter, the proposed detection method is evaluated through several drilling tests with fractured drills. Furthermore, the filtering effect of the RDF is confirmed through a time-domain simulation.

6.2 Concept of Drill Fracture Detection

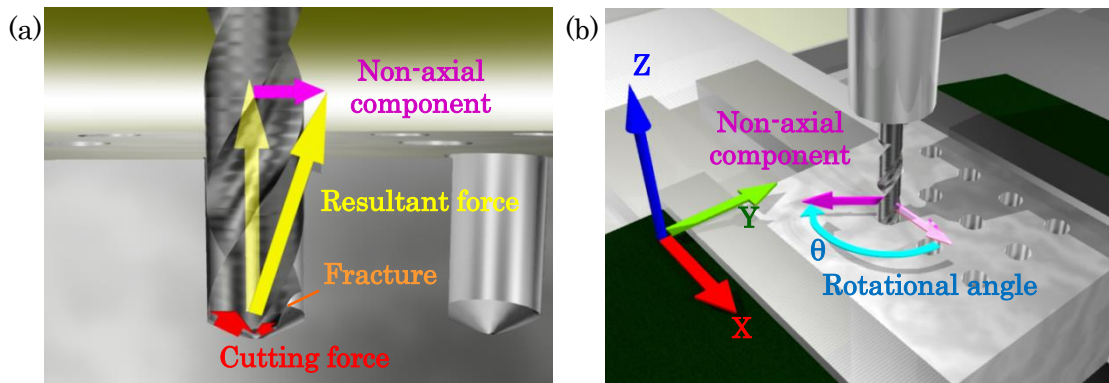How to detect a drill fracture is explained in this section. Under usual drilling

Fig. 6-1   Cutting force direction in drilling with a fractured drill:
(a) inclined resultant force, (b) rotation of XY component in cutting force.

condition, the resultant cutting force generates in the axial direction because of the axial symmetrical structure of the drill. However, the resultant force has non-axial component when the drill fracture occurs because the structure becomes axially asymmetrical as shown in Fig. 6-1 (a). The generated non-axial component rotates along with the spindle rotation as Fig. 6-1 (b); thus, the tool fracture can be detected by capturing the vibration at the spindle rotation frequency in X and Y directions with the proposed cutting force estimation.

Furthermore, the non-axial component moves in clockwise direction because a drill generally rotates in the clockwise direction from the spindle side. To enhance the detection accuracy of drill fracture, this research invented the RDF theory.

6.3 Proposal of Rotational Digital Filter

6.3.1 Investigation of the Characteristics with a Time-Domain Simulation

Firstly, the filtering effect of RDF is evaluated by inputting a combined wave as shown in Fig. 6-2 on a time-domain simulation. The combined wave has three

$$\begin{cases} x = 100\sin\left(2\pi t \times 150 - \dfrac{\pi}{2}\right) \\ y = 100\sin(2\pi t \times 150) \end{cases} \cdots \begin{array}{l}\text{150Hz Signal in} \\ \text{Clock-Wise} \\ \text{Direction}\end{array}$$

$$\begin{cases} x = 120\sin\left(2\pi t \times 180 - \dfrac{\pi}{4}\right) \\ y = 120\sin(2\pi t \times 180) \end{cases} \cdots \text{Noise 1}$$

$$\begin{cases} x = 70\sin\left(2\pi t \times 110 - \dfrac{2\pi}{3}\right) \\ y = 70\sin(2\pi t \times 110) \end{cases} \cdots \text{Noise 2}$$

Combined Signal   150Hz RDF   Filtered Signal

Fig. 6-2　Extracting performance of RDF for a signal moving in clockwise direction.

114

circular signal components; 150 Hz clock-wise circular orbit signal, and 110 Hz noise and 180 Hz noise. In this case, the RDF actually extracts the 150 Hz clock-wise signal as confirmed from the output signal. Although 110 Hz and 180
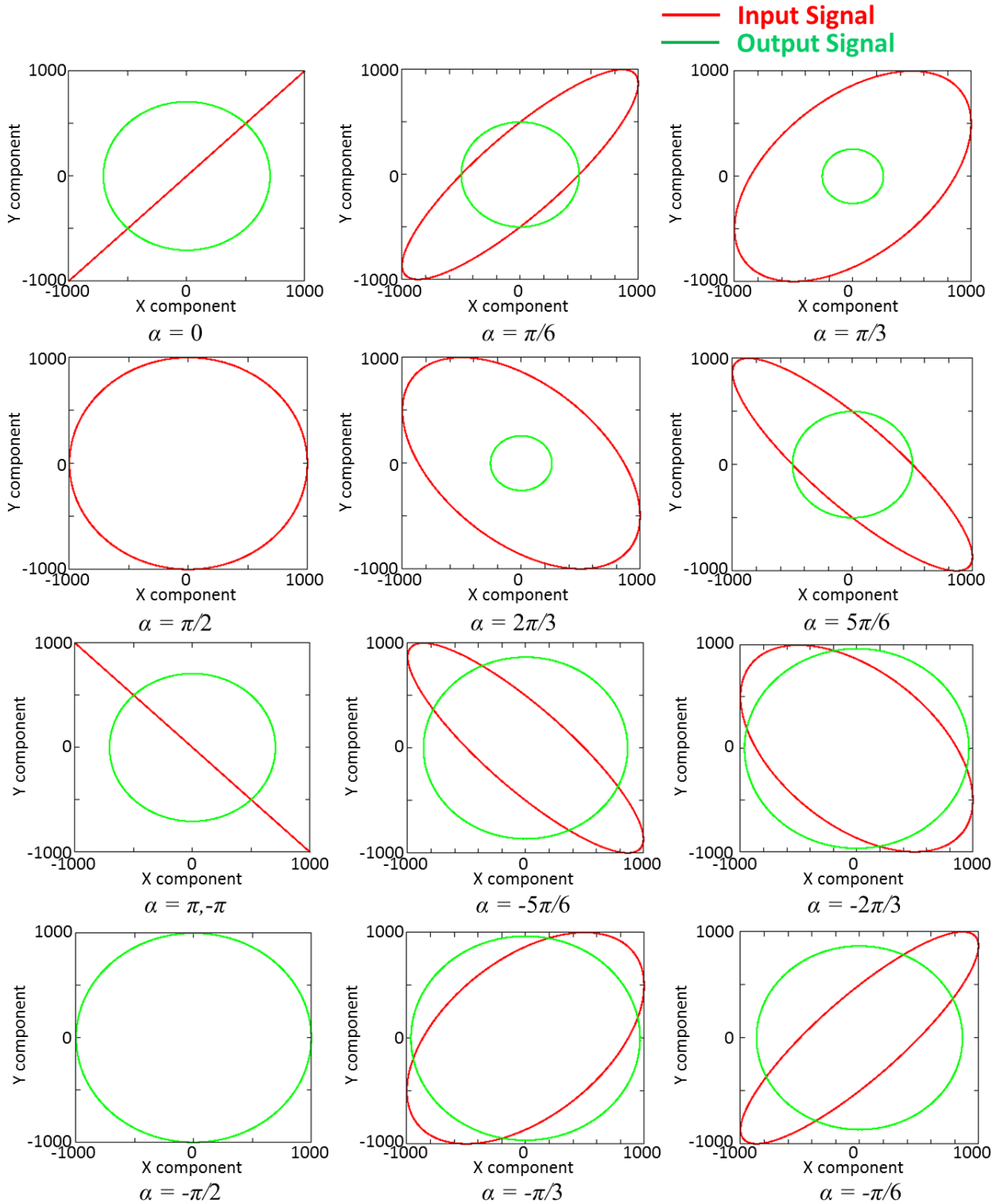

Fig. 6-3 Each output signals of RDF when various phase difference is applied to input signals.

115

Hz noises move on an elliptic orbit in the clock-wise direction, the influence of the both noises is hardly confirmed in the output signal. Therefore, RDF would have a band-pass filtering effect and a clock-wise rotating signal pass effect simultaneously.

As a next step, the influence of the phase lag between x and y components in case of only 150 Hz is input, where the components of input signal are described as Eq. 6-1.

$$\begin{cases} x = 1000\sin(2\pi t \times 150 + \alpha) \\ y = 1000\sin(2\pi t \times 150) \end{cases} \qquad (6\text{-}1)$$

Figure 6-3 shows the output signal of the RDF corresponding to the each phase delay in the input signal components α.

The output signal always draws a circular orbit and its radius varies according to the phase lag α in the input signal. In particular, the output radius becomes zero when the phase lag is $\alpha = \pi/2$, i.e., the input signal is rotating in counter-clock-wise direction. Furthermore, the input signal just passes when the phase lag is $\alpha = -\pi/2$, i.e., the input signal is rotating in clock-wise direction. From these results, the RDF certainly provides a clock-wise signal pass effect as expected in the proposed theory.

An interesting point of the results shown in Fig. 6-3 is that the RDF always outputs a circular orbit even if the input signal moves in an elliptic orbit or a line orbit. Moreover, the output with small radius is observed even when the input signal draws elliptic orbit in counter-clock-wise direction. The output becomes a zero matrix only when the input signal moves on a circular orbit in counter-clock-wise direction. The mathematical meaning of the RDF output is discussed here.

Theoretically, two types of RDF can be created for clock-wise signals and counter-clock-wise signals. Although it is difficult to image that a signal is rotating in the clock-wise and the counter-clock-wise directions at the same time, symmetrical results can be obtained by analyzing the input signals in Fig. 6-3 with a counter-clock-wise RDF. Therefore, excepting complete circular orbits, all elliptic orbits can be said to have both a clock-wise component and a counter-clock-wise component. From this viewpoint, a hypothesis can be established, which assumes that all circular, all elliptic, and all linear movements
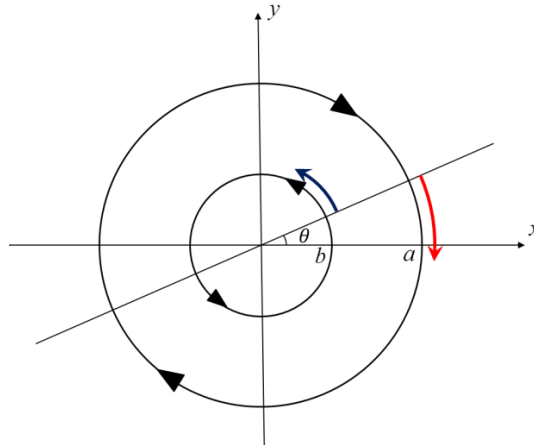
Fig. 6-4 Orbits of signals represented with Eq. 6-2.

on a two dimensional plane at a certain frequency can be separated into the clock-wise and the counter-clock-wise components of the same frequency. In an opposite way, all circular, all elliptic, and all linear movement at a certain frequency can be generated by combining a clock-wise signal and a counter-clock-wise signal at the same frequency. This assumption is mathematically proven in this section.

On an XY plane, a clock-wise signal $(x_{cw}(t), y_{cw}(t))$ and a counter-clock-wise signal $(x_{ccw}(t), y_{ccw}(t))$ can be represented as Eq. 6-2, where $a \geq b$.

$$(x_{cw}(t), y_{cw}(t)) = (a \cos(\omega t + \theta), a \sin(\omega t + \theta)),$$
$$(x_{ccw}(t), y_{ccw}(t)) = (b \cos(-\omega t + \theta), b \sin(-\omega t + \theta))$$

$$(6\text{-}2)$$

Their orbits can be drawn on the XY plane as shown in Fig. 6-4.

By adding both signals in Eq. 6-2, the combined signal $(x(t), y(t))$ is derived as follows:

$$(x(t), y(t)) = (a \cos(\omega t + \theta) + b \cos(-\omega t + \theta), \quad a \sin(\omega t + \theta) + b \sin(-\omega t + \theta)) \qquad (6\text{-}3)$$

Equation 6-3 can be transformed as Eq. 6-4.

$$(x(t), y(t)) = \left(\sqrt{a^2 + b^2 + 2ab \cos 2\theta} \, \cos(\omega t + \alpha), \, \sqrt{a^2 + b^2 - 2ab \cos 2\theta} \, \sin(\omega t + \beta) \right)$$

where

$$\cos \alpha = \frac{(a + b) \cos \theta}{\sqrt{a^2 + b^2 + 2ab \cos 2\theta}}, \qquad \sin \alpha = \frac{(a - b) \sin \theta}{\sqrt{a^2 + b^2 + 2ab \cos 2\theta}}, \qquad (6\text{-}4)$$

$$\cos \beta = \frac{(a - b) \cos \theta}{\sqrt{a^2 + b^2 - 2ab \cos 2\theta}}, \qquad \sin \beta = \frac{(a + b) \sin \theta}{\sqrt{a^2 + b^2 - 2ab \cos 2\theta}}$$

In order to confirm whether the combined signal of Eq. 6-4 describes an elliptic
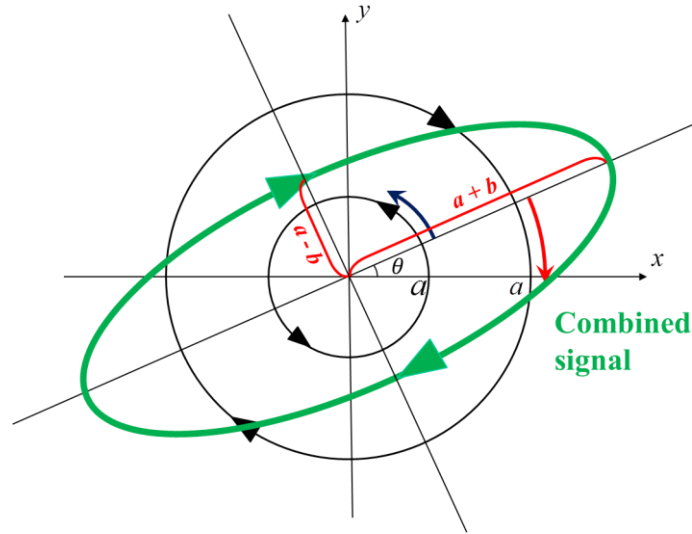
Fig. 6-5   The combined signal.

orbit or not, the rotated coordinate system at $-\theta$ rad is introduced. The combined signal $(x(t), y(t))$ can be translated to the signal on the rotated coordinate system $(X(t), Y(t))$ as follows:

$$\begin{bmatrix} X(t) \\ Y(t) \end{bmatrix} = \begin{bmatrix} \cos\theta & \sin\theta \\ -\sin\theta & \cos\theta \end{bmatrix} \begin{bmatrix} \sqrt{a^2 + b^2 + 2ab\cos 2\theta}\,\cos(\omega t + \alpha) \\ \sqrt{a^2 + b^2 - 2ab\cos 2\theta}\,\sin(\omega t + \beta) \end{bmatrix} = \begin{bmatrix} (a+b)\cos\omega t \\ (a-b)\sin\omega t \end{bmatrix} \tag{6-5}$$

Thus,

$$\sin^2\omega t + \cos^2\omega t = \left(\frac{X(t)}{a+b}\right)^2 + \left(\frac{Y(t)}{a-b}\right)^2 = 1 \tag{6-6}$$

Therefore, the combined signal actually draws an elliptic orbit which has $a + b$ length long axis and $a - b$ length short axis on the rotated coordinate system at $-\theta$ rad as shown in Fig. 6-5. The rotational angle θ is arbitrary, thus, all elliptic movement can be generated by combining proper clock-wise and counter-clock-wise components. Furthermore, a circular orbit and a linear orbit can be generated by substituting $b = 0$ or $b = a$ respectively.

Following the inverse order, it is clear that all circular, elliptic, and linear orbits can be separated into a clock-wise component and a counter-clock-wise component. Moreover, the same procedure can be applied to the case of $a < b$. Considering the linearity of trig functions and the counter-clock-wise signal cancelation characteristic of RDF shown in Eqs. 2-63 to 2-65, it is obvious that only the clock-wise component is extracted by the clock-wise-type RDF.

This proof also can be referred to a discrete domain as similar procedures. As a

conclusion, all circular, elliptic, and linear orbits can be separated into clock-wise and counter-clock-wise components, and the clock-wise-type RDF can extract the clock-wise component from the signal moving on the two dimensional coordinate.

The characteristic of RDF would be useful to enhance the detection accuracy of drill fracture because the non-axial component of the resultant cutting force moves in clockwise direction as explained in Section 6.2. By applying RDF to the estimated cutting force in X and Y directions, the fracture-induced fluctuation could be extracted more clearly.

6.3.2 Investigation of the Pass Region with a Time-Domain Simulation

The output of RDF draws a circular orbit as shown in the previous section. In this research, the radius of the output orbit of RDF is defined as spectrum density, and the pass region of the clock-wise-type RDF for 150 Hz is investigated with the spectrum density by applying various inputs as shown in Eq. 6-7.

$$\begin{cases} x = \sin 2\pi f t \\ y = \sin(2\pi f t + \theta) \end{cases}$$

(6-7)

where $100 \leq f \leq 200, \ -\pi \leq \theta \leq \pi$

The distribution of the spectrum density is shown in Fig. 6-6. The band-stop effect of RDF is certainly confirmed because the spectrum density appears only the frequency region around 150 Hz. Furthermore, the signal is cut when the y
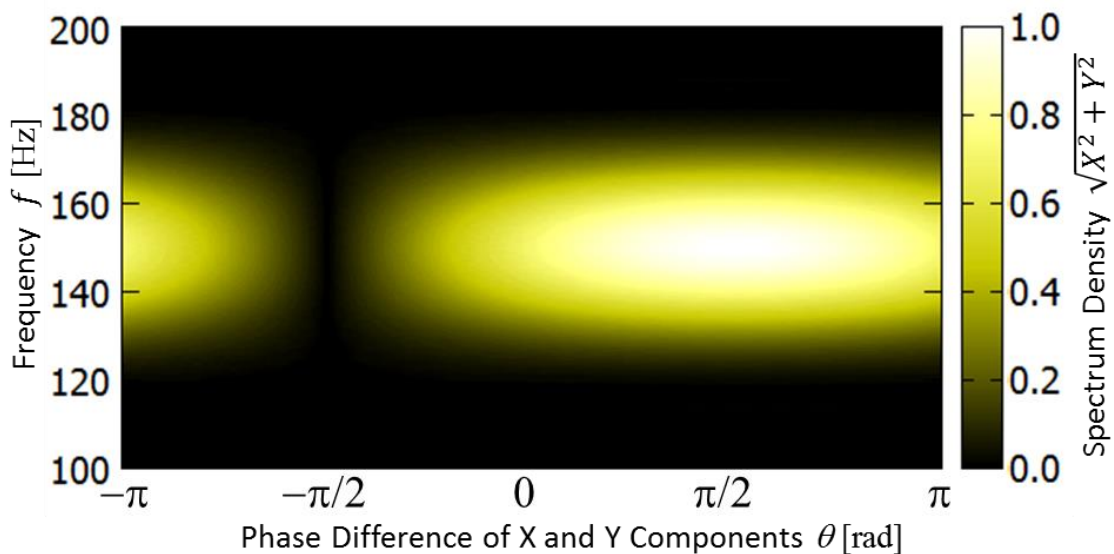

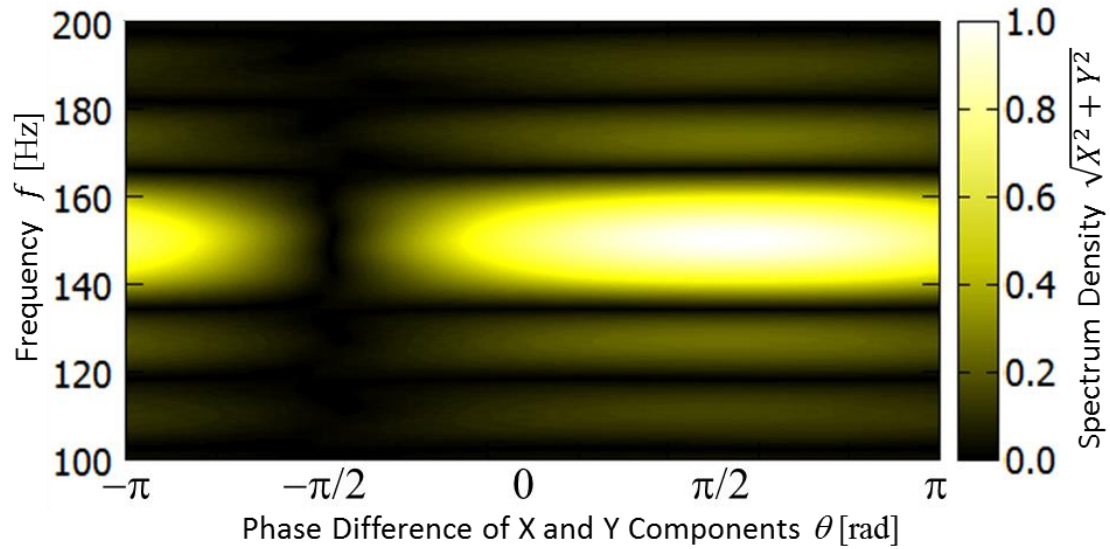Fig. 6-6   Passband of 150 Hz clockwise-pass-type RDF.

Fig. 6-7 Passband of 150 Hz clockwise-pass RDF (without a window function).

component has $\pi/2$ rad phase delay against x component, i.e., the signal rotating in counter-clock-wise direction, even if the signal frequency is 150 Hz.

The necessity of the window function is also discussed in chapter 2. Figure 6-7 shows the distribution of the spectrum density of RDF when the input is defined as Eq. 6-7. In this pass region characteristic, 130 and 170 Hz fluctuation also can pass the RDF to some extent, which should be regarded as signal noises. Thus, the window function should be installed to regulate the pass region more strictly. Furthermore, the RDF can evaluate the fracture-induced fluctuation separately from the low-frequency component due to modeling error of friction shown in Fig. 5-4 in Chapter 5, because the RDF extracts only a special frequency component.

As a conclusion of the time-domain simulation, it is obvious that the RDF certainly provides band-pass effect and clock-wise signal pass effect at the same time. In the next section, the performance of the RDF is experimentally evaluated through several drilling tests.

6.4 Drilling Test

6.4.1 Conditions

The proposed method detects a drill fracture by monitoring the integrated information of the estimated disturbance force in X and Y directions. The cutting

condition is summarized in Table 6-1. Although the drilling experiments are conducted basically with spindle rotation of 9000 min^{-1}, spindle rotations of 8000 and 10000 min^{-1} are also used only to confirm the adequacy of the proposed concept of drill fracture detection.

The drilling test is intermittently performed along with X axis with 16 mm intervals as shown in Fig. 6-8. Carbide drills with 6 mm diameter are used in the experiment, and one new drill and nine types of fractured drills having different corner edge fractures are prepared. The picture and the fractured area are shown in Fig. 6-9, where two values are shown for drills with fractures on both teeth.

Table 6-1   Drilling condition for fracture detection.

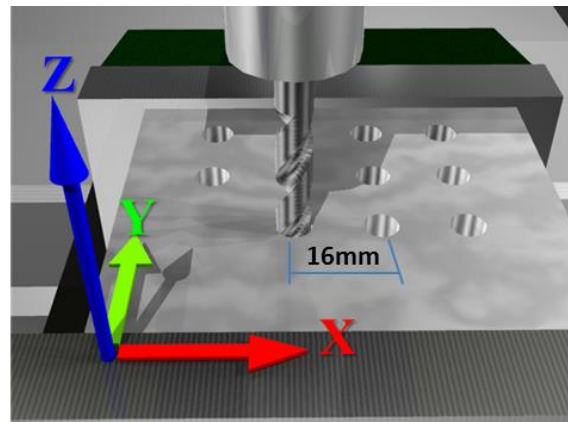|	
Drill diameter	6 mm
Rotational speed of the spindle [min^{-1}]	9000, (10000, 8000)
Feed rate [mm/min]	1800
Shape of holes	20mm blind hole
Workpiece	Aluminum alloy (A2017)
Cutting fluid	Soluble cutting oil

Fig. 6-8   Tool path of the drilling test.

Fig. 6-9   Appearances of fractured drills.

6.4.2 Experimental Result

First of all, continuous wavelet transform (CWT) is applied as a conventional analysis method to the estimated disturbance force in X and Y direction respectively to confirm the possibility to detect a drill fracture. The analyzed result with CWT is compared with that with RDF later.

Figure 6-10 shows the examples of CWT analysis results on the estimated disturbance force in y axis in drilling with a new drill and one of the fractured drills. The spectrum density clearly becomes large in drilling using the fractured drill, though no remarkable change is observed in drilling using the non-fracture drill.

Furthermore, the relation between the fractured area and the spectrum density is investigated by comparing three different fracture drills as shown in Fig. 6-11. The spectrum density gets larger with larger fractured area, though it is not a simple linear relation. This result is adequate because larger fracture leads to the more unbalanced cutting forces on the tool edges and the x and y components in the resultant force also get larger.

In order to investigate the adequacy of the proposed concept for drill fracture detection, drilling tests with other rotational speeds 10000 and 8000
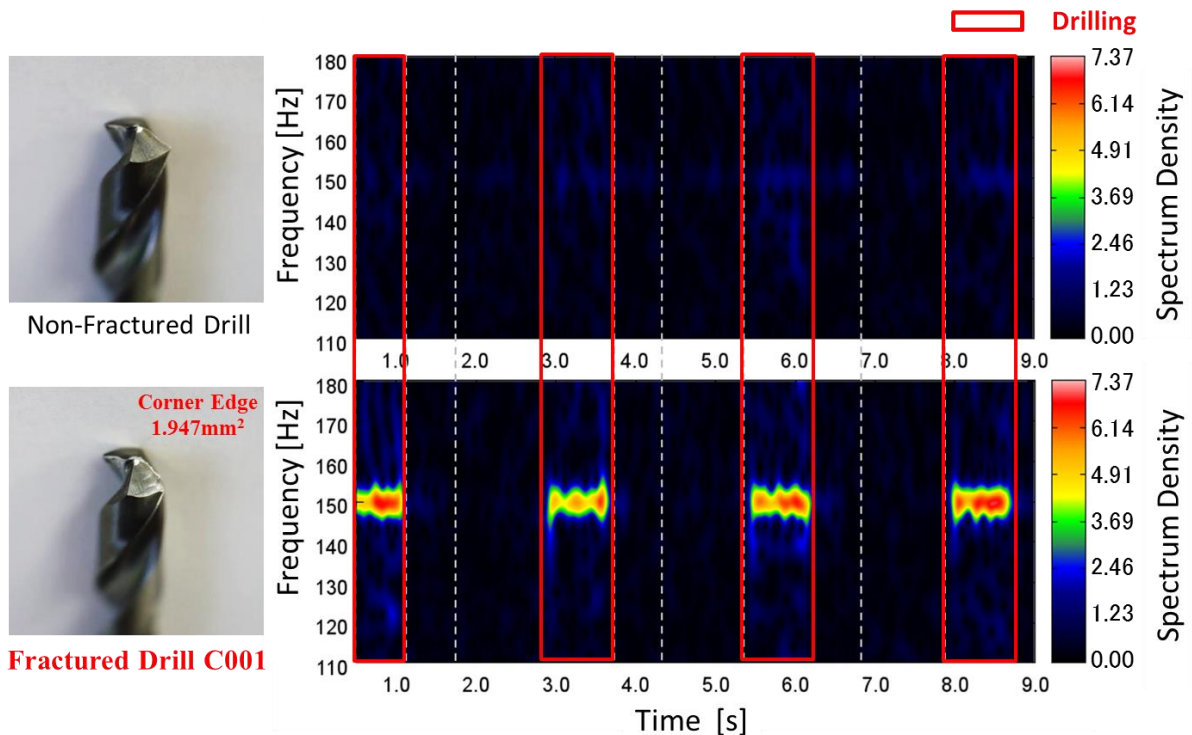

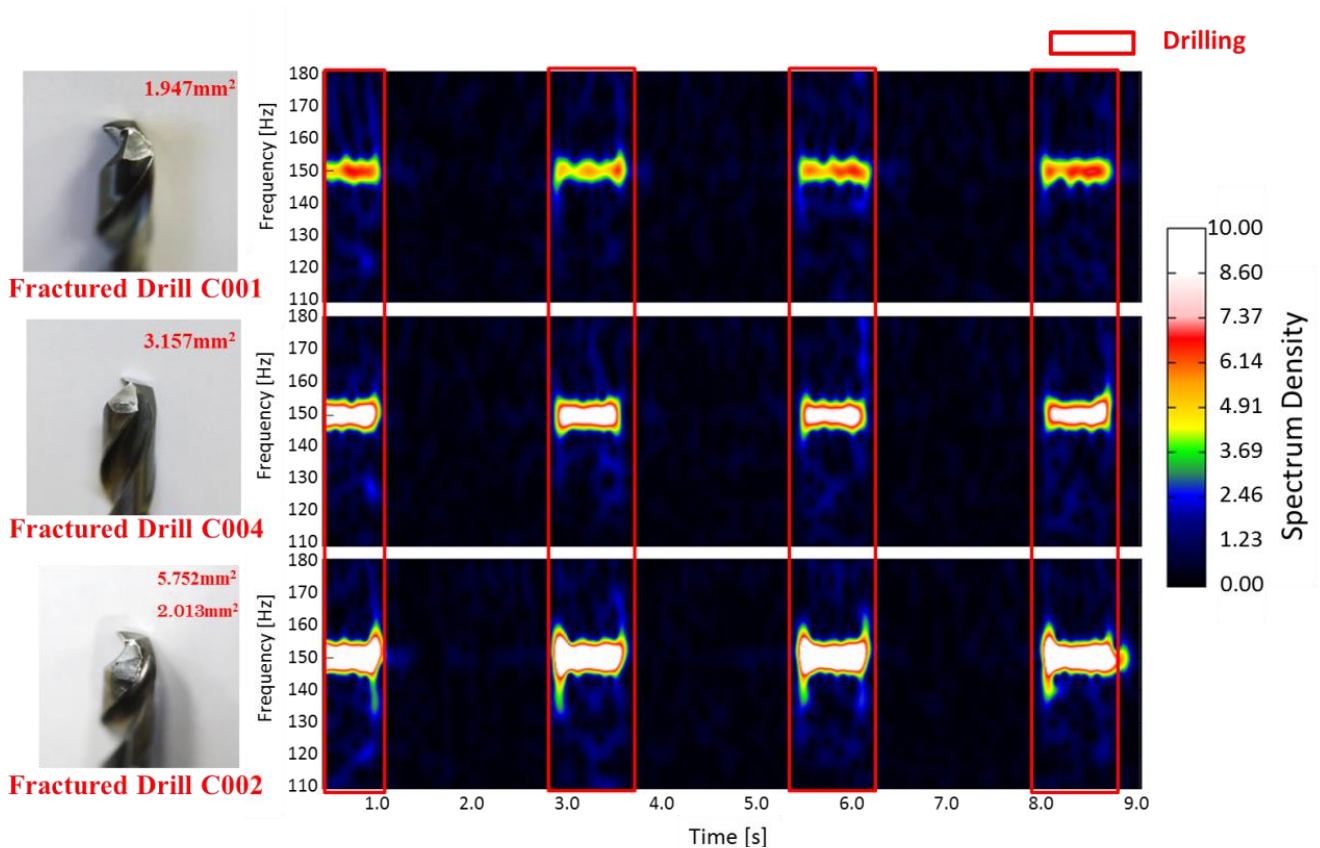Fig. 6-10   CWT analysis results of Y-axis disturbance force.

Fig. 6-11 CWT analysis results of 3 different fractured drills.

min^{-1} are also conducted and the CWT analysis results are shown in Fig. 6-12. The large spectrum density is clearly observed at 167 Hz when the rotational speed is 10000 min^{-1} (=167 Hz) and at 133 Hz when the rotational speed is 8000 min^{-1} (= 133 Hz). This result also indicates that the fracture-induced variation in the disturbance force certainly depends on the spindle rotation as explained in the concept for the proposed drill fracture detection.

As a next step, the analysis results with RDF are discussed. The simulation result has shown that the RDF output has two components and they draw a circular orbit. The each component is not suitable to evaluate stably because of the drastic fluctuation. Therefore, the geometric mean of both RDF output components (i.e., the radius of the circular orbit) is utilized as spectrum density.
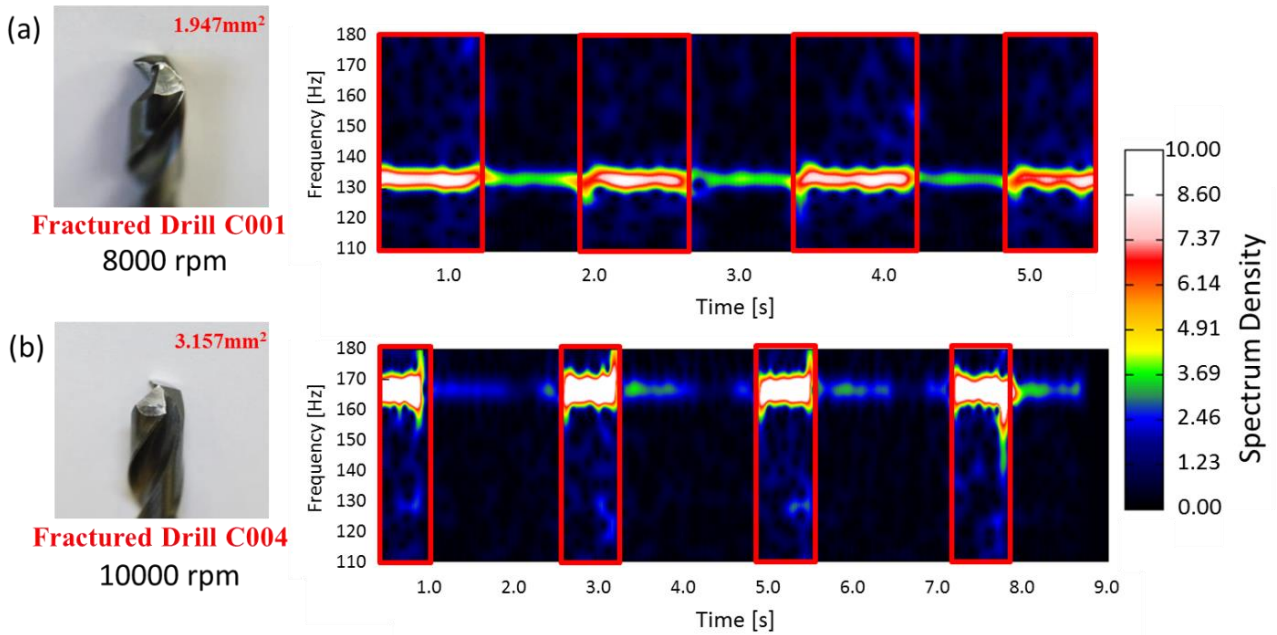
Fig. 6-12   CWT analysis results in drilling with other rotational speeds
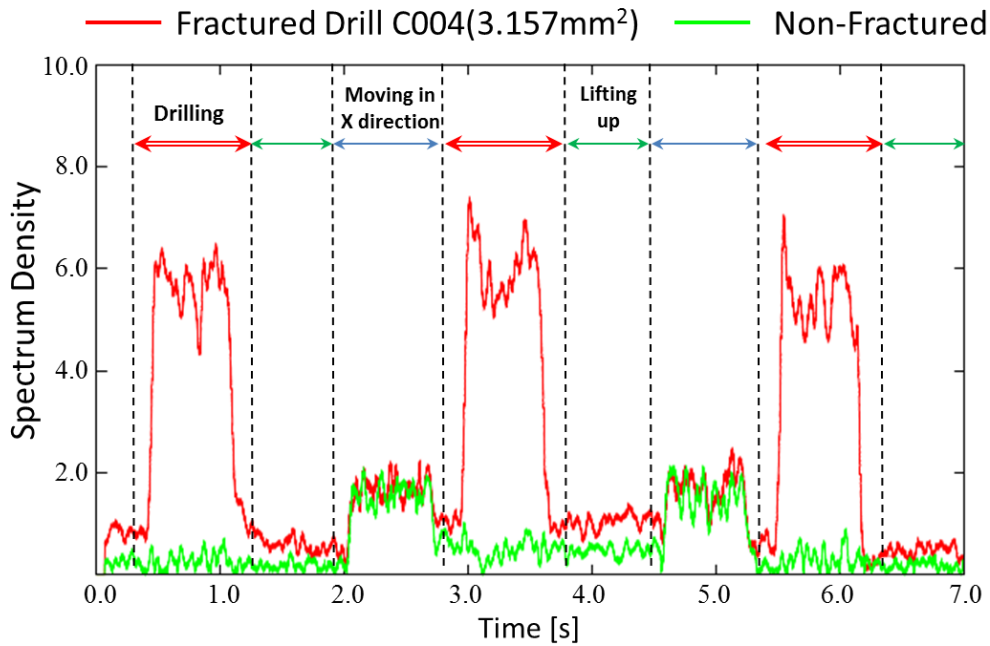(a) 8000 rpm (b) 10000 rpm.

Fig. 6-13   The frequency analysis result with an 150 Hz clockwise pass RDF.

Figure 6-13 shows the 500th order clock-wise-type RDF analysis result on a drilling test with a fractured drill. The spectrum density of RDF also becomes large in drilling using the fractured drill, and this spectrum density variation is not observed in drilling with the non-fractured drill. Therefore, the drill fracture detection also can be performed with the RDF-based analysis.
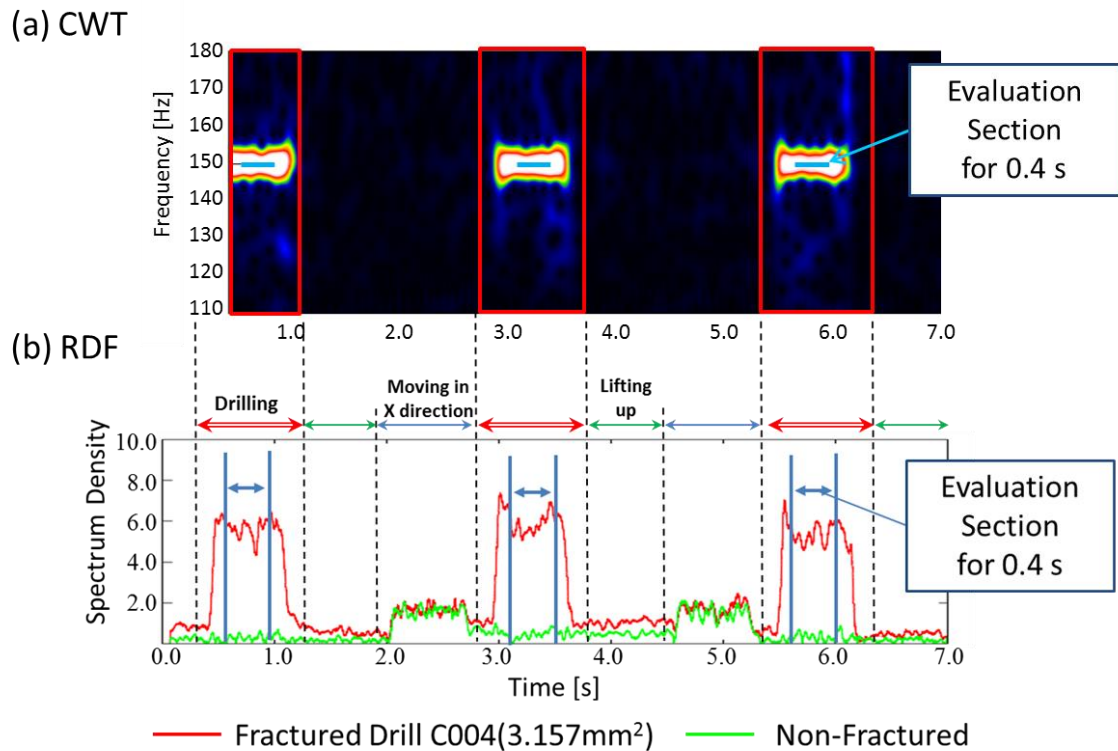
124

(a) CWT

(b) RDF

Fig. 6-14   The evaluation sections of spectrum density: (a) CWT, (b)RDF.

In the light of calculation load, there is no remarkable difference between the CWT and the RDF assuming that the number of analyzed samples is more or less the same. The detection delay is also similar because the both analysis methods introduce same window function. Therefore, the robustness of both methods should be discussed in order to distinguish the fractured tool without mistakes. The detection accuracy can be evaluated by comparing how they can emphasize the difference between the non-fractured drill and the fractured drills.

To evaluate the detection accuracy quantitatively, 0.4 s evaluation sections are set to the drilling terms as shown in Fig. 6-14 and the average value of spectrum density is calculated. The CWT is only performed for 150 Hz component.

By repeating the drilling tests 20 times with the non-fractured drill and the nine fractured drills respectively, the relation between the fractured area and the spectrum density is obtained with CWT (Fig. 6-15) and RDF (Fig. 6-16), where the spectrum density of the CWT here is defined as a geometric mean value of both spectrum densities of x and y disturbance force. The blue square plot shows the result of each drilling test and the yellow circular plot shows the average value of 20 drilling tests.
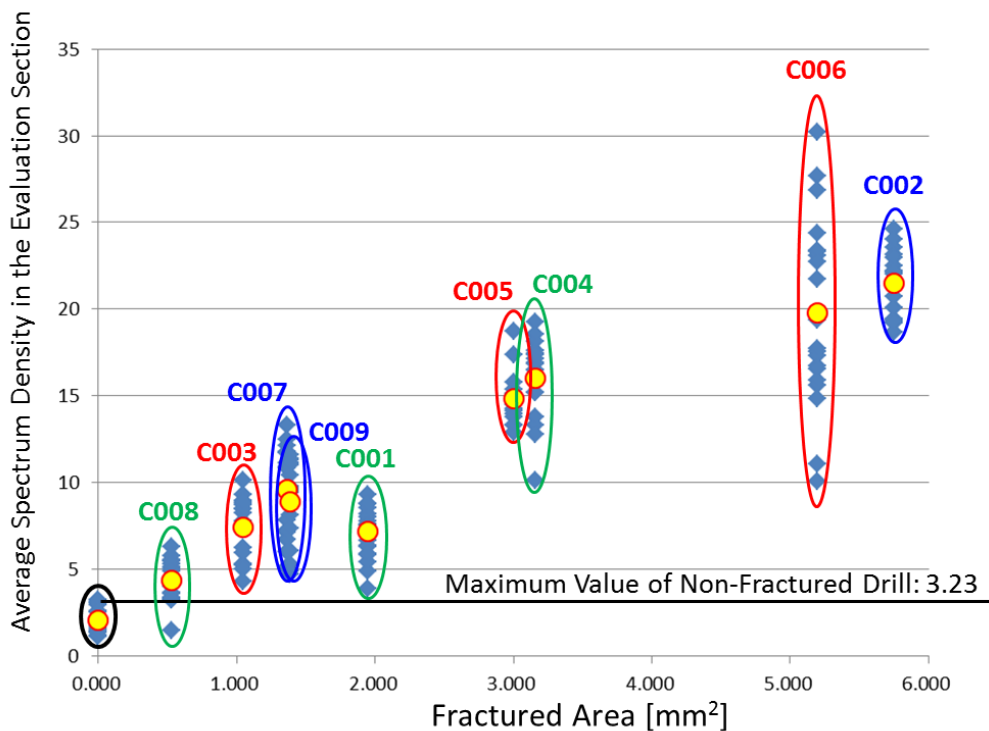
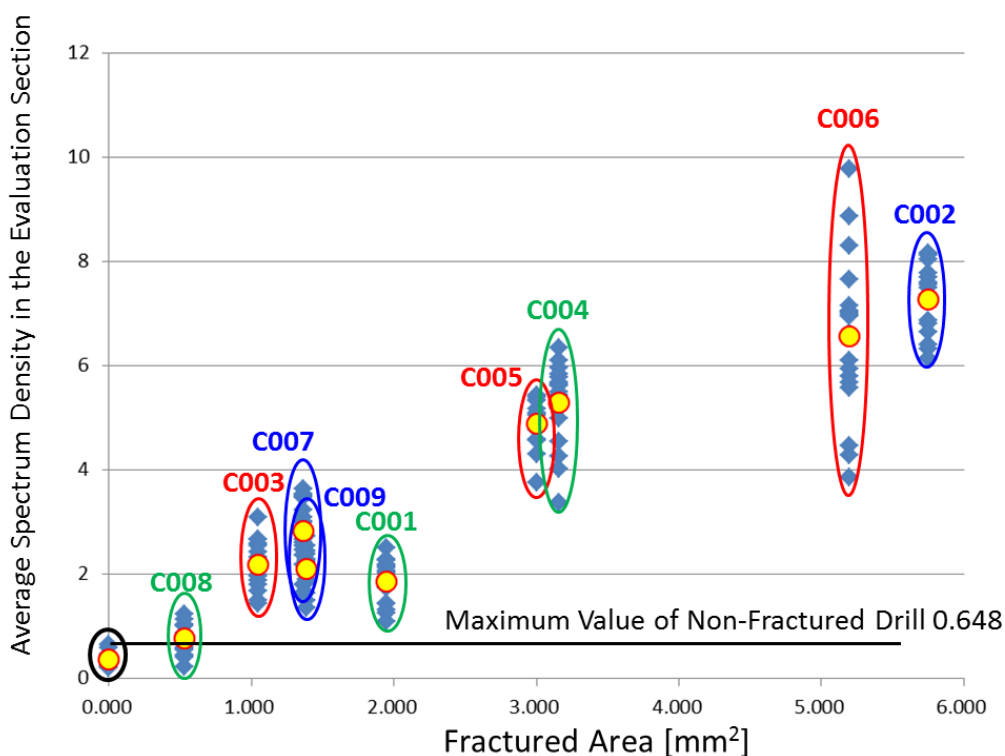Fig. 6-15   Average spectrum density with CWT.

Fig. 6-16   Average spectrum density with RDF.

126

Both Figs. 6-15 and 6-16 show that the nine fractured drills induce higher spectrum density than the non-fractured drill. These results sufficiently indicate the versatility of the observer-based drill fracture detection. Then, the detection accuracy should be compared between the CWT and the RDF more quantitatively. Although the resultant cutting force on a non-fractured drill does not have x and y components theoretically, low spectrum density is actually observed in the analysis results on the drilling using the non-fractured drill because of the signal noise. The noise has to be suppressed enough with a low-pass filter in order to enhance the detection accuracy. However, the cutoff frequency of the low-pass filter cannot get down lower than the target frequency (spindle rotational frequency). On the other hand, the RDF reduces the noise from a viewpoint of rotating direction, without reducing the cutoff frequency. Because the signal noise expanded by the differential process does not move in a special direction, the fracture-included fluctuation can be extracted as the clock-wise component more clearly.

Therefore, the spectrum density due to drilling with the non-fractured drill would be smaller by applying the RDF, but this change is difficult to confirm Figs. 6-15 and 6-16. To compare the detection accuracy, (1) ratio of average values and (2) ratio between the minimum spectrum density of fractured drill and the maximum spectrum density of non-fractured drill (Fig. 6-17) are required. These evaluation values are important factor to emphasize the difference between
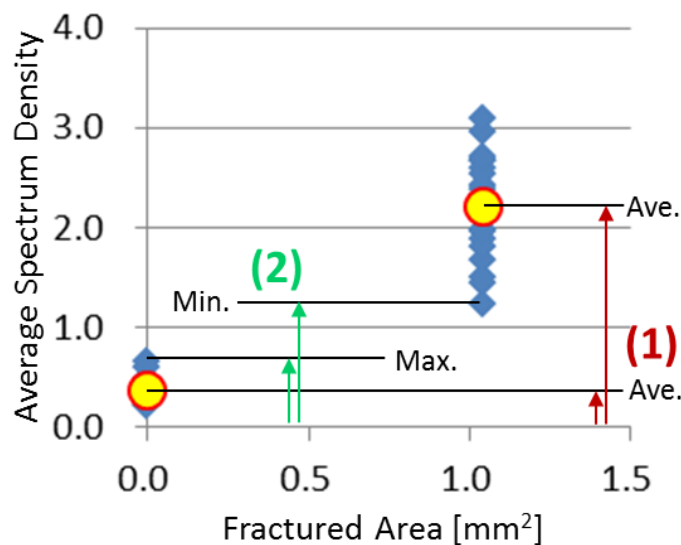

Fig. 6-17   Evaluation of difference between fractured and non-fractured drill.
(1) ratio of Average. (2) ratio between fractured min. and non-fractured max.

fractured drills and non-fractured drills. The analysis result is summarized in Table 6-2.

Table 6-2   Evaluation result of Fig. 6-17 (1) and (2).

Sample	Fractured area [mm²]	(1)		(2)	
		CWT	RDF	CWT	RDF
C001	1.947	3.480	5.174	1.213	1.692
C002	5.752	10.414	20.302	5.782	9.459
C003	1.046	3.591	6.076	1.339	2.206
C004	3.157	7.772	14.781	3.142	5.196
C005	3.002	7.180	13.660	3.994	5.809
C006	5.199	9.597	18.310	3.125	5.953
C007	1.362	4.640	7.903	1.589	2.516
C008	0.526	2.113	2.136	0.459	0.347
C009	1.386	4.317	5.896	1.468	2.081

In Table 6-2, the columns are filled with green when the RDF shows a larger value than CWT and filled with red in the opposite case. Excepting the sample C008, the evaluation values (1) and (2) of RDF become two times as large as the CWT results. This is because the spectrum density of drilling using the non-fractured drill gets lower by the RDF.

In case of the sample C008, the evaluation value (2) of the RDF is smaller than the CWT. However, the outer edge is mainly fractured and its area is small as 0.526 mm² on the sample C008, and the cutting edge is almost left as shown in Fig. 6-18. Furthermore, the snuggling chip as explained in chapter 1.2.3 does not appear during drilling with the sample C008. As a result, the sample C008 can be regarded as a normal drill which is available for usual drilling.

As a conclusion of the drill fracture detection, the proposed method certainly can detect a small drill fracture on the tool edge without any additional sensors. Furthermore, the experimental results show that a new signal processing method named rotational digital filter can enhance the accuracy of the drill fracture detection.
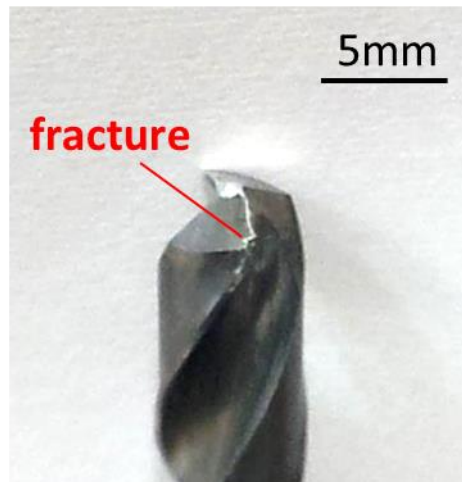
Fig. 6-18   Appearance of the fractured drill sample C008.

6.5 Summary

An observer-based drill fracture detection method is proposed and evaluated through the drilling experiments in this chapter. Furthermore, a novel signal processing method named "rotational digital filter" is proposed to enhance the detection accuracy, which has a unique characteristic to distinguish the clock-wise component and the counter-clock-wise component in a signal moving on a two dimensional plane. The archived results are summarized as follows.

1. The experimental results with nine fractured drills and one non-fractured drill indicate that the fracture-induced fluctuation in the x and y components of resultant cutting force is certainly detectable by applying the disturbance observer to the ballscrew-driven stage control system and analyzing the estimated disturbance information in frequency domain.

2. Rotational digital filter is invented to enhance the detection accuracy. Its characteristics are investigated with time-domain simulations, and the simulation results clearly shows that the rotational digital filter realizes the band-pass filtering effect and the clock-wise signal pass effect simultaneously.

3. By applying the rotational digital filter to the estimated disturbance force in the X and Y directions, the fracture-induced variation can be captured from the servo information more clearly. The experimental results show that the RDF-based fracture detection has higher accuracy than a conventional frequency analysis method. The proposed detection method has enough accuracy to detect a drill fracture as small as 1 mm^2 under the cutting condition given in this study.

7 Chatter Detection System

7.1 Introduction

In order to ensure a stable machining, many researchers focus on mechanism of chatter vibration and propose various stability prediction methods by constructing precise cutting models [33-39]. Although these approaches are theoretically reliable, the stability prediction result often does not agree with real process because the required parameters for stability prediction like modal parameters are difficult to identify accurately. As a countermeasure of unexpected chatter, automatic chatter detection is strongly demanded to monitor the process at all times.

From practical viewpoint, this research presents sensorless approaches for various problems in process and evaluates the applicability of disturbance observer to realtime process monitoring. In this chapter, observer-based chatter detection is developed by analyzing the estimated cutting torque in milling. Performance of the proposed signal processing method named "integration of moving variance and moving Fourier transform algorithm (MV+MFT)" is experimentally evaluated, which is specialized for realtime chatter detection.

7.2 Performance Evaluation of Moving Variance and Moving Fourier Transform

Frequency analysis is an efficient approach to evaluate chatter-induced fluctuation separately from the other components like modeling error of friction. In order to perform a realtime process monitoring, an introduced signal processing method has to be suitable for realtime usage. Regarding the realtime characteristic, fast Fourier transform (FFT) is widely used as a low computation-load frequency analysis method. However, the number of computation in FFT is not so small to perform in realtime as explained in Section 2.3.3. This section firstly confirms that FFT algorithm is actually not suitable to perform in realtime by measuring the computational time.

Computer technology is progressing exponentially and recent high-spec

```
#include    <time.h>

hrtime_t start, end;

int main(void){
                    ⋮

        start = gethrtime(); //Start time

        /*Process*/

        end = gethrtime();//End time

                    ⋮

        rtl_printf("%d ns is elapsed¥n", (unsigned)(end - start) );

        return 0;
}
```

Fig. 7-1   An example of C language program to measure the processing time.

computer can perform enormous number of computation in a slightly short time. However, it is a fundamental rule that longer computational time is required for larger number of computation. In order to perform an algorithm in realtime, the computation time must be well considered because the processes have to be strictly scheduled along with the time table. This research preliminarily performs a computational time measurement to evaluate the realtime characteristic of the algorithm as following procedures.

The calculation-time measurement is carried out by applying RT-Linux module to a linux operating system in order to enhance the realtime characteristic of computer. To measure the computational time of algorithm, a function named "gethrtime.3" is introduced, which returns an integer-type value of the time in nanoseconds since the system bootup. Therefore, the computational time can be measured by applying gethrtime in front and just after the process and requiring the difference of them as shown in Fig. 7-1. The performance of the computer used in this experiment is as shown in Table 7-1.

Table 7-1   Performance of computer for computational time measurement.

PC	EPSON MT-7500
OS	Red hat ver. 9.0 (rtlinux-3.2-pre3 patch applied)
CPU	Intel Pentium 4 HT 3.00GHz
Memory device	512MB

By replacing the calculated part (/*Process*/) in Fig. 7-1, to various processes, the calculation time of multiplication and twiddle factor are measured as summarized in Table 7-2.

Table 7-2　100000 times measurement results of computational time.

/*Process*/	Maximum computational time [ns]	Average computational time[ns]	Remarks column
/*blank*/	64	4	Nothing to process
for(i=0;i<10000;i++){ }	13,536	5,120	The int-type addition (increment) is repeated 10000 times.
for(i=0;i<1000;i++){ }	1,472	550	The int-type addition (increment) is repeated 1000 times.

for(i=0;i<10000;i++){
c[i]=a[i]*b[i];
}
	42,528	25,103	10000 times double-type multiplications. Random values from -1.0 to 1.0 are substituted to a[i] and b[i].

for(i=0;i<1000;i++){
c[i]=sin(2*pi*i/N);
}
	82,720	78,046	1000 times twiddle factor calculations.

The above measurement result shows that only 25 μs are required for even 10000 times multiplications, although multiplication generally requires longer computation time than addition in binary number system. Because 10240 times actual multiplications are required for FFT of $N = 512(= 2^9)$ and the sampling time is set to 125 μs in the machine tools used in this research, the FFT algorithm for less than 512 samples has a possibility to finish within one sampling time. However, the calculation time of twiddle factor is 30 times as long as that of double-type multiplication. The twiddle factor calculation is also repeated 10240 times in the FFT algorithm, thus, the FFT can be no longer performed in one sampling time.

However, the calculation time of FFT algorithm can be reduced more with some improvements. Except parallel calculation with GPU or computer cluster system, following improvements are considerable to reduce the computation time.

133

① Conducting the twiddle factor calculation in the main function and storing its result in ensured memory sections in advance.

② Employing float-type variables instead of the double-type.

③ Reducing the number of multiplication including for int-type variables.

Figure 7-2 shows the competition between a conventional FFT algorithm and the improved FFT algorithm, where both codes are written in c language. In the improved FFT algorithm, the twiddle factor calculation is conducted and its result is stored in a global variable array preliminarily in order to eliminate the twiddle factor calculations from the FFT function. Although float-type (32bit) variable is used instead of double-type (64bit) to reduce the computation load, the calculation accuracy reduction due to quantum error expansion should be taken care when analyzing an actual data.

Normal FFT Algorithm

```c
void FFT(int n, double theta, double *ar, double *ai,
double *tmpr, double *tmpi){

int nh, j;
double xr, xi, wr, wi;

if(n <= 1)return;
nh = n / 2;

for(j = 0; j < nh; j++){

tmpr[j] = ar[j] + ar[nh + j];
tmpi[j] = ai[j] + ai[nh + j];
xr = ar[j] - ar[nh + j];
xi = ai[j] - ai[nh + j];
wr = cos(theta * j);
wi = sin(theta * j);
tmpr[nh + j] = xr * wr - xi * wi;
tmpi[nh + j] = xi * wr + xr * wi;
}

FFT(nh, 2 * theta, tmpr, tmpi, ar, ai);
FFT(nh, 2 * theta, &tmpr[nh], &tmpi[nh], ar, ai);

for (j = 0; j < nh; j++) {
    ar[2 * j] = tmpr[j];
    ai[2 * j] = tmpi[j];
    ar[2 * j + 1] = tmpr[nh + j];
    ai[2 * j + 1] = tmpi[nh + j];
  }
}
```

Improved FFT Algorithm

Main Function
```c
for(i=0; i<N; i++){
    fft_sin[i] = sin(2 * pi * (float)i / N);
    fft_cos[i] = cos(2 * pi * (float)i / N);
  }
```

```c
float fft_sin[N];
float fft_cos[N];

void FFT(int n, int theta, float *ar, float *ai, float *tmpr,
float *tmpi){

 int nh, i, j, k;
 float xr, xi;

 if(n<=1)return;
 nh = n / 2;

 for(i=0, k=0; i<nh; i++, k+=theta){

  tmpr[i] = ar[i] + ar[i + nh];
  tmpi[i] = ai[i] + ai[i + nh];
  xr = ar[i] - ar[i + nh];
  xi = ai[i] - ai[i + nh];
  tmpr[nh + i] = xr * fft_cos[k] - xi * fft_sin[k];
  tmpi[nh + i] = xi * fft_cos[k] + xr * fft_sin[k];
 }

 FFT(nh, 2 * theta, tmpr, tmpi, ar, ai);
 FFT(nh, 2 * theta, &tmpr[nh], &tmpi[nh], ar, ai);

 for(i =0,j=0; i<nh; i+=2,j++){
  ar[i] = tmpr[j];
  ai[i] = tmpi[j];
  ar[i+1] = tmpr[nh + j];
  ai[i+1] = tmpi[nh + j];
 }
}
```
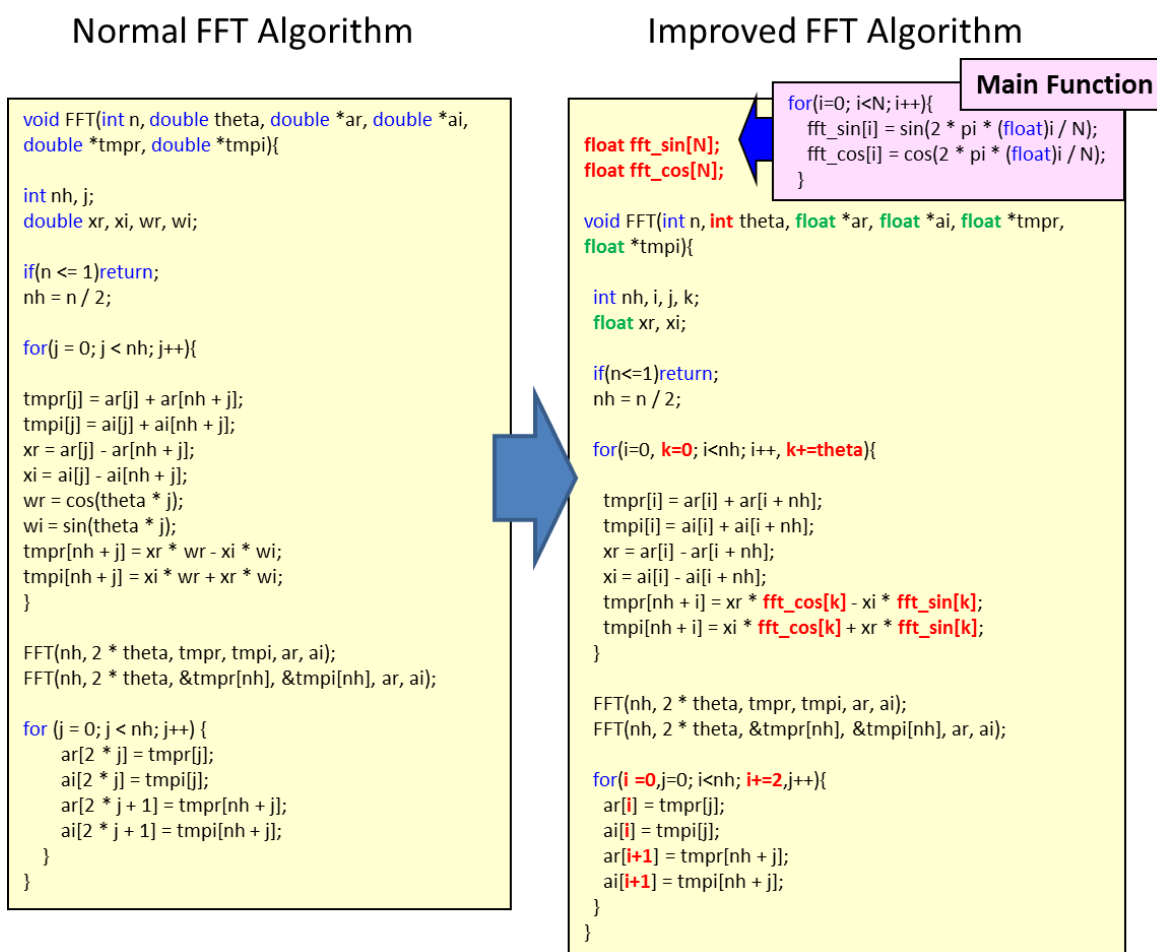
Fig. 7-2   Competition between usual FFT and improved FFT algorithms.

The computational time of the improved FFT algorithm is summarized in Table 7-3, where each column is filled with green when the time is less than 125 μs and red in opposite case. Even in case of the improved algorithm, the FFT cannot be performed within 125 μs when the window width is wider than 512 samples for float-type variables and 256 samples for double-type variables.

Table 7-3   100000 times measurement results of computational time of FFT.

Number of samples	Float type (32bit)		Double type (64bit)	
	Maximum processing time [ns]	Average processing time [ns]	Maximum processing time [ns]	Average processing time [ns]
$128(=2^7)$	18,304	13,657	31,232	26,515
$256(=2^8)$	35,040	29,912	64,928	60,123
$512(=2^9)$	69,248	64,541	157,760	133,152
$1024(=2^{10})$	143,936	139,097	648,672	605,522
$2048(=2^{11})$	311,648	301,582	769,568	679,287

The improvement points may still exist excepting from ① to ③. However, the FFT, which is an $O(N \log N)$ algorithm, basically requires larger number of computation to expand the window wider. To make matters worse, the width of window has to be a bit number to use the FFT algorithm. The window width option is strictly limited and the frequency resolution cannot be modified arbitrarily.

In contrast, MV+MFT is an $O(1)$ algorithm and reduces the computation number to analyze a signal in time-frequency domain. The computational time of MV+MFT is measured and summarized as shown in Table 7-4, in which columns are colored in the same manner with Table 7-3.

Table 7-4   100000 times measurement results of computational time of MV+MFT.

Number of samples	Double type (64bit)	
	Maximum processing time [ns]	Average processing time [ns]
$128(=2^7)$	960	286
$256(=2^8)$	1,120	283
$512(=2^9)$	1,184	284
$1024(=2^{10})$	1,088	284
$2048(=2^{11})$	1,056	285
500 (frequency resolution: 16 Hz)	1,472	311
1000(frequency resolution: 8 Hz)	1,152	312
2000(frequency resolution: 4 Hz)	1,152	313
4000 (frequency resolution: 2 Hz)	1,600	313
8000 (frequency resolution: 1 Hz)	1,152	319
16000 (frequency resolution: 0.5 Hz)	1,280	312

In the upper half of Table 7-4, the window widths are set to bit numbers to correspond to the measurement results in FFT calculation. The computational time of MV+MFT are decisively small compared with that of FFT, even using double-type variables. Additionally, the measurement results indicate that the proposed MV+MFT certainly an $O(1)$ algorithm because the computation times are almost same even if the window widths are different.

Furthermore, the window width can be modified arbitrarily because it does not have to be a bit number and there is no limitation due to computational load. In the lower half of Table 7-4 shows the computational time measurements when the window widths are not a bit number. Compared with the result with bit number window widths, the average computation time gets to be about 25 ns longer when the window width is not a bit number. Although this would be because the compiling process is different between for bit and non-bit numbers, it is a negligibly-small difference which does not have any influences on the realtime characteristic of MV+MFT.

As a conclusion, the proposed MV+MFT is certainly a super-low computation load algorithm and solves trade-off relation between the increase in number of computation and the frequency resolution enhancement. Therefore, when the

MV+MFT algorithm is employed, we can just focus on the trade-off relation between the frequency resolution and the time response, which is so-called uncertainty principle in Fourier transform.

As a remaining problem, the chatter detection performance of MV+MFT also will be experimentally evaluated in the later section.

7.3 Prediction of Chatter Frequency

Chatter vibration generally has a frequency close to resonance frequency. Therefore, in order to roughly find a frequency band including the chatter frequency, a modal analysis test should be performed on the tool to identify the resonance frequency.

The milling tests are conducted with two kinds of machine tools as explained in Chapter 3: TC-S2C and S500X1. Figure 7-3 shows the appearance of hammering tests in the X and Y directions on a tool in the machine tool TC-S2C.

The instruments used in the impulse-response tests are summarized in Fig. 7-4 and Table 7-5. By calculating a ratio between the applied force and the acceleration for each frequency, a frequency response function (FRF) of the tool and the resonance frequencies can be identified.

Table 7-5   Instruments of the impulse response test.

Impulse hammer	Dytran Instruments Inc. 58500B4
Acceleration sensor	Dytran Instruments Inc. 3225F1
DA converter	National Instruments Co. NIUSB-9263
Software	MAL Inc. CutPRO

The obtained FRF of TC-S2C in X direction is shown in Fig. 7-5, and that in Y direction is shown in Fig. 7-6 respectively. As a result, the tool would have resonance frequencies of 818, 1653, 1696 and 1715 Hz in X direction, and 849, 1534 and 1730 Hz in Y direction. The chatter may have a close frequency of these peak frequencies in TC-S2C.

The FRFs of S500X1 in X and Y directions are shown in Figs. 7-7 and 7-8 respectively. The resonance frequencies are mainly 822 and 1841 Hz in X direction and 823, 1392 and 1692 Hz in Y direction. Although the chatter vibration would occur around these resonance frequencies theoretically, the
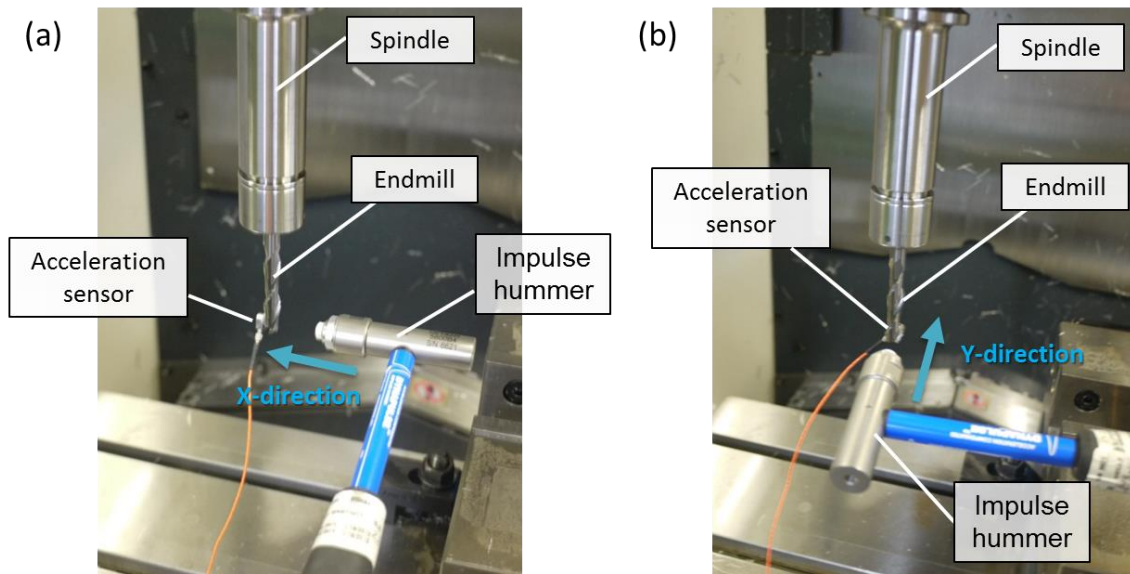
Fig. 7-3　Appearance of impulse response tests for a tool in TC-S2C:
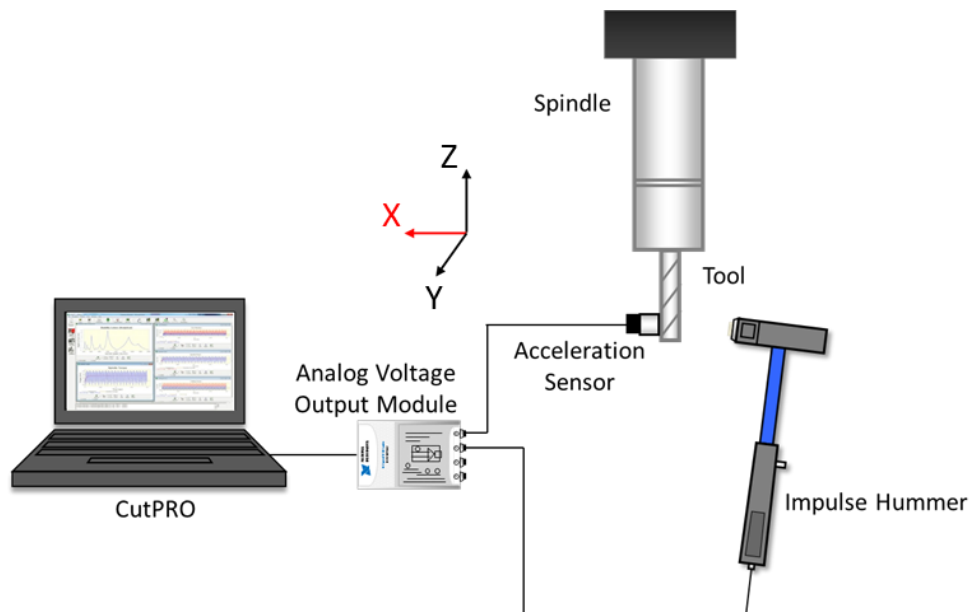(a) X direction (b) Y direction.

Fig. 7-4　Schematic of the system of the impulse-response test.

resonance frequency has a possibility to change according to the spindle rotation because of heat generation in bearings, centrifugal forces on rotation elements, lubrication oil films at contact points and so on [53]. Furthermore, in Figs. from 7-5 to 7-8, several small peaks can be confirmed from 1000 to 2000 Hz. These resonance frequencies also have a possibility to be a cause of chatter.

As a conclusion, chatter vibration may occur at frequency in the range from 700 to 1000 Hz and from 1300 to 2000 Hz in both machine tools.
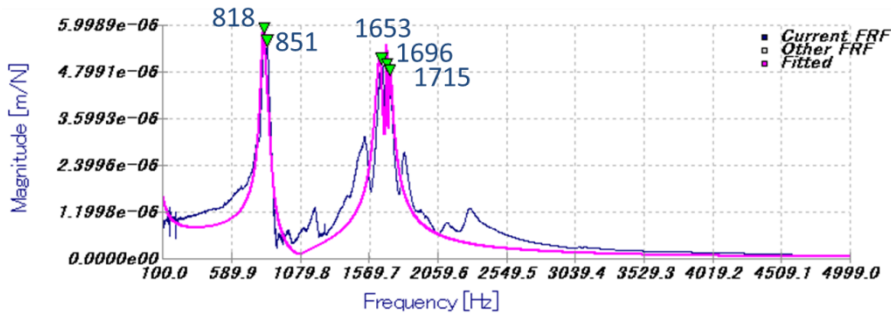
Fig. 7-5   FRF analysis result in X direction of TC-S2C.
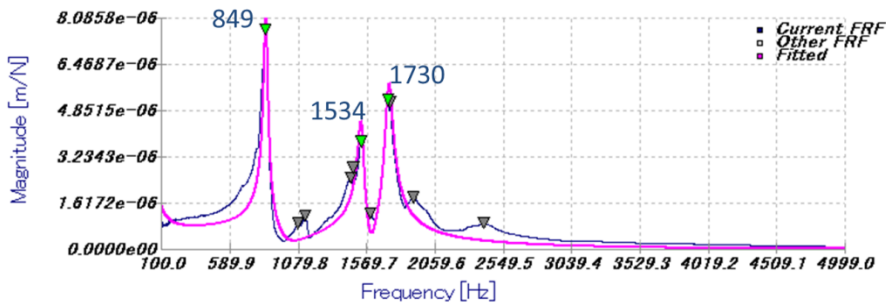
Fig. 7-6   FRF analysis result in Y direction of TC-S2C.
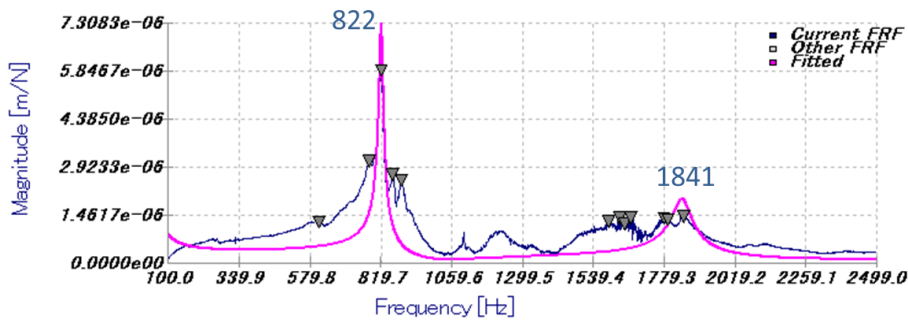
Fig. 7-7   FRF analysis result in X direction of S500X1.
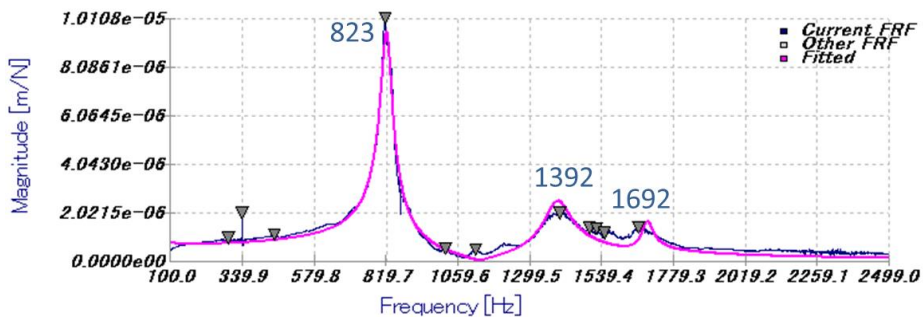
Fig. 7-8   The analysis result in Y direction of S500X1.

7.4 Chatter Detection in Side Milling

Side milling tests with square endmills with 10 mm diameter are performed.

7.4.1 Conditions of Chatter Detection Test

Chatter stability depends on the spindle rotation and the axial depth of cut. The number of experiments gets large beyond necessity if milling tests are conducted for each combination of spindle rotation and axial depth of cut. Because the spindle rotation is constant in usual milling process, the axial depth of cut is changed in order to change the chatter stability in one milling test to reduce the number of experiments. That is why a triangle-shaped workpiece is used as shown in Fig. 7-9. The cutting conditions are summarized in Table 7-5.

The spindle rotation changes from 5000 to 9000 min^{-1} in TC-S2C and from 7000 to 15000 min^{-1} in S500X1 with 100min^{-1} interval, i.e., 41 kinds of side milling

Table 7-5　Cutting condition.

Tool	10mm square endmill
Number of Tooth	2
Rotational Speed [min^{-1}]	5000 – 9000 (TC-S2C) 7000 – 16000 (S500X1)
Feed Rate [mm/tooth]	0.0875
Type of Cut	Down milling
Workpiece	Aluminum alloy (A2017)
Radial Depth of Cut [mm]	0.3
Axial Depth of Cut [mm]	5 – 25
Cutting Oil	Dry cutting
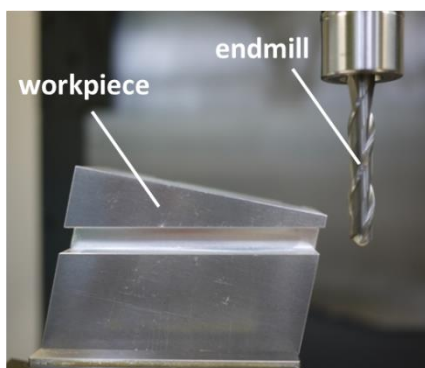
Fig. 7-9　Triangle-shaped workpiece.

Fig. 7-10　Surface roughness meter.

tests are conducted in TC-S2C and 81 kinds of side milling tests are conducted in S500X1. The machining results are evaluated by measuring the surface roughness with a stylus-type surface roughness tester (SJ-400, Mitsutoyo Corporation) as shown in Fig. 7-10.

7.4.2 Experimental Result

As an evaluation criterion to confirm the adequacy of MV+MFT analysis results, the arithmetic average roughness (Ra) is measured. Although the Ra is derived as one value for one evaluation section usually, 4 mm window is employed and the roughness of 103 mm section on the machined surface is evaluated by sliding the 4 mm window and continuously requiring the Ra.

First of all, the experimental results with spindle rotations of 6400 min^{-1} and 7700min^{-1} in TC-S2C are explained as examples of side milling tests on triangle-shaped workpiece.

Figure 7-11 shows the experimental result with the spindle rotation of 6400 min^{-1}. Note that the picture of workpiece surface is reversed horizontally, corresponding to the time axis. Because the machined surface drastically waves and the Ra value gets large just after the milling starts, it is clear that the chatter vibration generates from the beginning of milling. Furthermore, the pattern of the chatter mark changes and the Ra value gets larger at near the end of milling. In the analysis result of the estimated disturbance torque with the MV+MFT, the chatter component gets large during milling, although the forced vibration component hardly varies. The drastic generation of chatter components from 5.3 s to 6.0 s has high coherence with the Ra variation and also indicates that the chatter vibration gets larger at the end of milling.

To confirm the adequacy of the MV+MFT analysis result, Sliding FFT (N=512) analysis is also performed offline, which slides the window and draws the power spectrum density for each frequency with color gradation (Fig. 7-12) in order to capture the time-dependent variation of frequency components. As a result it can be said that the forced vibration certainly does not generate in this milling test because the spindle rotational frequency is 106.7 Hz (=6400min^{-1}) and each frequency peak is not a harmonic of the spindle rotational frequency.

Then, the side milling test results with the spindle rotation of 7700 min^{-1} are explained here. Focusing on the Ra variation and the surface appearance,
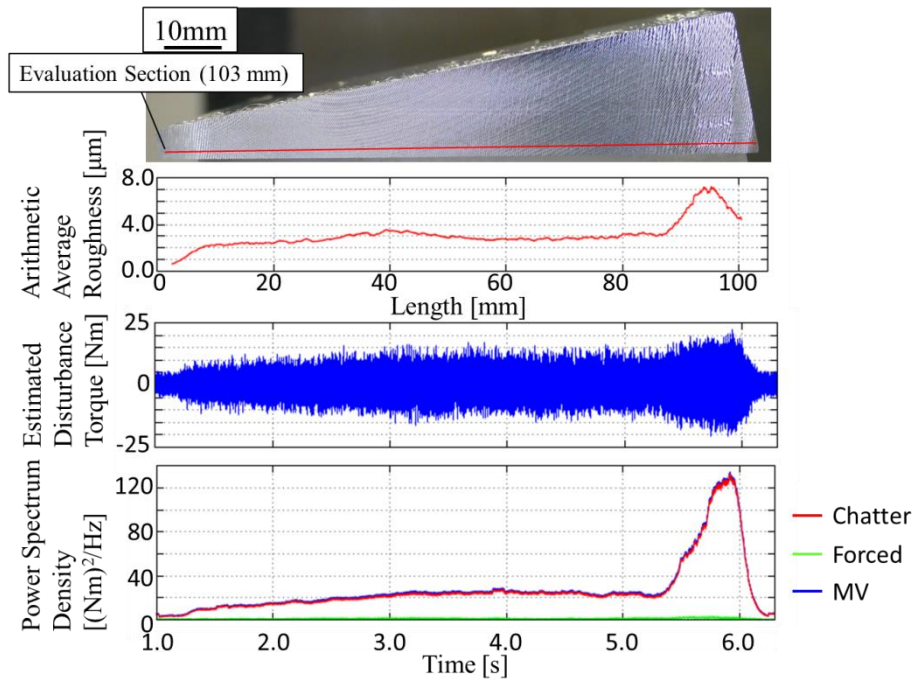
141

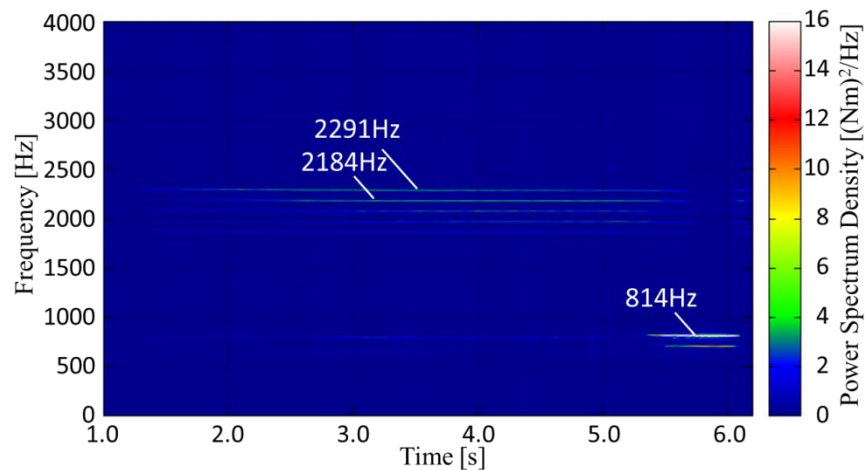Fig. 7-11　MV+MFT analysis result in 6400 min⁻¹ in TC-S2C.

Fig. 7-12　Short-time Fourier transform analysis in 6400 min⁻¹ in TC-S2C.

the chatter would occur from a middle point of the workpiece in milling. On the other hand, in the MV+MFT analysis result, large chatter component is observed in the section of 3.8 s − 5.0 s, and the forced vibration component gets larger at three sections: 0.5 s − 1.3 s, 1.8 s − 3.2 s, and 3.9 s − 4.8 s.

In the sliding FFT analysis result, it is confirmed that frequency peak of 770 Hz generates in three sections. Furthermore, the 770 Hz vibration can be regarded as a forced vibration because it is a harmonic of the spindle rotational frequency. In detail, 7700 min⁻¹ is equal to 128.3 Hz and the tool-passing frequency is 256.7 Hz, and product of 256.7 and 3 is 770, i.e. 770 Hz is a harmonic
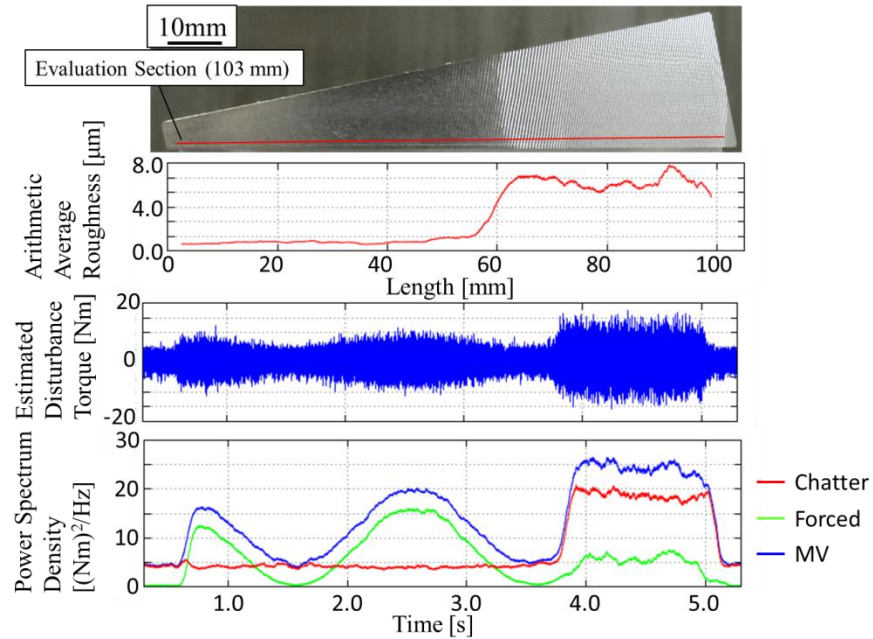
Fig. 7-13　MV+MFT analysis result in 7700 min⁻¹ in TC-S2C.
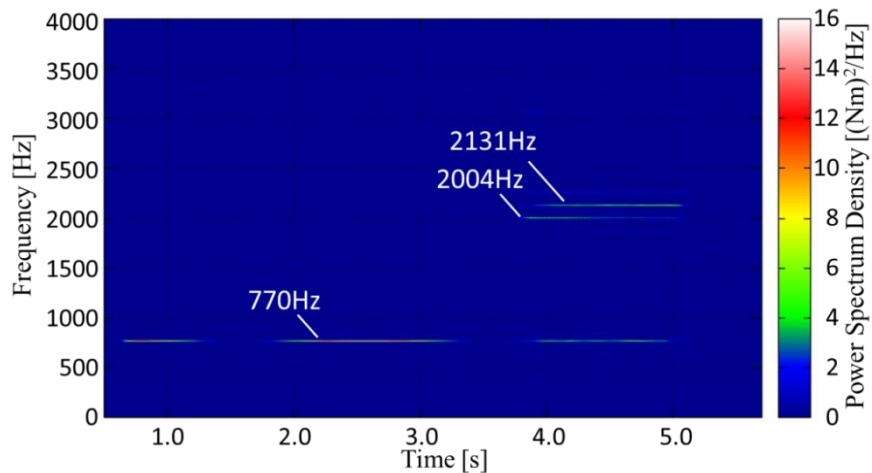
Fig. 7-14　Short-time Fourier transform in 7700 min⁻¹ in TC-S2C.

of the spindle rotational frequency. On the other hand, 2004 Hz and 2131 Hz are not the harmonics, i.e., these components are induced by chatter. From these results, it can be assumed that the forced vibration hardly has influence on the surface roughness and only chatter vibration deteriorates the surface quality. If this assumption is correct, the detection result of MV+MFT in 7700 min⁻¹ is an adequate result.

When the endmill vibrates at 770 Hz during rotating at 7700 min⁻¹, the vibration of endmill is just 6 cycles in one spindle rotation. Thus, the phase of present tool vibration and the phase of machined surface waviness left by the tool
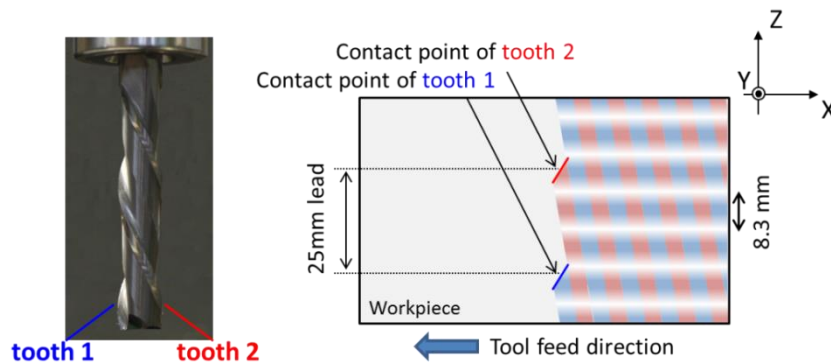
Fig. 7-15   Machining mark due to 770 Hz vibration during 7700 min^{-1} spindle rotation.
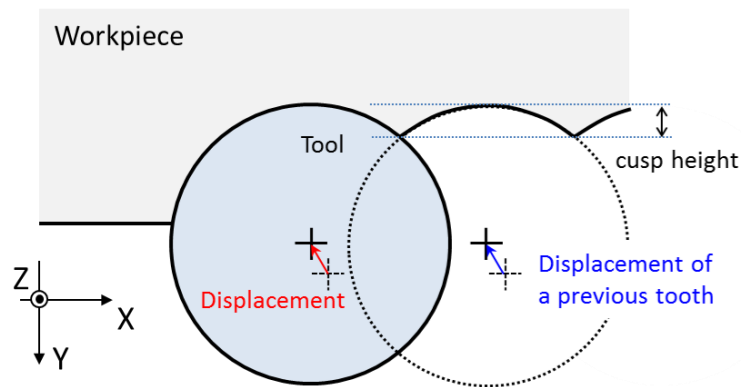

Fig. 7-16   A present tool displacement and the previous term tool displacement.

vibration in previous term become same, and the milling mark on the machined surface becomes a stripe pattern in horizontal direction as shown in Fig. 7-15. In this case, the cusp does not get high compared with stable machining because the present tool displacement is almost same with the previous term (Fig. 7-16). As a result, no large waviness appears in the horizontal direction and the Ra remains small, even if a large forced vibration occurs. In contrast, the stripe pattern would appear at 8.3 mm intervals in the vertical direction, considering that the tool lead is 25 mm in this experiment. However, a gentle waviness is generally filtered with a high-pass filter in the Ra measurement in order to evaluate only the surface roughness. In case of this research, the evaluation section is set to 4 mm, thus, the waviness of 8.3 mm interval is filtered naturally.

From these reasons, any influence of forced vibration cannot be confirmed with the Ra measurement. However, the forced vibration also should be captured because it would yield a machining error for a wide area.

As a conclusion, the MV+MFT certainly can capture chatter vibration separately from forced vibration by analyzing the estimated disturbance torque information.

7.5 Evaluation of Coincidence between Surface Quality and Detection Result

This section presents the competition between surface roughness and MV+MFT analysis result to confirm the adequacy of proposed chatter detection.

The chatter stability diagram generally shows a relation between the critical depths of cut and rotational speeds, which is obtained by analyzing the interaction between the process and the transfer function of the tool in frequency domain. On the other hand, in this study, the chatter stability diagrams are drawn by arranging the experimental results in each spindle rotation in parallel. As explained in section 7.4.1, the side milling experiments are conducted on the triangle-shaped workpiece to change the depth of cut from 5 mm to 25 mm gradually. The critical depth of cut at each spindle rotation can be measured from these milling test results, because chatter vibration occurs when the depth of cut becomes larger than the critical depth of cut. Figure 7-17 shows the milling test result with 8400 min^{-1} spindle rotation and how to determine the critical depth of cut from the analysis result. In the Ra measurement result, the Ra value suddenly gets larger in x position from 20 to 30 mm. This result is converted to a gradation bar by setting 1.0 µm threshold on the Ra value as shown in Fig. 7-17
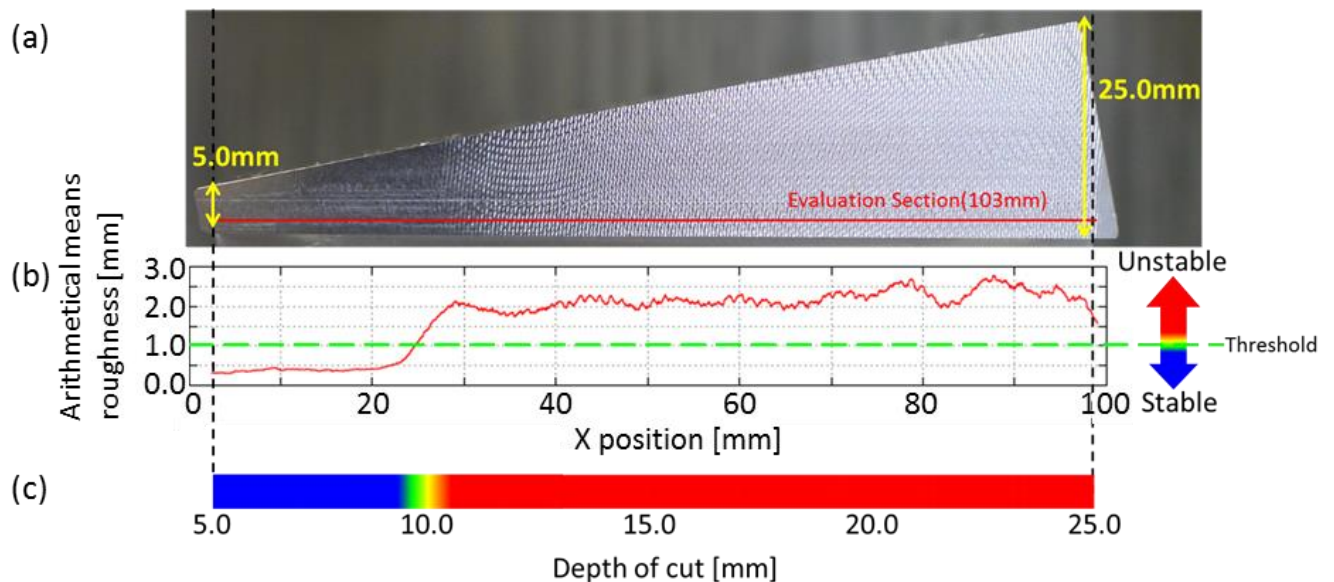

Fig. 7-17   Explanation to draw the stability lobe experimentally (a) Picture (b) surface roughness Ra (c) color gradation expressing the surface roughness.
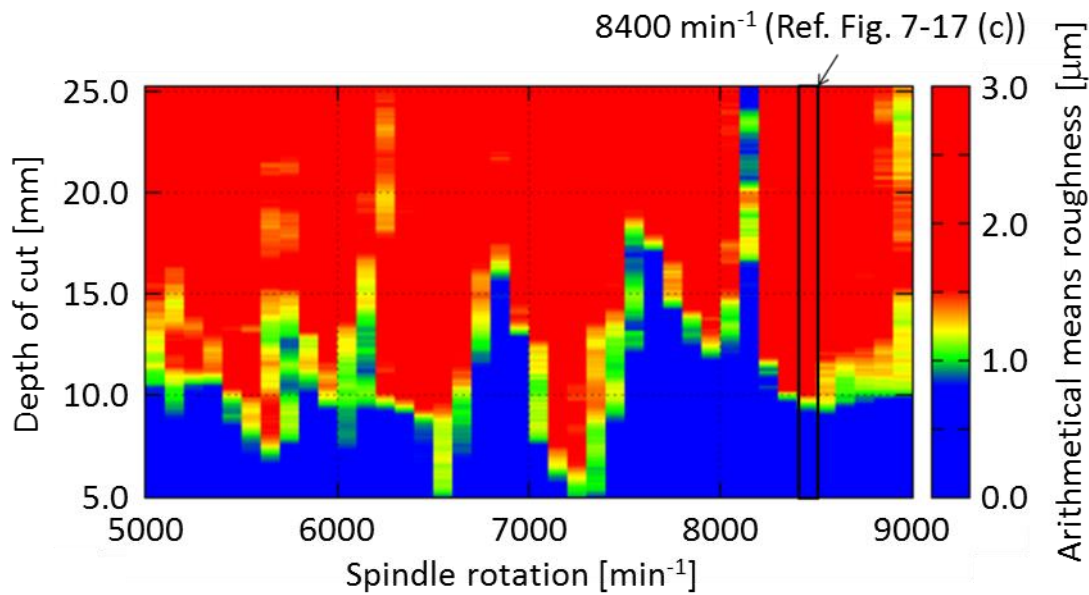
Fig. 7-18   Stability lobes based on the surface roughness in TC-S2C.
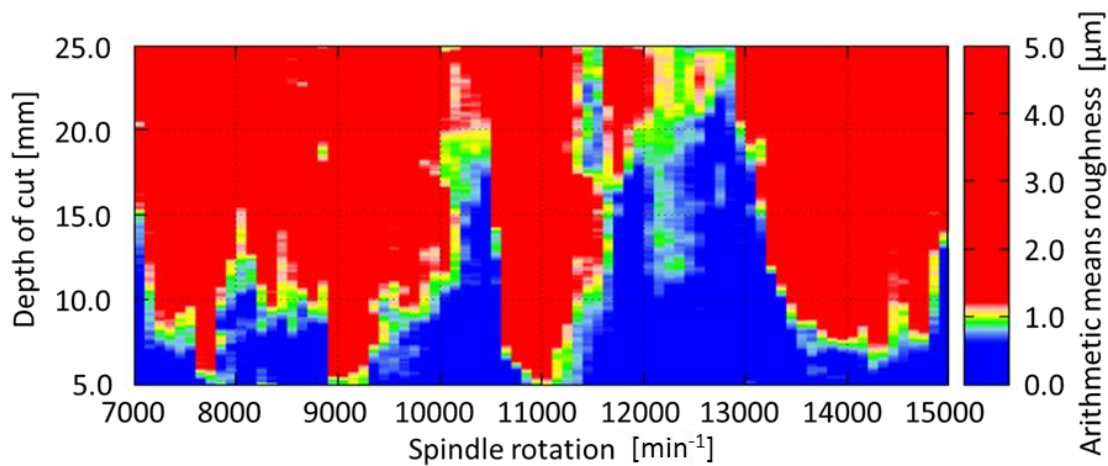

Fig. 7-19   Stability lobes Based on the surface roughness in S500X1.

(c). By requiring the gradation bar of each spindle rotation and arranging in parallel rows, the surface roughness-based chatter stability diagram can be obtained for TC-S2C as Fig. 7-18 and S500X1 as Fig. 7-19.

Focusing on the measurement results in TC-S2C shown in Fig. 7-18, the critical depth of cut certainly varies according to the spindle rotation and stable regions and unstable regions appear alternately. In particular, the critical depth of cut locally gets large at 6800, 7700, 8200 min^{-1}, whereas the chatter easily occurs with small depths of cut at 6500, 7200 min^{-1}.

Similar results are observed in the experimental results of S500X1 shown in Fig. 7-19. The stable regions appear around the spindle rotations of 10500 and
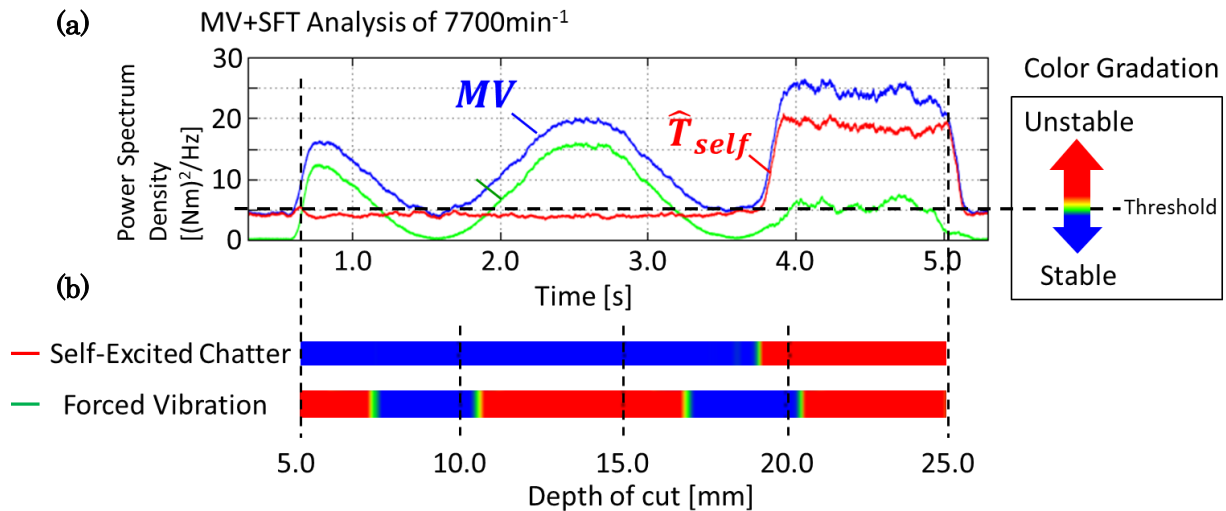
146

(a) MV+SFT Analysis of 7700min^{-1}

(b)

— Self-Excited Chatter

— Forced Vibration

Fig. 7-20 Threshold to draw the stability lobe (a) MV+MFT analysis (b)color gradation to draw the stability Lobe with the Result of MV+MFT.

12800 min^{-1}, whereas the unstable regions exist around 9100, 11000, 14000 min^{-1}.

It is experimentally confirmed in both machine tools that the stability lobes certainly can be drawn based on the relation between the critical depth of cut and the spindle rotation as explained in the chatter stability prediction method in Section 2.4.1.

Then, the MV+MFT analysis results are evaluated by comparing the obtained stability diagrams drawn based on the Ra measurement. The MV+MFT result can be obtained a time-domain data as shown in Fig. 7-20. To evaluate the coincidence between the Ra measurement results and the MV+MFT analysis results, self-excited chatter component and forced vibration component are separately converted as gradation bars by setting the thresholds. The threshold is arbitrarily modified to the value able to emphasize the shape of stability lobes. The obtained gradation bars of each component are arranged in parallel rows. Figures 7-21 and 7-22 represent the chatter component in milling with TC-S2C and S500X1 respectively.

In the analysis results of the MV+MFT in milling with TC-S2C, the stable regions at spindle rotations of 6200, 6800, 7600, 8200 min^{-1} are confirmed in the chatter component shown in Fig. 7-21, that is a highly-similar behavior with the Ra measurement results shown in Fig.7-18. In the experimental results in milling with S500X1, the large stable regions appear around 10000 and 12500 min^{-1} in the chatter component shown in Fig. 7-22, which is also has a high
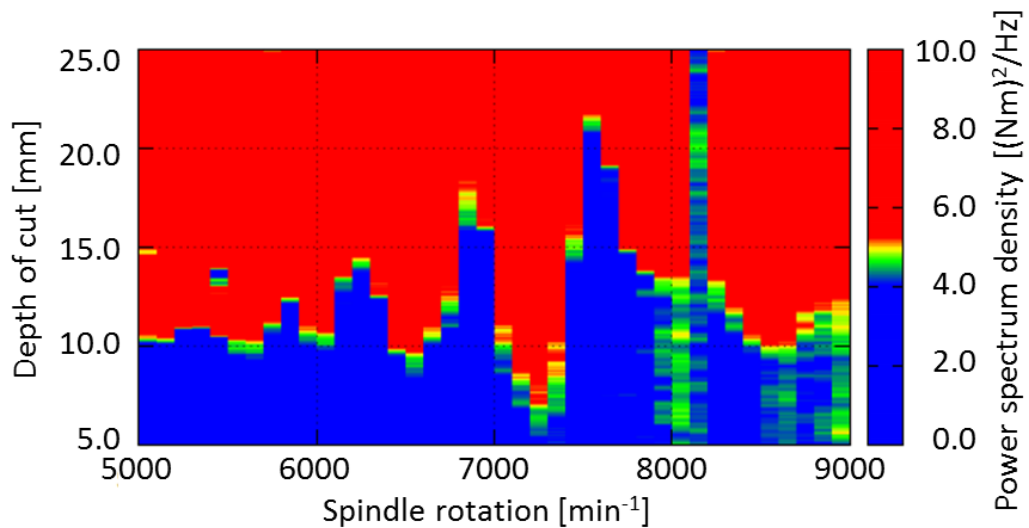
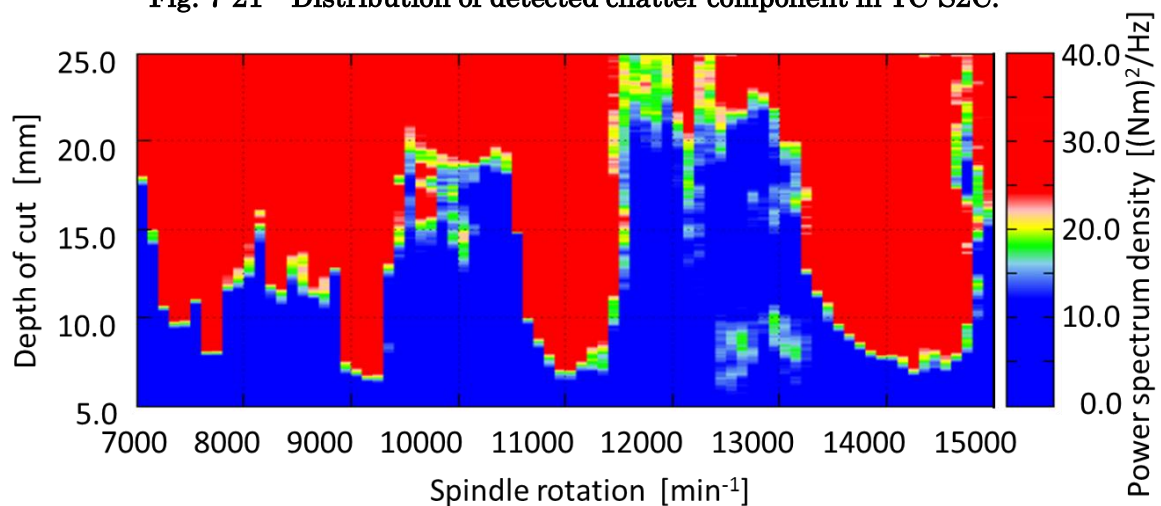Fig. 7-21　Distribution of detected chatter component in TC-S2C.

Fig. 7-22　Distribution of detected chatter component in S500X1.

correlation to the Ra measurements shown in Fig. 7-19 excepting the range from 9300 to 10000 min^{-1}. The Ra value becomes large in the spindle rotation region from 9300 to 10000 min^{-1}, although the chatter component hardly generate. In the milling result with 9800 min^{-1} shown in Fig.7-23, the chatter may grow gradually from the beginning because the Ra value exceeds the 1 μm threshold from just after milling starts. Furthermore, the Ra value gets large suddenly from the middle of workpiece. This would be because dominant vibration modes in the chatter are different between the former and the later section, and the chatter in former section is too small to detect from the servo information of the spindle. Considering that the chatter component slightly gets large in the former section, the more accurate detection result can be obtained by setting a lower threshold, whereas it leads to misdetection in other spindle rotation regions. The threshold should not be changed based on the each experimental result from the
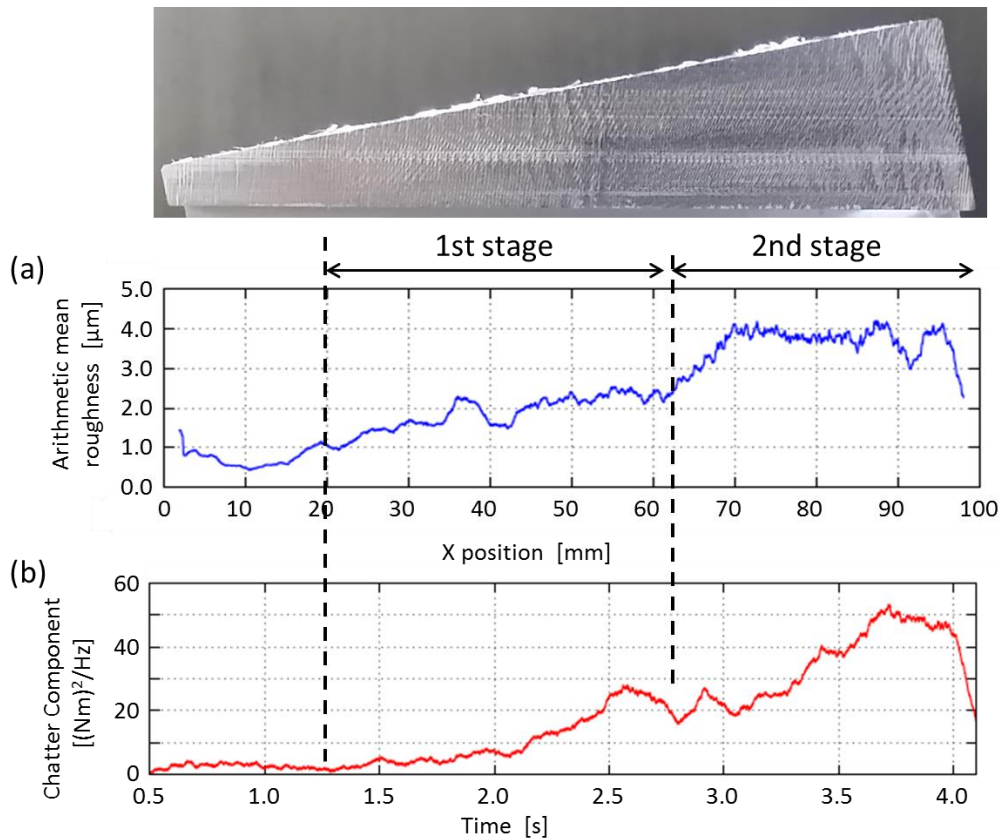
Fig. 7-23　Relation between surface roughness and chatter component in the milling test at spindle rotation of 9800 min^{-1}.

viewpoint of versatility. Thus, the chatter component is evaluated by a same threshold in all milling tests in this study.

Excepting the result around 9800 min^{-1} of S500X1, it is clear that the chatter component certainly has high correlation with the surface roughness.

On the other hand, no coincidence can be found in the forced vibration components which are summarized in Figs. 7-24 and 7-25. Although the forced vibration component is observed in some regions in the milling tests with TC-S2C (Fig. 7-24), its distribution no longer fits to the Ra measurements. This result also indicates that the forced vibration has no influence on the surface roughness and the chatter is a dominant factor in the machined surface quality. Furthermore, the forced vibration component is hardly observed in the milling experiment in S500X1 as shown in Fig. 7-25. (Note that the threshold is set to lower than that of chatter component to emphasize the distribution of the forced vibration component.) Additionally, the distribution of the forced vibration component is not similar to the Ra measurements. The milling tests with S500X1 also clearly
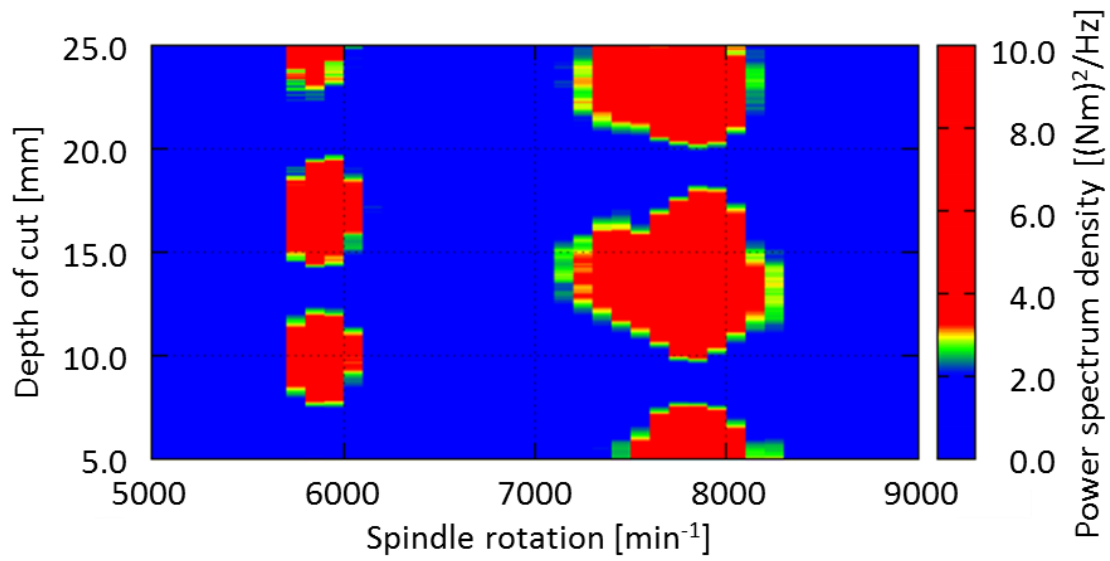
Fig. 7-24   Distribution of detected forced vibration component in TC-S2C.
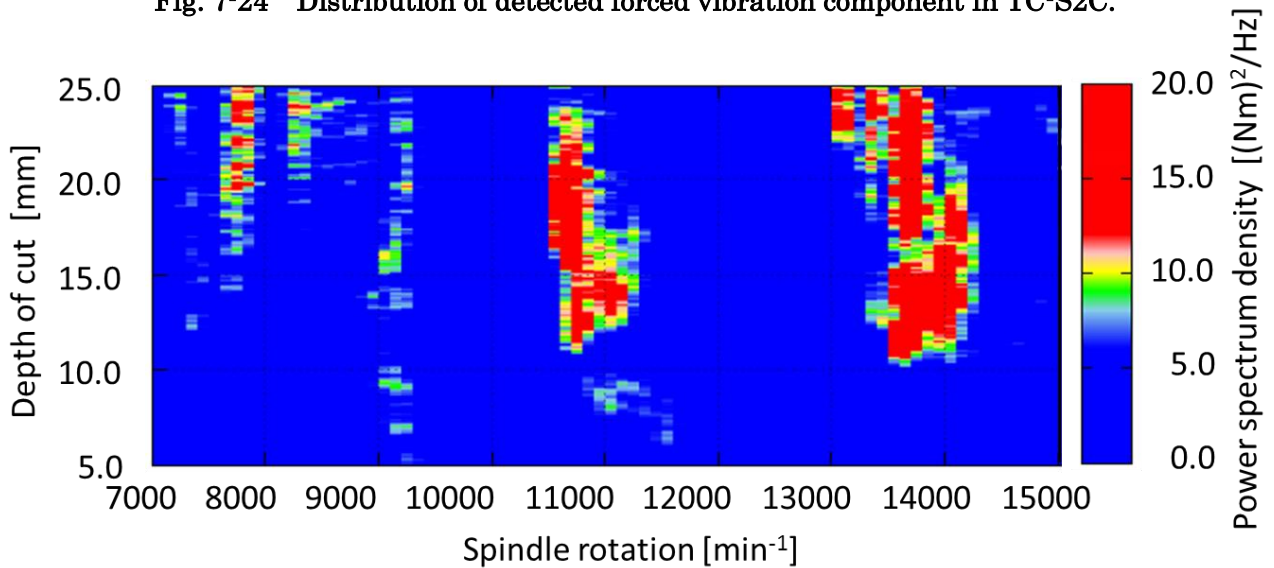

Fig. 7-25   Distribution of detected forced vibration component in S500X1.

indicate that the chatter is a dominant cause in tool vibration and surface quality deterioration.

As a conclusion, the proposed chatter detection based on MV+MFT is certainly applicable to milling process and able to detect chatter separately from forced vibration. It can be said that chatter is a main cause of the deterioration of surface roughness because the stable and unstable regions have highly-similar distribution between the analyzed chatter component and the surface roughness.

7.6 Summary

This chapter proposes a sensorless chatter detection in milling based on the servo information and evaluates the detection accuracy through side milling tests with two kinds of machine tools. In particular, the applicability of MV+MFT algorithm to realtime process monitoring is investigated by measuring the computational time. The obtained results are summarized as follows:

① In order to evaluate the realtime characteristic of the proposed MV+MFT algorithm, the computational time is measured and compared with FFT. The computational time measurement result shows that it only takes about 300 ns to process the MV+MFT analysis in one periodic term, which is enough short time to perform in realtime. Furthermore, it is experimentally confirmed that the MV+MFT algorithm is actually an $O(1)$ algorithm because the computation time hardly changes even adopting different window widths.

② By applying MV+MFT analysis to the disturbance torque estimated with disturbance observer in the spindle control system, chatter can be detected in realtime, separating from the forced vibration. Under the cutting condition in this study, the chatter is a dominant factor in the machined surface roughness. The distribution of the obtained chatter components is highly-similar to that of the Ra measurement results.

③ The forced vibration has no coincidence with the Ra value because the forced vibration does not have influence of cusp height on the surface.

8 Identification System for Stable Cutting Condition

8.1 Introduction

Chatter stability analysis has been focused on for a long time in order to enhance the machining efficiency. In past few decades, many researchers have proposed chatter stability prediction methods and analyzed the mechanism of chatter vibration. These studies have described that the chatter stability in milling heavily depends on the axial depth of cut and the spindle rotation. Therefore, the most stable spindle rotation against chatter should be found, at which stable cutting can be performed even with a large depth of cut.

Although the chatter mechanism is theoretically clarified by many researchers, chatter stability prediction often does not agree with the real process because the transfer function of the tool system is difficult to identify accurately. From this viewpoint, an experiment-based approach should be taken to obtain a reliable analysis result on the chatter stability.

In this chapter, the proposed identification method for stable spindle rotation against chatter, which is explained in section 2.4.1, is experimentally evaluated through side milling tests. Furthermore, the mechanism analysis and the identification error of the proposed method are discussed through the developed time-domain milling simulator explained in sections 2.5 and 3.3.

8.2 Identification of Stable Spindle Rotation with Contentious Spindle Rotation Variation

In milling, spindle rotation and critical depth of cut have a unique relation as shown in Fig. 8-1, where the parameters are given as Table 8-1 and 8-2. Note that the immersion angle is defined as an angle section between start angle and exit angle as show in Fig. 8-2, and cutting coefficient is a proportional constant expressing the relation between the cutting force and the cutting area. The critical depth of cut gets large in some spindle rotation regions, so-called "stability pockets". Identification of stability pocket is necessary to enhance the cutting efficiency because the process stability can be ensured even with a large
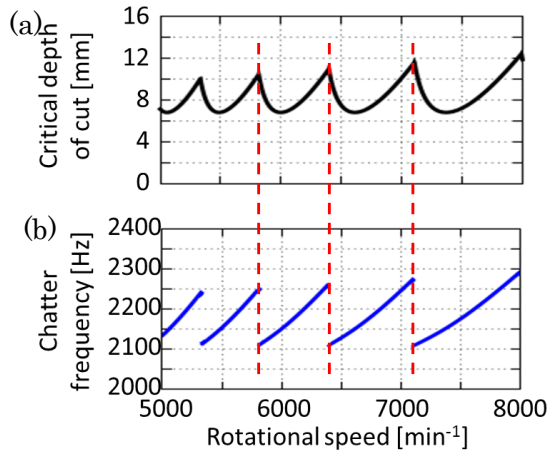
(a)

(b)

Fig. 8-1 Relation between rotational speed
and (a) critical depth of cut, (b) chatter frequency.

Table 8-1 Modal parameters of the tool.

	X direction	Y direction
Natural frequency Hz	2080	2090
Damping ratio	0.01	0.01
Mass kg	0.050	0.040

Table 8-2 Other parameters for the chatter stability prediction.

Number of tooth		2
Immersion angle deg		$-25.8\sim 0.0$
Cutting coefficient	Tangential MPa	1500
	Radial MPa	450

θ_{st}: start angle
θ_{ex}: exit angle
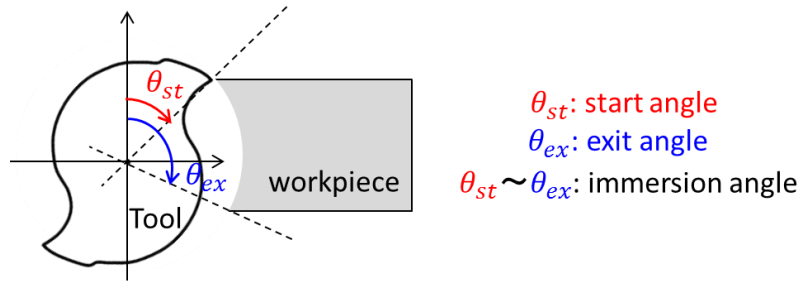$\theta_{st}\sim\theta_{ex}$: immersion angle

Fig. 8-2 Definition of the immersion angle.

depth of cut. Chatter frequency also shows a unique behavior along with the spindle rotation variation. The chatter frequency gradually gets higher with higher spindle rotation, and drastically shifts at a certain spindle rotation at which the critical depth of cut gets locally largest value. Based on this characteristic, a stability diagnosis method for stable spindle rotation is proposed by changing the spindle rotation during chatter, the stable spindle rotations would be captured from the chatter frequency information. In the proposed identification method, following points should be discussed experimentally and theoretically.

① Which types of the spindle rotation variation should be used: acceleration or deceleration.

② How large the spindle rotation changing rate should be set.

③ How large the identification error occurs.

In following Sections 8.3, the above points of ② and ③ are discussed through the milling tests in which the spindle rotation is gradually changed. Section 8.4 mainly focuses on ① and ③ based on the milling simulation.

8.3 Evaluation of Proposed Method by Milling Test

This section presents a feasibility of the proposed method through the milling tests in two kinds of 3-axis machining centers: TC-S2C and S500X1.

8.3.1 Conditions

Although the milling tests are basically conducted under the same conditions with the tests in Chapter 7, the spindle rotation and the shape of workpiece are different in the stable spindle identification test. The spindle rotation is gradually accelerated or decelerated by changing the override rate continuously. At the same time, the feed rate is also changed at the same override changing rate in
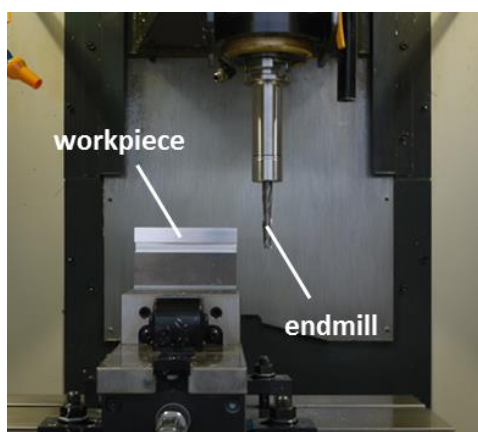
Table 8-3 Cutting condition for identification test in TC-S2C.

Rotational speed min^{-1}	5400–9000 (base:7200)
Feed rate mm/min	1575–875 (base: 1260)
Feed per tooth mm	0.0875
Number of tooth	2
Override change rate %/s	15, 30, 50, 75
Override range %	-25% − +25%
Axial depth of cut mm	15.0
Radial immersion mm	0.5
Workpiece	Aluminum (A2017)

Fig. 8-3   Appearance of milling test.

Table 8-4   Cutting condition for identification test in S500X1.

Rotational speed min^{-1}	7000–16000 (base:10000)
Feed rate mm/min	2800–1225 (base: 1750)
Feed per tooth mm	0.0875
Number of tooth	2
Override change rate %/s	40, 50, 60
Override range %	-30% − +60%
Axial depth of cut mm	15.0
Radial immersion mm	0.5
Workpiece	Aluminum (A2017)

order to keep the feed per tooth to avoid a sudden change in the cutting force. Furthermore, square-shaped workpiece (Fig. 8-3) is used in this test from viewpoint of versatility. The proposed method has to be utilizable in usual milling processes, i.e., the special shaped workpiece should not be used.

Including other cutting conditions, the details of the milling test condition are summarized in Table 8-3 for TC-S2C and Table 8-4 for S500X1.

8.3.2 Experimental Result

Firstly, the milling tests results in TC-S2C are explained.

When spindle rotation variation of 50 %/s shown in Fig. 8-4 (a) is given, the estimated disturbance torque drastically fluctuates during accelerating or decelerating the spindle rotation as shown in (b). To confirm the chatter frequency shift visually, short-time Fourier transform (STFT) is conducted on the estimated disturbance torque as shown in (c). Although STFT is an unsuitable
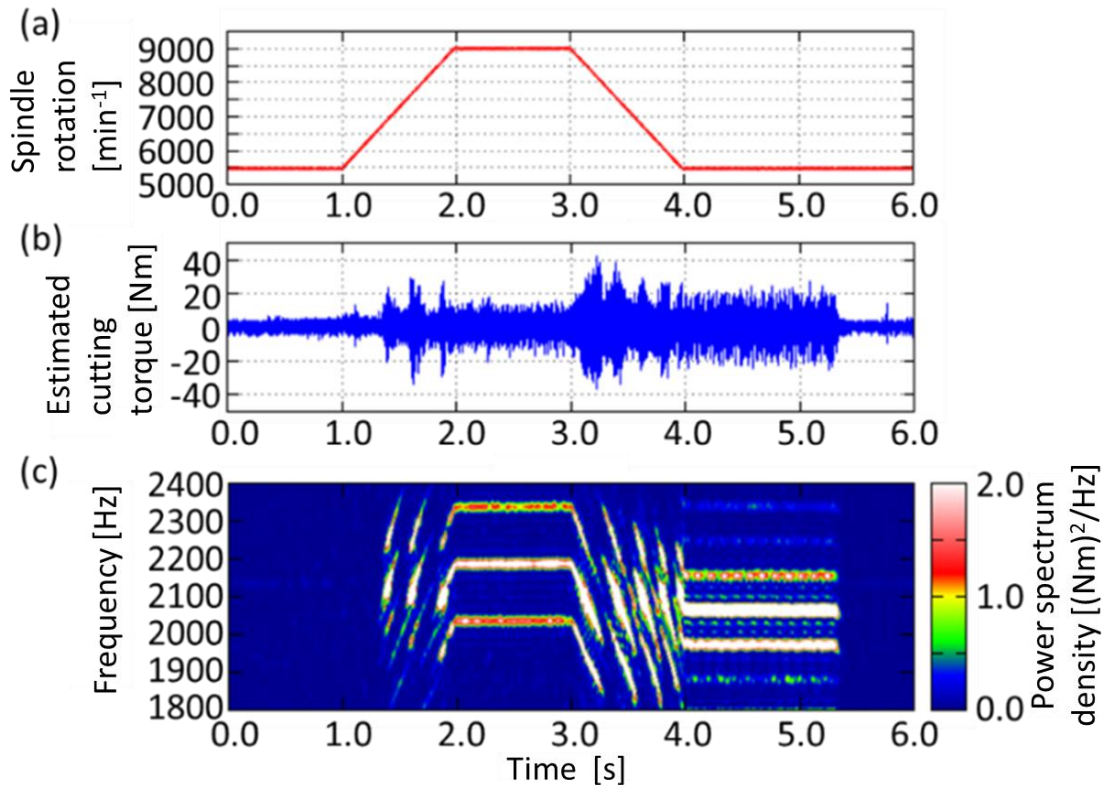

Fig. 8-4   Result of the identification test with 50 %/s: (a) spindle rotation: (b) estimated disturbance torque: (c) short-time Fourier transform analysis.
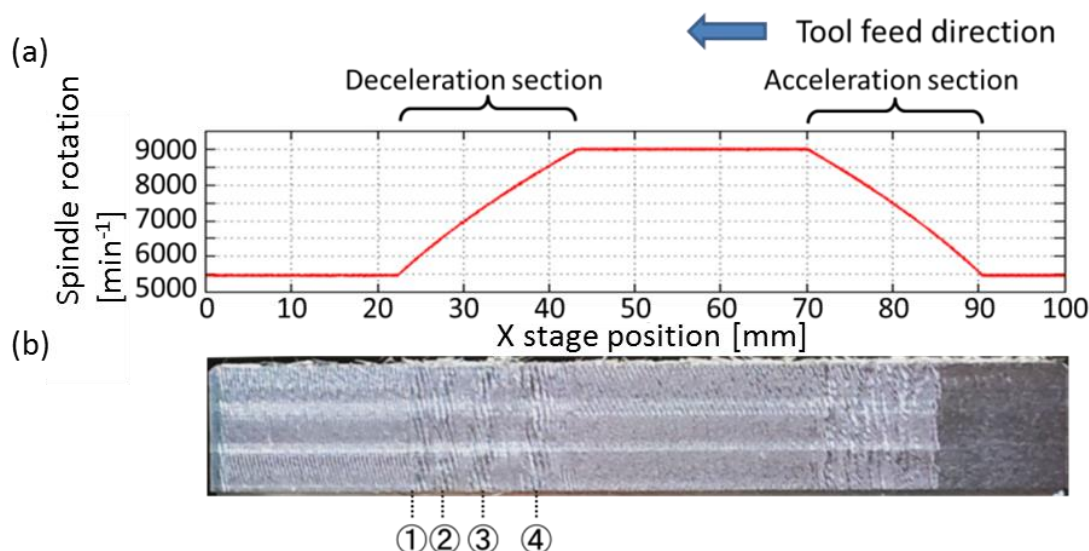
Fig. 8-5 Milling test with 50 %/s override changing: (a) spindle rotation (b) appearance of machined surface.

analysis method to use in realtime on the aspect of computational load, the realtime characteristic is not required for the proposed diagnosis method because time-frequency analysis can be performed offline afterward, if the disturbance torque is successfully sampled in the experiment. In the STFT analysis result, four times chatter frequency shifts are clearly observed in the deceleration section. The frequency shifts are also confirmed in the acceleration section, however, the frequency variation is small compared with the deceleration area.

Figure 8-5 represents the surface appearance after the experiment. A unique chatter mark of four lines obviously appears in the deceleration section, whereas no discriminative pattern can be found on the surface in the acceleration section. Therefore, the surface appearance also indicates that the chatter frequency shifts occur four times in the deceleration section and the frequency shift is observed more clearly during decelerating than accelerating the spindle rotation. From these results, it can be said that the spindle rotation should be decelerated to capture the chatter frequency shifts. This assumption will be theoretically discussed with the time-domain milling simulator in the later section.

In order to capture the chatter frequency shift quantitatively, the power spectrum density of peak frequency would be a useful criterion. Figure 8-6 shows the extended figure of STFT analysis in the deceleration section of Fig. 8-4 (c) and the power spectrum density of peak frequency. In the deceleration section, the power spectrum density of peak frequency repeats up and down, then, some minimum points can be captured. Drawing the moving average of 1.0 s window and separating the sections on the condition that the power spectrum density of
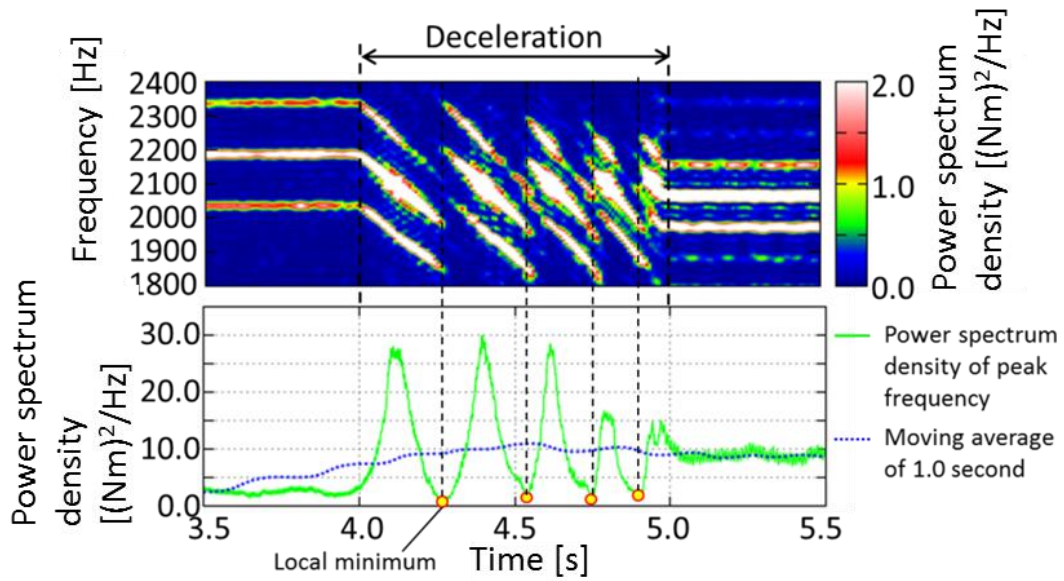
Fig. 8-6　Behavior of power spectrum density of peak frequency test with 50 %/s override changing.
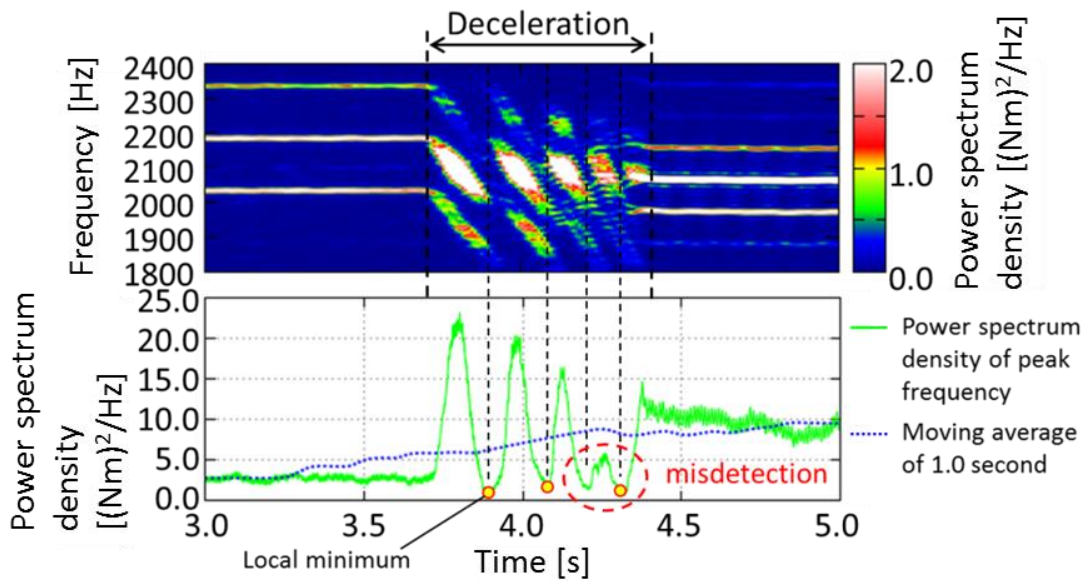

Fig. 8-7　Behavior of power spectrum density of peak frequency test with 75 %/s override changing.

peak frequency gets lower than the moving average, the local minimum values can be captured by requiring the minimum value of each section. Comparing the STFT analysis result, it is clear that these local minimum values are taken when the chatter frequency drastically shifts. This result is adequate considering that the chatter frequency shifts theoretically occurs in the stability pockets at which the chatter is highly damped. In this study, this physical phenomenon is adopted to identify the stable spindle rations.

The override changing rate also should be discussed because the test time

157

should be as short as possible from the practical viewpoint. The chatter frequency shift is not observable when the override changes excessively drastically. Figure 8-7 shows the milling test result with override changing rate of 75 %/s. The frequency shifts are observed 4 times as shown in STFT analysis result, however, the spectrum density of peak frequency does not generate enough and only three minimum values are captured. Although there is a possibility to be able to capture the chatter frequency shifts correctly by shortening the window width of moving average, the misdetection would occur much more easily if the moving average value more drastically fluctuates due to the shorter window.

As a conclusion, 50 %/s is regarded as the proper override changing rate to capture the chatter frequency shift without misdetections in this study. In case of 50 %/s, the identification test time to perform the proposed method is only 1.0 s, which would be enough short for practical usage.

Here, the repeatability of the proposed method is also evaluated. The 15, 30, and 50 %/s deceleration tests are repeated 5 times respectively and each result is summarized in Table 8-5 and Fig. 8-8.

The chatter frequency shifts are observed four times in all tests even with different override changing rates. The each shift is captured in four sections: 8000 − 8100 min^{-1}, 7000 − 7100 min^{-1}, 6300 − 6400 min^{-1}, and 5700 − 5800 min^{-1}. The maximum error of identified spindle rotation in 5 times milling tests of each override changing rate is 117 min^{-1} as shown in Table 8-4. These results clearly indicate that the proposed method has sufficiently high repeatability.

Table 8-5　Identified stability pockets with each override changing rate.in TC-S2C.

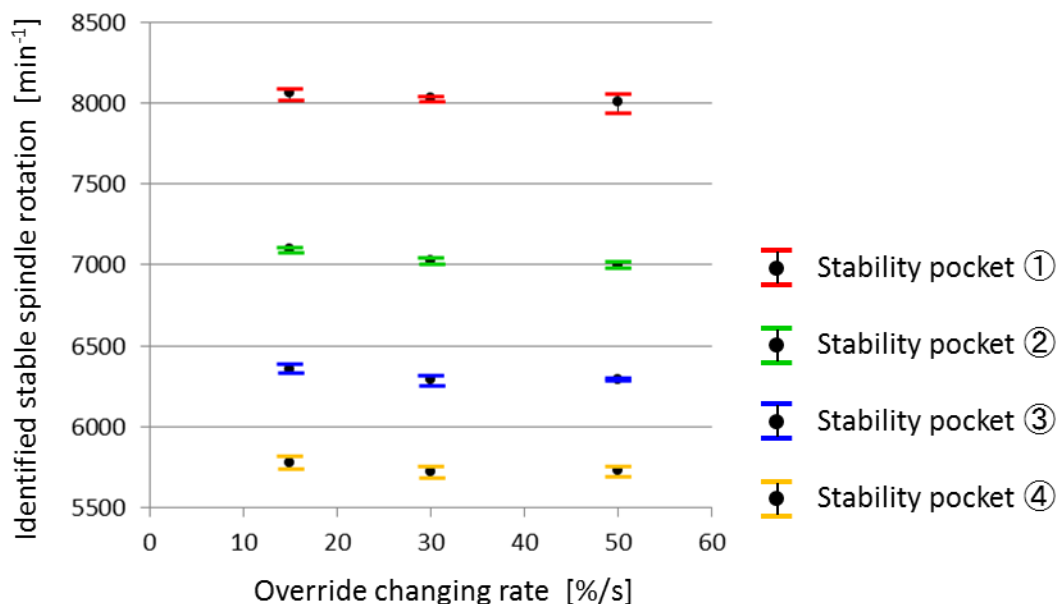| Override changing rate		Stability pocket ①	Stability pocket ②	Stability pocket ③	Stability pocket ④
15 %/s	Ave.　min^{-1}	8059	7098	6358	5781
	Difference of identified spindle rotations between Max. and Min. in five times tests　min^{-1}	69	31	54	83
30 %/s	Ave.　min^{-1}	8031	7027	6293	5721
	Difference of identified spindle rotations between Max. and Min. in five times tests　min^{-1}	34	34	56	61
50 %/s	Ave.　min^{-1}	8006	6999	6292	5727
	Difference of identified spindle rotations between Max. and Min. in five times tests　min^{-1}	117	43	12	64

Fig. 8-8 Identified stable spindle rotations in tests with each override changing rate in TC-S2C.

As a next step, the applicability of the proposed method to a different machine tool is evaluated by conducting similar experiments on S500X1. The cutting conditions are summarized in Table 8-4. Note that the base conditions of the rotational speed and the feed rate are different from the conditions in TC-S2C. As an example of the identification test results, the milling test with 40 %/s override changing rate is shown in Fig. 8-9 and its surface appearance is shown in Fig. 8-10.

The frequency shifts can be observed 7 times from 7000 to 16000 min^{-1} as shown in Fig. 8-9 (b). Compared with the experimental results with TC-S2C, the power spectrum density of peak frequency does not fluctuates in a regular manner, thus, spindle rotations of ③ and ⑥ are not captured in the proposed algorithm. The identified spindle rotations are summarized in Table 8-6. Furthermore, the power spectrum density of peak frequency is low in sections between ②－③ and ④－⑤. This result would indicates that wide stable regions spread in the spindle rotation ranges of ②－③ and ④－⑤, i.e., the cutting depth would be too small to capture the chatter frequency shifts.

As a result, some chatter frequency shifts cannot be captured in the experiment in S500X1. The meaning of the experimental result and the cutting condition modification will be discussed in the next section.
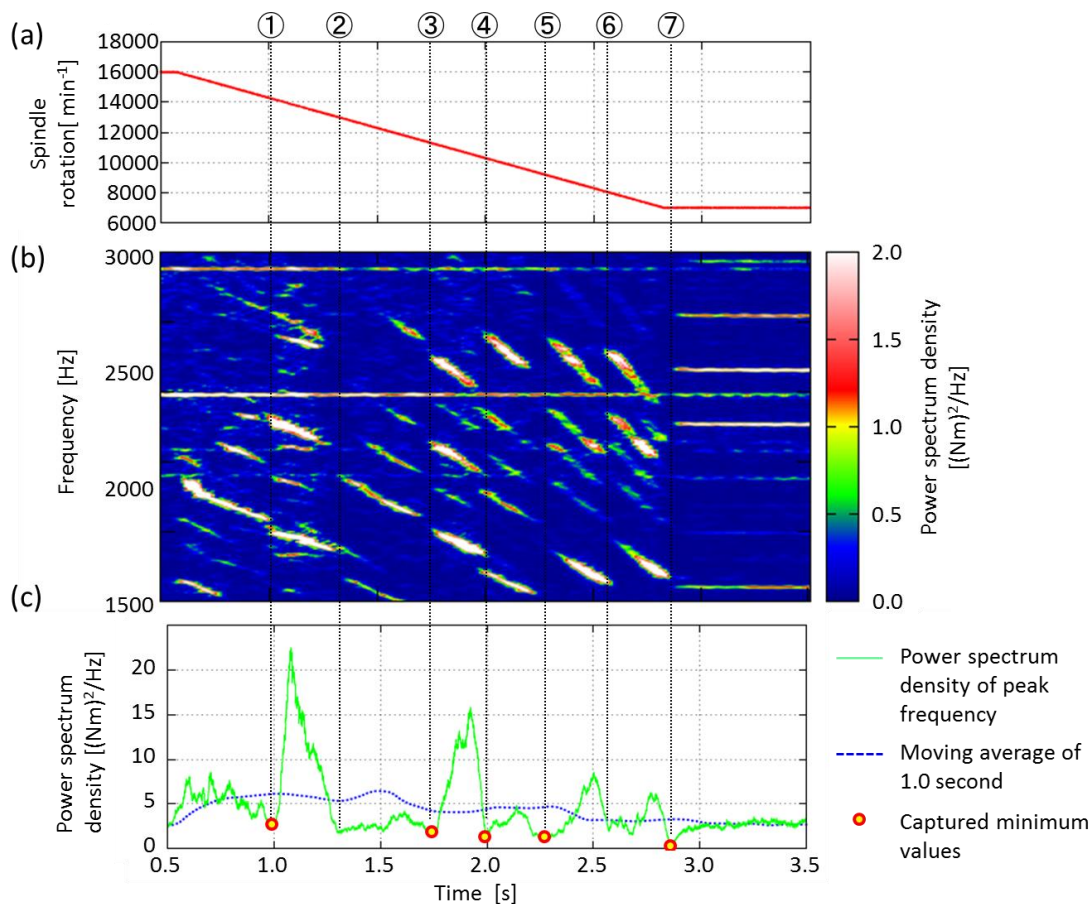
Fig. 8-9   The diagnosis experiment in S500X1 with 40 %/s override changing rate:

(a) spindle rotation, (b) STFT analysis, (c)behavior of power spectrum density

Table 8-6   Identified spindle rotations in Fig. 8-9.

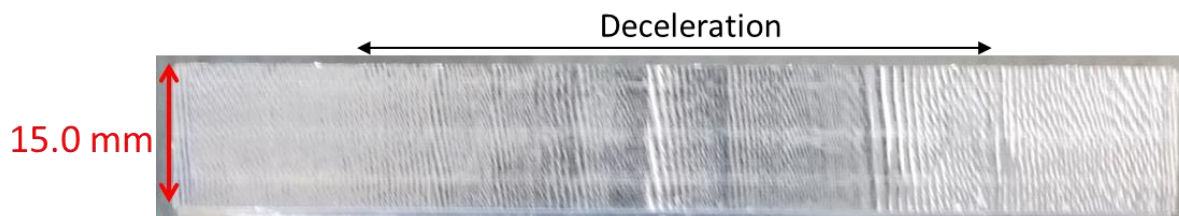|	①	②	③	④	⑤	⑥	⑦
Spindle rotations at which chatter frequency shift occurs min⁻¹	14293	(Miss)	11375	10306	9255	(Miss)	7000

Fig. 8-10   Surface appearance of the diagnosis experiment in S500X1

with 40 %/s override changing rate

8.4 Adequacy Investigation for Identified Stable Spindle Rotations

In order to confirm that the critical depth of cut is large at the identified stable spindle rotations in previous section, comparison with the obtained results in Chapter 7 would be useful. Figure 8-11 draws the Ra (arithmetic average
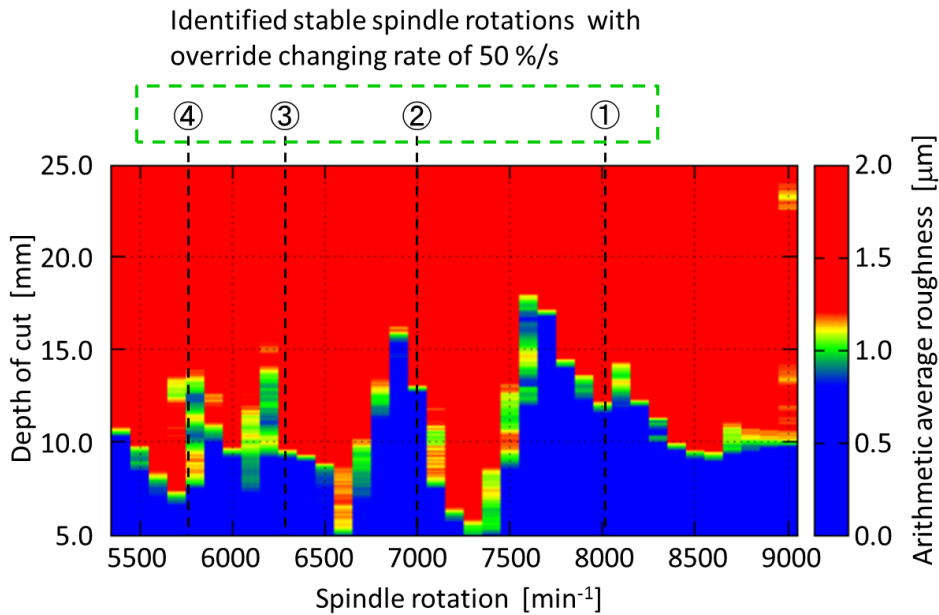

Fig. 8-11   Comparison between the Ra distribution and the identified stable spindle rotations with 50 %/s override changing rate in TC-S2C.
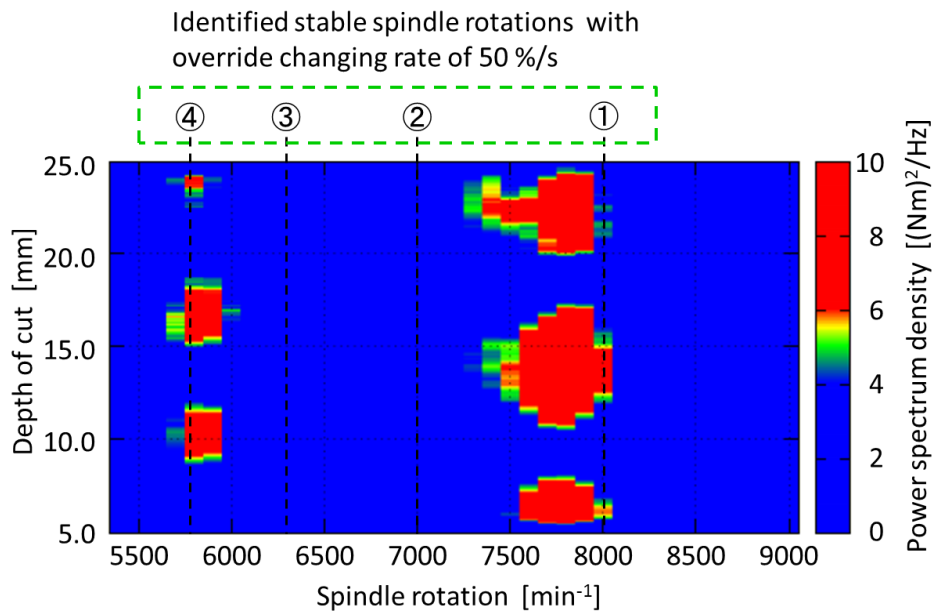

Fig. 8-12   Comparison between the power spectrum density of forced vibration and the identified stable spindle rotations with 50 %/s override changing rate in TC-S2C.

161

roughness) distribution including the identified stable spindle rotations with 50 %/s deceleration shown in Table 8-5. According to the Ra measurement results, the critical depth of cut gets locally large at 5800, 6200, 6900, 7700 min^{-1}, whereas, the identified spindle rotations are ④5727 min^{-1}, ③6292 min^{-1}, ②6999 min^{-1} and ①8006 min^{-1}. Excepting the spindle ration of ①, the stable spindle rotations are successfully identified within 100 min^{-1} error. The identification error of ① is about 300 min^{-1} and it is clear that the spindle rotation of ① actually missed the stable pocket of 7700 min^{-1} in Fig. 8-11. On the other hand, Fig. 8-12 shows the distribution of power spectrum density of forced vibration including the identified spindle rotations. Large power spectrum density of the forced vibration is particularly confirmed in the area between the depth of cut from 11 to 17 mm at spindle rotation around 7700 min^{-1}. Therefore, the forced vibration would be dominant in this area and suppress the chatter by disturbing the regenerative effect due to the waviness of machined surface. Furthermore, even in case that the large forced vibration occurs, the forced vibration hardly has influences on the surface roughness as explained in Chapter 7.

Although the proposed method is focusing on chatter stability and does not consider the influence of forced vibration, the spindle rotation of 7700 min^{-1} also should be avoided because the forced vibration leads to the large waviness of the machined surface in the wide range. In practical usage, not only the chatter stability diagnosis method but also forced vibration monitoring method should be used to ensure the cutting stability.

Here, the identification results in S500X1 are also compared with the Ra distribution as shown in Fig. 8-13. Although the critical depth of cut is actually large at the spindle rotations of ②, ④, ⑥, and ⑦, the spindle rotations of ①, ③, ⑤ completely direct the unstable conditions. Three misdetections are found in seven spindle rotations, thus, the proposed method cannot be used for this experimental condition. However, these spindle rotations would have relation to the chatter stability because the behavior of the power spectrum density shown in Fig. 8-8 has some common characteristics with the Ra distribution, e.g., the wide stable region spreads between the spindle rotations of ② and ③.

Considering that the chatter does not occur in the range from 11700 to 13000 min^{-1} even if the depth of cut is large as 15.0 mm, the cutting condition is not suitable for the proposed diagnosis method because the chatter should always occur during spindle deceleration in order to capture the chatter frequency shifts
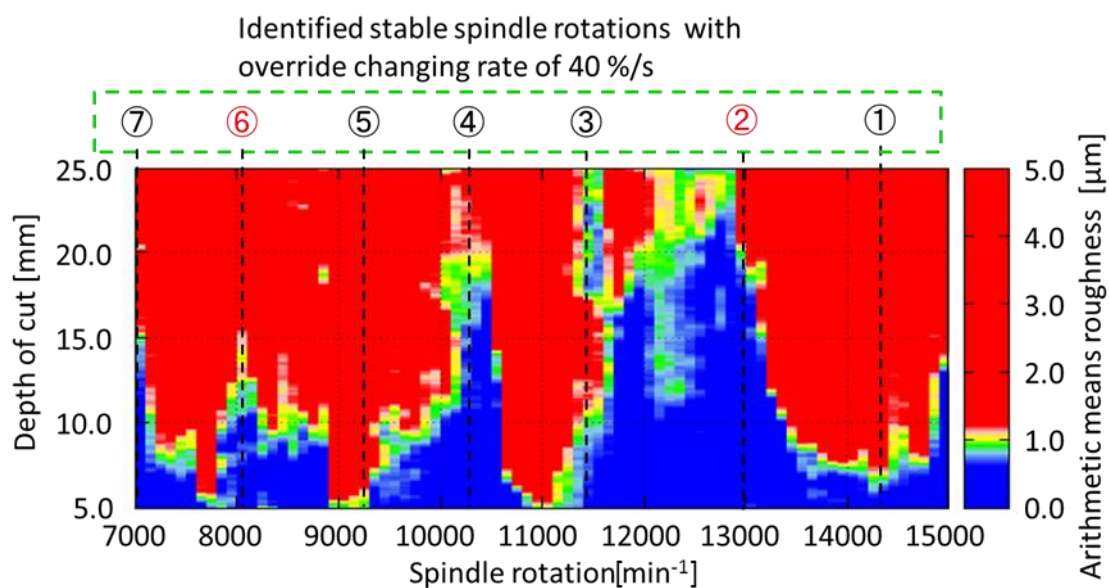
Fig. 8-13   Comparison between the Ra distribution and the identified stable
spindle rotations with 40 %/s override changing rate in S500X1.
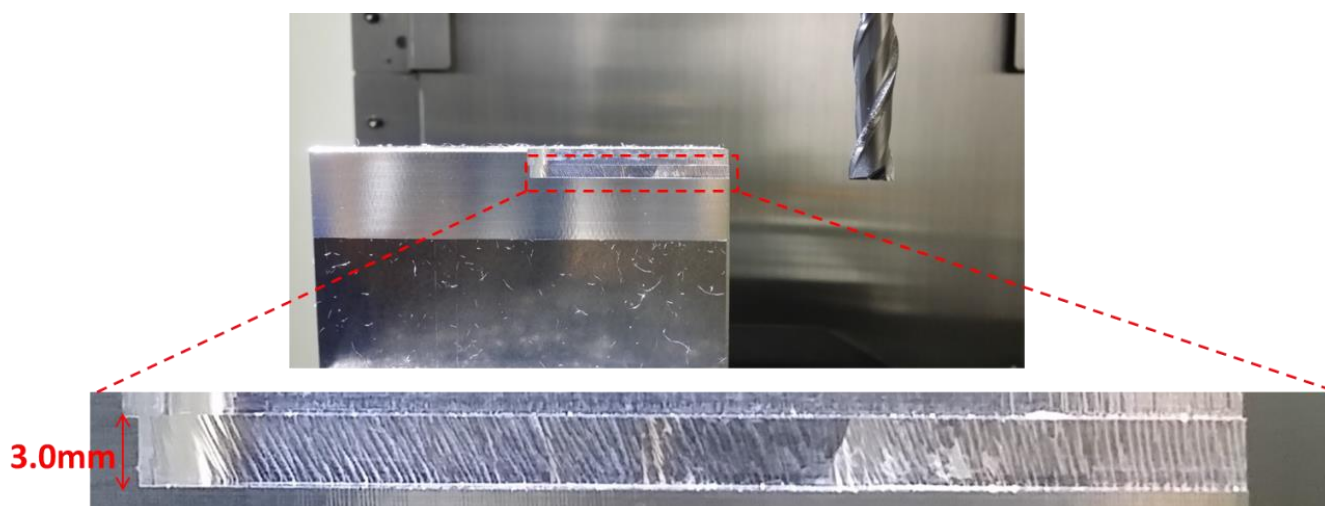

Fig. 8-14   Machined surface appearance with 2.5 mm
radial immersion and 3.0 mm axial depth of cut.

clearly. Thus, another milling test is conducted with a cutting condition having a
large radial immersion. The cutting condition is basically same with Table 8-4;
however, the radial immersion and the axial depth of cut are changed.

The radial immersion and the axial depth of cut are set to 2.5 mm and 3.0 mm
respectively in this test. Although no remarkable chatter mark can be observed
on the machined surface as shown in Fig. 8-14, the chatter frequency shifts are
obviously confirmed by analyzing the disturbance torque information with STFT

163

in the deceleration section of the spindle rotation as shown in Fig. 8-15. Compared with the experimental result with small radial immersion shown in Fig. 8-9, the repetition pattern of chatter frequency is clear and the local minimum values can be captured in the power spectrum density of frequency peak as shown in Fig. 8-15 and 8-16. Although the local minimum value at spindle rotation of ① is captured by the proposed algorithm, this is clearly an
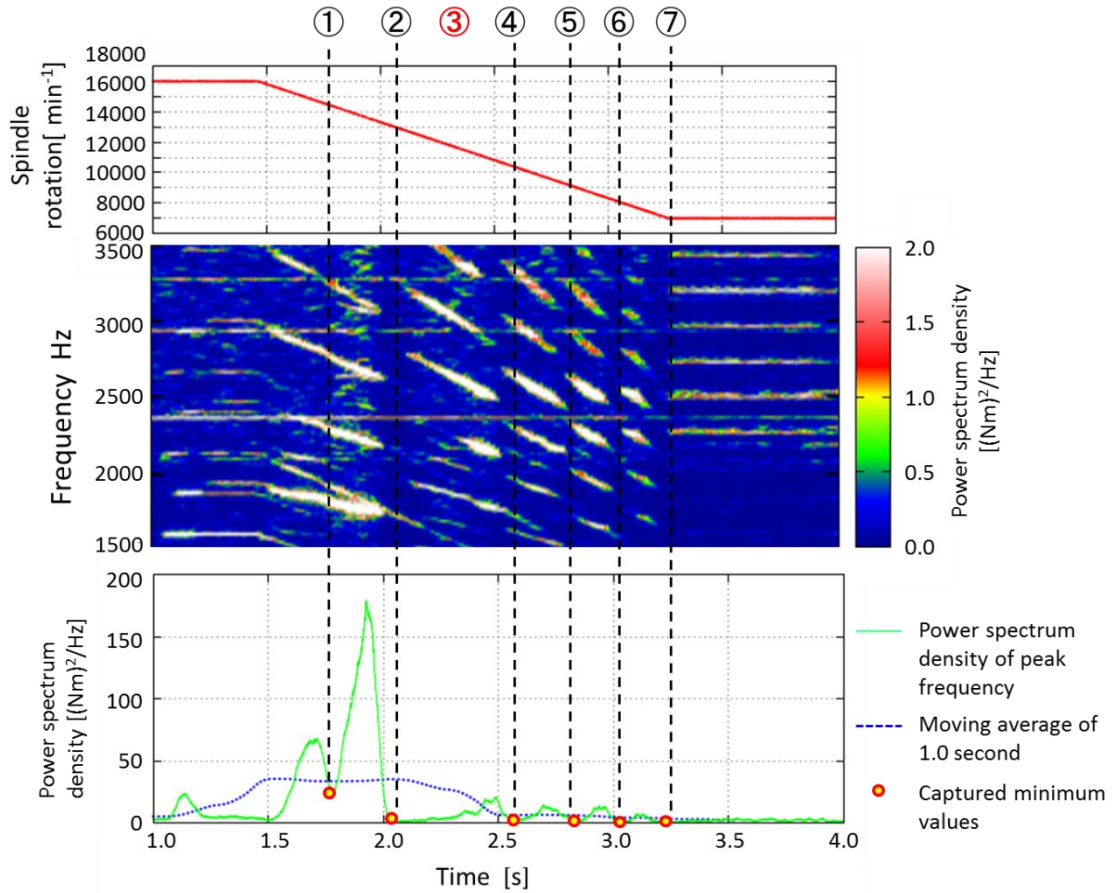

Fig. 8-15   Relation between spindle rotation and STFT analysis on
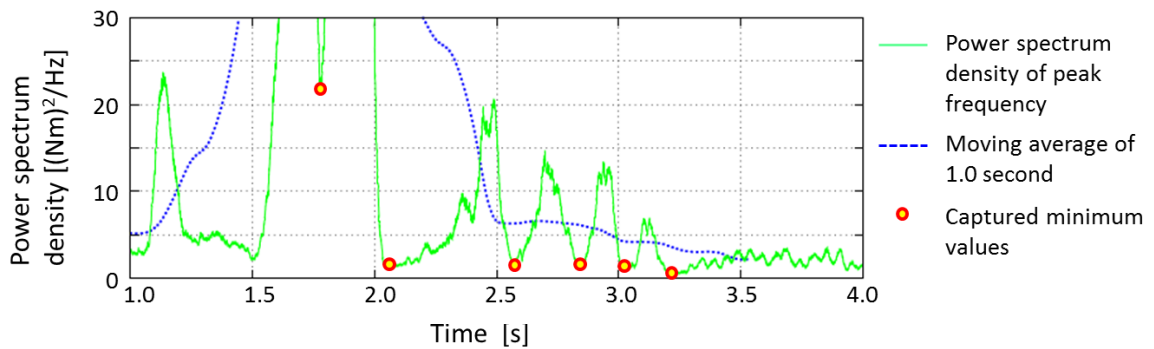the estimated disturbance torque.

Fig. 8-16   Expanded figure of behavior of power spectrum density of peak frequency.

unstable spindle rotation because the chatter shift does not occur in this section and the spectrum density is too large compared with the other local minimum values. This misdetection should be eliminated as an outlier by setting a threshold.

The repeatability of the proposed method is also evaluated here. The five identified spindle rotations of five times tests are summarized in Table 8-7. Although the difference between the maximum and minimum in the identified spindle rotation of ② in five tests is large as 579 min^{-1}, this is because the stable region widely spreads around ②. The power spectrum density does not get high in the stable region and the local minimum value easily changes. Excepting the spindle rotation ②, the proposed method provides high repeatability even if the radial immersion and the axial depth cut are different. Furthermore, spindle rotation of ③ is not detected in this test, although a chatter frequency shift is observed at ③ when the radial immersion is small. From the result of milling on triangle-shaped wookpiece, the critical depth of cut is clearly low at ③; thus, it can be said that the one of the misdetections is eliminated when the diagnosis is performed with large radial immersion.

To confirm the adequacy of these identified stable spindle rotations, the milling tests are conducted on triangle-shaped workpiece as shown in Fig. 8-17. Although

Table 8-7　Identified stability pockets in 5 time tests with 50 %/s override changing rate.

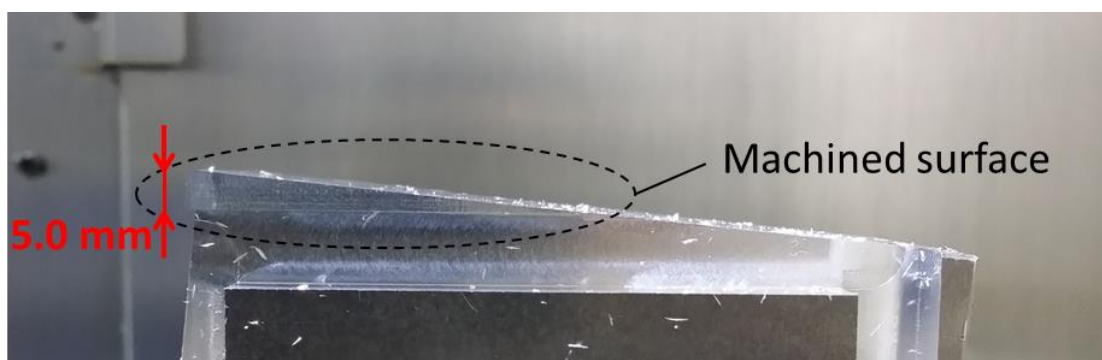| Override changing rate		Stability pocket ①	Stability pocket ②	Stability pocket ④	Stability pocket ⑤	Stability pocket ⑥	Stability pocket ⑦
50 %/s	Ave.　min^{-1}	14565	12889	10464	9118	8124	7179
	Difference of identified spindle rotations between Max. and Min.　in five times tests　min^{-1}	383	579	84	177	208	230

Fig. 8-17　Triangle-shaped workpiece which applies axial depth of cut variation from 0.0 to 5.0 mm.

similar tests are conducted in Chapter 7, the radial immersion is set to 2.5 mm
and the depth of cut is changed from 0 to 5 mm in this test. The critical depth of
cut is determined by measuring the surface roughness (Ra) and setting a 0.5 μm
threshold. The milling tests are carried out with spindle rotations of ①, ②, ③,
and other 9 kinds of spindle rotations as summarized in Table 8-8 and the detail
cutting conditions are described in Table 8-9.

Figure 8-18 shows an example of the Ra measurement results. At the spindle
rotation of 13495 min^{-1}, it is clear from the Ra variation that the chatter occurs
just before the end of machining. The Ra exceeds the threshold when the depth of
cut is 4.30 mm. Therefore, the axial depth of cut can be determined as 4.30 mm at
spindle rotation of 13495 min^{-1}. In the same manner, the critical depth of cut at
each spindle rotation is summarized in Fig. 8-19, in which the circular plots
represent the results with the identified spindle rotations and the diamond plots
shows the results with the other spindle rotations. The critical depth of cut
certainly gets the locally largest values at the identified spindle rotations. As a
result, the proposed diagnosis method also can be performed in S500X1 by
applying a cutting condition at which the chatter sufficiently occurs.

Table 8-8   Evaluated spindle rotations.

	Spindle rotation min^{-1}	Feed rate mm/min
	13495	1180.81
②	12889	1127.79
	12283	1074.76
	11677	1021.74
	11070	968.63
④	10464	915.60
	10128	886.20
	9791	856.71
	9455	827.31
⑤	9118	797.83
	8870	776.13
	8621	754.34

Table 8-9   Cutting condition for adequacy tests.

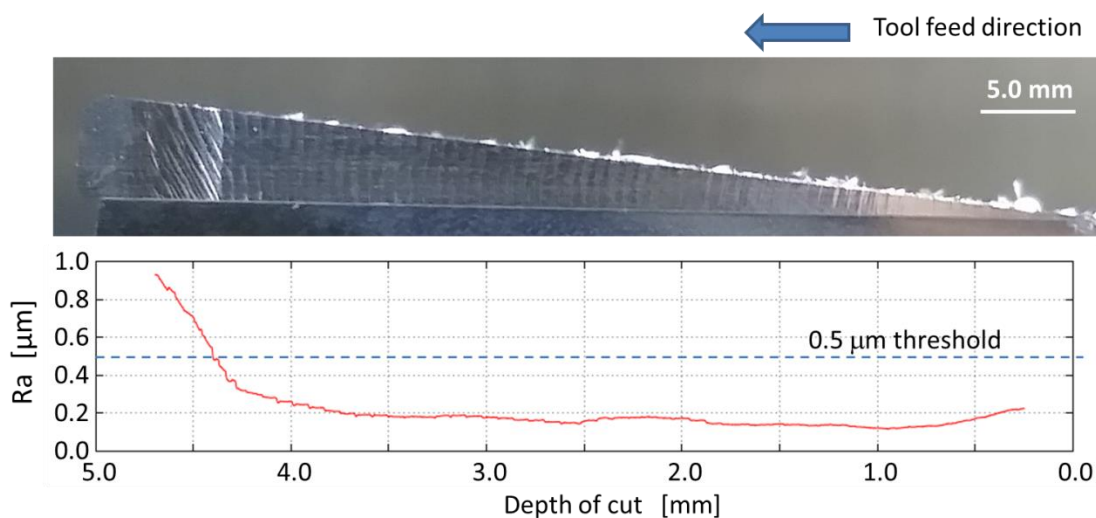|	
Feed per tooth mm	0.0438
Number of tooth	2
Override change rate %/s	50
Override range %	-30% − +60%
Axial depth of cut mm	0.0 − 5.0
Radial immersion mm	2.5

Fig. 8-18 The machined surface at the spindle rotation of 13495 min^{-1}.
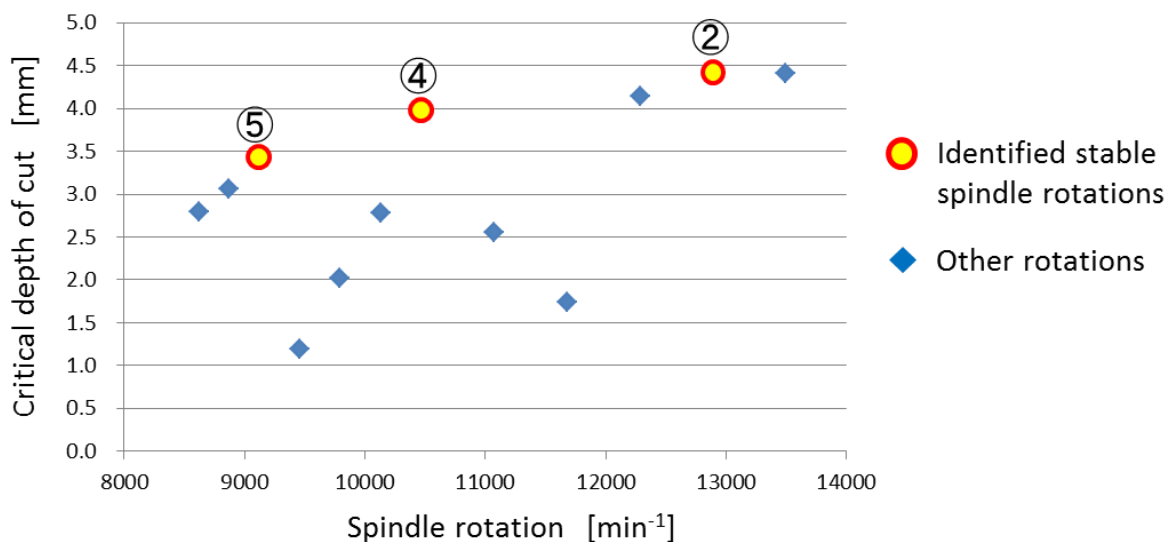

Fig. 8-19 The stability competition between the identified stable spindle rotations and others.

As a conclusion, the proposed diagnosis method certainly identifies stable spindle rotations against chatter, although the cutting conditions should satisfy following points.

Firstly, the spindle should be decelerated to capture stable spindle rotations because chatter frequency shifts are observed more clearly in the deceleration section than the acceleration section. The reason of difference between the deceleration and the acceleration is theoretically discussed by using time-domain milling simulator in the next section.

Secondary, the cutting condition should be suitable to generate large chatter. This is because the chatter frequency shifts cannot be clearly observed and the

stable spindle rotation cannot be identified stably when the chatter vibration is small.

8.5 Chatter Mechanism Analysis Based on a Time-Domain Milling Simulator

The reason of the difference between acceleration and deceleration in the proposed method tries to be clarified by two kinds of approaches here: time-domain simulation and frequency domain analysis.

If the cause of the difference between acceleration and deceleration is chatter mechanism itself, the difference would also appear in time-domain simulation results. By applying the modal parameters in Tables 8-10 and 8-11 and the cutting condition shown in Table 8-3, the time-domain milling simulations are conducted and the results are shown in Fig. 8-20 and 8-21. The frequency shifts are observed in both spindle rotation variations and certainly clearer in the deceleration section than in the acceleration section because the power spectrum density is high overall and the frequency component less than 1900 Hz is observable in the deceleration result. In the milling simulator, only cutting process including regenerative effect is realized as an excitation source of the tool, thus, it is theoretically clear that the difference between acceleration and deceleration is induced by the process itself.

Considering chatter mechanism in a frequency domain, the detailed reason of the difference can be explained clearly. Section 2.4.1 explains regenerative chatter mechanism, and the following equation is derived as a critical condition of

Table 8-10   Modal parameters of the tool.

	X direction	Y direction
National frequency Hz	2082	2082
Damping ratio	0.018	0.018
Mass kg	0.043	0.043

Table 8-11   Other parameters for the chatter stability prediction.

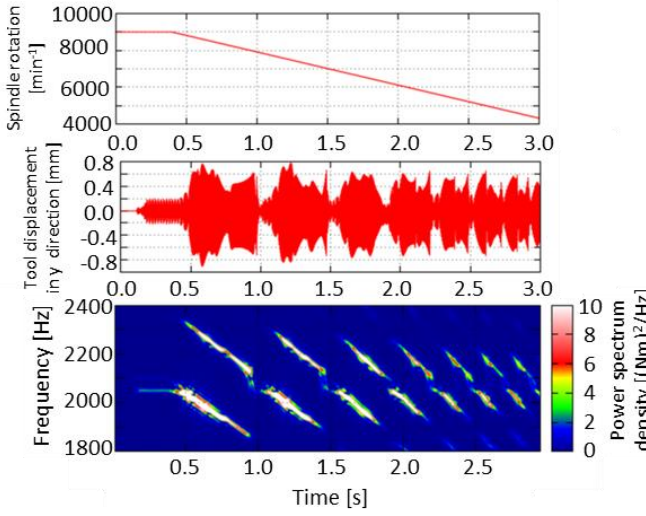| Number of tooth		2
Immersion angle deg		- 25.8～ 0.0
Cutting coefficient	Tangential MPa	1500
	Radial MPa	500

Fig. 8-20 Time-domain simulation of the proposed method of deceleration type.
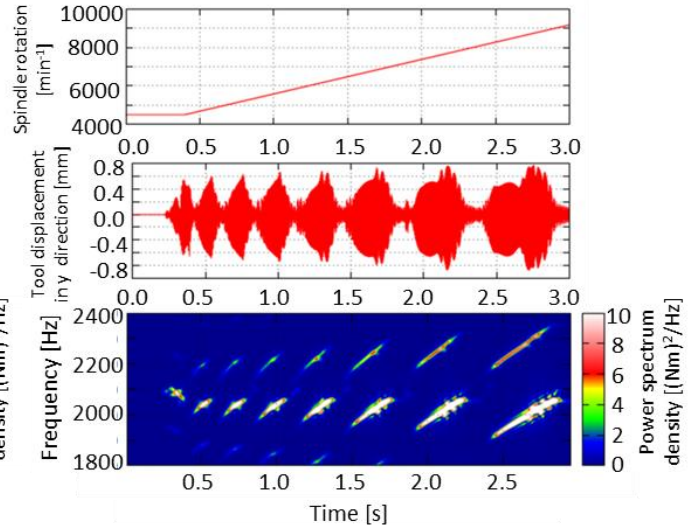
Fig. 8-21 Time-domain simulation of the proposed method of acceleration type.

the chatter stability.

$$\{F\}e^{j\omega_c t} = \frac{1}{2}aK_c[1 - e^{-j\omega_c T}][A_0][G(j\omega_c)]\{F\}e^{j\omega_c t} \tag{2-87}$$

where $\{F\}e^{j\omega_c t}$ is the dynamic component in the cutting force, $[G(s)]$ is the transfer function of the tool, $[A_0]$ is the directional dynamic cutting force matrix, K_c is the cutting coefficient, and a is the depth of cut. Furthermore, $[1 - e^{-j\omega_c T}]$ expresses the difference between the present value and the previous term value. Checking each part of this equation carefully, the product of $[G(j\omega_c)]\{F\}e^{j\omega_c t}$ in the right-hand side of the equation means the chatter frequency component of the present tool displacement. Thus, $[1 - e^{-j\omega_c T}][G(j\omega_c)]\{F\}e^{j\omega_c t}$ describes the tool displacement difference between present and previous term. Furthermore, the cutting force is defined as a product of tool displacement, the axial depth of cut, the directional matrix and the cutting coefficient as follows:

$$\{F(t)\} = \frac{1}{2}aK_c[A_0]\{\Delta(t)\} \tag{2-82}$$

where $\{\Delta(t)\}$ is the tool displacement.

Therefore, it can be said that Eq. 2-87 expresses the present dynamic cutting force $\{F\}e^{j\omega_c t}$ based on the dynamic cutting force itself including the transfer function of tool and the directional matrix. To have a solution in Eq. 2-87 excepting $\{F\} = \mathbf{0}$, its determinant must be zero.

In this theory, the amplitude of the dynamic cutting force in previous term is
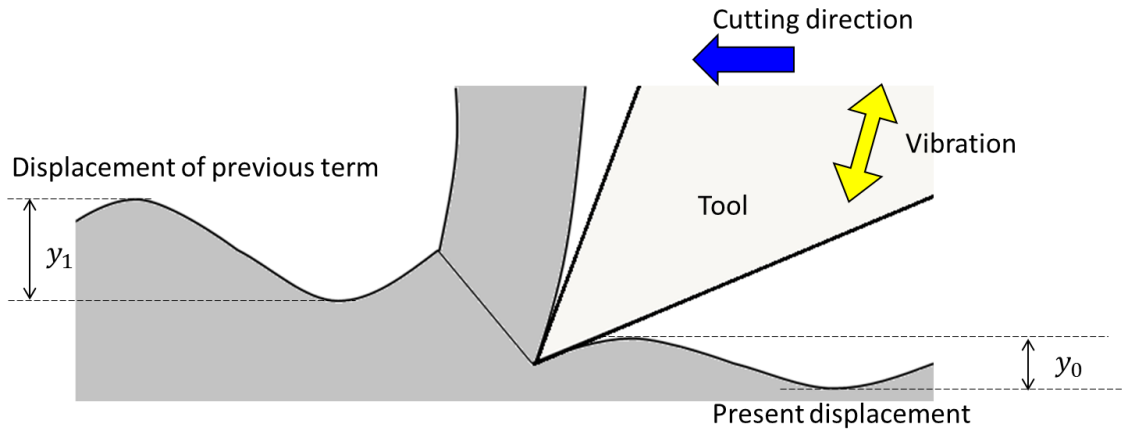
Fig. 8-22 A simple orthogonal cutting model.

assumed to be equal to the present dynamic cutting force. In other words, the dynamic force is not damped or expanded but continues fluctuating at static amplitude. Therefore, it is clear that the chatter stability analysis is not directly applicable to consider the time-dependent variation in the cutting force. For example, the chatter amplification must be higher at the larger axial depth of cut in the unstable region, however, the chatter stability analysis cannot distinguish the difference excepting the determination of stable or unstable.

The difference of three kinds of states (stable, unstable, critical) in the chatter stability analysis can be explained considering the amplitude ratio. As shown in Fig. 8-22, the amplitude of tool displacement is different between the present term y_0 and the previous term y_1. When the amplitude ratio is defined as $\mu = y_0/y_1$, the process can be regarded as the stability limit in case of $\mu = 1$. If $\mu < 1$, the chatter is exponentially damped, and the cutting stability is higher with smaller μ. In contract, when $\mu > 1$, the chatter is exponentially expanded at the ratio of μ, i.e., the chatter grows large more drastically with higher μ. Therefore, not only the stability limit but also the degree of stability would be possible to evaluate by installing μ to the chatter analysis.

Based on the above discussion, the amplitude ratio μ is applied into the equation explaining regenerative effect mechanism as follows:

$$\{F\}e^{j\omega_c t} = \frac{1}{2}aK_c\left[1 - \frac{1}{\mu}e^{-j\omega_c T}\right][A_0][G(j\omega_c)]\{F\}e^{j\omega_c t} \tag{8-1}$$

By multiplying $1/\mu$ to the tool displacement in previous term, the cutting condition, in which the present tool displacement is μ times as large as the previous one, can be expressed. To have a solution in Eq. 8-1 excepting $\{F\} = \mathbf{0}$, its determinant must be zero.

$$\det\left[[I] - \frac{1}{2}aK_c\left[1 - \frac{1}{\mu}e^{-j\omega_c T}\right][A_0][G(j\omega_c)]\right] = 0 \qquad (8\text{-}2)$$

Like the chatter stability analysis method, one diagram can be drawn for each μ based on Eq. 8-2 corresponding to the spindle rotation and the depth of cut. Therefore, By changing μ and repeating drawing the diagram for each μ, the amplitude ratio distribution can be drown as shown in Fig. 8-23. To compare with a usual stability lobe diagram, the obtained amplitude ratio is actually high at center of the unstable region and gets low in the stable region. Furthermore, the diagram of $\mu = 1$ theoretically fits with the stability lobes.

Focusing on the amplitude ratio distribution in the unstable region, the large amplitude ratio appears in the right side of the lobe disproportionally. Therefore, it can be assumed that chatter expands earlier in the right side of the lobe than left side. This assumption is discussed through the time-domain simulation here.

By the way, when the radial immersion is small, the stable region of real process is wider than that analyzed with a frequency domain model. This is because the frequency domain model ignores the situation that the tool jumps out from the workpiece, which easily occurs when the radial immersion is small. Although such non-linearity is difficult to consider in the frequency domain, it is easy to realize in a time-domain simulator. Therefore, the stability lobe diagram
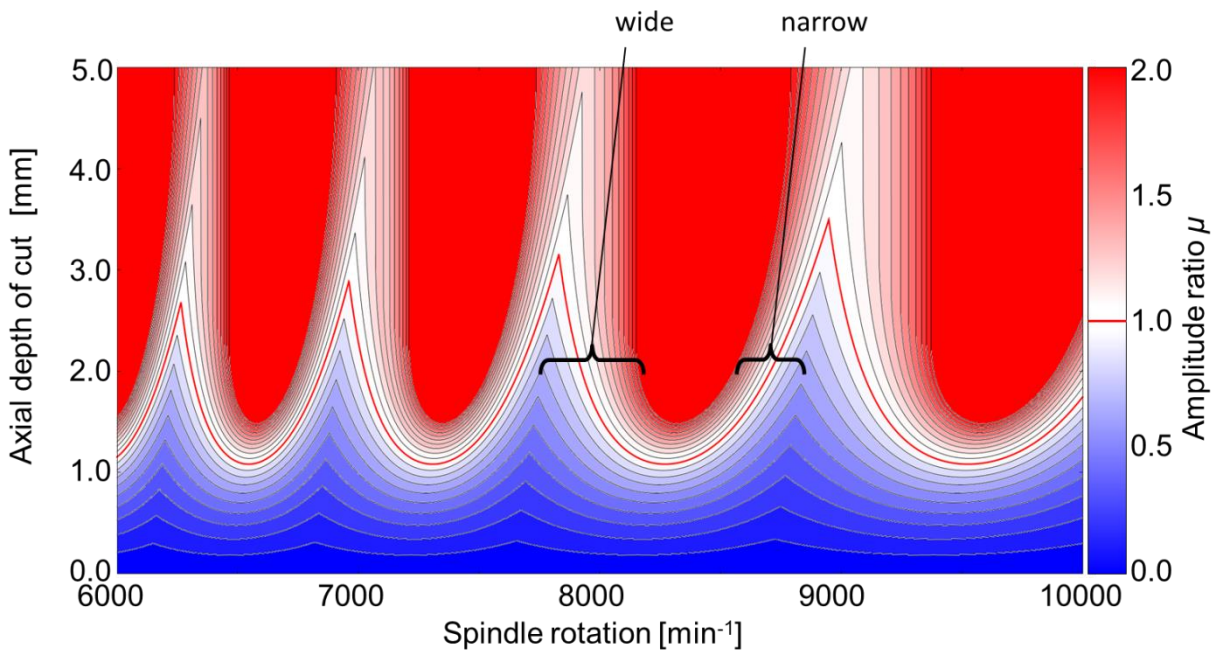

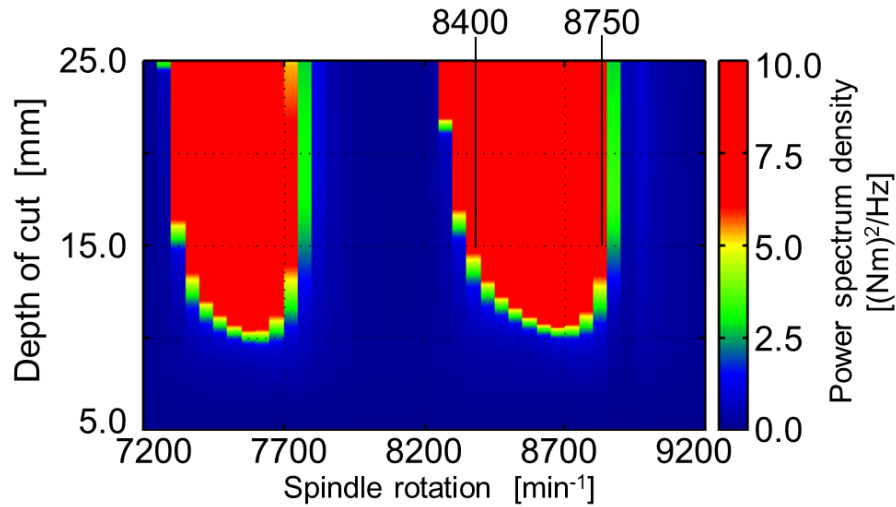Fig. 8-23   The distribution of amplitude ratio.

Fig. 8-24　Time-domain simulation-based stability lobe diagram.

of time-domain milling model is drawn by simulating the milling on a triangle shaped workpiece, as the experiments in Chapter 7. By arranging the color gradation based on the power spectrum density of cutting torque in each simulation result in parallel, the stability diagram can be derived as Fig. 8-24. Focusing on the lobe between 8200 to 8800 min^{-1}, the spindle rotations from 8400 to 8500 min^{-1} are regarded as left side of the lobe and that from 8650 to 8750 min^{-1} are regarded as right side of the lobe here.

　Figure 8-25 shows the time-domain simulation results with various spindle rotations in the unstable spindle rotations. To evaluate the chatter generations at each spindle rotation fairly, the simulations are conducted by placing the surface profiles as the tool has already immersed into the workpiece as shown in Fig. 8-26. Furthermore, to evaluate the chatter generation, power calculation of cutting torque is conducted by requiring the average of square values of the cutting torque as shown in Fig. 8-27. In Fig. 8-25, chatter occurs at the spindle rotations from 8500 to 8700 min^{-1}. Comparing the time-dependent variation of chatter at 8500 and 8550 min^{-1}, the chatter generates clearly earlier at the spindle rotation of 8650 and 8700 min^{-1}. This result also indicates that chatter generates more drastically under the conditions of right side of the stability lobe than that of left side.

　From these theoretical discussions and simulation results, the reason of the difference between acceleration and deceleration in the proposed method is obvious. The acceleration of the spindle rotation can be regarded as the variation from the left side to right side in the chatter stability diagram. In this case, the
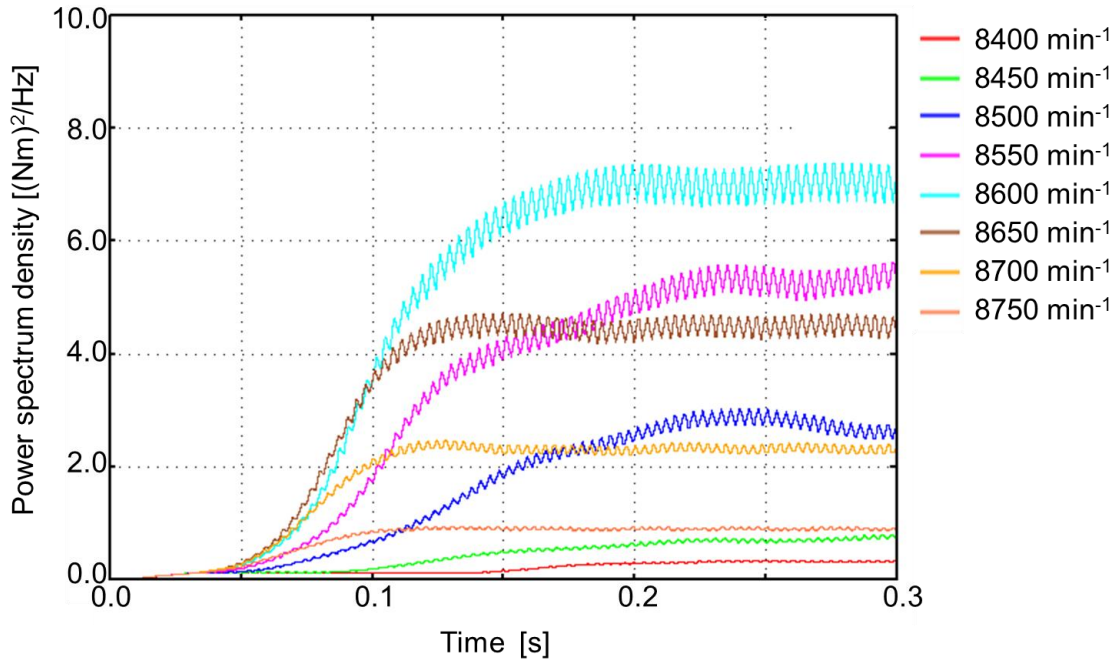
Fig. 8-25　Time-domain simulation results of each spindle rotation.
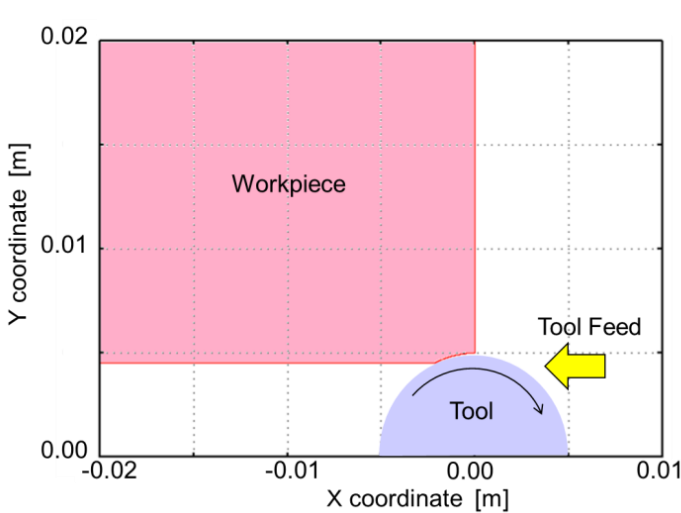
Fig. 8-26　Initial placement of workpiece and tool.
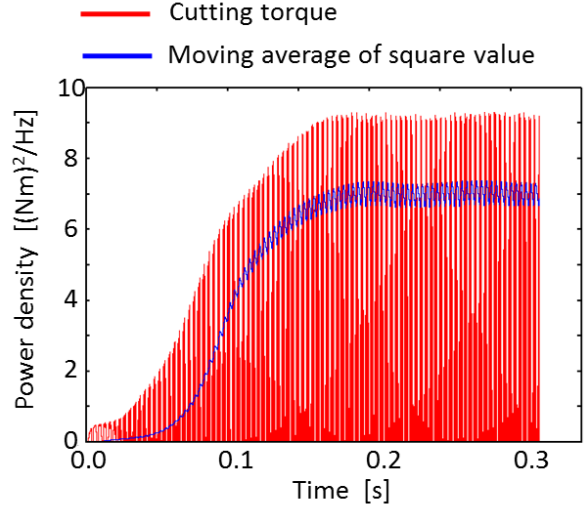
Fig. 8-27　Moving average of square value.

chatter gradually grows at left side of a stability lobe. On the other hand, when the spindle rotation is decelerated, i.e. in case of the variation from the right side to left side, the chatter suddenly expands at the right side of the stability lobe. In both cases, the chatter continues in the section above the stability lobe and is suppressed when the cutting condition gets into the stable region. Although the chatter does not behave as these variations in real process because the tool jumps out from the workpiece when the tool displacement becomes large, the difference of the amplitude ratio is a capital cause of the difference between the acceleration

173

and deceleration in the proposed method.

Finally, the relation between the override changing rate and the identification error is discussed through the time-domain milling simulation here.

Figures 8-28 and 8-29 show the time-domain result of the diagnosis method, where the modal parameters and the other conditions are given as Tables 8-10 and 8-11. The axial depth of cut is set to 15 mm and radial immersion is set to 0.5 mm respectively. As the STFT analysis result shows, chatter frequency shift occurs four times during decelerating the spindle rotation. This is also confirmed from the machined surface appearance as the unique chatter mark of four lines in the deceleration section. For comparison, a stability lobe diagram is drawn by using the same parameters in Fig. 8-30. Four stability pockets are confirmed and each s table spindle rotations are obtained from 5400 to 9000 min^{-1}.

The identification error of the stability pocket theoretically would be suppressed if the identification time is ensured sufficiently long, because
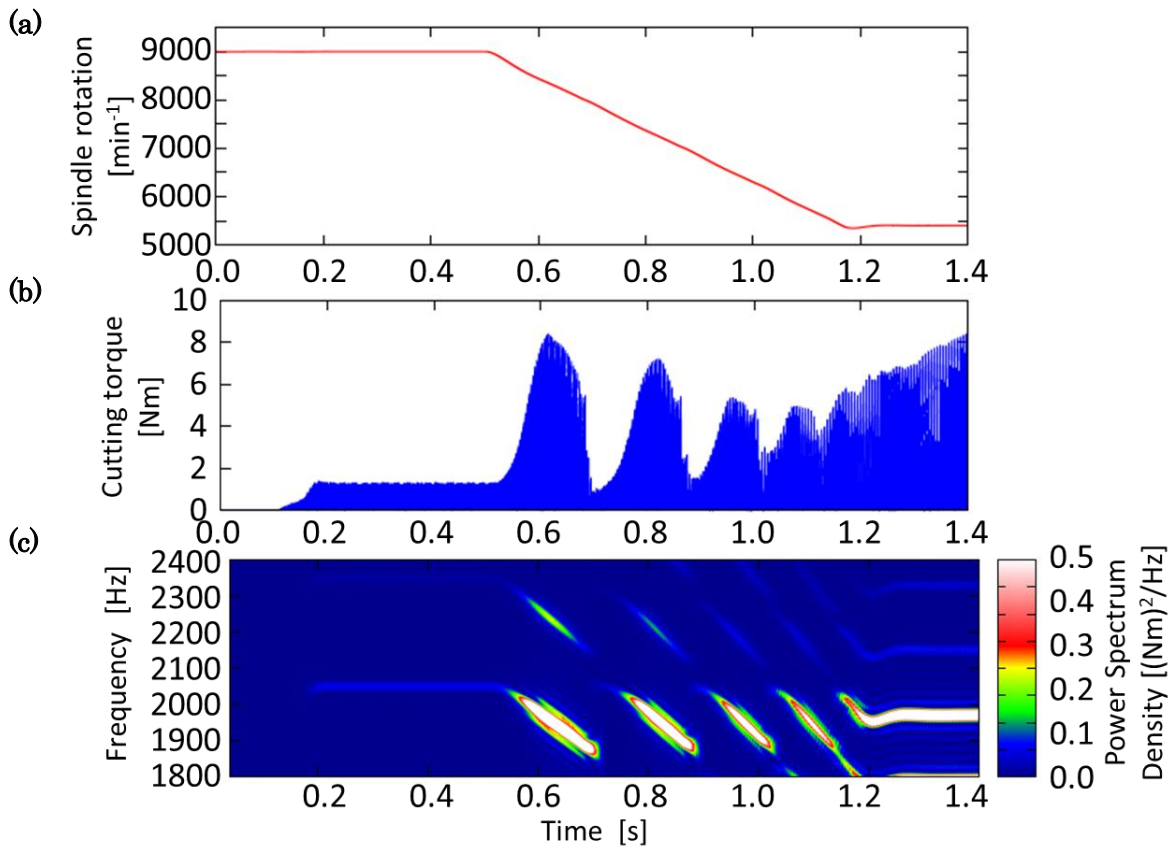
Fig. 8-28 Simulation result (50 %/s override changing rate); (a) spindle rotation; (b) cutting torque; (c) short-time Fourier transform analysis.

174
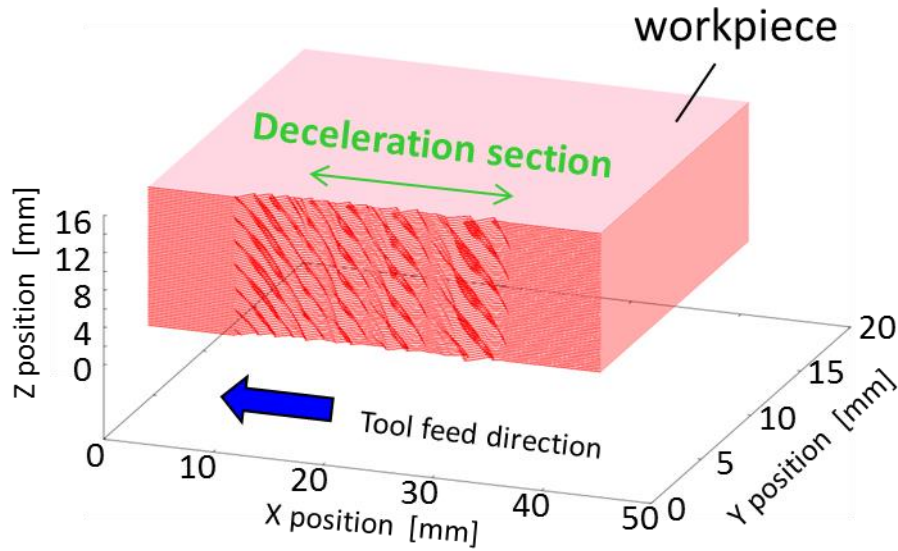
Fig. 8-29 The workpiece surface in the simulation (50 %/s override changing rate).
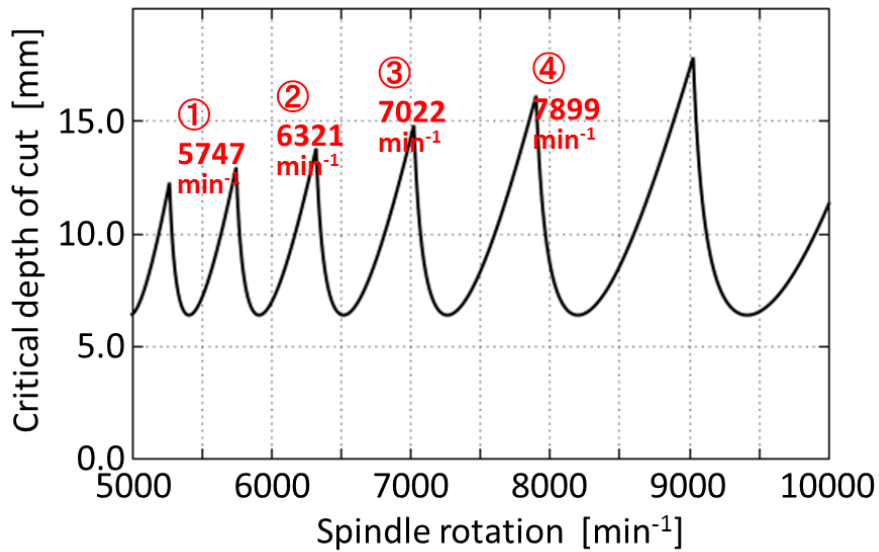
Fig. 8-30 Stability lobes drawn with a frequency-domain milling model.

frequency-domain analysis assumes infinite response time and its response can be acquired approximately with enough long response time. In contrast, the response time has to be as short as possible because the identification time is limited in process. From this viewpoint, if the expected identification error is preliminarily known, the identification accuracy can be enhanced by compensating the error, even if the identification time is strictly limited. To derive a theoretical compensation equation, the time-domain milling simulation is repeated with various override changing rates. Figure 8-31 shows the relation
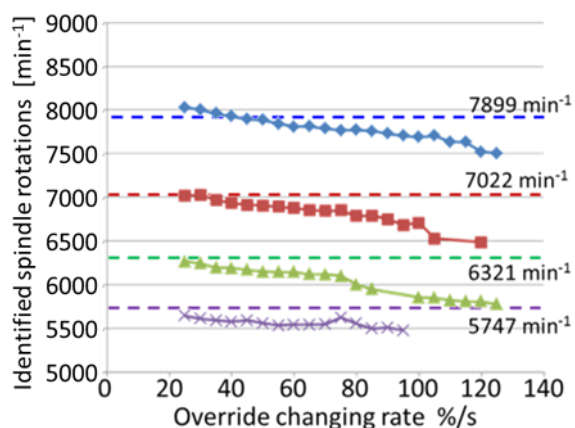
Fig. 8-31 Identified stability pocket in each override changing rate.
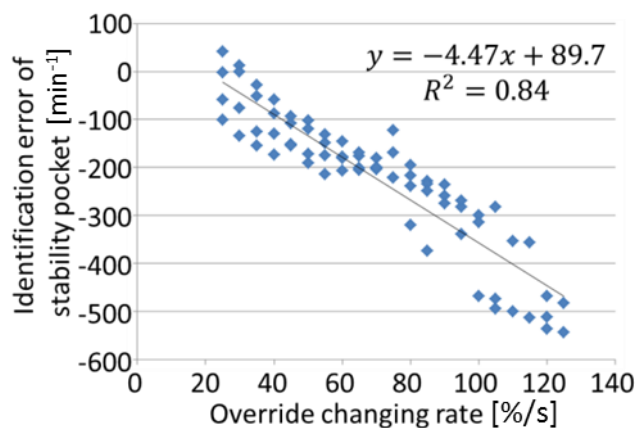
Fig. 8-32 Identification error of stability pocket in each override changing rate.

between the override changing rate and the identified stable spindle rotations with the proposed method. The identified spindle rotations gradually get lower with larger override changing rate, thus, the error becomes larger with larger override changing rate between the theoretical stable spindle rotation and the identified one. However, even at 50 %/s override changing rate which is employed in this research, the identification error is only from -200 to -100 min^{-1}. It can be said that the time response of chatter frequency is sufficiently high to perform the proposed diagnosis method in a short time.

Figure 8-32 summarizes the identification error of the stable spindle rotations for each override changing rate. The coherence coefficient is high as 0.84 between the identification error and the override changing rate. Although the compensation equation can be developed by performing the simulation with various parameters, this approach would finally require the accurate identification of various parameters such as modal parameters. However, it is against the purpose of this research focusing on the simplification. Consistently, the proposed method should be an approach available without complicated modal analysis. As a future step of this research, a simple system identification method, which never requires sensor devices and complicated operations, would be a significant challenge to enhance the identification accuracy of the proposed method.

8.6 Summary

This chapter proposes a chatter stability diagnosis method and evaluates it through side milling tests with two kinds of 3-axis vertical machine tools. On the basis of chatter frequency characteristic, the proposed diagnosis method can identify the stable spindle rotations against chatter only with once milling test. The obtained results are represented as follows.

①   The proposed stability diagnosis method experimentally shows that the stable spindle rotations against chatter can be identified by contentiously decelerating spindle rotation during chatter and capturing a drastic shift in the chatter frequency with disturbance observer. This technique is applicable even under a large override changing rate as 50 %/s. However, in order to observe the chatter frequency shift clearly, the cutting condition is required to ensure comparatively large depth of cut to generate large chatter.

②   By discussing the chatter mechanism with the developed time-domain milling simulator and frequency-domain milling model, this research theoretically shows that expansion rate of chatter varies according to the spindle rotation and depth of cut, and the process easily becomes unstable when spindle is decelerated. Therefore, it is concluded that the spindle rotation should be decelerated in the proposed diagnosis.

③   The identification error of the proposed diagnosis method is discussed with the milling simulator. Although the identification error certainly gets large when changing rate of the spindle rotation is too high, the identification error is small enough even with high override changing rate as 50 %/s.

The proposed technique is actually practical because it can be performed with only once milling test without any additional devices and complicated operations. This research experimentally shows the practicability and usability of the proposed stability diagnosis; on the other hand, applicability and versatility to other machine tools and processes would be significant issues as future works.

9 Conclusions

In this thesis, realtime process monitoring method is developed to detect tool wear progress, tool collision, tool fracture, and chatter vibration by means of disturbance observer which estimates disturbance force using servo information. Furthermore, chatter stability diagnosis method is established by integrating chatter stability theory with disturbance estimation technique. The feasibility of both proposals is experimentally evaluated through various tests in machine tools.

In first chapter of this thesis, background and purpose of this research are described by introducing significant issues in machine tools and state-of-the-art challenges for process monitoring and stability analysis. The necessity of sensorless approach is emphasized from the viewpoint of practicability and usability.

In Chapter 2, essential theories for the proposed process monitoring and stability diagnosis are described. Firstly, disturbance observer theory is explained to propose observer-based cutting force/torque estimation. Because cutting force/torque is regarded as a disturbance interfering on the precise motion control of the spindles and stages in a machine tool, disturbance observer theory is applicable to estimate cutting force/torque only from servo information in a machine-tool control system. As many researchers have experimentally proven, cutting force/torque is critically useful to grasp the machining states, e.g., the cutting force/torque gradually increases according to tool wear progress, drastically increases when tool collision occurs, and periodically fluctuates when chatter or tool fracture occurs. In order to purely estimate cutting force/torque from servo information, the proposed method compensates friction and gravity from the estimated disturbance force/torque by considering physical models of a spindle and a ballscrew-driven stage.

Moreover, novel signal processing methods named "integration of moving variance and moving Fourier transform (MV+MFT)" and "rotational digital filter (RDF)" are proposed. The MV+MFT is time-frequency-domain analysis algorithm specialized for realtime chatter detection, whose computation load is abundantly low. The MV+MFT can detect chatter separately from forced vibration. The RDF

has a unique characteristic to extract a clock-wise component from a signal moving on a two dimensional surface. Considering that the fracture-induced fluctuation in cutting force moves in X and Y directions along with the spindle rotation in drilling, the drill fracture can be detected with RDF much more accurately than conventional frequency analysis methods. Applying these signal processing methods to the estimated cutting force/torque, the applicability and the detection accuracy of the proposed process monitoring are enhanced.

Finally, the concept of stability diagnosis for chatter is introduced by explaining chatter mechanism with a frequency-domain milling model. Focusing on a characteristic of chatter frequency, identification for stable spindle rotation against chatter is proposed, which gradually decreases the spindle rotation during chatter and captures drastic shifts in chatter frequency from the estimated cutting torque. Furthermore, how to create a time-domain milling simulation is also introduced to theoretically evaluate the proposed stability diagnosis method.

Based on these fundamentals, the realtime monitoring and stability diagnosis of cutting process are developed without any additional sensors and measurement devices. The performance evaluations of the proposed methods are presented in Chapters 4 – 8.

In Chapter 3, experimental apparatuses for cutting tests and simulations are introduced. Two kinds of 3-axis vertical machine tools are used in this research to evaluate the proposed methods, thus, both of their mechanical characteristics and nominal parameter settings are listed. Furthermore, fundamentals of CUDA (compute unified device architecture) are introduced because this research employs a CUDA-based parallel calculation system for the time-domain milling simulation. Generally speaking, a time-domain simulation requires much computation time compared with a frequency-domain analysis. Therefore, this research applies the CUDA-based parallel calculation to the time-domain milling simulation, and successfully shortens the computation time to one eighty-third compared with CPU calculation.

In Chapter 4, tool wear monitoring is conducted in drilling and tapping with the proposed cutting force/torque estimation. The results of drilling and tapping tests clearly show that the thrust force and cutting torque are certainly able to be estimated from a ball-screw driven stage and a spindle control system.

In drilling with 3-mm-diameter drills, no remarkable change in the estimated cutting torque is observed, although increase in the thrust force is confirmed. In tapping, the wear-induced increase is observed only in the estimated cutting torque. Although the proposed cutting force/torque estimation has enough accuracy to detect the increase of cutting force and torque due to tool wear progress, the reliable criterion for wear monitoring should be carefully selected considering the wear-induced variation in each process.

In Chapter 5, tool collision detection is performed with the proposed cutting force estimation algorithm. The collision force is regarded as an instant external load and is observable in the proposed method. The proposed collision detection uses a pseudo-differential value of the estimated collision force to emphasize the collision-induced fluctuation. Furthermore, a modification method for the cutoff frequency of low-pass filters is proposed to enhance the time response and the robustness against errors of detection.

The experimental results show that tool collisions with 7- and 5-mm-diameter drills in horizontal direction can be sufficiently detected within 3 ms. However, collisions with 3-mm-diameter drills in the horizontal direction cannot be detected because the collision-induced fluctuation in the pseudo-differential value is too small to exceed the threshold. In the vertical direction, the tool collisions clearly can be detected even with a long-type 3-mm-diameter tool. However, the fluctuation at resonance frequency exceeds the threshold during accelerating/decelerating when the feed rate is set to 5000 mm/min. Although a two-mass-system would be able to eliminate the fluctuation from the pseudo differential value, it is not acceptable because the number of nominal parameters increases, which have to be identified accurately. To avoid the misdetection, a dynamic threshold would be a practical approach, which takes different values depending on the motion of the stage.

In Chapter 6, drill fracture detection method is proposed and evaluated through drilling tests with non-fractured and fractured drills. Firstly, the characteristics of RDF are evaluated and confirmed through time-domain simulations. The simulation results clearly shows that the RDF certainly has band-pass filtering effect and clock-wise signal pass effect simultaneously.

By applying RDF to the estimated cutting force in X and Y directions, the fracture-induced clock-wise fluctuation in cutting force is captured with high

accuracy. Comparing contentious wavelet transform analysis, RDF-based analysis can emphasize the difference between non-fractured and fractured drills because the RDF can reduce the signal noise more efficiently. The proposed fracture detection method has sufficiently high accuracy to detect a small drill fracture only with the servo information in X- and Y-direction ballscrew-driven stage system.

In Chapter 7, chatter vibration detection in milling is presented by analyzing the estimated cutting torque. Moreover, the applicability of the MV+MFT algorithm to realtime process monitoring is evaluated with computational time measurements, comparing with that of fast Fourier transform (FFT) algorithm. Although FFT requires large number of computations which cannot be finished within a servo cycle, MV+MFT consumes only about 300 ns in one periodic term, which is sufficiently short time to perform in realtime.

The milling tests are conducted with two kinds of 3-axis vertical machine tools. By applying the MV+MFT analysis to the estimated cutting torque, the chatter can be detected separately from forced vibration in realtime. The distribution of the obtained power spectrum density of chatter is highly-similar to that of the surface roughness measurement results. The analysis results also indicate that the forced vibration has no influences on the roughness of machined surface. This is because the forced vibration does not change cusp height on the machined surface.

In Chapter 8, the proposed stability diagnosis for chatter is performed to identify the stable spindle rotations. The experimental result shows that deceleration is a suitable variation for spindle rotation in the stability diagnosis because chatter frequency can be observed more clearly than the result in acceleration. The reason of difference between acceleration and deceleration is theoretically discussed with time-domain simulation and frequency-domain analysis. As a result, it is clarified that the expansion rate of chatter is larger at right side of a stability lobe diagram than the left side and the chatter easily gets large when the spindle rotation is decelerated.

The experimental results also indicate that the proposed stability diagnosis cannot identify the stable spindle rotations when enough depth of cut cannot be ensured. In this case, chatter does not occur largely and the chatter frequency shift cannot be observed clearly. The chatter frequency shift itself can be observed

even under the large variation of spindle rotation such as 50 %/s override changing rate. Furthermore, the repeatability of the proposed method is sufficiently high when the chatter frequency shift is clearly observed.

The time-domain milling simulation results show that the identification error gets large when the spindle rotation variation is large and the error compensation equation can be derived with the simulation results. However, the simulation-based approach requires accurately-identified parameters, which is against demand of simplification. The practical usage of the simulation results would be a future work for the proposed stability diagnosis.

Because combined and parallel machine tools start to be used in recent industries, process monitoring and stability diagnosis will be focused on much more as indispensable technologies to ensure efficiency, usability, stability, and safety in machining in the near future. Against this background, this thesis provides a sensorless approach to grasp the machining state in realtime based on the disturbance observer theory. Focusing on tool wear, tool collision, tool fracture, and chatter as problems in process, this research theoretically and experimentally shows that the proposed process monitoring can detect each problem with high accuracy and reliability without any additional sensors. Furthermore, the proposed chatter stability diagnosis method can identify the stable spindle rotations accurately with only once milling test without any measurement devices. From viewpoint of the practicability and usability, the proposed methods in this research certainly provide new sensorless solutions which sufficiently satisfy the demands of industries.

The proposed realtime process monitoring and stability diagnosis of cutting process will contribute to the progress of manufacturing technology and be widely applied as one of the fundamental technologies.

Acknowledgement

I would like to express my deepest gratitude to my supervisor Associate Professor Yasuhiro Kakinuma, for high continuous support and exceptional guidance throughout this challenging and rewarding research work.

I would also like to express my appreciation to Professor Toshiyuki Murakami, Professor Yan Jiwang, and Associate Professor Masaki Takahashi at Keio University for reviewing the dissertation and providing me with helpful suggestions and comments. My gratitude also goes to Professor Tojiro Aoyama and Professor Kouhei Ohnishi at Keio University for their helpful guidance and support in my research.

I also thank Teruhisa Kojima, Hiroaki Nomura, and Yuzuru Terada from Brother Industries, Ltd. for their technical supports and suggestions in my research.

I would like to thank Michie Ishiwata for her kind supports to my research. My warmest regard goes to former and current members in Aoyama and Kakinuma laboratories at Keio University, both the graduates and undergraduates.

I would also like to acknowledge to financial supports by scholarship from Japan Student Services Organization and the Grant-in-Aid for JSPS Fellows from the Japan Society for the Promotion of Science.

Finally, I would like to express special thanks to my father Jun Koike and my mother Naomi Koike for their continuous encouragement and support.

January 7, 2016

Ryo Koike

Reference

[1] I. Inasaki, Machining system, Youkendou, (2009), pp. 72. (in Japanese)

[2] T. Moriwaki, Multi-functional machine tool, CIRP Annals – Manufacturing Technology, 57(1), (2008), pp. 736-749.

[3] I. Inasaki, Machining system, Youkendou, (2009), pp. 71. (in Japanese)

[4] R. Teti, K. Jemielniak, G. E. O'Donnell, D. Dornfeld, Advanced monitoring of machining operations, CIRP Annals – Manufacturing Technology, 59(2), (2010), pp. 717-739.

[5] G. Byrne, D. Dornfeld, I. Inasaki, G. Ketteler, W. König, R. Teti, Tool condition monitoring (TCM) – The status of research and industrial application, CIRP Annals – Manufacturing Technology, 44(2), (1995), pp. 541-567.

[6] H. K. Tönshoff, J.P. Wulfsberg, H. J. J. Kals, W. König, C. A. van Luttervelt, Development and trends in monitoring and control of machining process, CIRP Annals – Manufacturing Technology, 37(2), (1988), pp. 611-622.

[7] J. Tlusty, G. C. Andrews, Acritical review of sensors for unmanned machining, CIRP Annals – Manufacturing Technology, 32(2), (1983), pp. 563-573.

[8] D. F. Micheletti, W. König, H. R. Victor, In process tool wear sensor for cutting operations, CIRP Annals – Manufacturing Technology, 25(2), (1976), pp. 483-496.

[9] Japanese Standards Association, JIS handbook 5. Tool, Japanese Standards Association, (2014), pp. 81, 107, 155. (in Japanese)

[10] Y. Altintas, Manufacturing automation, Cambridge, University Press, (2012), pp. 54-61.

[11] I. Inasaki, Machining system, Youkendou, (2009), pp. 46. (in Japanese)

[12] E. O. Ezugwu, J. Bonney, D. A. Fadare, W. F. Sales, Machining of nickel-base inconel 718 alloy with ceramic tools under finishing conditions with various coolant supply pressures, Journal of Materials Processing Technology, 162-163, (2005), pp. 609-614.

[13] Y. Hou, D. Zhang, B. Wu, M. Luo, Milling force modeling of worn tool and tool flank wear recognition in end milling, IEEE/ASME Transactions on Mechatronics, 20(3), (2015), pp. 1024-1035.

[14] F. Halila, C. Czarnota, M. Nouari, New stochastic wear law to predict the abrasive flank wear and tool life in machining process, Proceedings of the Institution of Mechanical Engineers, Part J: Journal of Engineering Tribology, 228 (11), (2014), pp. 1243-1251.

[15] F. W. Taylor, On the art of cutting metals, The American Society of Mechanical Engineers, (1906), paragraph 700 and 718.

[16] E. Abele, M. Dervisopoulos, M. Kreis, Beeinflussbarkeit von Lebenszykluskosten durch Wissensaustausch–Produzieren mit Blick auf die Lebenszykluskosten. wt Werkstattstechnik Online, 96(7-8), (2006), pp.447 - 454.

[17] M. Metzele, Zustandsorientierte Instandhaltung von schnelllaufenden Werkzeugmaschinen-Hauptspindeln. Doctoral Thesis, (2008), WZL-RWTH Aachen.

[18] E. Abele, D. Korff, Avoidance of collision-caused spindle damages – challenges, methods for high dynamic machine tools, CIRP Annals – Manufacturing Technology, 60(1), (2011), pp. 425-428.

[19] M. Schumann, M. Witt, P. Klimant, A real time collision prevention system for machine tools, Procedia CIRP 7, (2013), pp.329-334.

[20] F. Bandini, R. Parigi, Collision avoidance smoothing: a viscous-elastic model, Procedia CIRP 8, (2013), pp.9-14.

[21] X. Zhang, X. Tian, K. Yamazaki, On-machine 3D vision system for machining setup modeling, Int J Adv Manuf Technol, 48, (2010), pp. 251-265.

[22] G. Byrne, G. E. O'Donnell, An integrated force sensor for process monitoring of drilling operations, CIRP Annals – Manufacturing Technology, 56 (1), (2007), pp.89-92.

[23] M. S. Uddin, K. Yamazaki, Study of distance computation between objects represented by discrete boundary model, International Journal of Graphics, 1 (1), (2010), pp. 29-43.

[24] T. Rudolf, C. Brecher, F. Possel-Dölken, Contact-based collision detection – a new approach to avoid hard collisions in machine tools. (2007), International Conference on Smart Machining Systems.

[25] T. N. Moore, R. Kiss, Detection of milling cutter insert fracture using vibration signals, International Matador Conference, 31, (1995), pp. 255-260.

[26] F. Čuš, U. Župerl, Real-time cutting tool condition monitoring in milling, Strojniški vestnik – journal of mechanical engineering, 57(2), (2011), pp. 142-150.

[27] H. Takeshita, I. Inasaki, Monitoring of milling process with an acoustic emission sensor, The Japan Society for Precision Engineering, 59(2), (1993), pp. 269-274. (in Japanese)

[28] K. Nagayoshi, K. Mori, G. H. Ruiz, Detection of tool failure in milling process using discrete wavelet transform, Transactions of the Japan Society of Mechanical Engineers , 61(583), (1995), pp. 1204-1210. (in Japanese).

[29] A. Thangaraj, P. K. Wright, Drill wear and failure prediction for untended machining, Robotics and computer-integrated manufacturing, 4(3), (1988), pp. 429-435.

[30] M. Takatsuto, N. Takada, K. Kato, K. Kishi, Judgement of tool life in drilling using acoustic emission, JSME International Journal Series C, 37(1), (1994), pp. 224-229.

[31] M. Routio, M. Säynätjoki, Tool wear and failure in the drilling of stainless steel, Journal of Materials Processing Technology, 52, (1995), pp. 35-43.

[32] N. Suzuki, Chatter vibration in cutting part 1, Journal of the Japan Society for Precision Engineering, 76(3), (2010), pp. 280-284. (in Japanese)

[33] H. E. Merritt, Theory of self-excited machine-tool chatter, contribution to machine-tool chatter, ASME J. Eng. Ind., 87, (1965), pp. 447-454.

[34] M. K. Das, S. A. Tobias, The relation between the static and the dynamic cutting of metals, International Journal of Machine Tool Design and Research, 7(2), (1967), pp. 63-89.

[35] T. Matsubara, H. Yamamoto, H. Mizumoto, Study on regenerative chatter vibration with dynamic cutting force, Journal of the Japan Society of Precision Engineering, 50(7), (1984), pp. 1079-1083. (in Japanese)

[36] Y. Altintas, E. Budak, Analytical prediction of stability lobes in milling, CIRP Annals – Manufacturing Technology, 44(1), (1995), pp. 357-362.

[37] S. Kato, E. Marui, Some considerations on prevention of chatter vibration in boring operation, Transaction of JSME, 33(254), (1967), pp. 1685-1692.

[38] H. Ota, and K. Kono, Chatter vibrations of machine tool or work with directional stiffness inequality, Transactions of JSME, 38(314), (1972), pp. 2543-2557.

[39] H. Ota, M. Kito, T. Handa, A study on primary chatter caused by mode coupling of machine tool structure, Transactions of the Japan Society of Mechanical Engineers Series C, 73(726), (2007), pp. 570-576. (in Japanese)

[40] J. Tlusty, G. C. Andrews, A critical review of sensors for unmanned machining, CIRP Annals – Manufacturing Technology, 32 (2), (1983), pp. 563-572.

[41] A. Thangaraj, P. K. Wright, Drill wear and failure prediction for untended machining, Robotics and Computer-Integrated Manufacturing, 4 (3-4), (1988), pp. 429-435.

[42] M. Takatsuto, N. Takada, K. Kato, K. Kishi, Judgement of tool life in drilling using acoustic emission, JSME International Journal Series C, 37(1), (1994), pp. 224-229.

[43] M. Rouito, M. Säynätjoki, Tool wear and failure in the drilling of stainless steel, Journal of Materials Processing Technology, 52, (1995), pp. 35-43.

[44] G. O'Donnell, P. Young, K. Kelly, G. Byrne, Towards the improvement of tool condition monitoring systems in the manufacturing environment, Journal of Materials Processing Technology, 119, (2001), pp. 176-195.

[45] K. Jemielniak, R. Teti, J. Kossakowska, T. Segreto, Innovative signal processing for cutting force based chip from prediction, 2nd I*PROMS Virtual International Conference on Intelligent Production Machines and Systems, (2006), pp. 7-12.

[46] C. Brecher, T. Rudolf, Adaptive logging module for monitoring applications using control internal digital drive signals, Production Engineering Research and Development, 3, (2009), pp. 305-312.

[47] A. Verl, U. Heisel, M. Walther, D. Maier, Sensorless automated condition monitoring for the control of the predictive maintenance of machine tools, CIRP Annals – Manufacturing Technology, 58(1), (2009), pp. 375-378.

[48] Y. Altintas, E. Shamoto, P. Lee, E. Budak, Analytical prediction of stability lobes in ball end milling, Transactions of the ASME, 121(4), (1999), pp. 586-592.

[49] S. S. Park, R. Rahnama, Robust chatter stability in micro-milling operations, CIRP Annals – Manufacturing Technology, 59(1), (2010), pp. 375-378.

[50] E. Budak, L. T. Tunc, Identification and modeling of process damping in turning and milling using a new approach, CIRP Annals – Manufacturing Technology, 59(1), (2010), pp. 403-408.

[51] I. Bediaga, M. Zatarain, J. Muñoa, R. Lizarralde, Application of continuous spindle speed variation for chatter avoidance in roughing milling, Proceeding of the Institution of Mechanical Engineers, Part B: Journal of Engineering Manufacture, 225(5), (2010), pp. 631-640.

[52] K. Shirase, M. Sano, M. Hirao, T. Yasui, Analysis and suppression of chatter vibration in end milling operation (1st report): analysis of chatter vibration for irregular tooth pitch end mill using time domain cutting simulation, Journal of the Japan Society for Precision Engineering, 64(3), (1998), pp. 465- 469. (in Japanese)

[53] A. Matsubara, T. Yamazaki, S. Ikenaga, Non-contact measurement of spindle stiffness by using magnetic loading device, International Journal of Machine Tools & Manufacture, 71, (2013), pp. 20-25.

[54] G. Quintana, J. Giurana, D. Teixidor, A new experimental methodology for identification of stability lobes diagram in milling operations, International Journal of Machine Tools & Manufacture, 48, (2014), pp. 1637-1645.

[55] N. Suzuki, Y. Kurata, T. Kato, R. Hino, E. Shamoto, Identification of transfer function by inverse analysis of self-excited chatter vibration in milling operations, Precision Engineering, 36, (2012), pp. 568-575.

[56] K. Ohnishi, Disturbance observer-based robust motion control, Journal of the Robotics Society of Japan, 11(4), (1993), pp. 568-575. (in Japanese)

[57] K. Ohnishi, Estimation, identification and sensor-less control in motion control system, Proceeding of the IEEE, 82(8), (1994), pp. 253-265.

[58] A. Matsubara, Control theory for precise positioning and stage system design, Morikita publishing, (2008), pp. 123-142.

[59] S. Takakura, T. Murakami, K. Ohnishi, An approach to collision detection and recovery motion in industrial robot, Proceeding of IEEE Int. IECON '89, 2, (1989), pp. 421-426.

[60] E. O. Brigham, The fast Fourier transform, Prentice-Hall, (1994), pp. 3, 148-154.

[61] Y. Mitani, Information mathematics, CQ publishing, (2008), pp.239-304.

[62] E. Jacobsen, R. Lyons, The sliding DFT, IEEE Signal Processing Magazine, 20, (2003), pp. 74-80.

[63] http://www.nvidia.com/object/cuda_home_new.html, November 11, 2015, NVIDIA Corporation's homepage.

[64] R. Farber, CUDA application design and development, Waltham, Mass: Morgan Kaufmann/Elsevier, (2011), pp. 8-11.